Responsive Shift Probes for Magnetic Resonance

HARNDEN, ALICE,CLAIRE

Responsive Shift Probes for Magnetic Resonance

Alice Claire Harnden

A thesis submitted for the degree of Doctor of Philosophy

2018

Abstract

Magnetic resonance chemical shift imaging can provide chemical information about biological tissue. However, ^{1}H MR shift imaging *in vivo* is a much less exploited technique than standard MRI, due to the presence of strong NMR signals from water and fat. Paramagnetic lanthanide(III) complexes, in which a *tert*-butyl reporter group is incorporated, can be used to shift a proton resonance ±80 ppm from the water signal allowing selective observation. The proximity of the paramagnetic lanthanide(III) ion enhances the longitudinal relaxation rates of the surrounding nuclei, permitting faster data acquisition per unit time.

The chemical shifts of paramagnetically shifted proton resonances, within kinetically stable macrocyclic lanthanide(III) complexes, inherently encode temperature information. The introduction of a phosphonate group adjacent to the *tert*-butyl reporter group introduces pH responsive behaviour. The dual sensitivity of such probes has allowed the simultaneous triple imaging of the water signal and the shifted *tert*-butyl signals of thulium(III) and dysprosium(III) complexes of a common ligand, separated by over 160 ppm. Spectral imaging experiments *in vivo* allow the pH and temperature of the liver, kidney and bladder to be measured within a mouse model. Further modification of the ligand structure changes the biodistribution profile of the complex whilst maintaining and even improving the chemical shift and relaxation rates of the probe.

In-depth structural and NMR analysis of a series of lanthanide complexes based on different ligand motifs has demonstrated that the MR properties of a paramagnetic complex cannot be readily predicted using the longstanding theories of shift and relaxation. Seemingly small modifications to ligand structure can significantly alter the size, magnitude, sign and orientation of the magnetic susceptibility tensor.

Finally, introduction of a specific zinc(II) ion chelating agent adjacent to the *tert*-butyl reporter group has created the first zinc(II) responsive paramagnetic probe for proton magnetic resonance spectroscopy. The strong and selective binding of zinc(II) was shown to be reversible.

Declaration

The research described herein was carried out at the Department of Chemistry, Durham University between October 2015 and December 2018. All of the work is my own, except where otherwise stated. No part has been previously submitted for a degree at this, or any other, university.

Statement of Copyright

Acknowledgements

Firstly, I would like to thank my supervisor, Prof. David Parker, for the opportunity to carry out this project and for his guidance and support over the last 3 years.

Within the Chemistry Department: A special thanks goes to the solution state NMR service, Dr. Alan Kenwright, Dr. Juan Aguilar, Catherine Heffernan and Dr. Raquel Belda-Vidal for letting me loose on the spectrometers, all their help with NMR and useful chats. The mass spectrometry service; Dr. Jackie Mosely, Pete Stokes and Dr. Dave Parker, thank you for putting up with my thousands of samples. Thank you to Dr. Andrei Batsanov and Dr. Dmitry Yufit in crystallography for their help with X-ray structural analysis. Thanks to Dr. Mark Fox for the DFT calculations. Thanks to Annette Passmoor, Gary Southern and all the stores and technical team for keeping me supplied with solvents and all the lab attendants for the daily supply of tea.

I would like to thank my collaborators for their contributions to this project: Prof. Andrew Blamire, Ian Wilson and Dr. Dara O'Hogain, at the Newcastle Magnetic Resonance Centre, for the phantom and *in vivo* imaging studies; Dr. Elizaveta Suturina at Bath University for the computational work

Thanks to Nicola and Katie for helping me settle into PARASHIFT and shaping me into the chemist I have become. I am incredibly grateful for all the life lessons and your continuing advice and friendship. Thank you to Kanthi for her invaluable experience and synthetic assistance throughout my PhD. Thanks to the past and present members of CG27, Laura, Sergey, Andrew, Jack, Ed, Kevin, Matthieu, Emily, Amandine, Adeline, Connor, Hannah, Ryan and Olga for their friendship and support. Thanks to Robek for the supportive coffee chats and letting me write up in your office.

Thanks to my few Durham pals/ex-housemates, Buz, Lillie and in particular Aisha. A special thanks to my friends down south, especially Fran. You have all been so invaluable to me the last three years and have genuinely kept me going.

Finally, the biggest thanks to my family; Mum, Dad, Kate and Brian, for their (mostly) unwavering support throughout my education and for keeping me supplied with pictures of Cleo.

List of Abbreviations

3DGE	three-dimensional gradient echo
Ar	aromatic
at	acquisition time
BMS	bulk magnetic susceptibility
BOC	*tert*-butoxycarbonyl
br	broad (NMR)
BRW	Bloch-Redfield-Wangsness
CEST	chemical exchange saturation transfer
CSI	chemical shift imaging
cyclen	1,4,7,10-tetraazacyclododecane
d, dd	doublet, doublet of doublets (NMR)
DFT	density functional theory
DO3A	1,4,7-tris(carboxymethyl)-1,4,7,10-tetraazacyclododecane
DOTA	1,4,7,10-tetraazacyclododecane-1,4,7,10-tetraacetic acid
DOTMA	tetramethyl-1,4,7,10-tetraazacyclododecane- 1,4,7,10-tetraacetic acid
DOTP	1,4,7,10-tetraazacyclododecane-1,4,7,10-tetrakis(methylene phosphinate)
DPA	dipicolylamine
DPTA	diethylenetriaminepentaacetic acid
dt	delay time
EDTA	ethylenediaminetetraacetic acid
EXSY	exchange spectroscopy
FWHM	full width half maximum
HMBC	heteronuclear multiple bond correlation
HPLC	high pressure/performance liquid chromatography
HRMS	high resolution mass spectrometry
HSQC	heteronuclear single quantum coherence spectroscopy
LCMS	liquid chromatography mass spectrometry
Ln	lanthanide
m	multiplet (NMR)
*m*CPBA	*meta*-chloroperbenzoic acid
MR	magnetic resonance
MRI	magnetic resonance imaging
MRS	magnetic resonance spectroscopy
NMR	nuclear magnetic resonance
NOE	nuclear Overhauser effect
NOESY	nuclear Overhauser effect spectroscopy
nt	number of transients
PARACEST	paramagnetic chemical exchange saturation transfer

PARASHIFT	PARAmagnetically SHIFTed
PCS	pseudocontact shift
PFC	perfluorocarbon
PPA	phenylphosphonic acid
q	complex hydration number
R_1	longitudinal relaxation rate, = $1/T_1$
R_2	transverse relaxation rate, = $1/T_2$
RF	radio frequency
ROI	region of interest
s	singlet (NMR)
SAP	square antiprism
SBM	Solomon-Bloembergen-Morgan
SNR	signal-to-noise
SVS	single voxel spectroscopy
SW	spectral width
t	triplet (NMR)
T_1	longitudinal relaxation time
T_2	transverse relaxation time
TACN	1,4,7-triazacyclononane
TE	echo time
TFA	trifluoroacetic acid
TFAA	trifluoroacetic anhydride
THF	tetrahydrofuran
THP	2-tetrahydropyranyl group
TLC	thin layer chromatography
TOCSY	total correlated spectroscopy
TPA	trispicolylamine
TR	repetition time
TSAP	twisted square antiprism

Table of Contents

1. Introduction

Magnetic resonance (MR) is one of the most important tools in diagnostic medicine and biomedical research due to its ability to give anatomical information of the soft tissue with high spatial resolution. It is a non-ionising technique that measures the signals from relaxing nuclei to distinguish between different environments within the body.

The nucleus typically observed in clinical magnetic resonance imaging is ^{1}H which, within water, makes up over 50% of the atoms in the body. Additionally, the ^{1}H nucleus is a good candidate for MR detection owing to its 100% natural abundance, simple nuclear spin angular momentum (I = ½) and high gyromagnetic ratio (γ = 42.6 MHz T^{-1}), arising from the presence of a large magnetic moment.

The signal intensity within an MRI image is dependent on the proton density and the longitudinal (T_1) and transverse (T_2) nuclear relaxation times of protons within a biological tissue. Pulse sequences can be designed to emphasise variations in T_1 or T_2 and can be referred to as T_1-weighted or T_2-weighted scans. Proton density, T_1 and T_2 values vary between different biological tissues, and it is these differences that enable tissue discrimination.

Whilst MRI is an important and powerful clinical imaging technique, the information gained from such scans is indirect, only the bulk water of tissue is imaged. The direct imaging of metabolic processes or endogenous probes is challenging, owing to the inherently low sensitivity of the NMR experiment. The lack of sensitivity leads to poor resolution, poor contrast and long scan times.

1.1 Contrast-enhanced MRI

Current MRI contrast agents available clinically are synthetic probes used to enhance contrast in MRI scans. The agents are not visualised directly, rather the contrast enhancement arises from the modulation of the relaxation rates of water protons in close proximity to the agent. T_1 contrast agents generally increase the longitudinal relaxation rates, R_1 (R_1= 1/T_1), of the surrounding water molecules, increasing the MRI

signal intensity in regions where the probe accumulates, referred to as positive contrast. Conversely, T_2 agents increase the transverse relaxation rates, R_2 ($R_2 = 1/T_2$), of protons thus yielding a reduction in MRI signal in areas of higher probe concentrations, known as negative contrast. The change in contrast an MRI probe produces is dependent on its effectiveness in enhancing the surrounding protons' relaxation rates (relaxivity) and the concentration of the probe in that location.

Most clinically used MRI contrast agents are T_1 agents, due to their positive image contrast. Typically, these probes are complexes of paramagnetic metal cations. The large oscillating magnetic moments arising from the unpaired electrons of such complexes provide additional relaxation mechanisms for surrounding protons. The trivalent lanthanide cations are an obvious choice for T_1-weighted contrast agents due to their large number of unpaired electrons. Gadolinium(III) is the metal ion present in all lanthanide-based contrast agents currently in clinical use, as it has the highest spin paramagnetism arising from seven unpaired electrons. However, it does not possess the largest magnetic moment of the lanthanides with both dysprosium(III) and holmium(III) displaying larger moments due to orbital contributions to angular momentum.[1] The electronic states of Dy^{3+} and Ho^{3+} are asymmetric, causing rapid electronic spin relaxation rates, whereas the isotopic distribution of electrons in Gd^{3+} leads to a symmetric S state. This symmetry gives rise to a much slower electronic spin relaxation rate that is much closer to the proton Larmor frequency and this allows faster relaxation of surrounding proton nuclei. The efficiency of a contrast agent to enhance the relaxation rates of protons with respect to the contrast agent concentration is referred to as relaxivity. The relaxivity is dependent on several factors, including the number of metal bound water molecules (q) and the mean residence time of bound water.

The Gd^{3+} aqua ion is toxic ($LD_{50} \approx 0.1$ mmol/kg) due to its similar size to Ca^{2+}, which is vital in cell signalling processes; hence the need to encapsulate the cation within a kinetically and thermodynamically stable multidenate ligand or chelate.[2] Due to the core-like nature of the 4*f* orbitals and their large ionic radius, the trivalent lanthanide ions favour complexes with high coordination numbers of 8 or 9. For imaging purposes these ligands are typically based upon polyaza-carboxylate ligands and may be acyclic (e.g. DPTA) or cyclic (e.g. DOTA) in nature (Figure 1.1). The majority of agents in clinical

use are non-specific extracellular agents, which distribute throughout the plasma and interstitial space in the body. They are typically excreted via the kidneys with a half-life of about 1.5 h.[1]

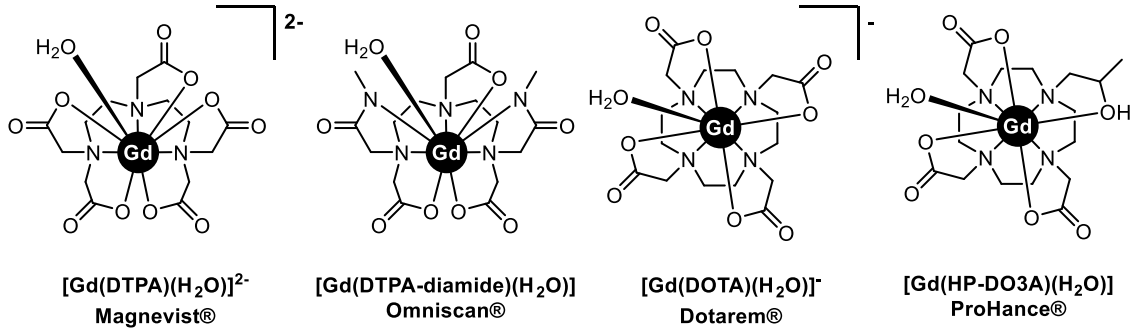

Figure 1.1 Structures of selected DPTA- and DOTA- based clinically-approved Gd^{3+}-based contrast agents.

1.2 Magnetic Resonance Spectroscopy

Magnetic Resonance Spectroscopy (MRS) is the clinical use of NMR spectroscopy. The presence and relative concentrations of analytes are probed directly by NMR within a region of interest (ROI), rather than looking at the bulk water signal. Unlike traditional MRI, which only yields structural images, MRS provides direct biochemical information on tissue using the frequencies (chemical shift) and relative intensities (integrals) of the observed NMR signals of metabolites (or exogenous probes).

MRS may be performed on a single voxel (single voxel spectroscopy - SVS) or multiple voxels (magnetic resonance spectroscopic imaging - MRSI or chemical shift imaging - CSI). Protons are the ideal nuclei for use in *in vivo* spectroscopy due to their high natural abundance in tissues and high magnetic sensitivity compared to other magnetically active nuclei. However, the intense background ^{1}H signals arising from the high concentrations of water and fat found in tissues require the use of signal suppression techniques to ensure other resonances of interest can be detected. Spectra must typically be run with water suppression and currently this technique has found most use in studies of the brain.[3]

1.3 Heteronuclear MRS

One method of avoiding the endogenous background signal problems arising from ^{1}H MRS is to perform heteronuclear MRS instead. Any NMR active ($I > 0$) nucleus, such as ^{31}P, ^{13}C, and ^{19}F, of endogenous metabolites or exogenous probes can be measured to report tissue information.

1.3.1 ^{31}P MRS

Initial studies into heteronuclei focused on ^{31}P due to its I = ½ nuclear spin, 100% natural abundance, large NMR shift range and biological relevance. Although the spectroscopic sensitivity of ^{31}P is lower than ^{1}H, the measurement of phosphorus-containing metabolites in the millimolar range has been achieved. The quantitative measurement and ratios of certain metabolites, such as adenosine triphosphate (ATP), phosphocreatine (PCr) and inorganic phosphate (Pi), can reveal various pathologies.[4–7]

The frequency of the ^{31}P chemical shift has also been utilised to measure pH *in vivo* non-invasively. Moon and Richards demonstrated that the difference between the two ^{31}P chemical shifts of the glycolytic intermediate 2,3-diphosphoglycerate (2,3-DPG – Figure 1.2) can be used as a measure of pH.[8] *In vitro* experiments showed that the relative shift separation of the 2-phosphate (pK_a = 7.0) and 3-phosphate (pK_a = 6.3) resonances varied by 1 ppm between pH 5 to 8 and could be used to estimate the intracellular pH of erythrocytes. However, both resonances experience a large chemical shift change upon interaction with deoxyhaemoglobin, resulting in the requirement of an additional calibration step in order to accurately measure pH. Numerous additional pH-sensitive phosphorus metabolites have been identified and studied as potential intra- and extra-cellular pH indicators; including, PCr, Pi and 3-aminopropylphosphonate (3-APP – Figure 1.2).[9,10]

Phenylphosphonic acid (PPA – Figure 1.2) has also been proposed as an exogenous ^{31}P MRS probe of extracellular pH *in vivo*. *In vitro* experiments on muscle tissue perfused with sodium phenylphosphonic acid enabled the measurement of pH between 6.4 -7.6, as the phosphonate ^{31}P resonance shifted 1.12 ppm per pH unit. An additional benefit of the use of PPA is that the ^{31}P chemical shift is found at 12.8 ppm which is relatively isolated from endogenous phosphorus-containing compounds.

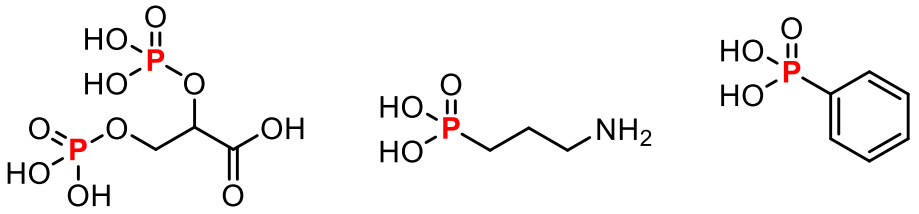

Figure 1.2 Structures of selected pH responsive ^{31}P MRS indicators.

1.3.2 ^{13}C MRS

Carbon is one of the most abundant elements in biology and the use of MRS to monitor metabolites *in vivo* is an attractive prospect. The larger chemical shift range allows for improved resolution compared to ^{1}H MRS. However, the natural abundance of the magnetically active ^{13}C (I = ½) is only 1.1% and the magnetic sensitivity of the nucleus is also diminished compared to ^{1}H. Thus, the intrinsic signal-to-noise ratio (SNR) of ^{13}C is much lower compared to ^{1}H and ^{31}P. There are two methods by which the sensitivity of ^{13}C MRS can be improved: labelling and hyperpolarisation.

Exogenous isotope labelling of ^{13}C into metabolic substrates such as glucose, lactate and acetate allows for imaging of these compounds and their metabolic pathways with effectively zero background.[11] Increasing the abundance of ^{13}C through isotopic labelling can be challenging and expensive. Additionally, even labelled species suffer from the inherently lower magnetic sensitivity of the ^{13}C nucleus so that long scan times are still required.

To further enhance the NMR response and increase the SNR of ^{13}C, hyperpolarisation of the nuclear spins can be achieved. Hyperpolarisation allows the imaging of nuclei that have much lower sensitivity (low γ). In the case of ^{13}C, hyperpolarisation is usually accomplished by dynamic nuclear polarisation (DNP). The technique utilises microwave irradiation to transfer polarisation from unpaired electrons to nuclei. It is carried out at low temperature (< 4 K), at 3 T and the presence of a free radical doping agent is required. The signal of such nuclei can be enhanced for a short period of time by more than 10,000-fold.[12]

Hyperpolarised ^{13}C-labelled metabolites provide the potential for mapping metabolic process and pathways. Several *in vivo* studies have evaluated the distribution of [1-^{13}C]pyruvate and its metabolic products, lactate, alanine and bicarbonate.[13–15] Whilst the technique shows promise, the polarised spins are unstable and will relax back to thermal equilibrium according to the longitudinal relaxation rates. Hence, scans must be completed within minutes after hyperpolarisation, limiting the clinical application of ^{13}C MRS.

1.3.3 Noble Gas MRI

Hyperpolarisation has also been utilised to image other magnetically active heteronuclei. The use of hyperpolarised gases allows the direct visualisation of the airspace of the lung (Figure 1.3). Inert noble gases such as ^{3}He and ^{129}Xe (I = ½) are typically hyperpolarised by spin-exchange optical polarising (SEOP).[16] Although ^{3}He has a higher magnetic sensitivity, the low natural abundance has led to the increased use of ^{129}Xe which accounts for 26% out of the 9 naturally abundant isotopes. Subjects inhale the isotopically enriched, hyperpolarised gas and images must be acquired within a single breath hold.[17,18]

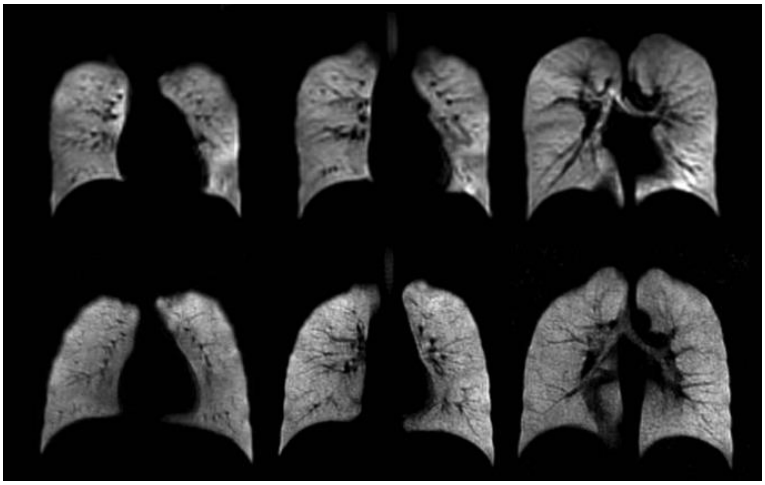

Figure 1.3 Ventilation MRI images of healthy lungs with ^{3}He (top row) and ^{129}Xe (bottom row).[17]

1.3.4 ^{19}F MRS

The ^{19}F nucleus (I = ½) is a promising candidate for heteronuclear MRS. It has the highest magnetic sensitivity of all heteronuclei and is 100% naturally abundant. An

additional advantage of ^{19}F is its trace presence *in vivo*. Whilst, there are high local concentrations of fluorine found in the bones and teeth, it is not visible by conventional MR methods due to extremely short T_2 arising from immobilisation.[19] This lack of background signal means that the ^{19}F resonances of fluorinated probes offer much higher SNR than ^{1}H and ^{31}P based probes. ^{19}F NMR has previously been used to track the *in vivo* drug metabolism of fluorine atom-containing therapeutics, including that of the prodrug 5-fluorocytosine (5-FC). A study in 1999 found ^{19}F NMR to be a non-invasive method to observe the enzyme-catalysed conversion of the prodrug into the chemotherapeutic agent 5-fluorouracil (5-FU).[20] However, the *in vivo* experiments required a large dosage in order to give acceptable image quality. A serum concentration of ~900 mg/L was required, whereas in humans a maximum serum concentration of ~50 mg/L is recommended.[21]

As with all MR techniques ^{19}F NMR has inherently low sensitivity and to achieve an image with a sufficiently high SNR, either the concentration of the nucleus must be high or an increase in the number of transients of the pulse and acquisition sequence is needed. Increasing the number of nuclei present either per molecule of probe or through packaging a greater number of probe molecules into nanoparticles has been shown to have a direct effect on sensitivity.[22,23] Probes such as perfluorocarbons (PFCs), which are simple organic compounds in which all the hydrogen atoms have been substituted by fluorine, increase the number of ^{19}F nuclei per probe. However, perfluorotributylamine (PFTA) and other PFCs such as perfluorooctylbromide (PFOB) suffer from the appearance of chemical shift artifacts which arise from the presence of inequivalent ^{19}F environments. In MRI, spatial position is frequency encoded in one direction, so when two differently shifted systems are in the same location they are seen at different frequencies, hence are not located in the same place within the image. There are NMR techniques that can reduce these effects,[24,25] but more recent developments of simple organic ^{19}F probes have focused on symmetrical perfluoropolyethers, due to the presence of many equivalent nuclei which give a single sharp resonance in the ^{19}F NMR.[26,27] These PFCs have the advantage of being chemically inert and non-toxic. However, they are usually extremely insoluble in water and hence have to be emulsified before being locally injected.[19]

Increasing the number of scans is not usually a practical option without vastly increasing total overall scan times. This is particularly true for small diamagnetic compounds in which the observed ^{19}F nucleus has a long longitudinal relaxation time, T_1. The longitudinal relaxation time determines the delay time between each pulse. A delay time approximately 5 times that of the T_1 is typically required to ensure full recovery of net magnetisation before the subsequent pulse. Therefore, the repetition time of the pulse sequence is long, with a significant proportion of 'dead time' where no data is being acquired (Figure 1.4).

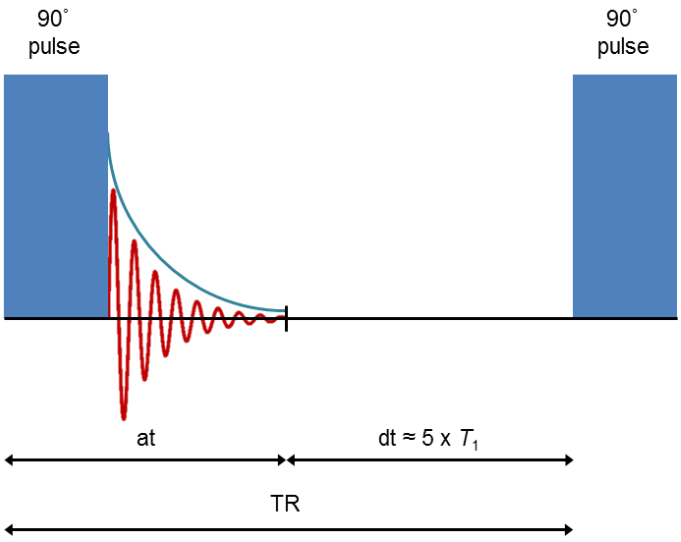

Figure 1.4 Example of a simple MRS pulse sequence where at = acquisition time, dt = delay time and TR = repetition time. The total scan time is given by n(TR).

A solution to this problem would be to increase the relaxation rate of the nucleus to allow for rapid pulsing, giving a shorter pulse repetition time and thus increasing the number of scans that can be taken per unit time. This has been achieved by the incorporation of a standard gadolinium contrast agent into the lipid monolayer surrounding a liquid PFC core, creating a nanoparticle that could be administered in a water soluble emulsion. The method was found to shorten the ^{19}F T_1 by up to 75%, but had a larger effect on T_2. The linewidth of the signals increased drastically, decreasing the observed signal intensity.[28] Another method is to introduce ^{19}F nuclei into a kinetically stable paramagnetic complex (Figure 1.5). The effects of paramagnetism on the NMR properties of surrounding nuclei are discussed in further detail in Sections 1.4 and 1.5.

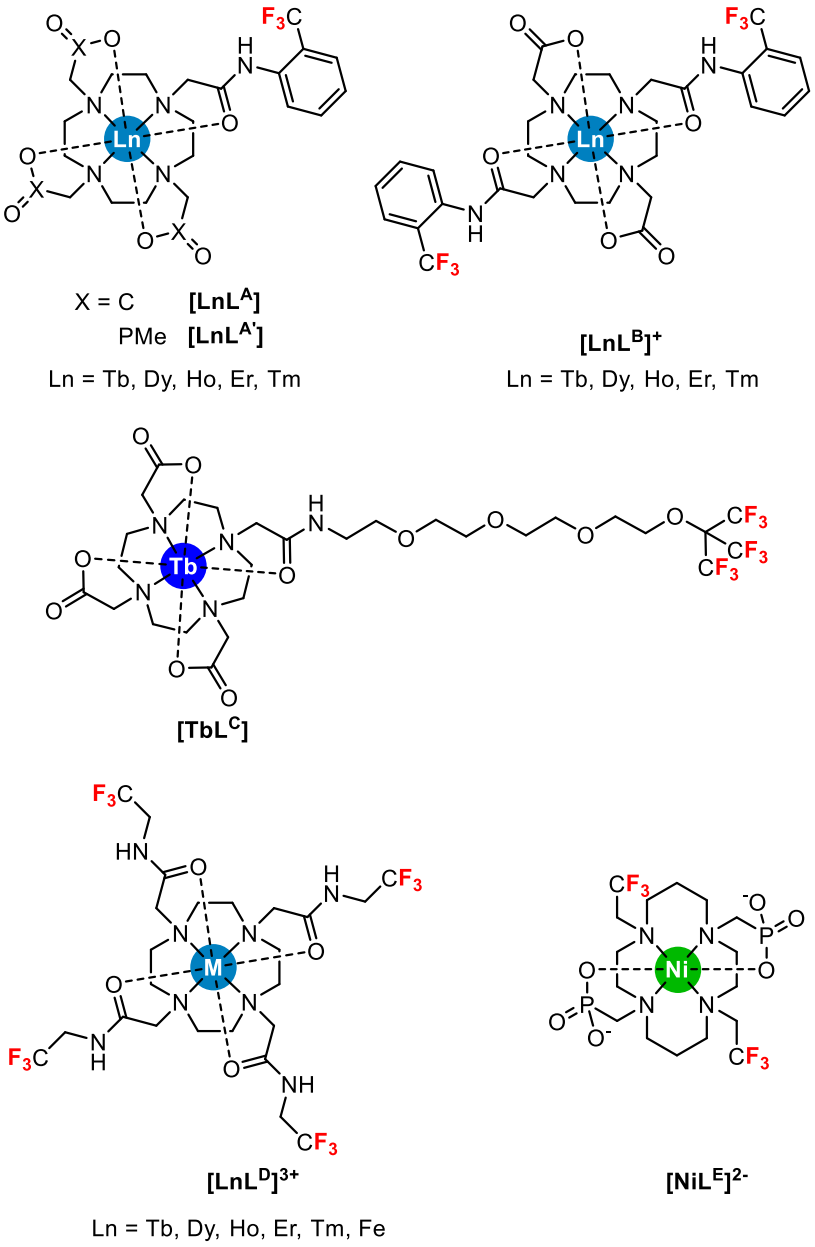

Figure 1.5 Structures of selected paramagnetic ^{19}F probes.

Incorporation of CF_3 reporter groups within paramagnetic complexes results in the enhancement of the chemical shift and relaxation rates of the ^{19}F nuclei. Parker and co-workers designed a number of ^{19}F MRS probes based on lanthanide complexes of 1,4,7,10-tetraazacyclododecane (cyclen).[29–37] The paramagnetic complexes of **[LnL^A]$^+$** (Figure 1.5), a CF_3-labelled mono-amide derivative of the tricarboxylate macrocycle (DO3A), increased the longitudinal relaxation rate of the reporter nuclei dramatically compared to the diamagnetic species.[32] However, the presence of diastereoisomers of the complex resulted in multiple ^{19}F resonances. The modification of ligand from carboxylate to methylphosphinate, **[LnL$^{A'}$]$^+$** (Figure 1.5), both increased the signal intensity of the major species and resulted in faster nuclear relaxation. The

dicarboxylate analogue, **[LnL^{B}]** (Figure 1.5), was also investigated, as the C_2 symmetric complex should double the number of equivalent ^{19}F nuclei.[32]

A different method to maximise ^{19}F nuclei within a probe was explored by Yu and co-workers.[38] The perfluoro-*tert*-butyl group of **[LnL^{C}]**, appended to a DO3A macrocycle via an oxyethylene chain, gave a single resonance corresponding to the 9 equivalent protons.[38] Modest increases in relaxation rates were found upon complexation with paramagnetic ions such as Gd^{3+}, Tb^{3+} and Cu^{2+}. The authors suggested that the probe could be used as a multi-chromic ^{19}F tracer by following different metal complexes independently by the different chemical shifts of the ($C(CF_3)_3$) reporter group. However, due to the length of the oxyethylene linker, the chemical shift variance across the entire series tested was <8 ppm. The *in vivo* measurement of paramagnetically broadened resonances with such small frequency variations would be difficult to achieve. The tetra-amide, C_4-symmetric complex **[LnL^{D}]$^{3+}$** has been proposed as a potential probe for ^{19}F.[39] The complex contains 12 magnetically equivalent ^{19}F nuclei that exist as a single resonance. It was found that the Fe^{2+} complex demonstrated the most potential as an imaging probe due to its favourable relaxation properties. Recently, ^{19}F-containing, paramagnetic Ni^{2+} complexes, such as **[LnL^{E}]$^{2-}$**, have also been investigated.[40,41]

In general, the successes of heteronuclear imaging, as described above, have largely failed to translate to clinical use. The use of isotope enrichment and hyperpolarisation methods are technically demanding and expensive, preventing widespread use of nuclei with extremely low natural sensitivity. MRS of heteronuclei with higher sensitivities, such as phosphorus and fluorine, still suffers from reduced sensitivity when compared to proton scans. Additionally, the imaging of heteronuclei requires specialist coils associated with non-proton MRI.[42] As such, protons remain the ideal nuclei for use for *in vivo* spectroscopy due to the ability to use existing clinical scanners with no hardware modifications.

1.4 The effect of paramagnetism on chemical shift

Direct detection by MRS of a proton-containing tracer molecule is possible, even at low concentration, by exploiting the paramagnetic shift phenomenon encountered in

metal complexes with an anisotropic magnetic susceptibility. The reporter signal can be shifted away from the diamagnetic window (0 – 12 ppm), allowing its visualisation against a zero background (Figure 1.6).

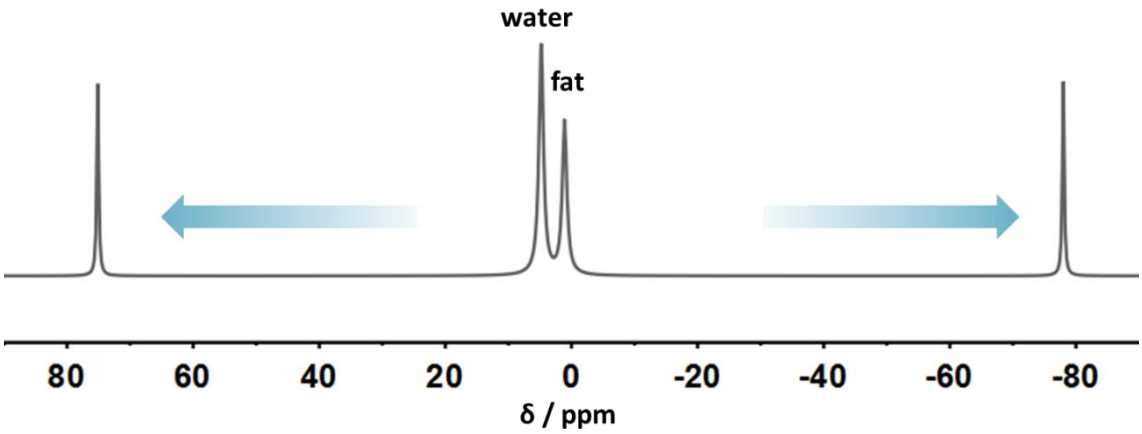

Figure 1.6 Schematic demonstrating paramagnetically-shifted ^{1}H proton resonances away from the diamagnetic window (containing water and fat resonances) against zero background.

The effect of paramagnetic species on NMR signals has been noted since the very beginnings of NMR.[43–46] In the 1950s, Bloembergen and Dickinson observed unexpected shifts in the NMR resonances of paramagnetic solutions, and subsequently suggested that *some* paramagnetic ions possess magnetic anisotropy, i.e. the magnitude of the electron-induced magnetic susceptibility varies with orientation (Figure 1.7).[47] A nucleus 'sees' the time-averaged magnetic moment of unpaired electrons, which is non-zero when the populations of the electronic states are not equal to one another. Such a situation occurs when there is a Boltzmann distribution across different low-lying energy states, e.g. across the crystal-field splitting in the *J* manifold in *f*-block compounds, or due to zero-field splitting and spin-orbiting coupling in *d*-block systems.

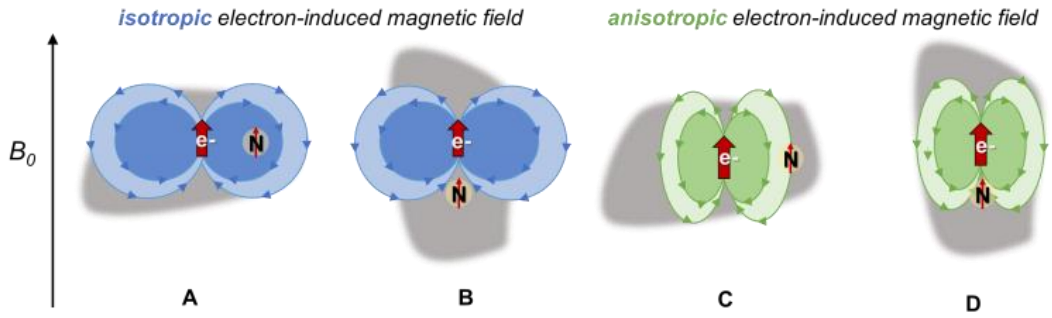

Figure 1.7 The nucleus 'N' feels the dipolar magnetic field of an unpaired electron 'e-', which subtracts (A, C) or adds (B, D) to the external field. Rotational motion averages these to zero for isotropic fields (A, B) but to non-zero for anisotropic fields (C, D).

Unpaired electrons of paramagnetic compounds can therefore produce a large, temperature-dependent contribution to the observed shift (δ_{obs}) of a nucleus, which adds to the orbital diamagnetic (δ_{dia}) term, and is often referred to as the hyperfine shift. Although there are many possible contributions to the hyperfine shift, only the pseudocontact term (δ_{PCS}) and/or the Fermi contact term (δ_{FCS}) are usually considered, as other contributions are negligible (Equation 1.1):

$$\delta_{obs} = \delta_{dia} + \delta_{FCS} + \delta_{PCS} \qquad (1.1)$$

The Fermi contact contribution, δ_{FCS}, is proportional to the fraction of the unpaired electron spin density present 'in contact' with the nucleus of interest. In molecular orbital theory this can be thought as the value of the square of the electronic wavefunction at a particular nucleus. The pseudocontact term, δ_{PCS}, describes the dipolar interaction (through-space) of the ligand nuclei and unpaired electrons on the metal ion and depends upon the geometry of the complex. A dipolar shift can only occur in complexes that have magnetic anisotropy; the dipolar coupling of isotropic complexes will average to zero with molecular tumbling in solution. In transition metal complexes, generally both δ_{FCS} and δ_{PCS} contribute to the observed chemical shift. However, in lanthanide complexes there is little delocalisation of electrons onto the ligand and so δ_{FCS} is only important for atoms directly bonded to the paramagnetic centre, as it rapidly attenuates with the number of separating bonds.[48]

1.4.1 The pseudocontact shift

A molecule containing unpaired electrons will produce a net magnetisation when placed in a strong magnetic field. This induced magnetisation produces a new magnetic field in the vicinity of the molecule, in addition to the static field of the spectrometer. The magnitude of the additional field at a particular nucleus depends on both the distance of the nucleus from the metal ion and the angle between the nucleus and the principal axes of the magnetic susceptibility tensor of the lanthanide ion, as given by Equation 1.2:[49]

$$\delta_{PCS} = \frac{1}{12\pi r^3}[X_{ax}(3\cos^2\theta - 1) + 3X_{rh}\sin^2\theta\cos 2\varphi] \quad (1.2)$$

where θ, φ and r are the polar coordinates of the nucleus with respect to the principal axis of the magnetic susceptibility tensor, X, and X_{ax} and X_{rh} are the axial and rhombic components of the magnetic susceptibility tensor defined as:

$$X_{ax} = X_{zz} - \frac{1}{2}(X_{xx} + X_{yy}) \quad (1.3)$$

$$X_{rh} = X_{xx} - X_{yy} \quad (1.4)$$

The δ_{PCS} of a particular nucleus within the ligand structure is therefore dependent on its geometry with respect to the principal (easy) axis of the magnetic field. The r^{-3} dependence arises from the dipolar nature of the nucleus-electron interaction and affects the magnitude of the pseudocontact shift. There is also an angular dependency with respect to the principal magnetic axis, usually resulting in a change in both the magnitude and sign of δ_{PCS}. A 3D scalar field can be used to represent the angular dependence of the δ_{PCS} and within the same ligand, depending on their location, nuclei can be shifted in opposite directions. The pseudocontact shift (PCS) field can be modelled using the assigned chemical shifts and solution structure of a given complex. A 'best-fit' traceless susceptibility tensor can then be used to model the axiality, X_{ax}, and rhombicity, X_{rh}, of the anisotropic magnetic susceptibility (Figure 1.8).[50]

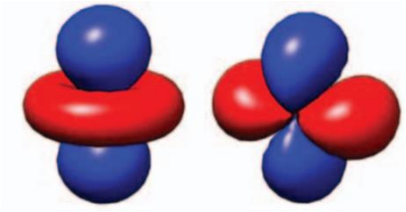

$|\Delta\chi_{rh}| = 0$ $|\Delta\chi_{rh}| = |\Delta\chi_{ax}|/3$

Figure 1.8 Ideal pseudocontact shift (PCS) field representing an ideally axial (*left*) and ideally rhombic (*right*) χ tensor. Positive PCS is shown in red, negative in blue.[51]

The tensor can be described using appropriate Euler angles, typically α, β and γ, which specify the orientation of the susceptibility tensor with respect to the chosen molecular frame.

However, the necessity for full assignment and analysis of the pseudocontact shifts make application of Equation 1.2 challenging and simplification can be achieved through consideration of the electronic energy levels of the lanthanide ion.

The electronic energy levels of lanthanide ions can be described using the Russell-Saunders coupling scheme. For a free lanthanide ion the total spin, *S*, angular momentum, *L*, can be used to give the total angular momentum, *J*. The energy levels can be described by an overall term symbol using these quantum numbers:

$$^{(2S+1)}L_J$$

In the Russell-Saunders coupling scheme, electronic repulsion (spin-spin coupling) is the largest interaction, and spin-orbit coupling further divides these energy levels to different *J* states. Upon complexation within a chelating ligand the electron cloud and symmetry of the lanthanide ion is disturbed, resulting in further 2*J*+1 splitting of the energy levels (m_J states). It is generally assumed that the crystal field splitting is smaller than that of the spin-orbit coupling. The crystal field splitting arises from the perturbation of the lanthanide ion electron cloud by all other electrons in the system (i.e. of the chelating ligand). These electrostatic interactions can be described by the rank crystal field parameters, B_q^k, which are directly linked to the symmetry of the complex.[52] In lanthanide systems k = 0, 1, …, 7; however, only the even values of k are responsible for crystal field splitting. Values of q are limited by the point group of the lanthanide ion, and non-zero (k, q) combinations are restricted and can be determined

from the point group symmetry elements. The crystal field, in some cases, can be determined by detailed examination of the Eu^{3+} emission spectrum.[52,53]

The axiality and rhombicity of the magnetic susceptibility tensor may be described by the second order crystal field parameters and lanthanide ion type by Equations 1.5 and 1.6, first proposed by Bleaney.[54]

$$X_{ax} = -\frac{\mu_0 \mu_B^2 C_J B_0^2}{10(kT)^2} \tag{1.5}$$

$$X_{rh} = -\frac{\mu_0 \mu_B^2 C_J B_2^2}{30(kT)^2} \tag{1.6}$$

where C_J is the Bleaney coefficient for a specific lanthanide, μ_B is the Bohr magneton, B_0^2 and B_2^2 are the second order crystal field splitting parameters. The Bleaney constant, C_J, for a given lanthanide ion can be described by Equation 1.7:

$$C_J = g^2 J(J+1)(2J-1)(2J+3)\langle J|\alpha|J\rangle \tag{1.7}$$

where $\langle J|\alpha|J\rangle$ is a numerical coefficient specific to a particular f^n configuration, g is the electron g-factor (Landé) and J the total angular momentum quantum number.[54] The pseudocontact shift can therefore be more simply expressed by Equation 1.8:

$$\delta_{PCS} = \frac{C_J {\mu_B}^2}{60(kT)^2}\left[\frac{(3\cos^2\theta - 1)}{r^3}B_0^2 + \frac{(\sin^2\theta \cos 2\varphi)}{r^3}B_2^2\right] \tag{1.8}$$

The pseudocontact shift is then proportional to the Bleaney constant, which varies with the electronic configuration of the lanthanide ion. Thus, the direction (sign) and magnitude of δ_{PCS} can be manipulated through lanthanide selection (Table 1.1).

Table 1.1 Overview of parameters affecting the pseudocontact shift for the ground states of selected lanthanide(III) ions.[54]

Ln^{3+}	$4f^n$	Ground state term	J	g	$\langle J\|\alpha\|J\rangle$	C_J	C_J[a] normalised
Eu	f^6	$^7F_0$	0	0	-[b]	-[b]	4[b]
Gd	f^7	$^8S_{7/2}$	7/2	2	0	0	0
Tb	f^8	$^7F_6$	6	3/2	-0.0101	-157.5	-87
Dy	f^9	$^6H_{15/2}$	15/2	4/3	-0.00635	-181	-100
Ho	f^{10}	$^5I_8$	8	5/4	-0.00222	-71.2	-39
Er	f^{11}	$^4I_{15/2}$	15/2	6/5	+0.00254	-58.8	+33
Tm	f^{12}	$^3H_6$	6	7/6	+0.0101	95.3	+53
Yb	f^{13}	$^2F_{7/2}$	7/2	8/7	+0.0318	39.2	+22

[a] The normalised (to Dy^{3+} = -100) values of C_J are typically quoted.

[b] The ground state of Eu^{3+} exhibits no angular momentum however thermal population of low lying excited states sees anisotropy arising from J=1 and J=2 states.[54]

Bleaney's theory has proved to be a useful approximation for estimating the pseudocontact shifts of nuclei within a paramagnetic complex. However, several assumptions are made that should be considered and scrutinised.

Firstly, in both Equations 1.2 and 1.8, the dipole of the unpaired electrons of the lanthanide ion is considered to be located at a single point on the lanthanide nucleus. The metal-centred point-dipole approximation fails to accurately evaluate the spatial distribution of the electron spin. The approximation has the greatest impact on nuclei in close proximity to the lanthanide ion. Recently, numerical methods have been utilised to better describe the distribution model of the *f*-electron density probability functions.[55–57] The quadrupole approximations of the *f*-electron charge clouds were modelled by Rinehart and Long using the angular dependencies of the 4*f* orbitals. The shape was found to vary between prolate (axially extended) and oblate (equatorially expanded) across the lanthanide series.[58] The variation across the series explains the change in sign seen in the magnetic anisotropy, as predicted by the Bleaney constant, C_J.

Bleaney's theory relies on the approximation that the ligand field splitting is much less than kT (205 cm^{-1} at 298 K), whilst also ignoring the contribution of higher order ligand field parameters. It has been shown that values of B_0^2 can be as high at 1500 cm^{-1} and

typically coordination complexes have B_0^2 values at least double kT.[59,60] The higher order crystal field terms that contribute to the overall crystal field splittings (e.g. B_0^4, B_0^6) are completely neglected by Bleaney's theory. Inclusion of these higher order parameters has been shown to result in large disparities from the use of only the second order parameters, especially in complexes of lower symmetry.[61–64] With larger ligand field splitting, the Russell-Saunders coupling scheme may not be appropriate for the relatively heavy lanthanide elements. As the ligand field splitting energies become of similar magnitude to the spin-orbit coupling energies, *J*-mixing can occur. The uncertainty of the energy levels increases and the quantum number *J*, used to calculate C_J, can no longer be assumed to be a 'good' quantum number.

It was also assumed by Bleaney that within an isostructural series of complexes the position of the magnetic axis does not vary with lanthanide. In this case, the pseudocontact shift for a given nucleus should only vary linearly with C_J. Recent studies have unequivocally demonstrated this assumption to be false.[50,60,65–67] Whilst in some circumstances the pseudocontact shift variation can be explained by dramatic structural variations,[68] in many cases there is no obvious explanation for the anomalous shift behaviour.

In complexes with small crystal field splittings it might be expected that the assumptions of Bleaney's were reasonable. However, in the case of a series of lanthanide complexes of a C_3-symmetric, 1,4,7-triazacyclononane-based (TACN) ligand, **[LnL^F]**, the magnitude and sign of the ^{1}H chemical shifts did not correlate with Bleaney's theory (Figure 1.9).[69] In particular, for the Dy^{3+} analogue the observed pseudocontact shift was found to be the opposite sign to that expected. Additionally, a large solvent dependence of the chemical shifts was observed beyond that expected from the diamagnetic Y^{3+} complex. Through CASSCF-SO and DFT calculations it was shown that a small change in angle (1°) of the three axial oxygen donors could induce significant variation to the magnetic susceptibility. The donor atom angle was found to vary between lanthanides and was hypersensitive even to solvent polarity.

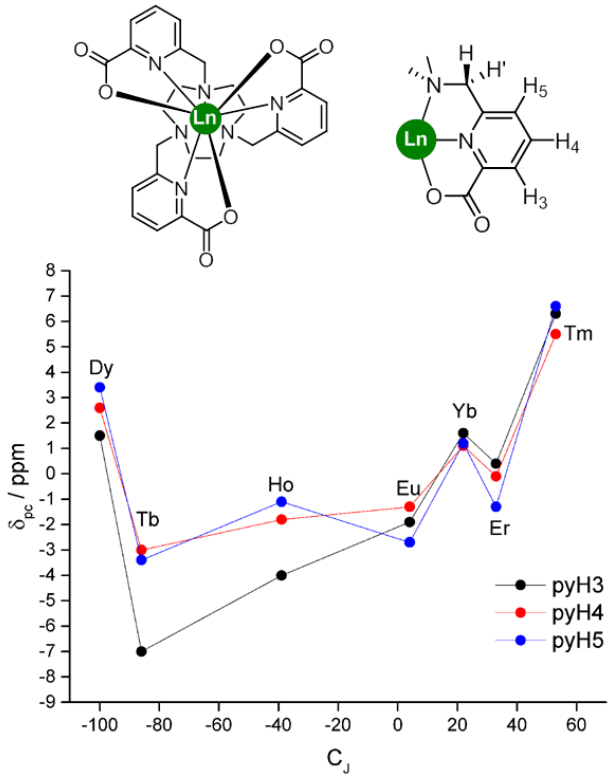

Figure 1.9 (*Top*) Structure of **[LnL^F]** and pyridine assignments. (*Bottom*) Variation of the ^{1}H pseudocontact shifts of the three pyridyl resonances of **[LnL^F]** as a function of the Bleaney constant, C_J (D_2O, 295 K).[69]

1.4.2 Employing Paramagnetic Shift

Due to the large chemical shifts induced by the anisotropy of the magnetic susceptibility and predictable coordination chemistry of the trivalent lanthanides, they offer a great deal of potential as paramagnetic ions for NMR applications. The early 1970s saw an increased interest in the systematic application of paramagnetic shift reagents as tools for the organic chemist to elucidate NMR spectra of molecules with a large number of overlapping resonances,[70,71] and enantiomerically pure lanthanide complexes have since been used as chiral shift reagents.[72,73] Paramagnetic shift agents have also been employed for solid state protein structural elucidation,[74,75] and have been investigated as potential *in vivo* shift agents for $^{23}Na^+$.[76]

Paramagnetically shifted proton signals, such as nuclei in the local chelating ligand structure of a paramagnetic metal centre, can resonate at frequencies significantly shifted away from the usual diamagnetic range, enabling PARAmagnetically SHIFTed MRI probes, coined 'PARASHIFT' probes, to be imaged *in vivo*.[77] Paramagnetic-induced hyperfine shifts have also been exploited in the field of Chemical Exchange Saturation

Transfer (CEST) imaging over the last 20 years,[78–80] although the long scan times, continual irradiation with saturating frequencies, and problems associated with inhomogeneities in the field, limit the potential use of 'PARACEST' in humans.

1.5 The effect of paramagnetism on nuclear relaxation

In addition to the hyperfine shift, paramagnetic centres can also enhance the relaxation rates of surrounding nuclei, which can be exploited to enhance sensitivity. The unpaired electrons provide addition relaxation mechanisms compared to analogous diamagnetic systems. In paramagnetic lanthanide complexes there are two dominant relaxation mechanisms; commonly referred to as the dipolar and Curie terms. These contributions both originate from the through-space interactions of the electronic and nuclear magnetic moment dipoles.

The dipolar mechanism describes the dipolar interactions between the magnetic moment of the resonating nucleus and fluctuating electronic magnetic moment of the lanthanide(III) ion. The unpaired electron spins produce fluctuating magnetic fields that can induce nuclear spin transitions as a relaxation pathway. It is dependent on the electronic relaxation rate of the metal ion and rotational correlation time of the molecule.

The Curie term arises from the dipolar coupling between the time-averaged electronic magnetic moment and the nuclear magnetic moment. This time-averaged moment arises from a small difference in the population of energy spin levels according to a Boltzmann distribution. This interaction is not dependent on electronic relaxation as it is already time averaged but does have a dependency on molecular tumbling and the effective magnetic moment.

The paramagnetic relaxation enhancement have classically been described by the Solomon-Bloembergen-Morgan (SBM) equations (Equations 1.9 and 1.10) which are derived from Bloch-Redfield-Wangsness (BRW) theory[81,82] and give a summation of the dipolar and Curie term for both R_1 and R_2.[83–86]

$$R_1 = \frac{2}{15}\left(\frac{\mu_0}{4\pi}\right)^2 \frac{\gamma_N^2 \mu_{eff}^2}{r^6}\left[\frac{7\tau_c}{1+\omega_e^2\tau_c^2} + \frac{3\tau_c}{1+\omega_N^2\tau_c^2}\right] + \frac{2}{5}\left(\frac{\mu_0}{4\pi}\right)^2 \frac{\omega_N^2 \mu_{eff}^4}{(3kT)^2 r^6}\left[\frac{3\tau_r}{1+\omega_N^2\tau_r^2}\right] \quad \begin{matrix} \textit{Dipolar term} \\ \textit{Curie term} \end{matrix} \quad (1.9)$$

$$R_2 = \frac{1}{15}\left(\frac{\mu_0}{4\pi}\right)^2 \frac{\gamma_N^2 \mu_{eff}^2}{r^6}\left[4\tau_c + \frac{13\tau_c}{1+\omega_e^2\tau_c^2} + \frac{3\tau_c}{1+\omega_N^2\tau_c^2}\right] + \frac{1}{5}\left(\frac{\mu_0}{4\pi}\right)^2 \frac{\omega_N^2 \mu_{eff}^4}{(3kT)^2 r^6}\left[4\tau_r + \frac{3\tau_r}{1+\omega_N^2\tau_r^2}\right] \quad \begin{matrix} \textit{Dipolar term} \\ \textit{Curie term} \end{matrix} \quad (1.10)$$

where μ_0 is the vacuum permeability, γ_N is the gyromagnetic ratio of the nucleus relaxing, r is the electron- nuclear distance, τ_r is the rotational correlation time of the molecule, ω_N is the nuclear Larmor frequency, ω_e is the electron Larmor frequency, μ_{eff} is the effective magnetic moment of the lanthanide(III) ion (Equation 1.11) and τ_c is the total correlation time in the absence of chemical exchange (Equation 1.12).

$$\mu_{eff}^2 = g_{Ln}{}^2 \mu_B{}^2 J(J+1) \quad (1.11)$$

$$\tau_c^{-1} = \tau_r^{-1} + \tau_e^{-1} \quad (1.12)$$

in which g_{Ln} is the Landé factor of the fundamental multiplet J of the free Ln^{3+} ion and τ_e is the relaxation time of the electron spin.

Both the longitudinal and transverse relaxation rates are governed by the same parameters and are proportional to the magnetic field strength. At lower fields, the dipolar term dominates. However, with increasing field strengths the Curie term is dominant. Whilst there is a geometric dependence within the SBM relaxation equations, both the dipolar and Curie relaxation mechanisms are assumed to depend only on the nucleus-lanthanide distance and have no angular dependency. However, during the course of the work undertaken in this thesis it has been demonstrated experimentally that this assumption is inadequate and there is a strong angular dependence of both the dipolar and Curie nuclear relaxation rates.[87] This analysis has led to a reappraisal of the key equations used to define paramagnetic relaxation.

1.6 PARASHIFT probes for imaging

In order to be employed as *in vivo* imaging probes, PARASHIFT agents need to be water soluble, stable in solution, and non-toxic at the appropriate imaging concentrations. Compared with other imaging techniques (radionuclear imaging, luminescence imaging) MRI is insensitive and maximising the SNR is integral to probe design. Ideally, the reporting proton resonance must be shifted as far away as possible from the endogenous protons, so that a large excitation bandwidth can be used to allow the use of fast imaging sequences.[77] In addition to the hyperfine shift, paramagnetic centres can also enhance the relaxation rates of surrounding nuclei, which can be exploited to enhance sensitivity. The paramagnetic induced nuclear relaxation gives rise to rapid longitudinal relaxation rates, R_1, facilitating fast-pulsed NMR techniques. An ideal rate is in the region of 100 s^{-1}, allowing for pulse sequences of the order of milliseconds.[33] The linewidth of the reporting resonance, however, needs to be narrow to avoid SNR losses due to T_2.

1.6.1 Lanthanide choice

The selection of the paramagnetic centre affects both the shift and relaxation properties of the PARASHIFT probe. From Equation 1.8 (see Section 1.4.1, page 15) we can see that that the Bleaney constant of a metal will affect both the magnitude and sign of the pseudocontact shift (Table 1.2). Of the lanthanides, the ions Dy^{3+} and Tb^{3+} have the largest negative Bleaney constants, -87 and -100 respectively. The lanthanide ion with largest positive Bleaney constant is Tm^{3+}, +53. The same proton within the Tm^{3+} complex of an isostructural ligand is expected to experience a pseudocontact shift of the opposite sign and smaller magnitude than that of Dy^{3+} and Tb^{3+}.

Lanthanide ion choice also affects the nuclear longitudinal and transverse relaxation rates through variations in the magnetic moment, μ_{eff}, and electronic relaxation time, τ_e. It is clear from Equations 1.9 and 1.10 (see Section 1.5, page 20) that an increase in μ_{eff} will result in an increased relaxation rate so the lanthanide ion must be chosen with this in mind. Tb^{3+}, Dy^{3+}, Ho^{3+}, Er^{3+} exhibit the largest magnetic moments (9.4 to 10.4 BM) and Tm^{3+} has a marginally smaller moment (7.6 BM), (Table 1.2). However, whilst at higher field strengths the magnetic moment is important due to the

dominance of the Curie term, most current clinical MRI instruments operate at 1.5 or 3 T. At these lower field strengths the dipolar term has the major influence on the relaxation rates and hence the size of τ_e has an increased impact. The electronic relaxation time is a function of both the lanthanide ion and the local ligand field; values of τ_e for lanthanide(III) complexes typically fall within the range of 10^{-12} to 10^{-13} s^{-1}.[88] Upon inspection of the reported electronic relaxation rates of the hydrated lanthanide ions, Ho^{3+} and Tb^{3+} appear to be less favourable candidates due to their slightly shorter electronic relaxation time. However, the size of τ_e cannot yet be predicted for novel lanthanide coordination complexes.

Whilst a fast longitudinal relaxation rate, R_1, allows the use of fast pulse NMR techniques, it should be noted that the transverse relaxation rate, R_2, should not be too fast. The linewidth of NMR signals are proportional to the transverse relaxation rate and hence when R_2 is increased the sensitivity is limited. Intrinsically the transverse relaxation rate must always be equal or larger than longitudinal relaxation rate ($R_2 \geq R_1$). Therefore, a balance must be sought in order to maximise R_1. A shorter T_2 results in increased line broadening and hence an R_1/R_2 as close to unity is desired.[33,77,88]

Table 1.2 Magnetic and relaxation properties of selected lanthanide(III) ions.

Ln^{3+}	μ_{eff} / BM[a]	τ_e / 10 s^{-13} [b]	C_J normalised
Eu	3.5	0.09	+4
Gd	7.9	$10^4 - 10^5$	0
Tb	9.8	2.03	-87
Dy	10.3	2.99	-100
Ho	10.4	1.94	-39
Er	9.4	2.38	+33
Tm	7.6	3.69	+53
Yb	4.3	1.37	+22

(a) Taken from reference.[89] (b) As aqua ion, 2.1 T, from references.[90–92]

1.6.2 Ligand design

It is imperative that PARASHIFT probes are kinetically and thermodynamically stable with respect to metal ion dissociation, as much like Gd^{3+}, other free Ln^{3+} ions are highly toxic and unstable complexes can trans-metallate in the body.[93] Kinetic and

thermodynamic stability with respect to the dissociation of the metal ion are required. As with Gd^{3+}-based MRI contrast agents, macrocyclic ligands possessing both oxygen and nitrogen donors are most commonly utilised in PARASHIFT probes. Such probes are typically functionalised derivatives of cyclen. The additional chelating groups typically are amides, carboxylates or phosphinates. In order to maximise signal intensity and minimise exchange broadening of a reporter signal it is preferred that a metal complex exists as one major conformation. Therefore, it is important to consider the symmetry, assess the possibility of forming diastereoisomers, and study the exchange dynamics of potential imaging resonances.[94] In complexes based on cyclen, at least two different forms of chirality arise, as illustrated by **[LnDOTA(H_2O)]$^-$** in Figure 1.10. The torsion angle of the NCCN link in the macrocyclic ring can have either a positive of negative sign, which define a δ or λ conformation, respectively. Additionally, the NCCX (X = O in the case of **[LnDOTA(H_2O)]$^-$**) torsion angle of the exocyclic pendant arms can be described as either positive or negative, which describes the Δ or Λ helicity, respectively, of the complex. The two modes of chirality result in four potential stereoisomers of two enantiomeric pairs. Existing as square antiprisms, the conformations can be described as twisted square antiprismatic (TSAP) or square antiprismatic (SAP). Typically in slow exchange on the NMR timescale, both diastereoisomers are often observed by NMR, however the ratio of SAP to TSAP varies between ligand structures and even across a set of lanthanide complexes of the same ligand.

In complexes containing chiral phosphinate chelators, the additional centre of chirality at the P atom introduces many more potential diastereoisomers.

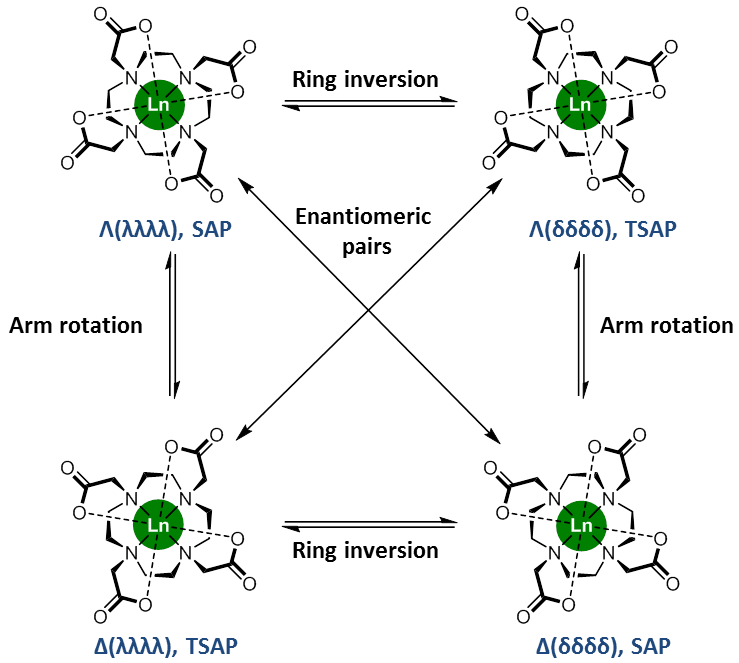

Figure 1.10 Schematic representation of the coordination geometries of **[LnDOTA(H_2O)]$^-$** and those typically adopted by octadentate cyclen-based complexes. The bound water molecule has been omitted for clarity.

In order to achieve a single, sharp resonance, as needed to maximise the SNR, the number of magnetically equivalent nuclei of the reporter resonance should be as large as possible. This can be achieved through increasing symmetry, as well as the use of homotopic reporter groups such as methyl groups (3 equivalent protons) or *tert*-butyl groups (9 equivalent protons).

Additionally, and perhaps most importantly, the geometry of the reporter with respect to the lanthanide ion and magnetic axis should be carefully considered. It has been shown in Equations 1.2 and 1.8 (see Section 1.4.1, pages 13 and 15) that the pseudocontact shift has a dependence on the internuclear distance of r^{-3}. Therefore, in order to induce the maximum chemical shift, the nucleus should be placed as close as possible to the lanthanide ion. However, the relaxation rate is also dependent on the internuclear distance with both longitudinal and transverse relaxation rates (Equations 1.9 and 1.10, see Section 1.5, page 20) containing an r^{-6} dependence. A balance must be achieved in which R_1 is enhanced sufficiently without increasing R_2 drastically. An R_2 value above approximately 300 s^{-1} results in the NMR signal being prohibitively broadened. Simulations of the relaxation rates against internuclear distance show that R_2 reaches this limit at ~5.8 Å. Hence, the reporter nucleus should not be found closer

to the lanthanide than this, in order to reduce losses in sensitivity due to line broadening (Figure 1.11).

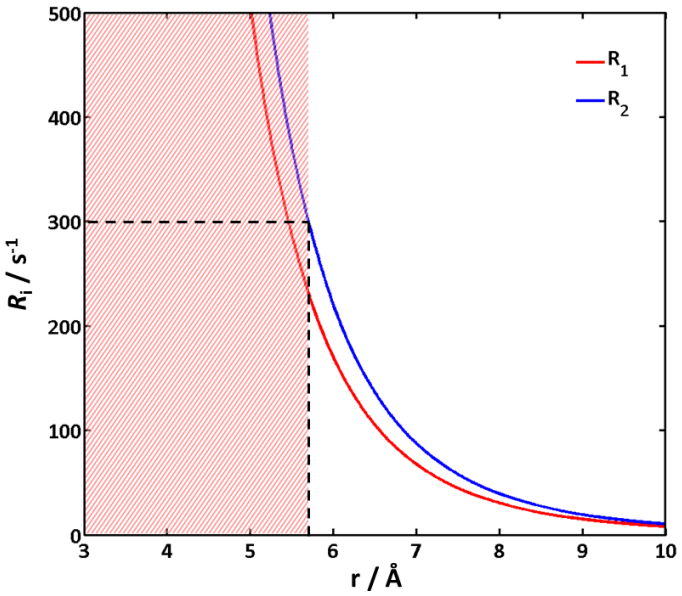

Figure 1.11 Simulated variation using SBM theory of ^{1}H longitudinal, R_1, (red) and transverse, R_2, (blue) relaxation rates with the Ln^{3+}-^{1}H internuclear distance, r (295K, B = 7 T, μ_{eff} = 10.4 BM, τ_e = 0.45 ps, τ_r = 350 ps).

The angular dependence is harder to model. Predicting the optimum geometry of the reporter group with respect to the principal magnetic axis is very challenging as the orientation of the major component of the susceptibility tensor cannot be determined ab initio.

An additional parameter that affects the relaxation rate is the rotational correlation time, τ_r, which describes the tumbling motion of molecules in solution. If this tumbling occurs at a similar frequency to the energy gap between the nuclear spin states, the rate of transitions between them can be increased. The motion is dependent on the size, shape and dynamics of the molecule and the properties of the solvent. The effect of the variation of the rotational correlation time on both R_1 and R_2 as modelled using SBM theory is shown in Figure 1.12. As the energy gap of spin states is field strength dependent, the modulation of τ_r varies with the magnetic field. At 7 T, R_2 increases much more rapidly than R_1, especially when τ_r > 250 ps. This suggests that in order to maintain R_1/R_2 as close to unity as possible we may want to minimise molecular volume. However, at lower, clinically relevant, field strengths there is little variation between R_1 and R_2.

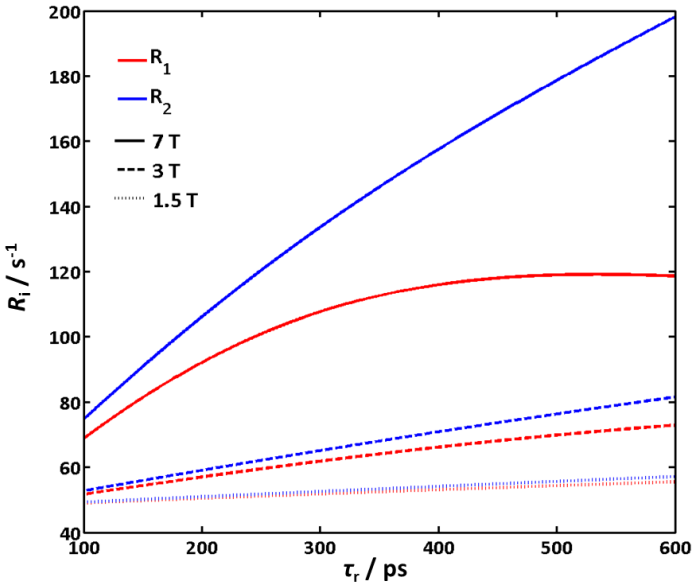

Figure 1.12 Simulated variation using SBM theory of ^{1}H longitudinal, R_1, (red) and transverse, R_2, (blue) relaxation rates with the Ln^{3+}-^{1}H internuclear distance, τ_r at three different fields (7 T – solid, 3 T – dashed, 1.5 T – dotted) (295 K, B = 7 T, μ_{eff} = 10.4 BM, τ_e = 0.45 ps, r = 6.6 Å).

1.7 Existing ^{1}H PARASHIFT probes

1.7.1 Lanthanide based MRS probes

One of the first examples of chemical shift selective imaging with a paramagnetic complex was published in 1996 by Aime, Botta and co-workers, using the complex **[YbL^{G}]$^{-}$**, known as **[YbDOTMA]$^{-}$** (Figure 1.13).[95] The intense C_4-symmetric methyl ^{1}H signal, at -14 ppm (300 K, 4.7 T, R_1 = 15 s^{-1}, R_2 ~ 30 s^{-1}), was imaged selectively in phantoms at 4.7 T. This first proof-of-concept study successfully demonstrated that paramagnetic complexes could be imaged selectively in the presence of water at physiologically relevant concentrations (LD_{50} = 10.5 mmol/kg) (Figure 1.13). However, the 2D single slice imaging experiment took over 6 h to observe the signal from a 3 mM solution.

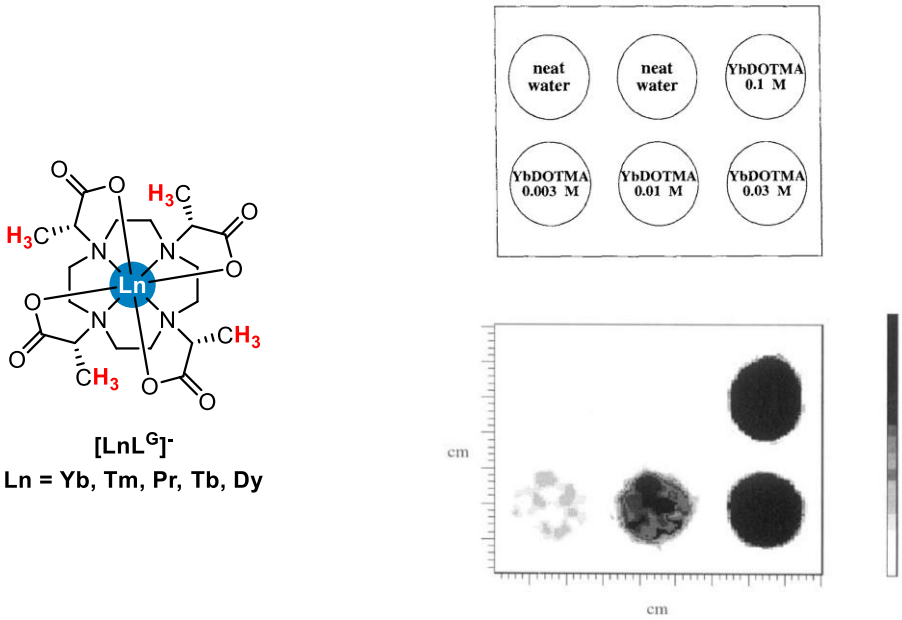

[LnL^G]$^-$
Ln = Yb, Tm, Pr, Tb, Dy

Figure 1.13 (*Left*) Structure of **[LnL^G]**. (*Right*) 2D spin echo chemical shift selective image of a phantom containing a series of aqueous solutions of **[YbL^G]$^-$** from 0 - 100 mM. Slice thickness 4.5 mm, TE = 23 ms, relaxation delay = 150 ms, nt = 2048 (voxel size 1.8 mm^3).[95]

The NMR properties of other **[LnL^G]$^-$** complexes were investigated by Bansal and co-workers, and **[TmL^G]$^-$** was deemed the most suited to chemical shift selective imaging, with its sharp methyl resonance at -100 ppm (308 K).[96] In 2014, Faber and co-workers successfully employed **[TmL^G]$^-$** in cell-labelling studies *in vivo*; the complex was internalised into HT-1080 (human fibrosarcoma) cells prior to injection, and tracked by MRI in mice for 8 days, at an equivalent dose of 1.6 mmol/kg.[97]

In 2013, Parker and co-workers began to investigate the optimisation of a series of proton PARASHIFT lanthanide complexes, analysing both shift and relaxation properties, to inform judicious design of imaging probes.[77] As the imaging sensitivity relies on the reporter group structure, its shift and relaxation properties,[98] PARASHIFT probes were designed with a *tert*-butyl reporter group placed around 6.6 Å from the lanthanide(III) ion enclosed within a cyclen-based macrocycle (**[LnL^H]** and **[LnL^I]$^+$**, Figure 1.14) to optimise fast longitudinal relaxation, whilst negating SNR losses to T_2.[60,77] The *tert*-butyl group provides nine, in **[LnL^H]**, or eighteen, in **[LnL^I]$^+$,** magnetically equivalent ^{1}H nuclei, giving a relatively intense resonance found between -20.5 and +10.8 ppm (295 K) depending on the lanthanide ion and complex.[77] Preliminary *in vivo* PARASHIFT imaging was performed on renally intact mice administered with clinically relevant doses (0.03 mmol/kg) of **[DyL^I]$^+$** by intravenous injection, at 7 T. Short echo times

(4 ms) and a narrow excitation bandwidth of 5 kHz were used, to observe **[DyL^{I}]$^{+}$** within skeletal muscles.[77]

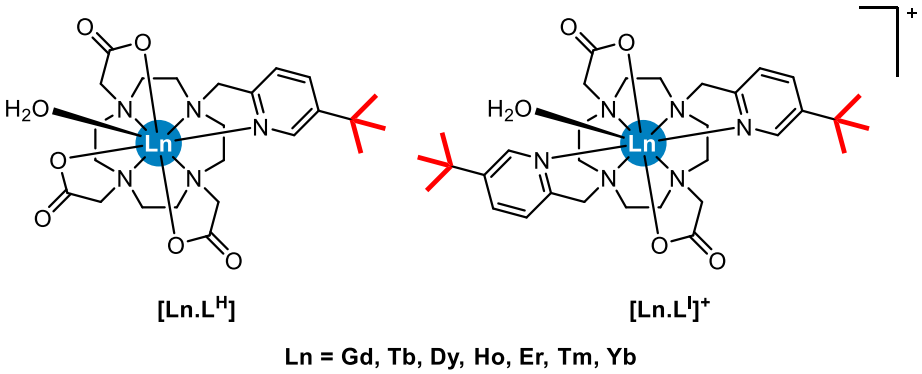

Figure 1.14 Structures of carboxylate Ln PARASHIFT probes optimised for imaging.

In pursuit of better sensitivity, Parker and co-workers developed better PARASHIFT agents with reporter groups shifted much further and > 70 ppm from the water and fat signals so that shorter excitation pulses (i.e. wider excitation bandwidths) could be used. It was hypothesised that increasing the excitation bandwidth to 20 kHz would significantly speed up image acquisition.[33] The structural modification from carboxylate (**[LnL^{H}]**) to methylphosphinate (**[LnL^{J}]**, Figures 1.14 and 1.15) chelating pendants was found to have a dramatic effect on the *tert*-butyl resonance frequency (Figure 1.15).[60]

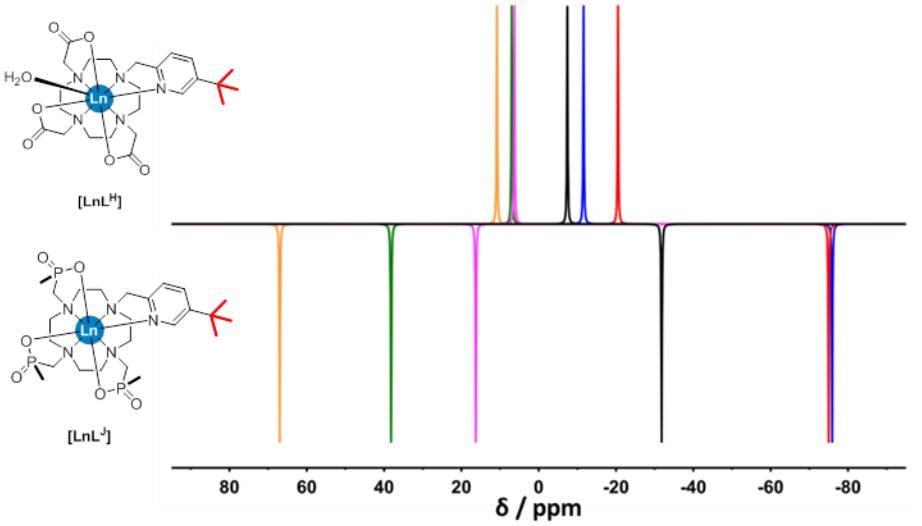

Figure 1.15 Schematic representation of the experimentally measured ^{1}H chemical shifts of *tert*-butyl signals in **[LnL^{H}]** (*top*) and **[LnL^{J}]** (*bottom*) (D_2O, 295 K) (yellow – Tm, green – Er, magenta – Yb, black – Ho, red- Dy, blue –Tb).

The chemical shift range of the *tert*-butyl resonances in **[LnL^{J}]**, 140 ppm (+67 to -77 ppm), is significantly larger than the range of **[LnL^{H}]**, 32 ppm

(+11 to -21 ppm). The loss of the axially coordinating water molecule in the **[LnL^{J}]** complexes (with respect to **[LnL^{H}]**) is the cause of this drastic increase in both shift and relaxation. The increase arises from a change in the size and orientation of the major axial component of the magnetic susceptibility tensor which points directly toward the reporting *tert*-butyl group (Figure 1.16).[94,98,99] Further detailed studies of the hyperfine shift and relaxation properties of a range of tricarboxylate and triphosphinate cyclen macrocyclic lanthanide complexes have shown that even small ligand variations can induce very large changes in the magnetic anisotropy.[60,99]

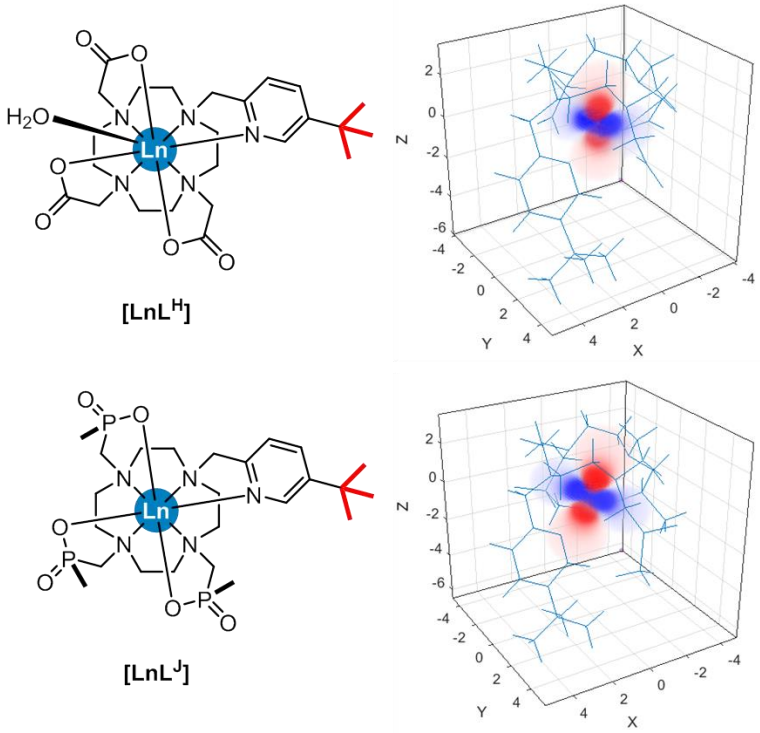

Figure 1.16 Pseudocontact shift field reconstructed using the best fit susceptibility tensor for **[YbL^{H}]** (*top*) and **[YbL^{J}]** (*bottom*) created in Spinach.[94]

The *tert*-butyl proton signal of **[DyL^{J}]** (Figures 1.15 and 1.17) resonates at -75 ppm (295 K), > 20 kHz away from the water signal at 7 T and is therefore suitable for fast imaging sequences.

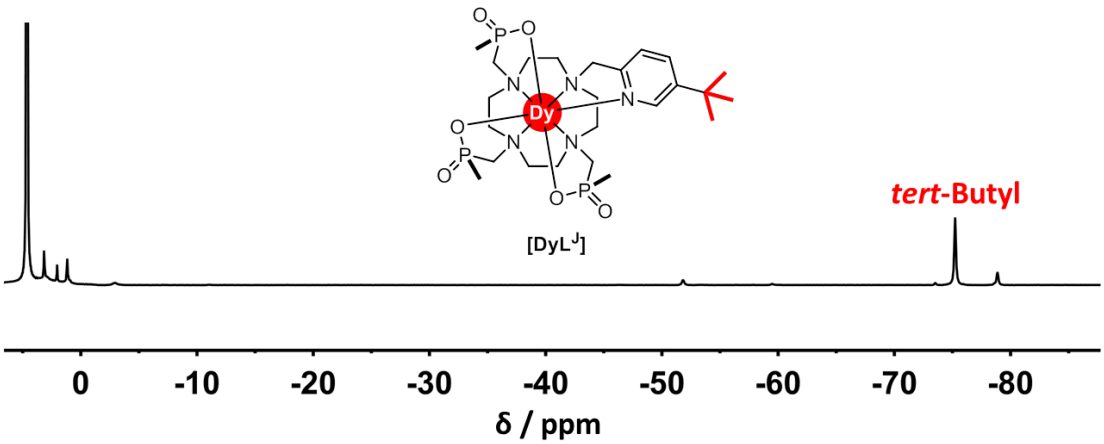

Figure 1.17 ^{1}H NMR spectrum and structure of **[DyL^{J}]** (D_2O, 9.4 T, 295 K).[60]

The anionic bismethylphosphinate complex, **[DyL^{K}]$^{-}$**, (Figure 1.18), introduced a thiol-linked carboxylate onto the pyridine ring in order to improve its biodistribution with respect to the cationic, dimethylphosphinate analogue, **[LnL^{I}]** (Figure 1.14).[100] The anionic Dy^{3+} complex was imaged *in vivo* with an optimised 3D gradient echo (3DGE) sequence at 7 T. The 18 proton *tert*-butyl NMR signal was excited at -60 ppm using a 20 kHz excitation bandwidth and much shorter echo times (TE = 1.45 ms, TR = 2.87 ms) and the image acquisition time was reduced to 60 s per 3D image (of 16 slices). An impressive detection limit of 23 µmol/dm^3 was achieved at this temporal resolution, which allowed dynamic time series of images to be implemented to follow the kinetics of the molecular probe within the body, following a tail-vein injection of a single 0.04 mmol/kg dose of **[DyL^{K}]$^{-}$** (Figure 1.18).

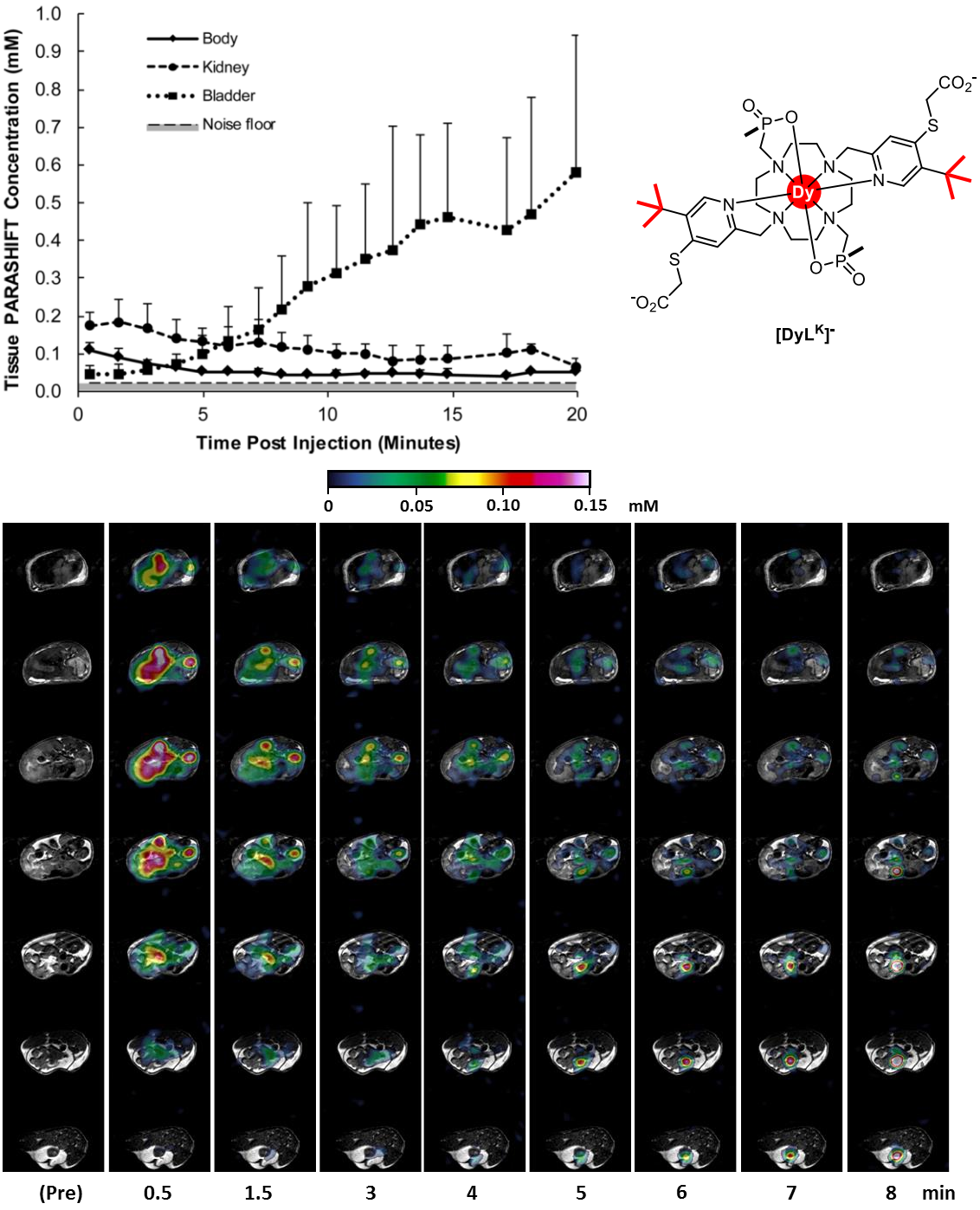

Figure 1.18 (*Top left*) Time series analysis of PARASHIFT concentration from selected regions of interest in six mice. *In vivo* 3DGE imaging of renally intact mice administered with 0.04 mmol/kg **[DyL^K]$^-$** by intravenous tail vein injection. Imaged using 7 T preclinical MRI system with a 39 mm birdcage RF coil, TE = 1.45 ms, TR = 2.87 ms, 20 kHz excitation bandwidth, voxel sixe = 32 mm^3, 62s per 3D image set (of 16 slices). (*Top right*) Structure of **[DyL^K]$^-$**. (*Bottom*) PARASHIFT signal from **[DyL^K]$^-$** (colour scale) overlaid onto conventional structural MRI scans. Each column represents a different time point post injection. Within each column the data represent different spatial axial slices through the mouse.[100]

Over the last 20 years several examples of PARASHIFT imaging have been reported using symmetrical cyclen-based macrocyclic lanthanide complexes that are relatively simple to synthesise, mainly by the groups of Hyder[101–105] and Bansal,[96,106,107] as well as

several optimised imaging probes synthesised by Parker and co-workers.[100] The magnitude of the paramagnetic shift is sensitive to physiological conditions including temperature, and efforts to convey functionality to these imaging probes has been exploited in spectroscopic imaging techniques, leading to sensing applications *in vivo*.

1.7.2 Temperature sensing

MRSI can be performed with responsive contrast agents, using the chemical shift of a probe in order to map physiological parameters, such as temperature. The paramagnetic hyperfine shifts of PARASHIFT nuclei are inherently temperature dependent because the magnetic anisotropy derives from the Boltzmann population of the m_J energy states. Therefore, the chemical shifts of protons within PARASHIFT complexes vary with temperature as shown in Equation 1.8 (page 15). Bleaney's theory indicates that the pseudocontact shift has a $1/T^2$ dependence. However, over small (physiological) temperature ranges an approximate linear dependence is observed and thus linear temperature coefficients are often quoted.

The clinical temperature measurement of deep tissue requires the use of invasive probes. The rise of non-invasive thermal therapies for diseases, such as cancer, has increased the demand for an accurate deep tissue temperature measurement method. A number of non-invasive temperature monitoring MRI techniques have been developed.[108] Currently, the most widely applied MRS thermometry method in the literature is the 'proton resonance frequency' technique, which exploits the temperature-dependent hydrogen-bonding of water protons; the proton resonance exhibits a linear shift response to temperature, with a very small temperature coefficient of 0.01 ppm/K.[109,110] This low thermal sensitivity limits the error of temperature measurements to approximately 2 K,[111] requires fat-suppression techniques, and is impractical for measuring small temperature differences *in vivo*.

The intrinsic temperature sensitivity of paramagnetically shifted resonances has enabled the development of a new method for *in vivo* temperature measurement. Accurate thermometry requires the temperature coefficient to be significant enough for high temperature resolution, without being too large to cause spatial distortion in the frequency encoding dimension. It is important that the reporter signal has a

narrow linewidth, to ensure that chemical shift data can be readily extracted, and that it responds to temperature only, without shifting due to modulation of other external variables.

In 1996, the complex **[YbL^{G}]$^{-}$** (Figure 1.13, pages 26 and 27) was proposed as a temperature-sensitive MRS probe and *in vitro* spectroscopic investigations of the methyl resonance revealed a linear 0.04 ppm/K temperature coefficient, four-times greater than that of water.[95]

Meanwhile, Frenzel, Weinmann and co-workers began to investigate the thermometry properties of **[PrL^{P}]** (Figure 1.19);[112,113] the methoxy group at -24.1 ppm (295 K, relative to the water signal) was selectively imaged in 10 mM phantoms, and a linear shift dependence with temperature of 0.13 ppm/K was observed.

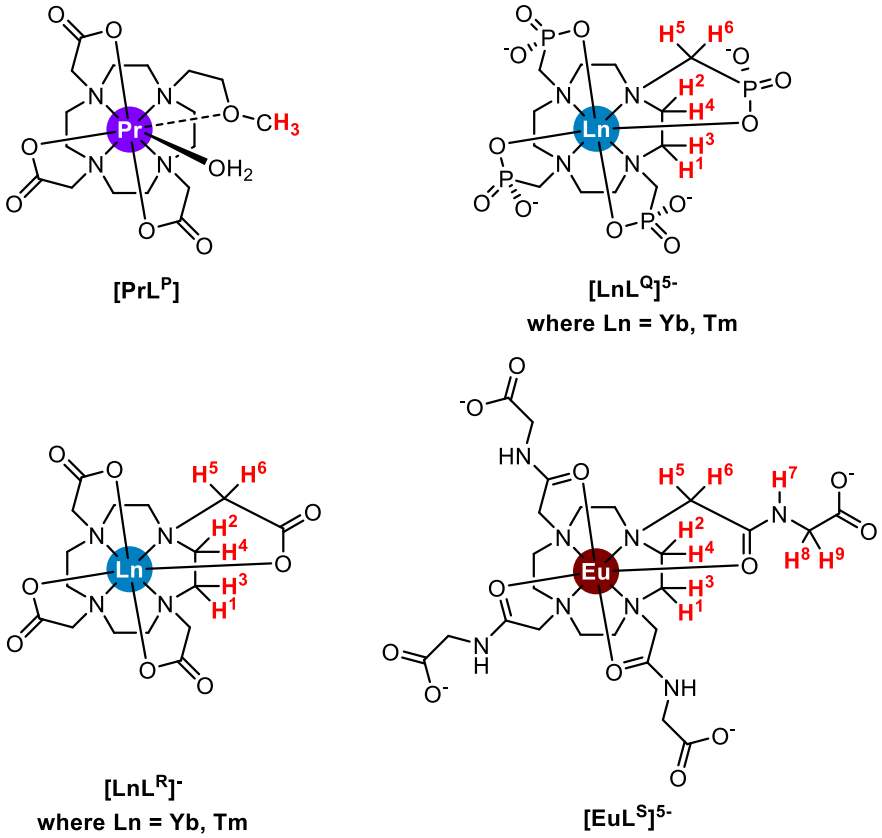

Figure 1.19 Structures of selected temperature responsive MRS probes.

The methoxy shift was shown to be independent of pH and was used to measure the absolute temperature of the liver in a rat model, and verified by a rectal thermocouple (deviation <±1 K), although a high dose was required for this study (1 mmol/kg). It was

later confirmed that the complex could be used to map temperature through the 2D spin echo spectroscopic imaging of phantoms.[114–116]

A comparison of the NMR properties of **[YbL^{G}]$^{-}$** with the analogous Pr^{3+}, Tb^{3+}, Dy^{3+} and Tm^{3+} complexes showed that **[TmL^{G}]$^{-}$** had the greatest temperature coefficient, 0.57 ppm/K, and its chemical shift was found to be insensitive to complex concentration, pH and the presence of Ca^{2+} ions.[96] **[TmL^{G}]$^{-}$** was successfully employed for temperature mapping in rats with millimetre resolution, using a frequency selective pulse.[102,106,107] However, these studies required surgical renal ligation and high doses of 1-2 mmol/kg in order to supress the fast clearance of **[TmL^{G}]$^{-}$** via the kidneys. Despite the remarkably short half-life of **[TmL^{G}]$^{-}$** in the blood (approximately 7 min), Sled and co-workers managed to measure the internal temperatures of the aorta, inferior vena cava and kidney within this time window at 11.7 T, following a single bolus injections of 0.7 mmol/kg within physiologically intact mice.[117]

Zuo *et al*. investigated the Tm^{3+} complex of the tetraphosphonate ligand, known as DOTP (**[TmL^{Q}]$^{5-}$**, Figure 1.19) as a potential probe for MR thermometry.[118] The Ln^{3+} complexes of DOTP had been originally studied as MR probes to distinguish intra- and extracellular concentrations of Na^{+} *in vivo,* by ^{23}Na and ^{31}P MR imaging.[76,119]

The H^{6} proton signal of **[TmL^{Q}]$^{5-}$** (Figure 1.19) resonates at -142 ppm (310 K) with a relatively narrow line width (~300 s^{-1} at 7 T) and a significant linear temperature dependence of 0.89 ppm/K, allowing greater thermal resolution than with **[TmL^{G}]$^{-}$**. Similarly to **[TmL^{G}]$^{-}$**, the chemical shift of the **[TmL^{Q}]$^{5-}$** proton resonance is unaffected by pH (between 6.5 and 8.5), and *in vivo* thermometry was demonstrated in renally ligated rats, dosed with 1 mmol/kg of **[TmL^{Q}]$^{5-}$**.[118] However, the sensitivity of the complex to variations in local Ca^{2+} concentration reduces the accuracy of the temperature measurement *in vivo*.

Complexes of the C_4 symmetric DOTA ligand, **[LnL^{R}]$^{-}$**, (i.e. analogous lanthanide complexes of the commercial gadolinium contrast agent Dotarem,[1] Figure 1.19) have also been employed successfully as MSRI thermometry probes.[120,121] The H^{5} resonance of the Tm complex, **[TmL^{R}]$^{-}$**, was observed at -227 ppm (310 K) and has a temperature coefficient of 0.91 ppm/K, and is insensitive to both pH and [Ca^{2+}]. *In vivo* temperature

measurements were performed, at 9.4 T, on tumour-bearing mice infused with 1-2 mmol/kg of **[TmL^{R}]**$^{-}$ and with scan times of 4 min.[121] Such a dose is generally regarded as being well beyond the safe dose for analogous Gd^{3+} MRI contract agents, and the ability to obtain fast temperature changes is limited by the acquisition time.

The magnitude and temperature dependence of a paramagnetically shifted proton resonance is a property of both the lanthanide ion and the ligand structure. As demonstrated by the examples discussed above, complexes of Tm^{3+}, with ligands of square antiprism based geometries, often have larger pseudocontact shifts and temperature sensitivities than predicted. This behaviour can be rationalised by considering the relative thermal population and anisotropy of the individual lanthanide(III) ion m_J states. Each m_J level will have different magnetic anisotropy, and the relative order and energy separation of the states is determined by the local ligand field. It is the weighted population of these states that determines the overall anisotropy, and therefore the pseudocontact shift and temperature dependence of a particular complex.[50,64]

Caravan and co-workers investigated the use of the Yb^{3+} complex of DOTA, **[YbL^{R}]**$^{-}$, for potential multiplex imaging by encapsulating the complex inside liposomal nano-carriers alongside a number of diamagnetic ^{1}H chemical shift imaging probes for MRS.[122] The liposomes contained a 1.2 M concentration of equivalent protons resonances of the diamagnetic probes and H^{2} of **[YbL^{R}]**$^{-}$ and all resonances were acquired simultaneously. Phantom imaging revealed highly sensitive detection, liposome concentrations as low as 57 pM were observable. The addition of diamagnetic MRS probes, however, meant long repetition times were required, although the inclusion of a traditional T_1 contrast agent into the liposome could be used to decrease this.

Tetra-amide based lanthanide(III) complexes have been thoroughly investigated for use in PARACEST imaging, and in 2011 Hyder,[123,124] Sherry and co-workers investigated the possibility of dual modality MRI by combining both the PARACEST and PARASHIFT imaging techniques to detect the Eu^{3+} complex of the carboxylate-appended tetra-amide ligand (**[EuL^{S}]**$^{-}$, Figure 1.19) in phantom solutions.[125] *In vitro* experiments of 20 mM phantoms were performed, using MRSI to detect the non-exchangeable cyclen

proton H_4, which has the largest temperature coefficient of 0.13 ppm/K. Direct MRSI of **[EuL^S]**$^-$ revealed the concentration of the probe and temperature information for each voxel. CEST experiments generally rely on the local tissue quantity of the probe being known as the PARACEST molecule is imaged indirectly. However the MRSI data allowed for quantitative information to be gained from the subsequent CEST images as probe concentration was known. The *in vitro* experiment was performed at 11.7 T and required relatively high saturation powers for the CEST imaging, with long scan times for both techniques, MRSI (4.5 min) and CEST (7 min).

Parker and co-workers have successfully used MRSI of PARASHIFT agents to map temperature information.[77,100,126] MRSI was performed *in vivo* on renally intact mice, following intravenous injection of 0.04 mmol/kg of the dimethylphosphinate complex **[DyL^K]**$^-$ shown in Figure 1.22 (temperature coefficient of the *tert*-butyl resonance was 0.28 ppm/K in mouse plasma). A shift in the *tert*-butyl frequency between the bladder and the kidney was observed, indicating a 4 K difference in temperature between these organs, and imaging was performed at relatively high temporal resolution (63 s per image set).[100]

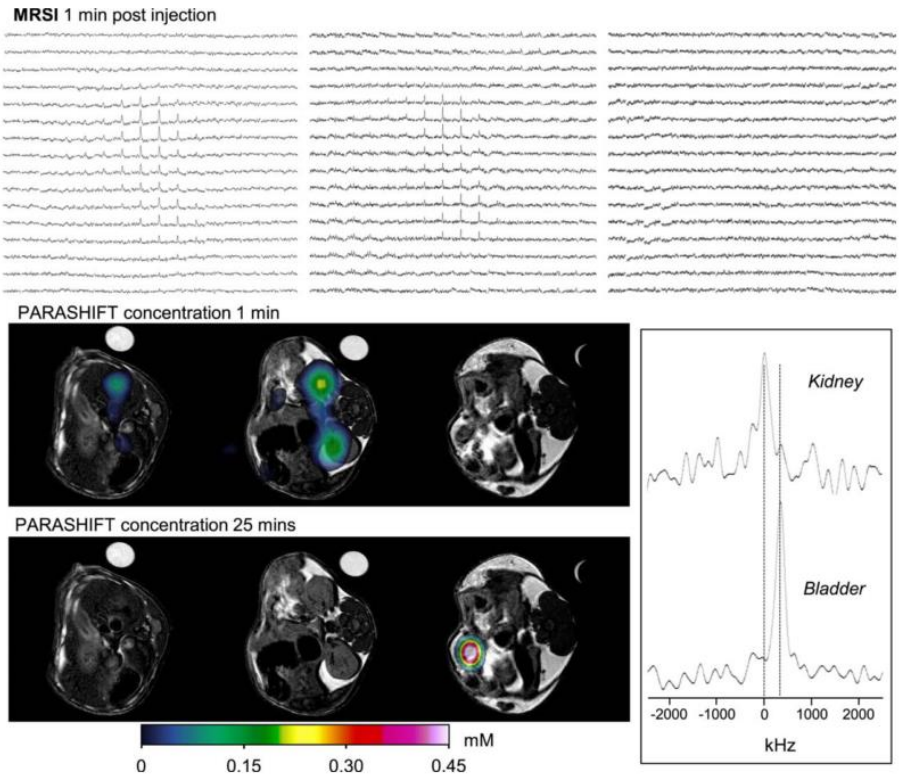

Figure 1.20 *In vivo* spectroscopic imaging of renally intact mice administered with 0.04 mmol/kg of **[DyL^{K}]**$^{-}$ by intravenous tail vein injection. (*Top*) Spectral grids for three of the MRSI slices acquired 1 minute after intravenous injection (*Bottom left*) Reconstructed PARASHIFT tissue distribution (derived from peak area for each voxel in 3DSI experiment) at 1 minute and 25 minutes post injection. (*Bottom right*) Spectra extracted from selected regions of interest. Imaged using 7 T preclinical MRI system with a 39 mm birdcage RF coil, TE = 0.73 ms, TR = 7.69 ms, 20 kHz spectral width, 63s per data set.[100]

1.7.3 Important considerations for *in vivo* imaging

Many examples of responsive molecular PARASHIFT probes have been employed successfully in imaging experiments, mainly with the C_4-symmetric DOTA-type lanthanide complexes **[TmL^{G}]**$^{-}$ and **[TmL^{Q}]**$^{5-}$, and with certain *tert*-butyl labelled Dy^{3+} and Tm^{3+} macrocyclic complexes. In order for PARASHIFT imaging to have clinical relevance however, it is important to consider the dose and method of administration required to produce adequate image sensitivity, as well as the pharmacokinetics/biodistribution of the molecular probe, and their interactions with other physiological species e.g. proteins and endogenous cations.

Most PARASHIFT agents studied to date suffer from a fast rate of clearance in the body, limiting the time-frame in which to image the molecular probe in organs other than the bladder to tens of minutes using a standard mouse model. Many early imaging studies were limited by the use of large doses (>0.1 mmol/kg, the clinical dose

advised for DOTAREM), the need for renally ligated animals to eliminate clearance pathways, or the application of continuous infusion of the PARASHIFT probe to maintain sufficient signal intensity.

Hyder and co-workers encapsulated the complex **[TmL^{Q}]$^{5-}$** (Figure 1.19) in 1,2-dipalmitoyl-sn-glycerophosphocholine (DPPC) liposomes in order to enhance local concentrations.[127] *In vitro* MRSI experiments suggested signal amplification could be achieved using nanomolar amounts of liposomes, compared to free **[TmL^{Q}]$^{5-}$**. Recently, investigation of the co-infusion of **[TmL^{Q}]$^{5-}$** with an anionic transport inhibitor showed enhanced probe concentrations, albeit with high infusion doses of 1 mmol/kg.[105]

Other approaches that can be employed to alter the pharmacokinetics involve changing the chemistry of the molecular probe; Parker found that anionic PARASHIFT complexes cleared slightly more slowly than structurally similar cationic complexes.[77,100] Both Parker and Hyder have sought to reduce clearance rates by increasing the size of the molecular probe by conjugation to biopolymers[37] or developing dendrimers containing **[TmL^{R}]$^{-}$**.[128] Unfortunately, Hyder and co-workers found that the loss of the C_4 structural symmetry resulted in the loss of sharp resonances and severe signal broadening was observed as the dendrimers increased in size.

1.7.4 Transition metal probes

Whilst the paramagnetic NMR properties of lanthanide complexes are better explored and understood, there have been some safety concerns about the use of lanthanide probes in patients with impaired kidney function. The medical community routinely use Gd^{3+}-based contrast agents for MRI, but in 2006 links to the rare but severe illness nephrogenic systemic fibrosis were found.[129] The European Medicines Agency has documented gadolinium accumulation in patients' brain tissue, leading to restrictions in the use of one of the most commonly used contrast agents, **[GdDTPA]$^{-}$**.[130] There has been an impetus to look towards *d*-block metals to replace gadolinium contrast agents,[131–133] and more recently the search for new PARASHIFT agents based on paramagnetic transition metal systems.

Morrow and co-workers have synthesised Fe^{2+} and Co^{2+} complexes using TACN and cyclen based ligands appended with 6-methyl-2-picolyl groups (Figure 1.21). These six-coordinate aza-macrocyclic based ligands were found to stabilise the high-spin forms of Fe^{2+} and Co^{2+}, due to the weaker ligand field produced as a result of the steric demand of the 6-methyl substituted pyridines. The cationic complexes are paramagnetic with an anisotropic magnetic susceptibility that gives rise to a large hyperfine shift.[134–136] The transition metal complexes **$[ML^L]^{2+}$** and **$[ML^M]^{2+}$** were found to be kinetically inert in biological media and the chemical shifts are insensitive to variation of both pH (within physiological range) and the concentration of biological ions (HPO_3^{3-}, HCO_3^-, Zn^{2+}, Ca^{2+}). A linear temperature dependence was observed for all complexes and the largest temperature coefficient was 0.52 ppm/K for **$[CoL^M]^{2+}$**.

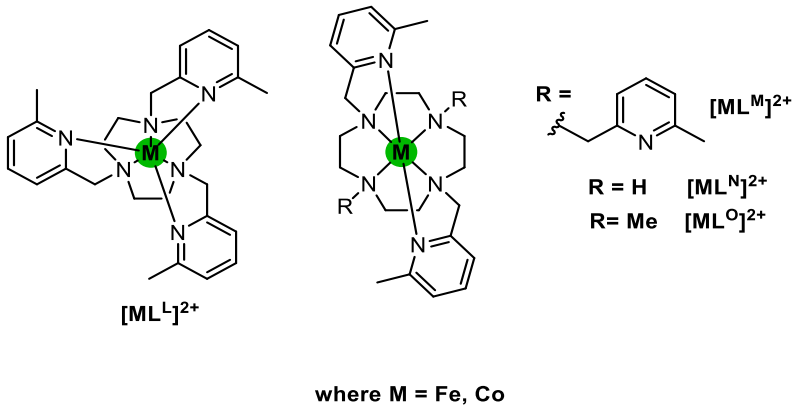

Figure 1.21 Structures of TACN and cyclen transition metal based PARASHIFT probes.

More recently, the spectral behaviour of the reporter methyl groups in the di-picolyl complexes **$[ML^N]^{2+}$** and **$[ML^O]^{2+}$** has been investigated (Figures 1.21 and 1.22).[136] The di-picolyl complex **$[ML^N]^{2+}$** exhibited similar MR properties to the tetra-picolyl analogue, **$[ML^M]^{2+}$**. The picolyl-methyl shifts of each complex were shifted well outside the diamagnetic region, between -22 and -113 ppm (298 K). The additional methyl groups in **$[ML^O]^{2+}$** were found to shift in the opposite direction to the picolyl methyl groups (Figure 1.22). The presence of two highly shifted resonances could allow for more accurate temperature measurements and the temperature coefficients ranged from 0.1 to 0.58 ppm/K. However, for both Co^{2+} complexes the linewidths of the methyl resonances were extremely broad reducing the potential for use *in vivo*. The linewidths of the analogous Fe complexes were significantly narrower, however they were less shifted. To date, no animal studies have been reported for these systems.

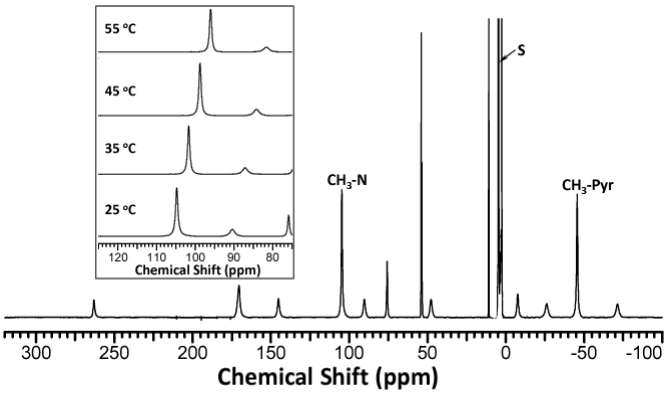

Figure 1.22 ^{1}H NMR of **[FeL^{O}]$^{2+}$** at (10 mM complex, 100 mM NaCl, D_2O, pD 7.2, 298 K). The proton resonances of pyridine and N-methyl groups on 12-N_4 are labelled CH_3-Pyr and CH_3-N, respectively. Solvent peak is labelled "S". Inset shows the effect of increasing temperature on the ^{1}H resonance of N-CH_3.[136]

New and co-workers have also developed a Co^{2+} based PARASHIFT complex that exhibits a distinctive NMR response to the presence of certain anions in aqueous solution.[137] The paramagnetically shifted *N*-Me resonance of $CoMe_6$TrenCl was observed to give a distinctive spectral profile within the +180 - +130 ppm region following reversible binding of fluoride, citrate, lactate and acetate.

Despite these *in vitro* spectroscopic studies with *d*-block PARASHIFT complexes, currently no imaging studies *in vivo* have been reported and optimised probes for imaging have not yet been designed. Little has been done in terms of modelling the shift and relaxation properties of paramagnetic *d*-block systems, where the contact shift is much more significant due to an increase in spin delocalisation onto the ligand in these coordination systems.[138–141]

1.8 Project Aims

The aim of this project is to synthesise and characterise novel paramagnetic lanthanide complexes for use as responsive ^{1}H PARASHIFT probes. The research in this thesis will focus on the modification of the PARASHIFT probes developed in Durham to incorporate varying functionalities, seeking to optimise the chemical shift and relaxation behaviour of the complexes.

The presence of a pH responsive, phosphonate group in close proximity to the *tert*-butyl group will give the pseudocontact chemical shift of the reporter pH dependence in addition to the inherent temperature dependence. *In vitro* experiments have been

undertaken in order to investigate and calibrate the pH and temperature sensitivities. *In* vivo experiments on a mouse model demonstrate the ability of the probe for non-invasive measurement by MRS. Structural modification of the ligand backbone is explored through the variation of the methylphosphinate groups to benzyl phosphinates and an increase in symmetry. *In vitro* experiments will be undertaken to explore the effects of these ligand modifications on the MR properties of the complexes. *In vivo* experiments will indicate how the biodistribution profile changes through ligand structure permutation in order to guide ligand design in the future.

In order to further probe how ligand structure affects the paramagnetic NMR properties of such probes in-depth NMR investigations will be undertaken on analogous complexes with no pH responsive behaviour.

Finally, a Zn^{2+} responsive probe will be sought through the incorporation of a specific Zn^{2+} chelating group (dipicolylamine). The Zn^{2+} chelating properties will be investigated using luminescence, solid state analysis, mass spectrometry and NMR methods.

1.9 References

1 P. Caravan, J. J. Ellison, T. J. McMurry and R. B. Lauffer, *Chem. Rev.*, 1999, **99**, 2293–352.
2 H. Sigel, A; Sigel, *Metal ions in biological systems. The lanthanides and their interactions with biosystems*, Marcel Dekker Inc. Netherlands, vol. 40., 2003.
3 B. Ross and S. Bluml, *Anat. Rec.*, 2001, **265**, 54–84.
4 F. Arias-Mendoza and T. R. Brown, *Dis. Markers*, 2004, **19**, 49–68.
5 V. Kumar, U. Sharma and N. R. Jagannathan, *Biomed. Spectrosc. Imaging*, 2012, **1**, 89–100.
6 J. Novak, M. Wilson, L. Macpherson, T. N. Arvanitis, N. P. Davies and A. C. Peet, *Eur. J. Radiol.*, 2014, **83**, e106–e112.
7 P. A. van Ewijk, V. B. Schrauwen-Hinderling, S. C. A. M. Bekkers, J. F. C. Glatz, J. E. Wildberger and M. E. Kooi, *NMR Biomed.*, 2015, **28**, 747–766.
8 R. B. Moon and J. H. Richards, *J. Biol. Chem.*, 1973, **248**, 7276–8.
9 R. J. Gillies, Z. Liu and Z. Bhujwalla, *Am. J. Physiol. Physiol.*, 1994, **267**, C195–C203.
10 J. Ren, A. D. Sherry and C. R. Malloy, *NMR Biomed.*, 2015, **28**, 1455–1462.
11 D. L. Rothman, H. M. de Feyter, R. A. de Graaf, G. F. Mason and K. L. Behar, *NMR Biomed.*, 2011, **24**, 943–957.
12 K. R. Keshari and D. M. Wilson, *Chemistry and biochemistry of 13C hyperpolarized magnetic resonance using dynamic nuclear polarization*, 2014, vol. 43.
13 S. J. Kohler, Y. Yen, J. Wolber, A. P. Chen, M. J. Albers, R. Bok, V. Zhang, J. Tropp, S. Nelson, D. B. Vigneron, J. Kurhanewicz and R. E. Hurd, *Magn. Reson. Med.*, 2007, **58**, 65–69.
14 I. Park, R. Bok, T. Ozawa, J. J. Phillips, C. D. James, D. B. Vigneron, S. M. Ronen and S. J. Nelson, *J. Magn. Reson. Imaging*, 2011, **33**, 1284–1290.

15 S. J. Nelson, J. Kurhanewicz, D. B. Vigneron, P. E. Z. Larson, A. L. Harzstark, M. Ferrone, M. Van Criekinge, J. W. Chang, R. Bok, I. Park, G. Reed, L. Carvajal, E. J. Small, P. Munster, V. K. Weinberg, J. H. Ardenkjaer-Larsen, A. P. Chen, R. E. Hurd, L. I. Odegardstuen, F. J. Robb, J. Tropp and J. A. Murray, *Sci. Transl. Med.*, , DOI:10.1161/01.RES.0000014966.97486.C0.

16 H. E. Möller, X. J. Chen, B. Saam, K. D. Hagspiel, G. A. Johnson, T. A. Altes, E. E. de Lange and H.-U. Kauczor, *Magn. Reson. Med.*, 2002, **47**, 1029–1051.

17 J. P. Mugler and T. A. Altes, *J. Magn. Reson. Imaging*, 2013, **37**, 313–331.

18 L. Ebner, J. Kammerman, B. Driehuys, M. L. Schiebler, R. V. Cadman and S. B. Fain, *Eur. J. Radiol.*, 2017, **86**, 343–352.

19 J. Ruiz-Cabello, B. P. Barnett, P. A. Bottomley and J. W. M. Bulte, *NMR Biomed.*, 2011, **24**, 114–129.

20 L. D. Stegman, a Rehemtulla, B. Beattie, E. Kievit, T. S. Lawrence, R. G. Blasberg, J. G. Tjuvajev and B. D. Ross, *Proc. Natl. Acad. Sci. U. S. A.*, 1999, **96**, 9821–9826.

21 A. Vermes, *J. Antimicrob. Chemother.*, 2000, **46**, 171–179.

22 M. Ogawa, S. Nitahara, H. Aoki, S. Ito, M. Narazaki and T. Matsuda, *Macromol. Chem. Phys.*, 2010, **211**, 1602–1609.

23 M. Ogawa, S. Nitahara, H. Aoki, S. Ito, M. Narazaki and T. Matsuda, *Macromol. Chem. Phys.*, 2010, **211**, 1369–1376.

24 US 4480228 A, 1984.

25 J. Frahm, K. D. Merboldt, W. Hanicke and A. Haase, *J. Magn. Reson.*, 1985, **64**, 81–93.

26 U. Flogel, Z. Ding, H. Hardung, S. Jander, G. Reichmann, C. Jacoby, R. Schubert and J. Schrader, *Circulation*, 2008, **118**, 140–148.

27 B. J. Dardzinski and C. H. Sotak, *Magn. Reson. Med.*, 1994, **32**, 88–97.

28 A. M. Neubauer, J. Myerson, S. D. Caruthers, F. D. Hockett, P. M. Winter, J. Chen, P. J. Gaffney, J. D. Robertson, G. M. Lanza and S. A. Wickline, *Magn. Reson. Med.*, 2008, **60**, 1066–1072.

29 P. K. Senanayake, A. M. Kenwright, D. Parker and S. K. van der Hoorn, *Chem. Commun.*, 2007, 2923–2925.

30 A. M. Kenwright, I. Kuprov, E. De Luca, D. Parker, S. U. Pandya, P. K. Senanayake and D. G. Smith, *Chem. Commun.*, 2008, 2514–6.

31 K. H. Chalmers, E. De Luca, N. H. M. Hogg, A. M. Kenwright, I. Kuprov, D. Parker, M. Botta, J. Ian Wilson and A. M. Blamire, *Chem. A Eur. J.*, 2010, **16**, 134–148.

32 K. H. Chalmers, M. Botta and D. Parker, *Dalton Trans.*, 2011, **40**, 904–913.

33 K. H. Chalmers, A. M. Kenwright, D. Parker and A. M. Blamire, *Magn. Reson. Med.*, 2011, **66**, 931–936.

34 P. Harvey, I. Kuprov and D. Parker, *Eur. J. Inorg. Chem.*, 2012, **2012**, 2015–2022.

35 P. Harvey, K. H. Chalmers, E. De Luca, A. Mishra and D. Parker, *Chem. A Eur. J.*, 2012, **18**, 8748–8757.

36 F. Schmid, C. Höltke, D. Parker and C. Faber, *Magn. Reson. Med.*, 2013, **69**, 1056–62.

37 E. De Luca, P. Harvey, K. H. Chalmers, A. Mishra, P. K. Senanayake, J. I. Wilson, M. Botta, M. Fekete, A. M. Blamire and D. Parker, *J. Biol. Inorg. Chem.*, 2014, **19**, 215–227.

38 Z.-X. Jiang, Y. Feng and Y. B. Yu, *Chem. Commun.*, 2011, **47**, 7233.

39 K. Srivastava, E. A. Weitz, K. L. Peterson, M. Marjańska and V. C. Pierre, *Inorg. Chem.*, 2017, **56**, 1546–1557.

40 J. Blahut, P. Hermann, A. Gálisová, V. Herynek, I. Císařová, Z. Tošner and J. Kotek, *Dalton Trans.*, 2016, **45**, 474–478.

41 J. Blahut, K. Bernášek, A. Gálisová, V. Herynek, I. Císařová, J. Kotek, J. Lang, S. Matějková and P. Hermann, *Inorg. Chem.*, 2017, **56**, 13337–13348.

42 E. T. Ahrens, B. M. Helfer, C. F. O'Hanlon and C. Schirda, *Magn. Reson. Med.*, 2014, **72**, 1696–1701.

43 B. V. Rollin, *Nature*, 1946, **158**, 669–670.

44 B. V. Rollin and J. Hatton, *Nature*, 1947, **159**, 201–201.

45 N. Bloembergen, E. M. Purcell and R. V. Pound, *Phys. Rev.*, 1948, **73**, 679–712.
46 J. A. Jackson, J. F. Lemons and H. Taube, *J. Chem. Phys.*, 1960, **32**, 553–555.
47 W. C. Bloembergen, N. Dickinson, *Phys. Rev.*, 1950, **79**, 179–180.
48 I. Bertini, C. Luchinat, G. Parigi and E. Ravera, in *NMR of Paramagnetic Molecules (Second Edition)*, eds. I. Bertini, C. Luchinat, G. Parigi and E. Ravera, Elsevier, Boston, Second Edi., 2017, pp. 61–76.
49 H. M. McConnell, *J. Chem. Phys.*, 1957, **27**, 226–229.
50 D. Parker, I. Kuprov, E. Suturina, K. Mason and C. Geraldes, *Angew. Chem. Int. Ed.*, 2017, 12215–12218.
51 G. Parigi and C. Luchinat, in *Paramagnetism in Experimental Biomolecular NMR*, 2018, pp. 1–41.
52 C. Görller-Walrand and K. Binnemans, in *Handbook on the Physics and Chemistry of Rare Earths 23*, 1996, pp. 121–283.
53 K. Binnemans and C. Görller-Walrand, *Chem. Phys. Lett.*, 1995, **245**, 75–78.
54 B. Bleaney, *J. Magn. Reson.*, 1972, **8**, 91–100.
55 G. T. P. Charnock and I. Kuprov, *Phys. Chem. Chem. Phys.*, 2014, **16**, 20184–20189.
56 B. J. Walder, K. K. Dey, M. C. Davis, J. H. Baltisberger and P. J. Grandinetti, *J. Chem. Phys.*, 2015, **142**, 1–16.
57 E. A. Suturina and I. Kuprov, *Phys. Chem. Chem. Phys.*, 2016, **18**, 26412–26422.
58 J. Rinehart and J. Long, *Chem. Sci.*, 2011, **2**, 2078–2085.
59 C. Görller-Walrand and K. Binnemans, in *Handbook on the Physics and Chemistry of Rare Earths*, 1996, pp. 121–283.
60 A. M. Funk, K.-L. N. A. Finney, P. Harvey, A. M. Kenwright, E. R. Neil, N. J. Rogers, P. K. Senanayake and D. Parker, *Chem. Sci.*, 2015, **6**, 1655–1662.
61 R. M. Golding and P. Pyykkö, *Mol. Phys.*, 1973, **26**, 1389–1396.
62 B. R. McGarvey, *J. Magn. Reson.*, 1979, **33**, 445–455.
63 V. S. Mironov, Y. G. Galyametdinov, A. Ceulemans, C. Görller-Walrand and K. Binnemans, *Chem. Phys. Lett.*, 2001, **345**, 132–140.
64 V. S. Mironov, Y. G. Galyametdinov, A. Ceulemans, C. Görller-Walrand and K. Binnemans, *J. Chem. Phys.*, 2002, **116**, 4673–4685.
65 G. Cucinotta, M. Perfetti, J. Luzon, M. Etienne, P. E. Car, A. Caneschi, G. Calvez, K. Bernot and R. Sessoli, *Angew. Chem. Int. Ed.*, 2012, **51**, 1606–1610.
66 M. E. Boulon, G. Cucinotta, J. Luzon, C. Degl'Innocenti, M. Perfetti, K. Bernot, G. Calvez, A. Caneschi and R. Sessoli, *Angew. Chem. Int. Ed.*, 2013, **52**, 350–354.
67 G. Castro, M. Regueiro-Figueroa, D. Esteban-Gómez, P. Pérez-Lourido, C. Platas-Iglesias and L. Valencia, *Inorg. Chem.*, 2016, **55**, 3490–3497.
68 N. Ouali, B. Bocquet, S. Rigault, P. Y. Morgantini, J. Weber and C. Piguet, *Inorg. Chem.*, 2002, **41**, 1436–1445.
69 M. Vonci, K. Mason, E. A. Suturina, A. T. Frawley, S. G. Worswick, I. Kuprov, D. Parker, E. J. L. Mcinnes and N. F. Chilton, *J. Am. Chem. Soc.*, 2017, **139**, 14166-14172
70 R. E. Sievers and R. E. Rondeau, *J. Am. Chem. Soc.*, 1971, **93**, 1522–1524.
71 C. F. G. C. Geraldes, in *Encyclopedia of Inorganic and Bioinorganic Chemistry*, John Wiley & Sons, Ltd, Chichester, UK, 2012, pp. 1–20.
72 G. R. Sullivan, in *Top. Stereochem.*, 2007, vol. 10, pp. 287–329.
73 T. J. Wenzel and J. D. Wilcox, *Chirality*, 2003, **15**, 256–270.
74 I. Sengupta, P. S. Nadaud and C. P. Jaroniec, *Acc. Chem. Res.*, 2013, **46**, 2117–2126.
75 C. P. Jaroniec, *J. Magn. Reson.*, 2015, **253**, 50–59.
76 A. D. Sherry, C. R. Malloy, F. M. H. Jeffrey, W. P. Cacheris and C. F. G. C. Geraldes, *J. Magn. Reson.*, 1988, **76**, 528–533.
77 P. Harvey, A. M. Blamire, J. I. Wilson, K.-L. N. A. Finney, A. M. Funk, P. K. Senanayake and D. Parker, *Chem. Sci.*, 2013, **4**, 4251.
78 M. Woods, D. E. Woessner and A. D. Sherry, *Chem. Soc. Rev.*, 2006, **35**, 500.
79 L. M. De Leon-Rodriguez, A. J. M. Lubag, C. R. Malloy, G. V. Martinez, R. J. Gillies and A.

D. Sherry, *Acc. Chem. Res.*, 2009, **42**, 948–957.
80 S. Viswanathan, Z. Kovacs, K. N. Green, S. J. Ratnakar and A. D. Sherry, *Chem. Rev.*, 2010, **110**, 2960–3018.
81 A. G. Redfield, *IBM J. Res. Dev.*, 1957, **1**, 19–31.
82 R. K. Wangsness and F. Bloch, *Phys. Rev.*, 1953, 89, 728–739.
83 I. Solomon, *Phys. Rev.*, 1955, **99**, 559–565.
84 N. Bloembergen, *J. Chem. Phys.*, 1957, **27**, 572.
85 N. Bloembergen and L. O. Morgan, *J. Chem. Phys.*, 1961, **34**, 842–850.
86 M. Goldman, *J. Magn. Reson.*, 2001, **149**, 160–187.
87 E. A. Suturina, K. Mason, C. F. G. C. Geraldes, N. F. Chilton, D. Parker and I. Kuprov, *Phys. Chem. Chem. Phys.*, 2018, **20**, 17676–17686.
88 A. M. Funk, P. H. Fries, P. Harvey, A. M. Kenwright and D. Parker, *J. Phys. Chem. A*, 2013, **117**, 905–917.
89 H. Gysling and M. Tsutsui, *Adv. Organomet. Chem.*, 1971, **9**, 361–395.
90 B. M. Alsaadi, F. J. C. Rossotti and R. J. P. Williams, *J. Chem. Soc. Dalt. Trans.*, 1980, 2151.
91 S. Aime, L. Barbero, M. Botta and G. Ermondi, *J. Chem. Soc. Dalt. Trans.*, 1992, 225.
92 I. Bertini, L. Banci and C. Luchinat, *Methods Enzymol.*, 1989, **177**, 246–263.
93 A. D. Sherry, P. Caravan and R. E. Lenkinski, *J. Magn. Reson. Imaging*, 2009, **30**, 1240–1248.
94 K. Mason, N. J. Rogers, E. A. Suturina, I. Kuprov, J. A. Aguilar, A. S. Batsanov, D. S. Yufit and D. Parker, *Inorg. Chem.*, 2017, **56**, 4028–4038.
95 S. Aime, M. Botta, M. Fasano, E. Terreno, P. Kinchesh, L. Calabi and L. Paleari, *Magn. Reson. Med.*, 1996, **35**, 648–651.
96 S. K. Hekmatyar, P. Hopewell, S. K. Pakin, A. Babsky and N. Bansal, *Magn. Reson. Med.*, 2005, **53**, 294–303.
97 R. Schmidt, N. Nippe, K. Strobel, M. Masthoff, O. Reifschneider, D. D. Castelli, C. Holtke, S. Aime, U. Karst, C. Sunderkotter, C. Bremer and C. Faber, *Radiology*, 2014, **272**, 785–795.
98 O. A. Blackburn, R. M. Edkins, S. Faulkner, A. M. Kenwright, D. Parker, N. J. Rogers and S. Shuvaev, *Dalt. Trans.*, 2016, **45**, 6782–6800.
99 N. J. Rogers, K.-L. N. A. Finney, P. K. Senanayake and D. Parker, *Phys. Chem. Chem. Phys.*, 2016, **18**, 4370–4375.
100 P. K. Senanayake, N. J. Rogers, K.-L. N. A. Finney, P. Harvey, A. M. Funk, J. I. Wilson, D. O'Hogain, R. Maxwell, D. Parker and A. M. Blamire, *Magn. Reson. Med.*, 2017, **77**, 1307–1317.
101 D. Coman, H. K. Trubel, R. E. Rycyna and F. Hyder, *NMR Biomed.*, 2009, **22**, 229–239.
102 D. Coman, H. K. Trubel and F. Hyder, *NMR Biomed.*, 2010, **23**, 277–285.
103 D. Coman, R. A. de Graaf, D. L. Rothman and F. Hyder, *NMR Biomed.*, 2013, **26**, 1589–1595.
104 D. Coman, Y. Huang, J. U. Rao, H. M. De Feyter, D. L. Rothman, C. Juchem and F. Hyder, *NMR Biomed.*, 2016, **29**, 309–319.
105 Y. Huang, D. Coman, P. Herman, J. U. Rao, S. Maritim and F. Hyder, *NMR Biomed.*, 2016, **29**, 1364–1372.
106 S. K. Pakin, S. K. Hekmatyar, P. Hopewell, A. Babsky and N. Bansal, *NMR Biomed.*, 2006, **19**, 116–124.
107 J. R. James, Y. Gao, M. A. Miller, A. Babsky and N. Bansal, *Magn. Reson. Med.*, 2009, **62**, 550–556.
108 V. Rieke and K. Butts Pauly, *J. Magn. Reson. Imaging*, 2008, **27**, 376–390.
109 J. C. Hindman, *J. Chem. Phys.*, 1966, **44**, 4582–4592.
110 B. Quesson, J. A. de Zwart and C. T. W. Moonen, *J. Magn. Reson. Imaging*, 2000, **12**, 525–533.
111 C. Weidensteiner, B. Quesson, B. Caire-Gana, N. Kerioui, A. Rullier, H. Trillaud and C. T.

W. Moonen, *Magn. Reson. Med.*, 2003, **50**, 322–330.
112 T. Frenzel, K. Roth, S. Koßler, B. Radüchel, H. Bauer, J. Platzek and H.-J. Weinmann, *Magn. Reson. Med.*, 1996, **35**, 364–369.
113 K. Roth, G. Bartholomae, H. Bauer, T. Frenzel, S. Kossler, J. Platzek and H.-J. Weinmann, *Angew. Chem. Int. Ed.*, 1996, **35**, 655–657.
114 M. Hentschel, P. Wust, W. Wlodarczyk, T. Frenzel, B. Sander, N. Hosten and R. Felix, *Int. J. Hyperth.*, 1998, **14**, 479–493.
115 M. Hentschel, W. Dreher, P. Wust, S. Röll, D. Leibfritz, R. Felix, S. Roll, D. Leibfritz, R. Felix, S. Röll, D. Leibfritz and R. Felix, *Phys. Med. Biol.*, 1999, **44**, 2397–2408.
116 M. Hentschel, M. Findeisen, W. Schmidt, T. Frenzel, W. Wlodarczyk, P. Wust and R. Felix, *Magn. Reson. Mater. Physics, Biol. Med.*, 2000, **10**, 52–59.
117 C. C. Heyn, J. Bishop, K. Duffin, W. Lee, J. Dazai, S. Spring, B. J. Nieman and J. G. Sled, *NMR Biomed.*, 2017, e3772.
118 C. S. Zuo, J. L. Bowers, K. R. Metz, T. Nosaka, A. D. Sherry and M. E. Clouse, *Magn. Reson. Med.*, 1996, **36**, 955–9.
119 A. D. Sherry, *J. Alloys Compd.*, 1997, **249**, 153–157.
120 C. S. Zuo, A. Mahmood and A. D. Sherry, *J. Magn. Reson.*, 2001, **151**, 101–106.
121 S. K. Hekmatyar, H. Poptani, A. Babsky, D. B. Leeper and N. Bansal, *Int. J. Hyperth.*, 2002, **18**, 165–179.
122 Y. Yang, D. T. Schühle, G. Dai, J. K. Alford and P. Caravan, *Contrast Media Mol. Imaging*, 2012, **7**, 276–279.
123 S. Aime, A. Barge, D. D. Castelli, F. Fedeli, A. Mortillaro, F. U. Nielsen and E. Terreno, *Magn. Reson. Med.*, 2002, **47**, 639–648.
124 S. Zhang and A. D. Sherry, *J. Solid State Chem.*, 2003, **171**, 38–43.
125 D. Coman, G. E. Kiefer, D. L. Rothman, A. D. Sherry and F. Hyder, *NMR Biomed.*, 2011, **24**, 1216–1225.
126 K.-L. N. A. Finney, A. C. Harnden, N. J. Rogers, P. K. Senanayake, A. M. Blamire, D. O'Hogain and D. Parker, *Chem. A Eur. J.*, 2017, **23**, 7976–7989.
127 S. Maritim, Y. Huang, D. Coman and F. Hyder, *J. Biol. Inorg. Chem.*, 2014, **19**, 1385–1398.
128 Y. Huang, D. Coman, F. Hyder and M. M. Ali, *Bioconjug. Chem.*, 2015, **26**, 2315–2323.
129 P. Marckmann, L. Skov, K. Rossen, A. Dupont, M. Brimnes Damholt, J. Goya Heaf and H. S. Thomsen, *J. Am. Soc. Nephrol.*, 2006, **17**, 2359–2362.
130 *EMA's final opinion confirms restrictions on use of linear gadolinium agents in body scans*, European Medicines Agency, 2017.
131 F. Touti, P. Maurin and J. Hasserodt, *Angew. Chem. Int. Ed.*, 2013, **52**, 4654–4658.
132 E. M. Gale, I. P. Atanasova, F. Blasi, I. Ay and P. Caravan, *J. Am. Chem. Soc.*, 2015, **137**, 15548–15557.
133 H. Wei, O. T. Bruns, M. G. Kaul, E. C. Hansen, M. Barch, A. Wiśniowska, O. Chen, Y. Chen, N. Li, S. Okada, J. M. Cordero, M. Heine, C. T. Farrar, D. M. Montana, G. Adam, H. Ittrich, A. Jasanoff, P. Nielsen and M. G. Bawendi, *Proc. Natl. Acad. Sci.*, 2017, **114**, 2325–2330.
134 P. B. Tsitovich and J. R. Morrow, *Inorganica Chim. Acta*, 2012, **393**, 3–11.
135 P. B. Tsitovich, J. M. Cox, J. B. Benedict and J. R. Morrow, *Inorg. Chem.*, 2016, **55**, 700–716.
136 P. B. Tsitovich, T. Y. Tittiris, J. M. Cox, J. B. Benedict and J. R. Morrow, *Dalton Trans.*, 2018, **47**, 916–924.
137 E. S. O'Neill, J. L. Kolanowski, P. D. Bonnitcha and E. J. New, *Chem. Commun.*, 2017, **53**, 3571–3574.
138 I. Bertini, C. Luchinat, G. Parigi and E. Ravera, in *NMR of Paramagnetic Molecules (Second Edition)*, eds. I. Bertini, C. Luchinat, G. Parigi and E. Ravera, Elsevier, Boston, Second Edi., 2017, pp. 175–253.
139 M. Atanasov, D. Aravena, E. Suturina, E. Bill, D. Maganas and F. Neese, *Coord. Chem.*

Rev., 2015, **289**–**290**, 177–214.

140 B. Martin and J. Autschbach, *J. Chem. Phys.*, 2015, **142**, 054108.

141 A. J. Pell, G. Pintacuda and C. P. Grey, *Prog. Nucl. Magn. Reson. Spectrosc.*, , DOI:10.1016/j.pnmrs.2018.05.001.

2. Development of pH responsive PARASHIFT probes

Whilst the hyperfine shifts of PARASHIFT agents have an inherent dependence upon temperature, the chemical shift may also be sensitive to other external variables, such as pH, which can be exploited for MRI sensing.

Altered extracellular pH *in vivo* is associated with certain chronic diseases.[1,2] There are very few clinical non-invasive methods to quantify pH *in vivo*. Preclinical studies have utilised heteronuclear ^{31}P MRS to measure the chemical shift of pH sensitive, phosphorus-containing metabolites[3] or probes.[4] pH responsive ^{1}H PARASHIFT molecular probes offer an alternative non-invasive MR technique that can be performed on existing clinical scanners with increased sensitivity.

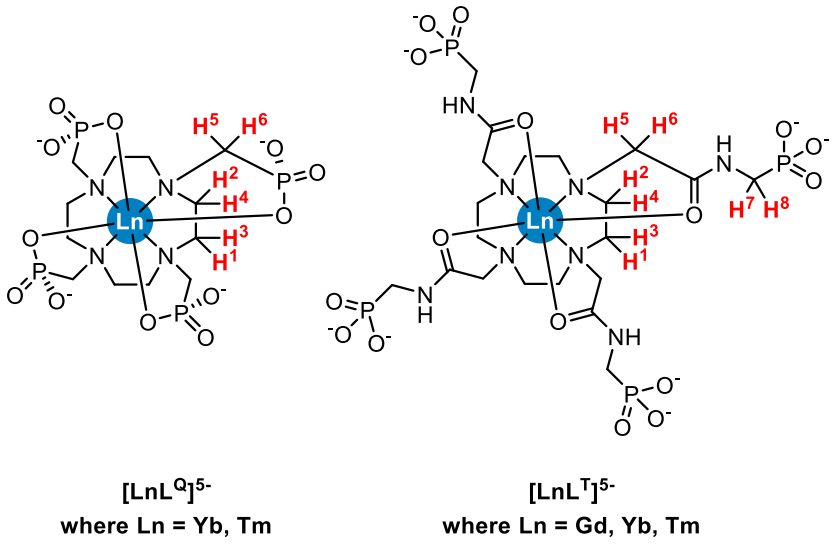

$[LnL^{Q}]^{5-}$
where Ln = Yb, Tm

$[LnL^{T}]^{5-}$
where Ln = Gd, Yb, Tm

Figure 2.1 Structures of selected pH responsive ^{1}H PARASHIFT probes.

The complex **$[TmL^{Q}]^{5-}$** (Figure 2.1) has been used as a temperature responsive probe for MRS (see Section 1.7.3, pages 33 and 34). Additionally, each phosphonate group can protonate stepwise, giving rise to a pronounced pH dependence of the proton resonance frequencies.[5] The chemical shift separation between selected pairs of ^{1}H resonances was found to have a linear dependence that was negligibly affected by complex concentration, ionic strength and, most crucially, temperature; allowing for ratiometric measurement of pH. NMR measurements of pH were similarly achieved by Zuo and Sherry using **$[TmL^{Q}]^{5-}$**, where it was found that H_6 (Figure 2.1) has a linear pH dependence of -3.27 ppm/pH unit in the pH range 5.5 to 7.5, albeit with a marked temperature dependence.[6] A deconvolution of variables was therefore necessary to unravel the dependences, monitoring the chemical shifts of two different proton

signals with different response coefficients to each variable using simultaneous equations (Equations 2.1 and 2.2):

$$\Delta\delta(i) = C_T(i)\Delta T + C_{pH}(i)\Delta pH \quad (2.1)$$

$$\Delta\delta(j) = C_T(j)\Delta T + C_{pH}(j)\Delta pH \quad (2.2)$$

where $C_T(i)$, $C_{pH}(i)$, $C_T(j)$, $C_{pH}(j)$ are the linear coefficients of the temperature and pH dependence of the chemical shifts in **[TmL^{Q}]$^{5-}$**, as measured *in vitro* for protons *i* and *j* respectively. This technique was used to simultaneously measure the temperature and pH changes in live rats undergoing ultrasonic hyperthermia treatment, following intra-peritoneal injection of 0.15 mmol/kg of **[TmL^{Q}]$^{5-}$** (2 T).[7] Analysis of the chemical shifts of H^2 and H^6 (Figure 2.1) allowed the measurement of temperature and pH that was concurrent with inserted pH electrode and thermocouple readings. Hyder and co-workers used a similar method to measure the brain temperature and pH of rats by focusing on two pairs of proton resonances shifted either side of the water resonance.[8,9] Animals were renally ligated and injected with 1.5 mmol/kg of **[TmL^{Q}]$^{5-}$** and each pair of resonances were acquired separately. Additional animal studies reduced the dose of complex to 1 mmol/kg and 2D CSI images of the brain (voxel size 10.2 µL) were obtained in 6 minutes (11.7 T).[10] The efficiency of the 2D and 3D mapping was further improved using spherical spatial encoding, which reduced the **[TmL^{Q}]$^{5-}$** dose to 0.5 mmol/kg, and increased the resolution (voxel size 1 µL) with 5 minute scan times (11.7 T).[11] Extracellular pH maps of rat brains were generated in animals bearing 9L and RG2 tumours,[12] and the extracellular pH within tumours (7.0) was found to be lower than that in normal brain tissue (7.4) (Figure 2.2).

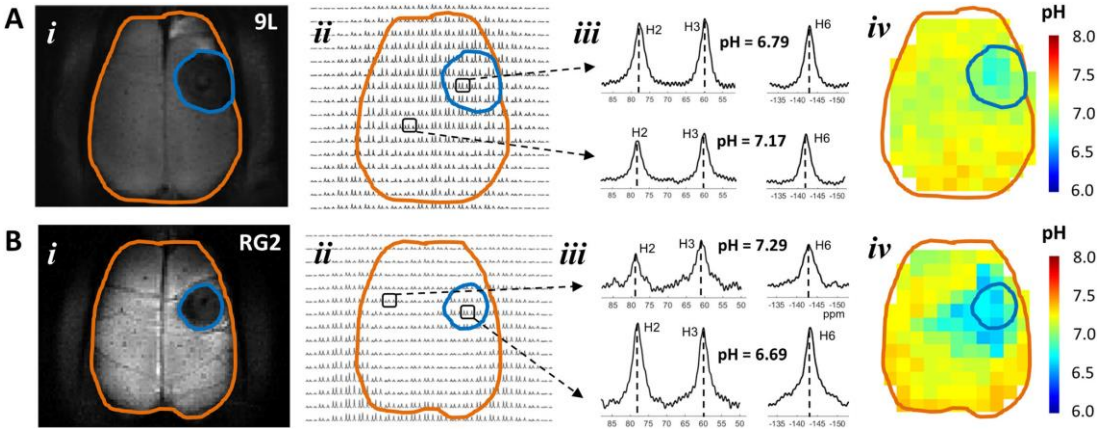

Figure 2.2 Representative extracellular pH maps of rats bearing (A) 9L and (B) RG2 tumours. (i) T_2-weighted image showing tumour localization (tumour = blue outline; brain = orange outline). (ii) A portion of the 3D chemical shift imaging (CSI) data for the slice in (i). (iii) Examples of spectra from intra-tumoural and peri-tumoural voxels. (iv) Quantitative maps of the extracellular pH were obtained using multiple $\mathbf{[TmL^{Q}]^{5-}}$ peaks and their respective pH sensitivities. Imaged using a 11.7 T horizontal-bore spectrometer, TR = 5 ms, SW = 35 kHz.[12]

The complex $\mathbf{[TmL^{Q}]^{5-}}$ was also used to map the effectiveness of temozolomide treatment (a chemotherapy drug) on U251 tumours by monitoring the pH of the tumour and brain,[13] and demonstrated that the pH of both tumour and brain tissue was higher in treated rats. Although these studies demonstrated the successful use of $\mathbf{[TmL^{Q}]^{5-}}$ to map temperature and pH *in vivo*, high doses of the probe were required together with renal ligation to supress rapid elimination of the hydrophilic complex.

The phosphonate-appended tetra-amide complex $\mathbf{[GdL^{T}]^{5-}}$ (Figure 2.1) has been studied as a pH responsive T_1 contrast agent because the relaxivity of the complex is pH dependent.[14–16] Additionally, the Yb^{3+} and Tm^{3+} complexes have been investigated as dual PARACEST and PARASHIFT probes.[17] The chemical shifts of the non-exchangeable resonances were pH dependent, with the most sensitive measurement, 5.2 ppm/pH unit (308 K), arising from the difference between H^6 and H^8 in $\mathbf{[TmL^{T}]^{5-}}$. The chemical shift difference also varied with temperature, 0.3 ppm/K (308 K). Determination of pH and T simultaneously required two pairs of chemical shifts, H^6-H^8 and H^2-H^3, each with different pH/T sensitivities. Phantom studies were used to compare the use of PARASHIFT and PARACEST in pH mapping which demonstrated that although CEST experiments could provide better spatial resolution PARASHIFT experiments had much higher pH sensitivities. High resolution pH mapping of $\mathbf{[LnL^{T}]^{5-}}$ may be feasible using a combination of PARACEST and PARASHIFT techniques.

However, further *in vitro* experiments are required to determine any sensitivity to biological cations, e.g. Ca^{2+} and Mg^{2+}, before *in vivo* capability can be realised.

In order for PARASHIFT imaging to have clinical relevance it is important to consider the dose and method of administration required to produce adequate image sensitivity. The pharmacokinetics/biodistribution of the molecular probe, and their interactions with other physiological species e.g. proteins and endogenous cations must also be considered. The *in vivo* experiments described above required high doses of probe (>0.1 mmol/kg) coupled with surgical renal ligation of the animal to reduce clearance rates, which inhibits the clinical application of such probes.

The phosphonate groups in compounds such as **$[LnL^{Q}]^{5-}$** and **$[LnL^{T}]^{5-}$** are known to bind divalent metal ions, often forming stable adducts, and interferences from interactions with Ca^{2+} ions within the body may pose a problem for *in vivo* imaging.[18] Although some studies have considered the effect of Ca^{2+} concentration,[10] absolute determination of pH and/or T *in vivo* is impractical using these probes.

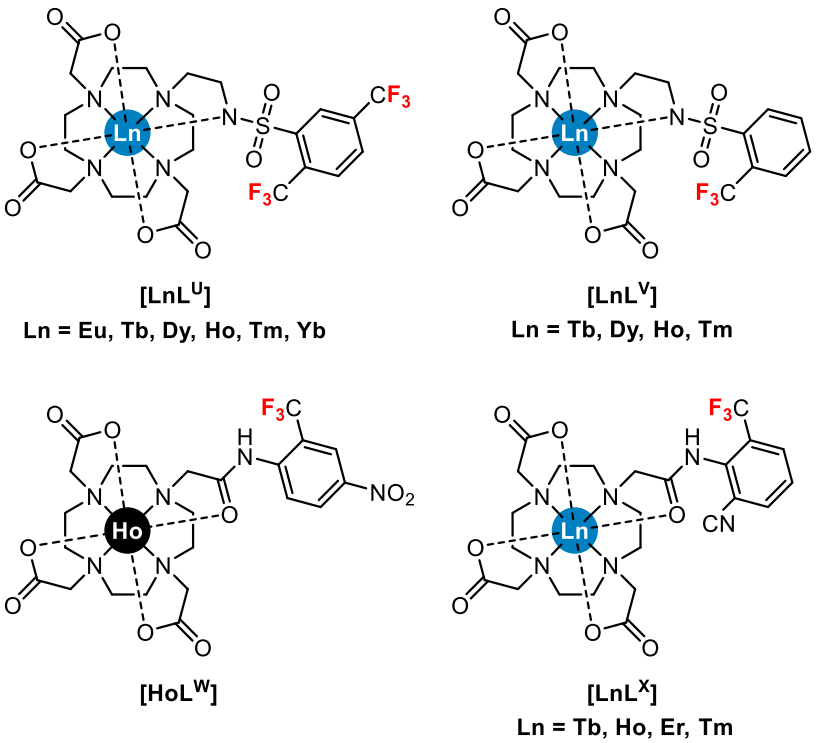

Figure 2.3 Structures of selected pH responsive ^{19}F PARASHIFT probes.

Several pH responsive ^{19}F PARASHIFT probes have been developed by Parker and co-workers (Figure 2.3).[19–21] The use of aryl CF_3 reporter groups in each complex results in three magnetically equivalent ^{19}F nuclei in order to increase signal

intensity.[19,20] The pH responsive behaviour of the complexes **[LnL^{U}]** and **[LnL^{V}]** was achieved through incorporation of a sulphonamide moiety that coordinates reversibly to the lanthanide(III) ion. Protonation of the sulphonamide N atom occurs around pH 5.5, resulting in the breaking of the N-Ln bond. Exchange between the bound and unbound complexes is slow on the NMR timescale. As a result, pH could be measured with the complex **[HoL^{V}]** by monitoring the ratio integrals of the ^{19}F resonance of both species. Modification of the pH responsive group to an amide resulted in fast exchange between the protonated and deprotonated species and hence only one ^{19}F resonance was observed (Figure 2.3 - **[LnL^{W}]** and **[LnL^{X}]**).[20,21] The chemical shift of this resonance corresponded to the weighted average of the two species. Varying the aryl substituents was found to regulate the acidity of the amide hydrogen and therefore the pH sensitivity and pK_a of the complex. The most promising results were found for the cyano-functionalised complex, **[HoL^{X}]**. The complex was found to exist as two isomers due to restricted rotation of the amide C-N bond and a large change in the ^{19}F chemical shift was observed between pH 5 and 9. Furthermore, the two isomers' shifts exhibited different pH dependencies allowing potential use as a ratiometric pH probe removing the need for calibration. However, the requirement of specialised dual ^{1}H and ^{19}F MRI coils still limits the clinical applications of these probes.

2.1 Trimethylphosphinate pH responsive PARASHIFT probe [LnL^{1}]$^{-}$

The optimised PARASHIFT probes discussed previously in Section 1.7.1 (pages 27-31) show that *in vivo* PARASHIFT imaging can be achieved on renally intact mice administered via tail vein injection with clinically relevant doses (<0.1 mmol/kg). In order to introduce pH responsive behaviour to the highly shifted, previously described PARASHIFT, trimethylphosphinate probe **[LnL^{J}]** (see Section 1.7.1, pages 28-30), the incorporation of a phosphonate group adjacent to the *tert*-butyl reporter group was proposed (Figure 2.4). The arylphosphonate group has a pK_a in the region of 7, similar to phenylphosphonate and is placed in close proximity to the reporter group in order that the protonation of this functional group will have an effect on the reporter chemical shift.

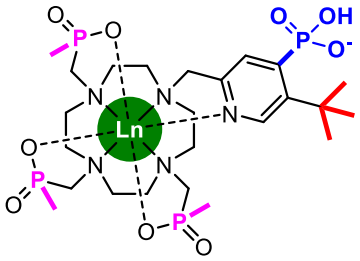

[LnL^1]$^-$

Ln = Tb, Dy, Ho, Er, Tm, Yb, Y, Gd

Figure 2.4 Structure of the trimethylphosphinate pH PARASHIFT probe, **[LnL^1]$^-$**.

2.1.1 Synthesis of [LnL^1]$^-$

The synthesis of **[LnL^1]$^-$** was carried out using a modification of reported procedures.[22]

The synthesis of the trimethylphosphinate cyclen macrocycle intermediate, **5**, is described in Scheme 2.1 and uses simple protecting group chemistry. Firstly, three of the cyclen amine sites were protected using benzyl chloroformate and triethylamine to create the tri-substituted carbamate, **1**. The macrocyclic product was purified on silica gel to ensure separation from di- and tetra-substituted analogues. The remaining secondary amine group was protected using di-*tert*-butyl dicarbonate to yield the fully substituted macrocycle, **2**. The benzyl carbamate protecting groups were then removed selectively via high-pressure hydrogenation, catalysed by $Pd(OH)_2/C$, to afford the mono-*tert*-butyloxycarbonyl (BOC) protected cyclen product, **3**. Condensation of **3** with paraformaldehyde in tetrahydrofuran led to the formation of an imine which was subsequently trapped by diethyl methylphosphonite to yield, via an Arbuzov reaction, the tri-phosphinate mono-BOC macrocycle, **4**. The macrocycle was purified by alumina gel column chromatography. The BOC group was deprotected with trifluoroacetic acid (TFA) to give the trimethylphosphinate macrocycle, **5**.

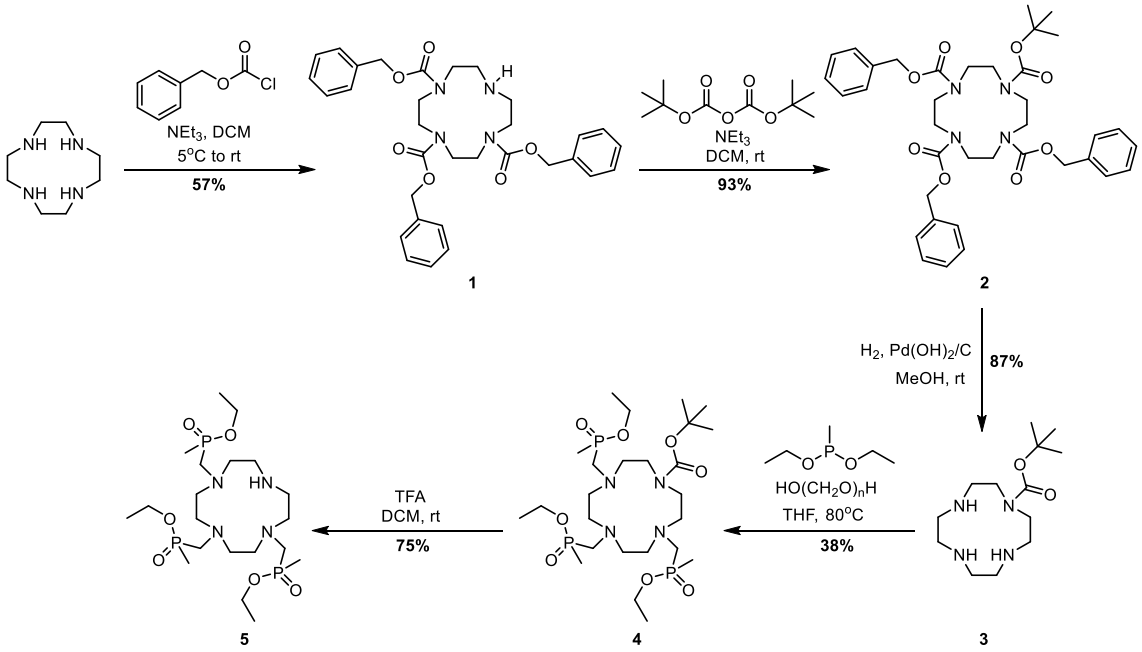

Scheme 2.1 The synthetic route to the trimethylphosphinate cyclen macrocycle, **5.**

The *tert*-butyl pyridine reporter moiety with a pH responsive phosphonate substituent in the 4-position was prepared as described in Scheme 2.2. The first step involved the introduction of the reporter *tert*-butyl group onto the pyridine ring, using a copper(I) cyanide catalysed Grignard alkylation, adapted from literature procedure.[23,24] The yield of this reaction is rather low (~50%) as the *tert*-butyl alkylated product, **6**, is produced in similar yield to the proton substituted by-product 2-methylpyridine. The *tert*-butyl product is volatile and column chromatography was avoided to reduce loss. Oxidation of the crude mixture of pyridines proceeded with *meta*-chloroperbenzoic acid (*m*CPBA). The 2-methylpyridine N-oxide produced from reaction of the by-product from the previous step and the *m*CPBA by-products were both removed by aqueous base washing to yield the N-oxide, **7**. The pyridine 4-position was nitrated using a mixture of concentrated HNO_3 and H_2SO_4 to form the 4-nitro product, **8**. Reduction of the nitro group to the amine, **9**, was achieved under high-pressure hydrogenation conditions, catalysed by Pd/C. A Sandmeyer reaction was used to generate the iodo-N-oxide pyridine compound, **10.** The diazotisation step was achieved by reaction with nitrous acid, generated *in situ* using sodium nitrite and fluoroboric acid. Upon addition of potassium iodide, the aryl iodide, **10**, was formed. The iodo group was chosen due to the weak carbon-halogen bond and its enhanced ability to undergo oxidative addition, in order to encourage the subsequent cross coupling reaction. A Boekelheide rearrangement occurred upon heating **10** in acetic anhydride. The

phosphonate species, **12**, was made via a palladium catalysed Arbusov-type reaction. Sodium ethoxide, formed by sodium metal in ethanol *in situ,* was used to cleave the acetate ester selectively, to yield the alcohol **13**. The reactive mesylate, **14**, was synthesised by reaction of the alcohol with triethylamine and methanesulfonyl chloride.

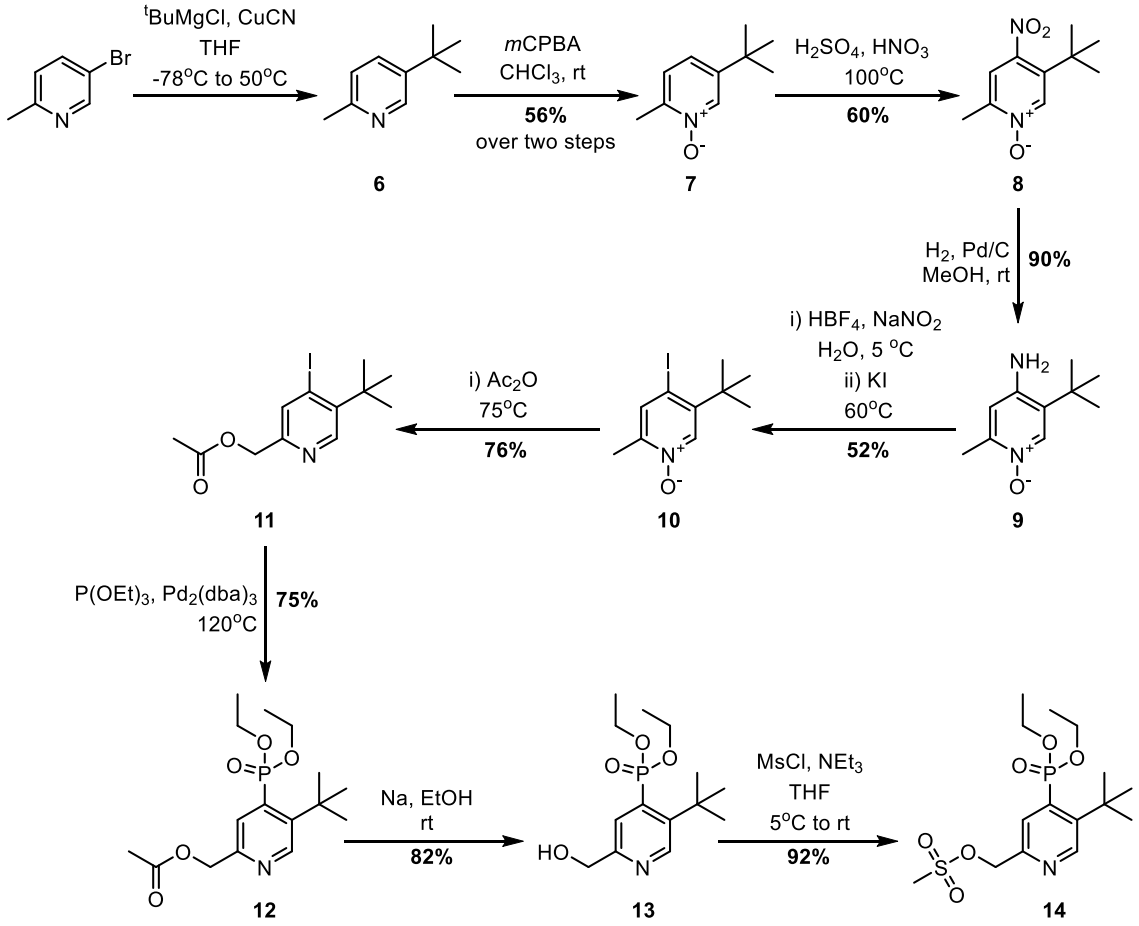

Scheme 2.2 Synthetic route to the phosphonate *tert*-butyl pyridyl moiety.

The alkylation of macrocycle **5** with the mesylate **14** proceeded as shown in Scheme 2.3 to give the ethyl protected ligand, $\mathbf{L^1}$. The deprotection of both the phosphinate and phosphonate ethyl esters was achieved by stirring at 70 °C with 6 M HCl. Finally, the deprotected macrocycle was complexed with the appropriate hydrated lanthanide(III) chloride salt in water, maintaining the pH at 5.5. The complexes were purified by reverse-phase preparative HPLC yielding $\mathbf{[LnL^1]^-}$, where Ln = Tb, Ho, Dy and Tm. High-resolution mass spectrometry and bulk magnetic susceptibility measurements were used to characterise each complex.

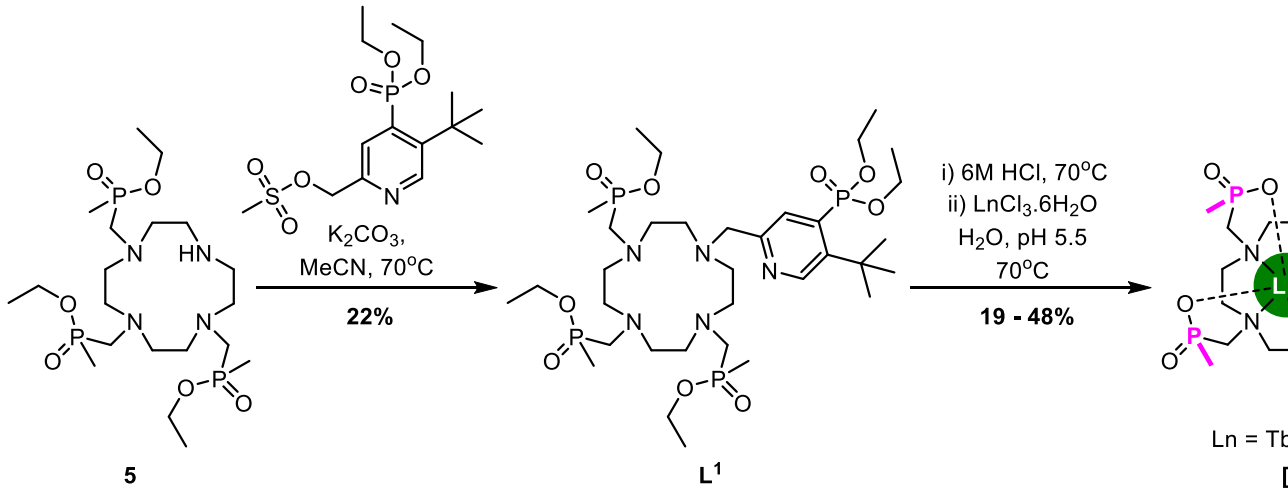

Scheme 2.3 General procedure for the synthesis of trimethylphosphinate pH PARASHIFT probe, **[LnL^1]$^-$**.

The luminescence lifetimes of the Eu^{3+} and Tb^{3+} excited states were measured in both H_2O and D_2O in order to calculate the metal hydration state of the complex, q. Inner sphere water molecules are able to quench lanthanide excited states due to the similar energy of the high vibrational levels of O-H oscillators. The vibronic quenching is much poorer in D_2O compared to H_2O due to the poorer energy overlap of O-D vibrational levels. Hence, the number of bound water molecules may be estimated using Equations 2.3 and 2.4.[25]

$$q_{Eu} = 1.2(k_{H_2O} - k_{D_2O} - 0.25) \quad (2.3)$$

$$q_{Tb} = 5(k_{H_2O} - k_{D_2O} - 0.06) \quad (2.4)$$

where k_{H_2O} and k_{D_2O} are the rate constants for luminescence decay. The q values for both **[TbL^1]** and **[EuL^1]** were both 0, consistent with the behaviour of the parent triphosphinate complex **[LnL^J]**.

2.1.2 Paramagnetic NMR studies of [LnL^1]$^-$: shift and relaxation

The shift and relaxation properties of **[LnL^1]$^-$** were investigated using ^{1}H NMR spectroscopy. Studies of **[LnL^1]$^-$** where Ln = Tb, Dy, Er and Tm were completed by Dr Katie-Louise Finney and are discussed here for comparison.

Chemical shift data of **[LnL^1]$^-$** shows that the paramagnetic shifts of the *tert*-butyl reporter resonance are greater than those of the parent complex lacking a phosphonate group, **[LnL^J]** (Figure 2.5). The PARASHIFT *tert*-butyl resonance of the

probe resonated well beyond the diamagnetic region, and was observed at +74 ppm for the Tm complex and -78 and -83 ppm for the Dy and Tb complexes respectively.

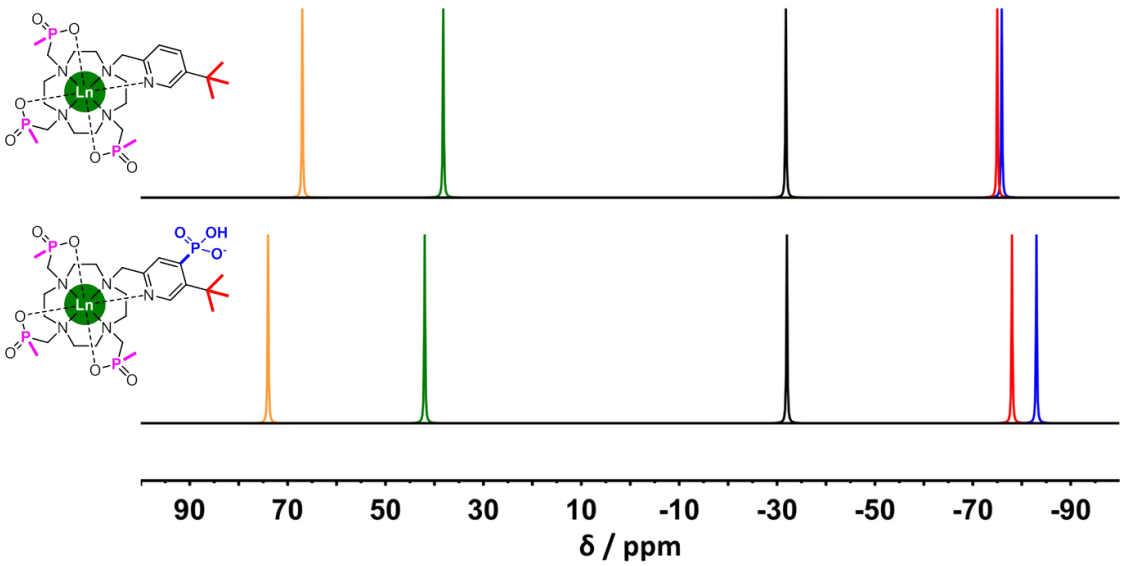

Figure 2.5 Schematic representation of the experimentally measured ^{1}H chemical shifts of the major *tert*-butyl signals in **[LnL^{J}]** (*top*) and **[LnL^{1}]$^{-}$** (*bottom*) (D_2O, 11.7 T, 295 K, pD 7.4) (yellow - Tm, green - Er, black - Ho, red - Dy, blue - Tb).

As seen with previous triphosphinate species the complex exists in two main TSAP conformers that are in slow exchange on the NMR timescale.[26] The isomer ratio observed by integration (7:1) for the major and minor species of **[LnL^{1}]$^{-}$** was larger than that of the parent triphosphinate complex **[LnL^{J}]** (5:1). Parker and co-workers found that phosphonate functionalisation does not drastically alter the rate of interconversion between the two TSAP isomers. Measurements of the ^{1}H and ^{31}P forward and reverse exchange rates using exchange spectroscopy (EXSY) spectroscopy allowed estimates of the equilibrium constant that were in agreement with those determined by direct integration.

A plot of the paramagnetic shift of the major *tert*-butyl resonance peak against the associated Bleaney constant reveals a poor agreement for the expected linear fit (Figure 2.6). The chemical shifts of the Tm^{3+} and Ho^{3+} complexes particularly are not adequately explained by Bleaney theory; such deviant behaviour has been observed previously.[23,27]

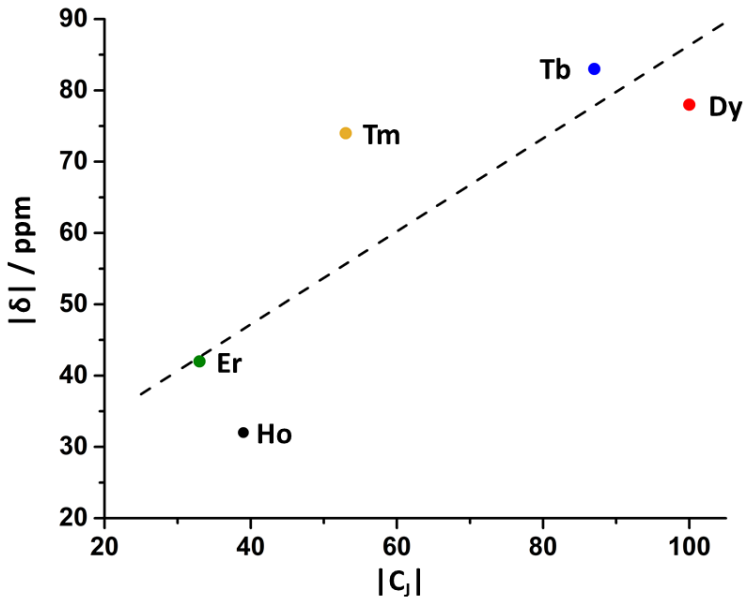

Figure 2.6 Variation of the paramagnetic ^{1}H NMR shift of the major *tert*-butyl resonance of **[LnL^{1}]$^{-}$** with the Bleaney constant, C_J (D_2O, 295 K, pD 7.4) $R^2 = 0.599$.

The longitudinal relaxation rate, R_1, was measured at six fields over the range 1 to 16.4 T (Table 2.1). The relaxation rates for each lanthanide complex of **[LnL^{1}]$^{-}$** were found to be increased when compared to the behaviour of the unsubstituted trimethylphosphinate **[LnL^{J}]**. The high longitudinal relaxation rates at clinically relevant field strengths (1 to 7 T) demonstrate that **[LnL^{1}]$^{-}$** is an attractive candidate for MRS imaging.

Table 2.1 ^{1}H NMR longitudinal relaxation rate data for the *tert*-butyl resonance of **[LnL^{1}]$^{-}$** as a function of magnetic field (D_2O, 295 K, pD 7.4).

Ln^{3+}	**R_1 / s^{-1} (± error)**					
	1 T	**4.7 T**	**9.4 T**	**11.7 T**	**14.1 T**	**16.4 T**
Tb	42 (3)	73 (1)	122 (2)	134 (1)	150 (1)	164 (1)
Dy	54 (5)	88 (3)	156 (2)	179 (1)	195 (1)	218 (1)
Ho	44 (4)	89 (5)	160 (2)	191 (2)	209 (1)	252 (1)
Er	92 (10)	117 (7)	173 (3)	198 (3)	214 (7)	239 (8)
Tm	25 (4)	99 (5)	139 (1)	160 (1)	179 (1)	190 (1)

The longitudinal relaxation rate data from all five complexes of **[LnL^{1}]$^{-}$** were analysed by global minimisation methods, assuming classical BRW theory (Equation 1.9, page 20) (Figure 2.7). The average internuclear distance, *r*, between the lanthanide ion and the *tert*-butyl protons was assumed to be 6.6 Å, as found in the X-ray studies of the unsubstituted trimethylphosphinate complex **[LnL^{J}]**.[26] The fitting procedure worked

well for Er^{3+}, Tb^{3+} and Dy^{3+}, but not for Tm^{3+} at low field or Ho^{3+} at higher fields. However, this fitting method relies upon the approximation that the electronic-nuclear interaction is simply distance dependent (r^{-6}) and does not take into account the angular dependence of lanthanide-induced relaxation.

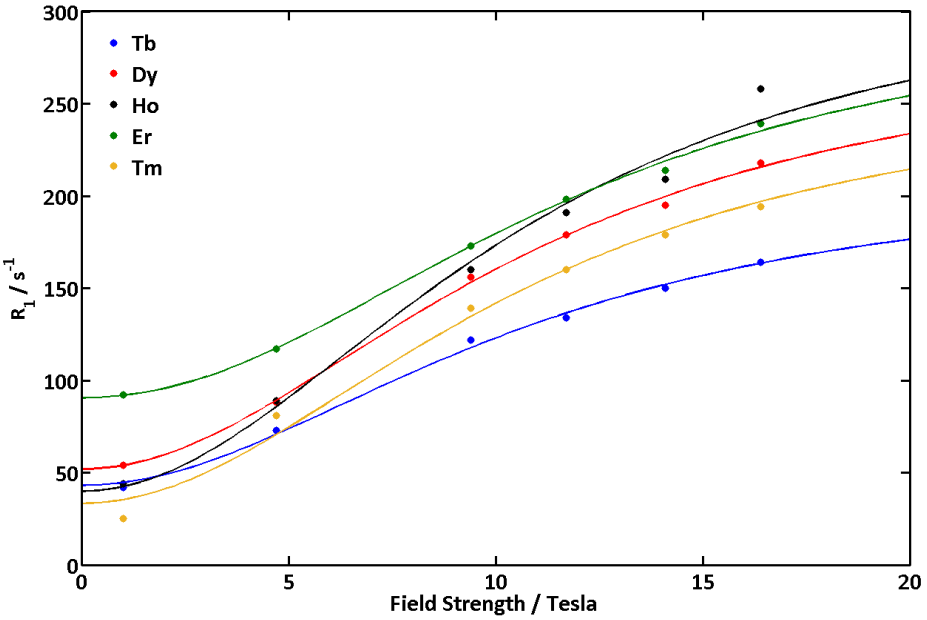

Figure 2.7 ^{1}H NMR relaxation rates (R_1 / s^{-1}) for the major *tert*-butyl resonance of **[LnL^1]**$^-$ as a function of magnetic field, showing the global fits (line) to the experimental data points (D_2O, 295K, pD 7.4, fixed r = 6.6 Å, minimizes to τ_r = 345(9) ps).

This minimisation process gives a common value for the rotational correlation time, τ_r, of 345 (±9) ps, and also predicts the effective magnetic moment for each lanthanide (Table 2.2). The value of τ_r is larger than that calculated for the non-phosphonated analogue **[LnL^J]** (249 ps).[28] Such behaviour is expected due to the increase in molecular volume and polarity conferred by the phosphonate group. The 'best-fit' values of the electronic relaxation rate, τ_e, and magnetic moment, μ_{eff}, are given in Table 2.2.

Table 2.2 Estimated 'best-fit' values for ^{1}H NMR relaxation parameters of **[LnL^1]$^-$** following global fitting with fixed r = 6.6 Å (D_2O, 295 K, pD 7.4).[a]

Ln^{3+}	τ_e / ps	μ_{eff} / BM[a]
Tb	0.44 (3)	9.89 (2)
Dy	0.46 (5)	10.65 (2)
Ho	0.34 (5)	10.99 (2)
Er	0.79 (9)	10.80 (4)
Tm	0.30 (4)	10.46 (3)

[a] Theoretical values for the magnetic moments of the lanthanide(III) ions are: Tb, 9.7; Dy, 10.6; Ho, 10.6; Er, 9.6; Tm, 7.6 BM.

Erbium(III) displays the highest value of τ_e, as expected from its high relaxation rates at low fields. The estimated magnetic moments show reasonable agreement with the classical values, except for Tm^{3+} which exhibits a significantly higher μ_{eff} value (+38%) than the theoretical one.

2.1.3 Paramagnetic NMR studies of [LnL^1]$^-$: temperature response

The temperature sensitivity of the *tert*-butyl chemical shift was investigated from 290 to 315 K and a linear dependence was observed against both T^{-2} and T (Figure 2.8).

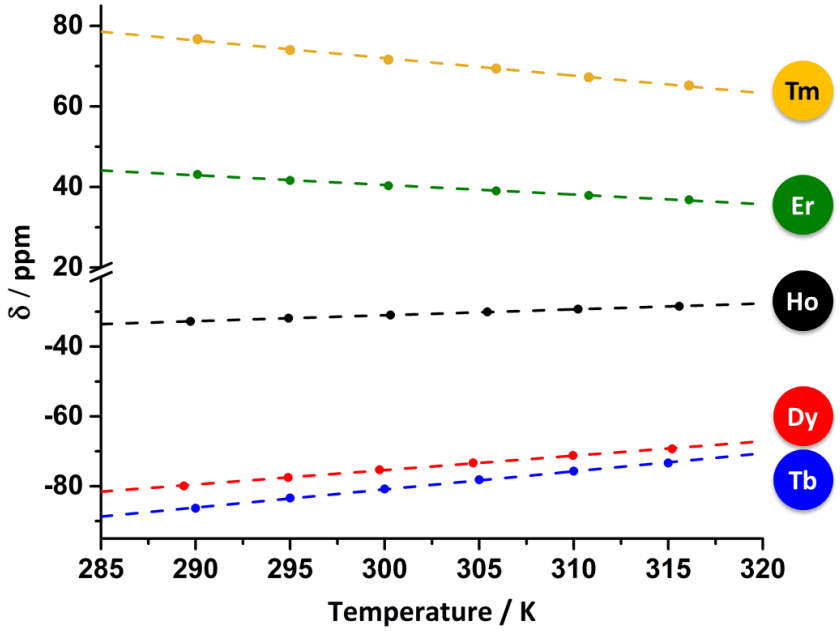

Figure 2.8 Variation in the chemical shift of the major *tert*-butyl resonance of **[LnL^1]**$^-$ as a function of temperature (D_2O, 11.7 T, pD 7.4): Tm (*yellow*) R^2 = 0.996; Er (*green*) R^2 = 0.996; Ho (*black*) R^2 = 0.999; Dy (*red*) R^2 = 0.998; Tb (*blue*) R^2 = 0.999.

The linear temperature dependences were generally proportional to the magnitude of the chemical shift (Table 2.3). The temperature sensitivity was found to be independent of pH, over the range 4.5 to 8.5.

Table 2.3 Comparison of the total shift and temperature sensitivities of the major *tert*-butyl resonance of **[LnL^1]**$^-$ (D_2O, 11.7 T, pD 7.4)

Ln^{3+}	δ_H ^{t}Bu / ppm	T sensitivity / ppm/K
Tb	-83	+0.52
Dy	-78	+0.41
Ho	-32	+0.17
Er	+42	-0.24
Tm	+74	-0.44

2.1.4 Paramagnetic NMR studies of [LnL^1]$^-$: pH response

The pH responsive chemical shift behaviour of the *tert*-butyl reporter group of **[LnL^1]**$^-$ was investigated by pD titration. The pD was altered using D_2O solutions of NaOD and DCl, and measured before and after each NMR using a pre-calibrated pH meter. The ^{1}H NMR spectra were acquired at different pD values, where pD = pH + 0.41 (Figure 2.9).

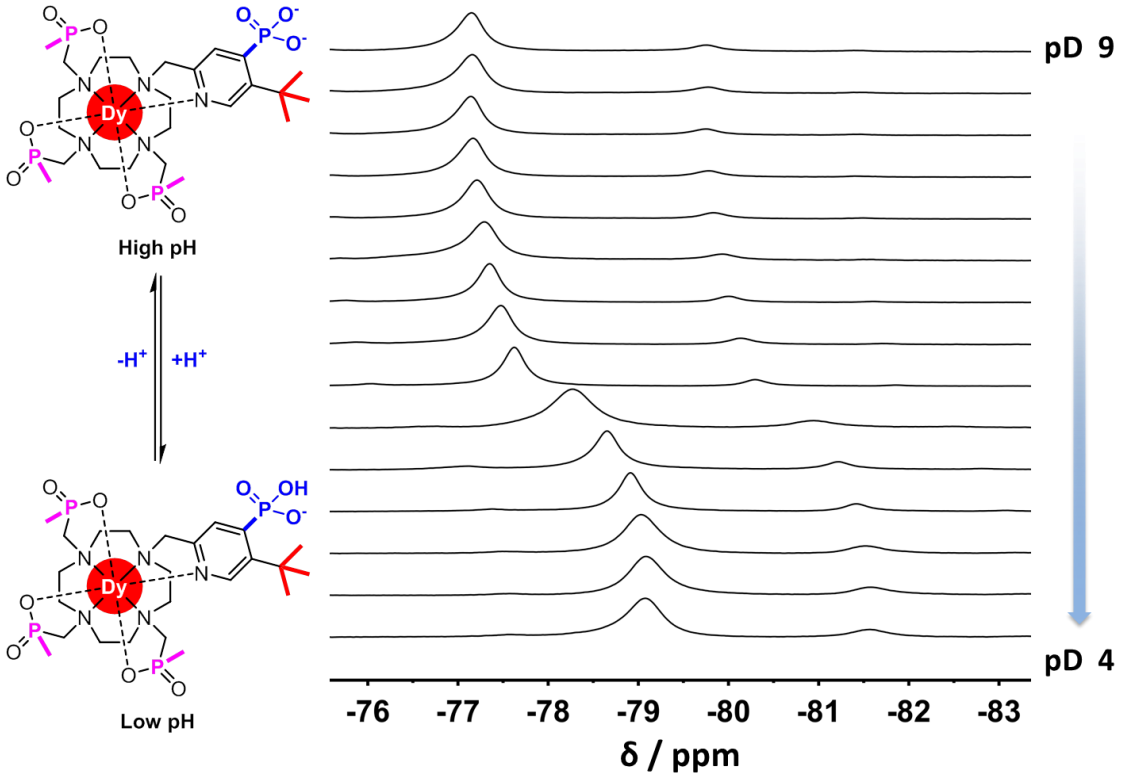

Figure 2.9 Stacked ^{1}H NMR spectra of the *tert*-butyl resonances of **[DyL^{1}]** as a function of pD (D_2O, 11.7 T, 295 K) and the corresponding pH equilibrium.

Chemical exchange between the protonated and deprotonated complex occurs fast relative to the NMR timescale and hence a single *tert*-butyl resonance is observed, that is a population weighted average of the two species. The ^{1}H chemical shift of the *tert*-butyl reporter group therefore varies as a sigmoidal function of pD, allowing the pK_a of the phosphonate protonation to be determined by non-linear least square iterative analysis to a Boltzmann function (Figure 2.10). The pseudocontact shift of the reporter group increases with decreasing pD for each lanthanide. ^{31}P NMR analysis of **[DyL^{1}]** demonstrated that the phosphonate pseudocontact chemical shift is also dependent on pD, as expected (Figure 2.10).

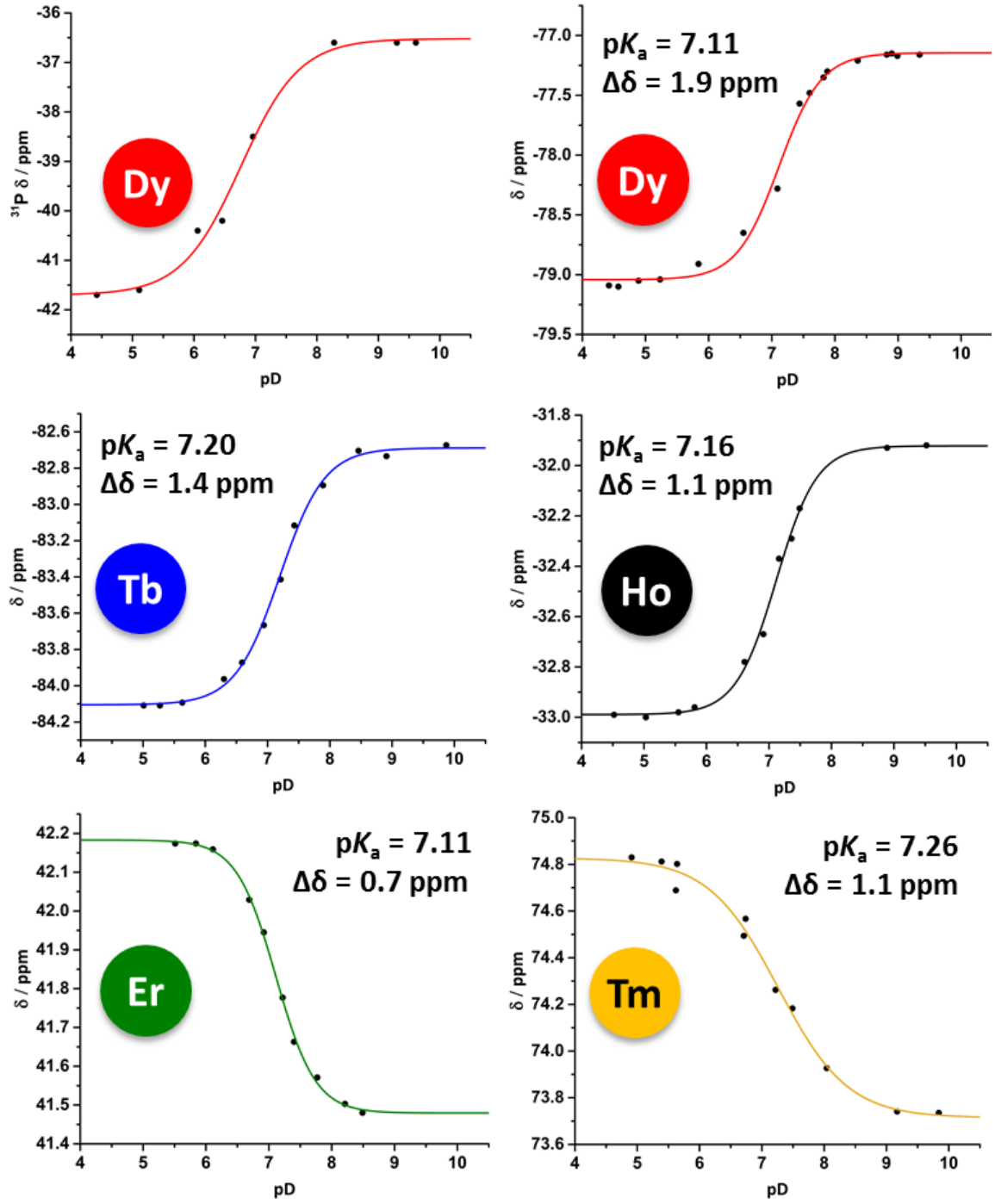

Figure 2.10 (*Top Left*) Variation in the ^{31}P phosphonate chemical shift of **[DyL^1]** as a function of pD. (*Remaining*) Variation in the ^{1}H chemical shift of the major *tert*-butyl resonance of **[LnL^1]**$^-$ as a function of pD (D_2O, 11.7 T, 295 K).

The pK_a values averaged 7.16 in D_2O at zero ionic strength (I = 0), in close agreement to that of phenylphosphonate (7.09) indicating that the close proximity of the large *tert*-butyl group to the phosphonate does not drastically alter the protonation equilibrium.

The longitudinal relaxation rate, R_1, of the *tert*-butyl reporter resonance was found to be unchanged with pH over the range measured (4.5 – 8.5). However, the transverse relaxation rate, R_2, was generally found to increase around the pK_a. If the R_2 of the

reporter resonance is too large, then the extent of line-broadening caused by this can inhibit signal detection. Equilibrium between two species in exchange can result in additional line broadening. The linewidth is greatest at the pK_a when the complex exists as a 50:50 mixture of both species. The full width half maximum (FWHM) of the *tert*-butyl resonance was measured as a function of pD, revealing that at the pK_a the linewidth was approximately doubled. The ratio of R_1/R_2 was also calculated around the pK_a; a value as close as possible to unity is ideal for optimal signal detection (Table 2.4).

Table 2.4 Linewidths and calculated ratios of R_1/R_2 of the major *tert*-butyl resonance of **[LnL^1]**$^-$ at the relevant pK_a value (D_2O, 11.7 T, pD 7.2).

Ln^{3+}	FWHM / s^{-1}	R_1/R_2
Tb	214	0.20
Dy	164	0.35
Ho	181	0.34
Er	133	0.47
Tm	123	0.41

pD/pH titrations of **[DyL^1]** were also undertaken in 0.1 M NaCl and a 50:50 murine plamsa:H_2O, giving pK_a values of 6.71 and 6.80 respectively. The decrease in pK_a demonstrated the expected effect of ionic strength on the protonation equilibrium and the small variance in plasma indicates that the presence of serum proteins has relatively little impact on the protonation equilibrium.

The total chemical shift change (Δδ) between high and low pD ranged from 0.7 ppm for **[ErL^1]** to 1.4 ppm for **[TbL^1]**. Interestingly, unlike the variation with temperature, Δδ was not proportional to the initial chemical shift of the *tert*-butyl resonance. Proportionally, the *tert*-butyl resonance of **[HoL^1]** is most affected by the change of pD and **[TmL^1]** the least. It can be assumed that there is no structural change of the ligand and that *r* remains approximately constant upon change in pH, as suggested by the consistent longitudinal relaxation rates above and below the pK_a.

A recent study of **[DyL^1]** and a series of trimethylphosphinate Dy^{3+} complexes with variation of the *para*-substituent of the single pyridine donor (Figure 2.11) suggested

that small changes in ligand structure can significantly alter the magnetic susceptibility anisotropy.[28]

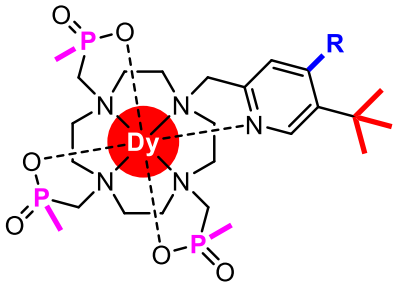

R = H, NMe_2, NO_2, $CONH_2$,
Cl, SCH_2CO_2-, PO_2OH^-

Figure 2.11 Structure of Dy^{3+} trimethylphosphinate complexes with variants of the 4-position of the pyridine studied.[28]

Emission and relaxation analysis demonstrated that the anisotropy is surprisingly sensitive to remote ligand substitution and the polarisability of one pyridine donor within the octadentate ligand. In 2018, similar studies on a series of C_3 symmetric TACN complexes highlighted the sensitivity of the ligand field to solvent polarisability.[29]

The protonation of the phosphonate group of **[LnL^1]$^-$** will lead to a change in polarisability of the pyridine group. It is likely that the magnetic susceptibility anisotropy difference between the two species is the cause of the chemical shift variation of the *tert*-butyl reporter resonance frequency.

One assumption arising from Bleaney's theory is that the principal axis of magnetisation is constant for each lanthanide ion, within the same ligand structure. It was originally demonstrated by Sessoli and co-workers that, in the solid state at 2 K, the position of this axis varies in C_4 symmetric **[LnDOTA(H_2O)]$^-$** complexes.[30] In the case of **[DyDOTA(H_2O)]$^-$** it was calculated that the presence of an axial bound water rotated the axis by about 90°.[31] More recently, Parker and co-workers revealed, with the aid of *ab initio* calculations, that the orientation of the major component of the magnetic susceptibility tensor differs significantly between complexes of different lanthanides for the same trimethylphosphinate complex, **[LnL^J]**.[27] This variation of angle may give rise to the differing pH sensitivities between the lanthanides for **[LnL^1]$^-$** although more

detailed analysis of the both species above and below the pK_a is required to fully describe the magnetic susceptibility anisotropy.

2.1.5 Triple imaging phantom and *in vivo* studies of $[LnL^1]^-$

The dual temperature and pH sensitivity of the reporter chemical shift requires the presence of two different lanthanide complexes of **$[LnL^1]^-$**, in order to observe two shift values concurrently. The use of simultaneous equations allows the T and pH of the region of interest to be calculated.

The complexes **$[DyL^1]^-$** and **$[TmL^1]^-$** were chosen for imaging studies as a suitable pair of complexes, due to their fast and similar relaxation rates around 7 T, large chemical shifts and favourable pH/T sensitivities (Table 2.5).

Table 2.5 Overview of properties of **$[DyL^1]^-$** and **$[TmL^1]^-$**.

Ln^{3+}	δ_H ^{t}Bu / ppm	R_1 / s^{-1} (± error)			T sensitivity / ppm/K	Δδ / ppm	pK_a (D_2O)
		4.7 T	9.4 T	11.7 T			
Dy	-78	88 (3)	156 (2)	179 (1)	+0.41	+1.9	7.11
Tm	+74	99 (5)	139 (1)	160 (1)	-0.44	+1.1	7.26

A pulse sequence was developed by Dr Dara O'Hogain and Prof. Andrew M. Blamire at Newcastle University to enable the simultaneous acquisition of the three resonances; the water and the two well-separated *tert*-butyl signals. The similar relaxation rates of the two complexes allowed for the frequency, shape, duration and power of the two excitation pulses to remain the same, with only a modified offset frequency. No specific excitation pulse was applied to the water signal as there was sufficient excitation within the bandwidth of the two RF pulses. The spectral width was increased to ~60 kHz to encompass signal from all three chemical shifts. Phantoms were created and imaged to test the pulse sequence and demonstrate the practicability of MRS *in vivo* studies (Figure 2.12). A 2D-MRSI acquisition was applied to generate a matrix of voxels, each of which can be inspected to show the full spectral range. Individual peaks from both complexes and water are clearly observed in the mixed solutions in the lower vial. A 3DGE triple image method was used for imaging the basic spatial distribution of the resonances. The triple imaging experiment allows sampling across the whole frequency range of all the signals allowing for acquisition of three entirely

independent, but simultaneously acquired MRI images offset by the frequency of the resonance. This method does not affect the signal to noise ratio of the scan in comparison to acquiring individual images of each component as the noise bandwidth per pixel is unchanged.

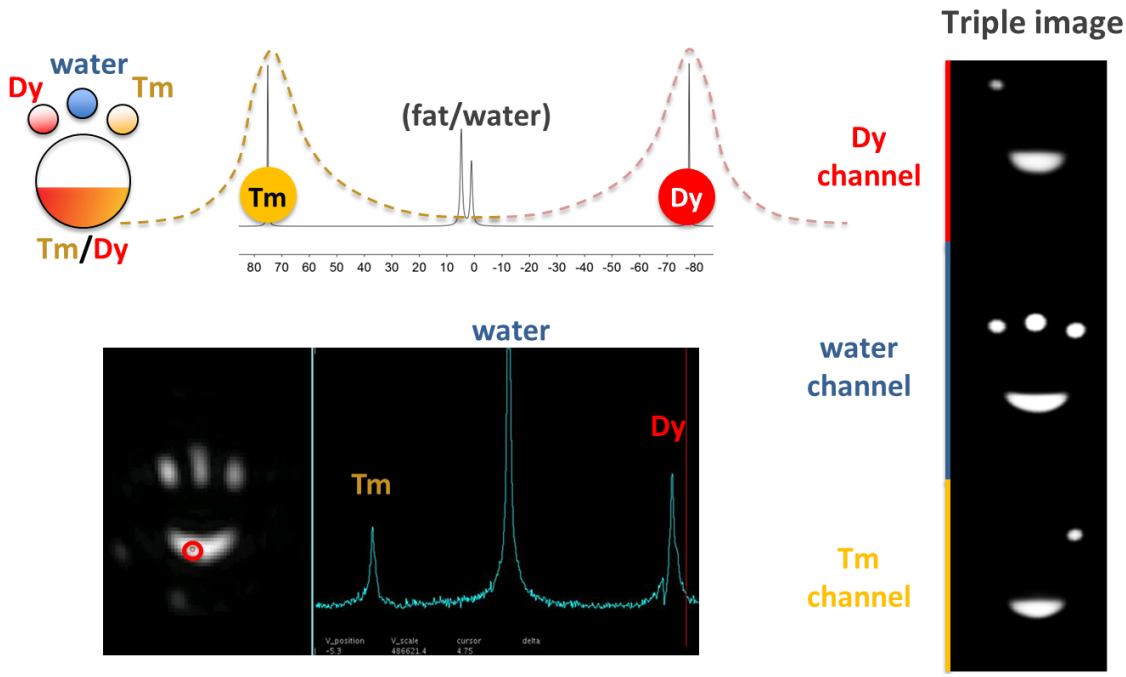

Figure 2.12 (*Left*) A 2D-MRSI spectral imaging sequence applied to a phantom set-up of **[LnL^1]**$^-$ with a TR of 19.5 ms, TE_1 of 0.95 ms, TE_2 of 0.45 ms and a spectral width SW = 54 kHz, 32 averages, scan time = 100 s. (*Right*) A 3DGE pulse sequence with a TR = 4.28 ms, TE_1 (Dy) = 0.87 ms, TE_2 (Tm) = 1.37 ms, SW = 60 kHz, 80 averages, scan time = 354 s. The phantom contains 1.2 mM **[TmL^1]**, **[DyL^1]**, a 1.2 mM equimolar mix of the complexes or water.

In vivo studies were performed by Dr. Dara O'Hogain and Ian Wilson (Newcastle University) on CD1 healthy mice *(n=3)* following a tail-vein injection with 0.05 mmoles/kg of an equimolar mixture of the Tm^{3+}/Dy^{3+} complexes in saline. Selected spectra from the MRSI were extracted to show the change in shift of each complex in different tissues (Figure 2.13).

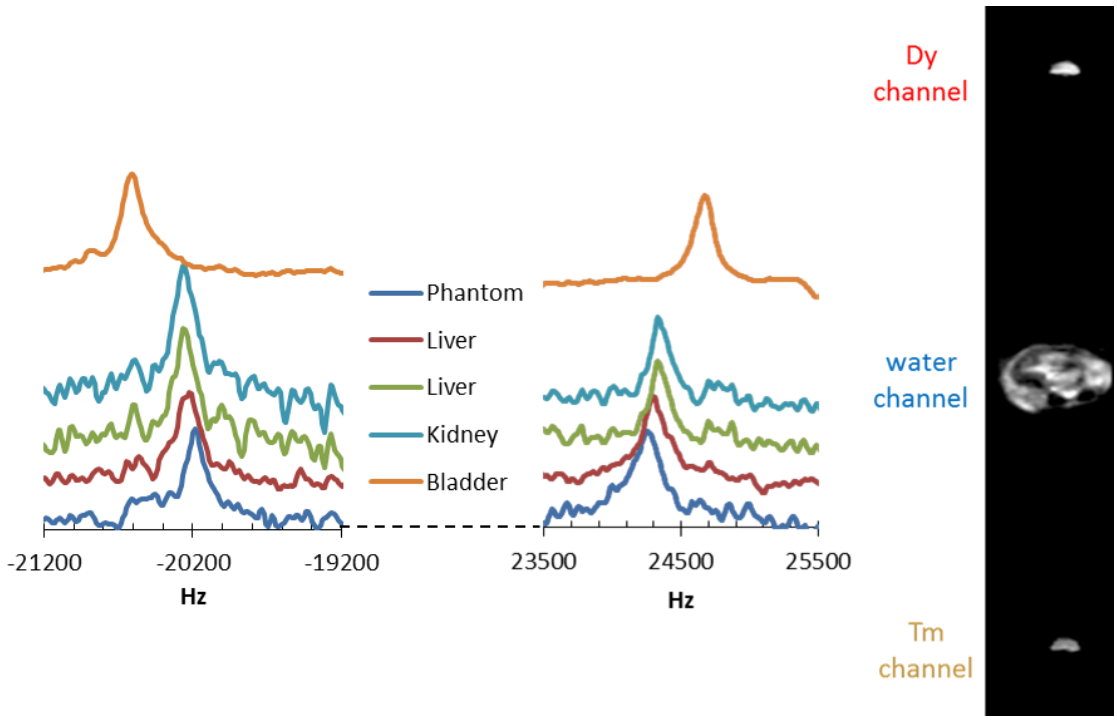

Figure 2.13 *In vivo* examples of MRSI acquisition in a healthy mouse following injection of a 1:1 mix of **[DyL^1]**$^-$ and **[TmL^1]**$^-$. (*Left*) Selected spectra from a time series of 2DSI acquisitions. The stacked spectra show the Tm^{3+} (*left*) and Dy^{3+} (*right*) spectral regions from voxels sampling liver, kidney, bladder and an external reference phantom. MRSI acquisition parameters were TR = 19.5 ms, TE_1 (Dy) = 0.45 ms, TE_2 (Tm) = 0.95 ms, SW = 54 kHz, 32 averages, scan time 100 s. (*Right*) A 3DGE triple image taken 40 minutes post injection using a pulse sequence with TR = 10.66 ms, TE_1 = 1.58 ms, TE_2 = 2.08 ms, SW= 54 kHz, 100 averages, scan time = 1092 s.

There are clear differences in the frequencies between tissues, most significantly in the bladder. The pH and temperature were calculated using simultaneous equations that define the frequency versus the sigmoidal pH and linear T dependence for each complex (developed by Dr. Dara O'Hogain).[32]

The pH values for the selected ROIs in the liver, kidney and bladder were measured to be 7.14, 6.92 and 6.80 respectively, which is consistent with the expected range of values for healthy 'wild-type' animals. The temperature in the bladder was found to be 3.5 K lower than core body temperature, which was the main cause of the large frequency difference in shift relative to the other tissues. This is consistent with the previously reported temperature difference between bladder and core of 4 K from *in vivo* studies of the dimethylphosphinate complex **[DyL^K]**$^-$.[33]

In the spectra extracted from both the *in vitro* and *in vivo* scans the peak picking of the **[DyL^1]**$^-$ *tert*-butyl resonance was more challenging than that of **[TmL^1]**$^-$. The linewidth of the Dy^{3+} complex was rather broad at 7 T, inhibiting the use of automatic peak

detection, and hence in future, complexes with narrower linewidths should be chosen for such imaging studies.

An additional challenge for the *in vivo* studies arose from the rather rapid clearance of the complex and its fast accumulation in the bladder (Figure 2.14). The majority of PARASHIFT signal was lost from the kidneys and the liver within 5 minutes of injection. The tissue retention and lipophilicity of the complex must be improved, to to more image other tissues more effectively, at least in this mouse model.

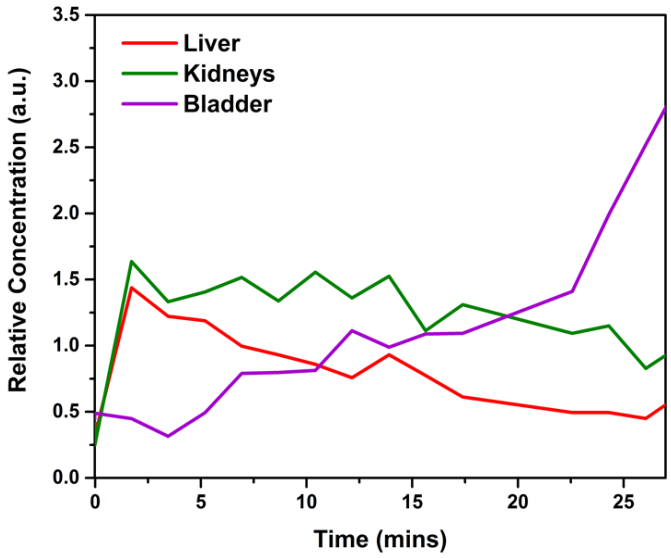

Figure 2.14 Relative concentration of **[DyL^1]$^-$** as a function of time in an intact, healthy mouse following single i.v. injection of 0.05 mmol/kg of a 1:1 mixture of the Tm/Dy complexes of **[LnL^1]**.

2.2 Tribenzylphosphinate pH responsive PARASHIFT probe [LnL^2]$^-$

The structure of **[LnL^1]$^-$** must be modified in order to lengthen the tissue retention time and increase lipophilicity, whilst maintaining favourable shift and relaxation properties. Manipulation of the R group on the phosphinate arms can be used to enhance lipophilicity. Several tetraphosphinate lanthanide complexes have made previously by Parker and co-workers, including a series of lanthanide tetrabenzylphosphinate complexes.[34] It was hoped that changing the phosphorus substituent from methyl to a bulkier, non-polar benzyl group would increase the tissue retention time of the complex, **[LnL^2]$^-$** (Figure 2.15), particularly in the liver as the presence of organic anion transporters in the hepatocytes may encourage clearance via the liver. The pyridine

moiety will remain unchanged to minimise changes to pH dependence, shift and relaxation.

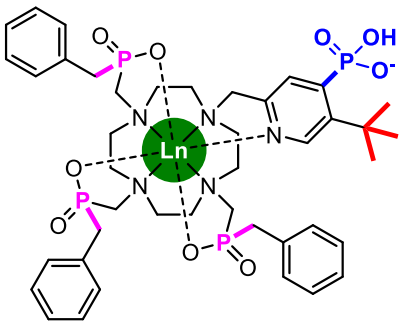

Figure 2.15 Structure of tribenzylphosphinate pH PARASHIFT probe, **[LnL^2]$^-$**.

2.2.1 Synthesis of [LnL^2]$^-$

The synthesis for the tribenzylphosphinate cyclen macrocycle is analogous to that of the methyl variant (Scheme 2.4). The mono-BOC protected macrocycle, **3**, was reacted instead with anhydrous paraformaldehyde and diethyl benzylphosphonite (synthesised by Dr. P. Kanthi Senanayake) to yield the ethyl ester-protected tribenzylphosphinate mono-BOC macrocycle, **15**. The BOC group was similarly deprotected with trifluoroacetic acid at room temperature to yield the macrocycle, **16**, ready for alkylation.

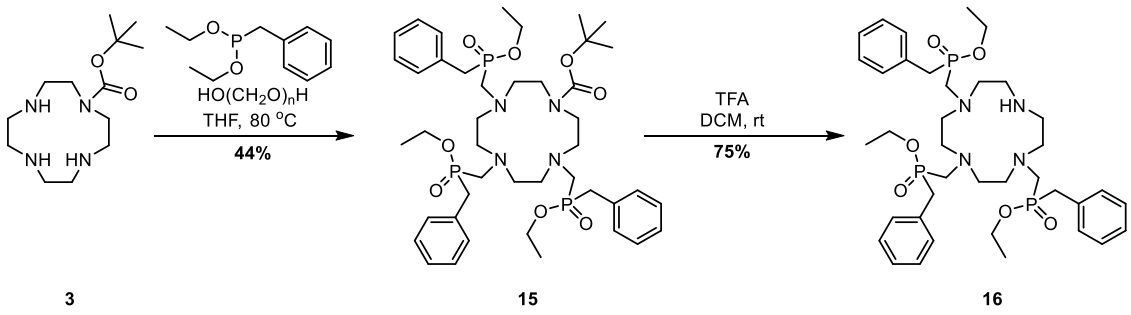

Scheme 2.4 Procedure for the synthesis of the tri-benzylphosphinate 12-N$_4$ macrocycle, **16**.

The alkylation of the macrocycle, **16**, with the mesylate**, 14**, proceeded in the presence of caesium carbonate and the tetra-alkylated ligand**, L^2** was purified on alumina column chromatography (Scheme 2.5). The phosphinate esters were hydrolysed in 6 M HCl before complexation with the appropriate lanthanide(III) chloride. The complex

[DyL^2]$^-$ was synthesised by Dr. P. Kanthi Senanayake, and complexes **[TbL^2]$^-$** and **[ErL^2]$^-$** were synthesised by Olga Tyurina.

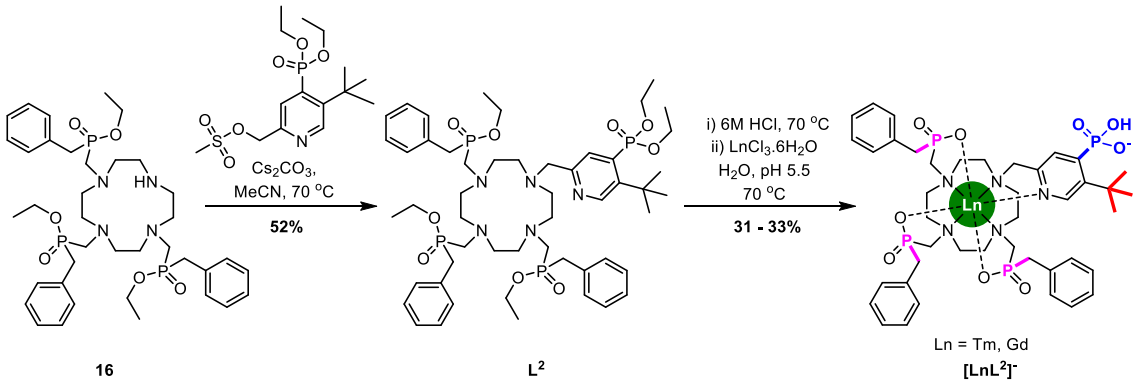

Scheme 2.5 Procedure for the alkylation and complexation of the tri-benzylphosphinate complex, **[LnL^2]**.

The luminescence lifetimes of the Tb^{3+} excited state were measured in both H_2O and D_2O in order to calculate the metal hydration state of the complex. The *q* value for **[TbL^2]$^-$** was found to be 0, consistent with the behaviour of the trimethylphosphinate complex, **[LnL^1]$^-$**.

2.2.2 Paramagnetic NMR studies of [LnL^2]$^-$: shift and relaxation

Initial ^{1}H NMR studies of **[LnL^2]$^-$** showed that the *tert*-butyl resonances were even further shifted (8 - 15%) than analogous **[LnL^1]$^-$** complexes (Figure 2.16). The Tb^{3+}, Dy^{3+} and Tm^{3+} complexes were shifted to -90, -86 and +85 ppm respectively.

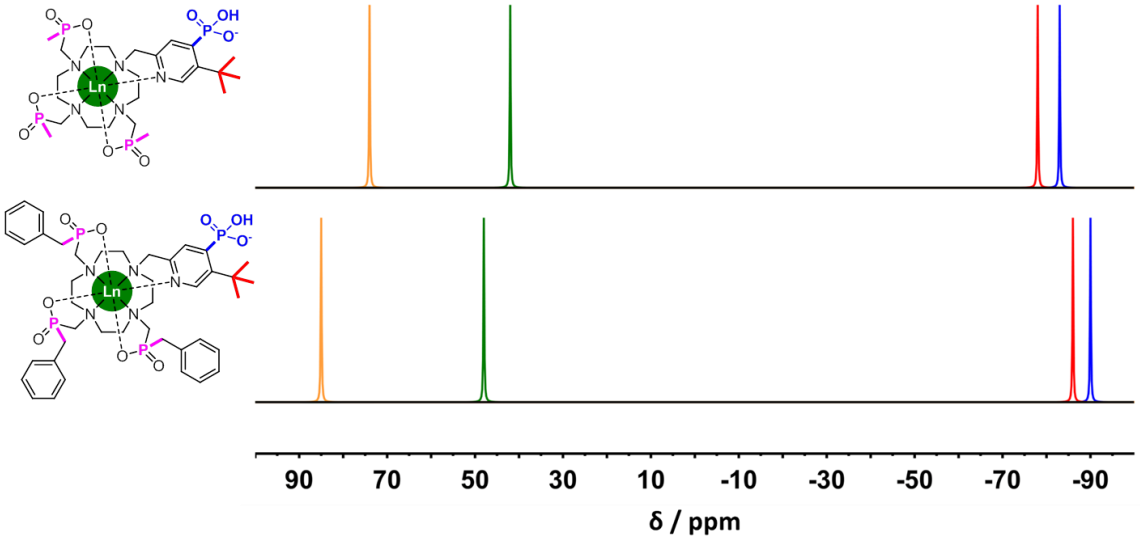

Figure 2.16 Schematic representation of the experimentally measured ^{1}H chemical shifts of the major *tert*-butyl signals in **[LnL^1]$^-$** (*top*) and **[LnL^2]$^-$** (*bottom*) (D_2O, 295 K, pD 7.4) (yellow - Tm, green - Er, red - Dy, blue - Tb).

Similarly to **[LnL^1]$^-$**, a major and minor *tert*-butyl resonance of **[LnL^2]$^-$** was observed, deemed to be the two TSAP diastereoisomers in solution. However, the observed signal intensity of the major isomer was found in a slightly higher ratio (9:1) than in the methylphosphinate analogue. The additional steric bulk of the benzyl group may cause the preferential destabilisation of the minor isomer.

The longitudinal relaxation rate, R_1, was measured at six fields, over the range 1 to 16.4 T (Table 2.6). The general trend found for the relaxation rates was in general agreement with that of **[LnL^1]$^-$** although the **[ErL^2]$^-$** complex exhibited significantly faster relaxation, particularly at low fields. The longitudinal relaxation rate of **[TmL^2]$^-$** was higher at every field, compared to **[TmL^1]$^-$**.

Table 2.6 Longitudinal relaxation rate data for the major *tert*-butyl resonance of **[LnL^2]$^-$** at different magnetic field strengths (D_2O, pD 7.4, 295 K).

Ln^{3+}	***R*$_1$ / s^{-1} (± error)**					
	1.0 T	**4.7 T**	**9.4 T**	**11.7 T**	**14.1 T**	**16.4 T**
Tb	45 (1)	69 (1)	111 (1)	126 (1)	140 (1)	151 (1)
Dy	56 (1)	94 (1)	143 (1)	175 (1)	196 (1)	213 (1)
Er	113 (3)	145 (1)	183 (1)	201 (1)	221 (1)	235 (2)
Tm	35 (1)	101 (1)	164 (1)	185 (1)	200 (1)	219 (1)

The relaxation data of the four complexes were again analysed by global minimisation methods assuming the internuclear distance, *r*, remains 6.6 Å (Figure 2.17). The fit for **[ErL^2]$^-$** and **[TmL^2]$^-$** is notably poor at low fields.

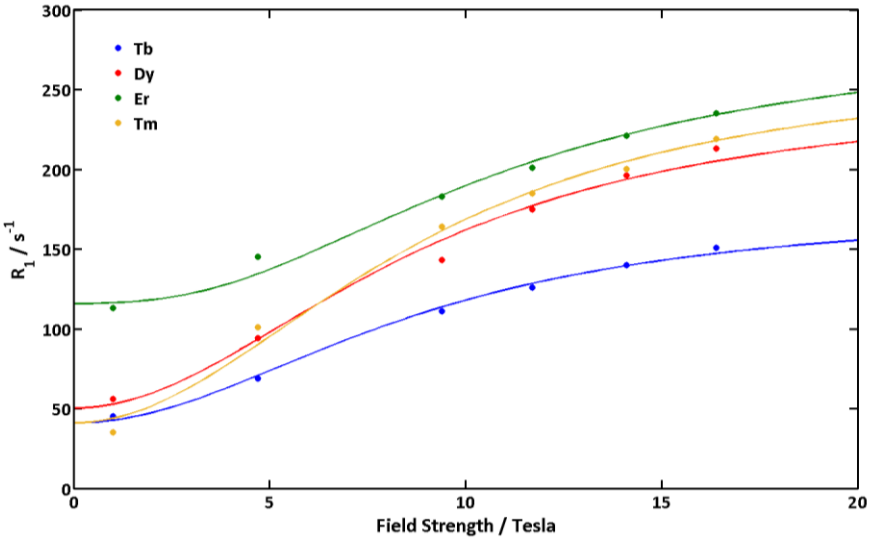

Figure 2.17 ^{1}H NMR relaxation rates (R_1 / s^{-1}) for the major *tert*-butyl resonance of **[LnL^2]$^-$** as a function of magnetic field, showing the global fits (line) to the experimental data points (D_2O, 295K, pD 7.4, fixed *r* = 6.6 Å, minimizes to τ_r = 400 (15) ps).

The minimisation process gave a common rotational correlation time, τ_r, of 400 (±15) ps, and also predicts the effective magnetic moment, μ_{eff}, and electronic relaxation time, τ_e, for each lanthanide ion (Table 2.7). The calculated value of τ_r is larger than that for the methylphosphinate analogue **[LnL^1]$^-$** (345 ps). Rotational correlation time is generally proportional to molecular volume and hence molecular weight, so the increase in τ_r is explained by the increase in mass associated with the three benzyl groups.

Table 2.7 Estimated 'best-fit' values for ^{1}H NMR relaxation parameters of **[LnL^1]$^-$** and **[LnL^2]$^-$** following global fitting with fixed r = 6.6 Å (D_2O, 295 K, pD 7.4).[a]

Ln^{3+}	τ_e / ps		μ_{eff} / BM[a]	
	[LnL^1]$^-$	[LnL^2]$^-$	[LnL^1]$^-$	[LnL^2]$^-$
Tb	0.44 (3)	0.43 (5)	9.89 (2)	9.77 (3)
Dy	0.46 (5)	0.44 (6)	10.65 (2)	10.68 (3)
Er	0.79 (9)	0.99 (12)	10.80 (4)	10.89 (4)
Tm	0.30 (4)	0.35 (3)	10.46 (3)	10.90 (5)

[a] Theoretical values for the magnetic moments of the lanthanide(III) ions are: Tb, 9.7; Dy, 10.6; Ho, 10.6; Er, 9.6; Tm, 7.6 BM.

The electronic relaxation times of the Tb^{3+}, Dy^{3+} and Tm^{3+} ions are close to those estimated for **[LnL^1]$^-$**, whilst **[ErL^2]$^-$** shows a significant increase. However, the high value may be a result of the poor fit of the relaxation rates at low field. The 'best-fit' values of μ_{eff} have increased for each **[LnL^2]$^-$** compared to **[LnL^1]$^-$**, most significantly demonstrated by **[TmL^2]$^-$** which now has the largest magnetic moment of all the lanthanide ions and is 43% larger than the theoretical value. Evidently, these values must be treated with considerable caution as the paramagnetic relaxation induced by the electron-nuclear dipolar interaction is anisotropic, whereas the theory applied here assumes it is isotropic.

2.2.3 Paramagnetic NMR studies of [LnL^2]$^-$: temperature response

The chemical shift of the *tert*-butyl resonance was linearly dependent on both T^{-2} and over the range measured directly on T. The temperature sensitivities of **[LnL^2]$^-$** were calculated from the linear fit (Figure 2.18 and Table 2.8).

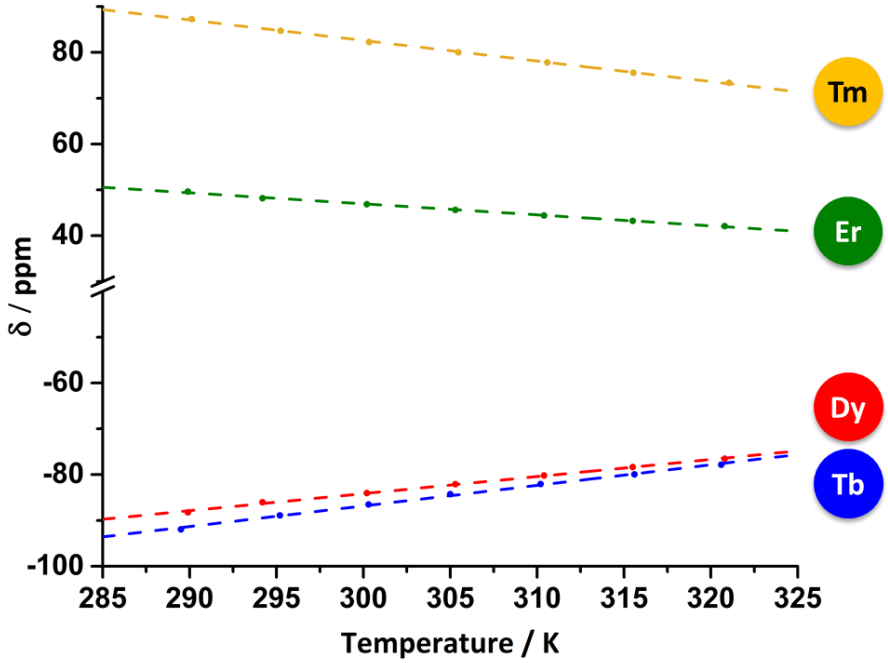

Figure 2.18 Variation in the chemical shift of the major *tert*-butyl resonance of **[LnL^2]**$^-$ as a function of temperature (D_2O, 11.7 T, pD 7.4): Tm (*yellow*) R^2 = 0.999; Er (*green*) R^2 = 0.997; Dy (*red*) R^2 = 0.998; Tb (*blue*) R^2 = 0.997.

Table 2.8 Comparison of the temperature sensitivities of the major *tert*-butyl resonance of **[LnL^1]**$^-$ and **[LnL^2]**$^-$ (D_2O, 11.7 T, pD 7.4).

Ln^{3+}	T sensitivity / ppm/K	
	[LnL^1]$^-$	**[LnL^2]**$^-$
Tb	+0.52	+0.45
Dy	+0.41	+0.37
Er	-0.24	-0.24
Tm	-0.44	-0.45

As the *tert*-butyl chemical shifts of **[LnL^2]**$^-$ are greater than **[LnL^1]**$^-$, it would be expected that the temperature dependences would be larger. However, whilst the sensitivities of the Er^{3+} and Tm^{3+} complexes are comparable, **[TbL^2]**$^-$ and **[DyL^2]**$^-$ have actually reduced slightly in magnitude.

2.2.4 Paramagnetic NMR studies of [LnL^2]$^-$: pH response

The behaviour of **[LnL^2]**$^-$ in response to changing pH was similar to the behaviour observed with **[LnL^1]**$^-$. The protonated and deprotonated species are in fast exchange on the NMR timescale, and the pseudocontact shift is greatest at low pD. Plots of the

chemical shift of the *tert*-butyl resonance against pD were again iteratively fitted to a sigmoidal curve to calculate the associated pK_a values (Figure 2.19).

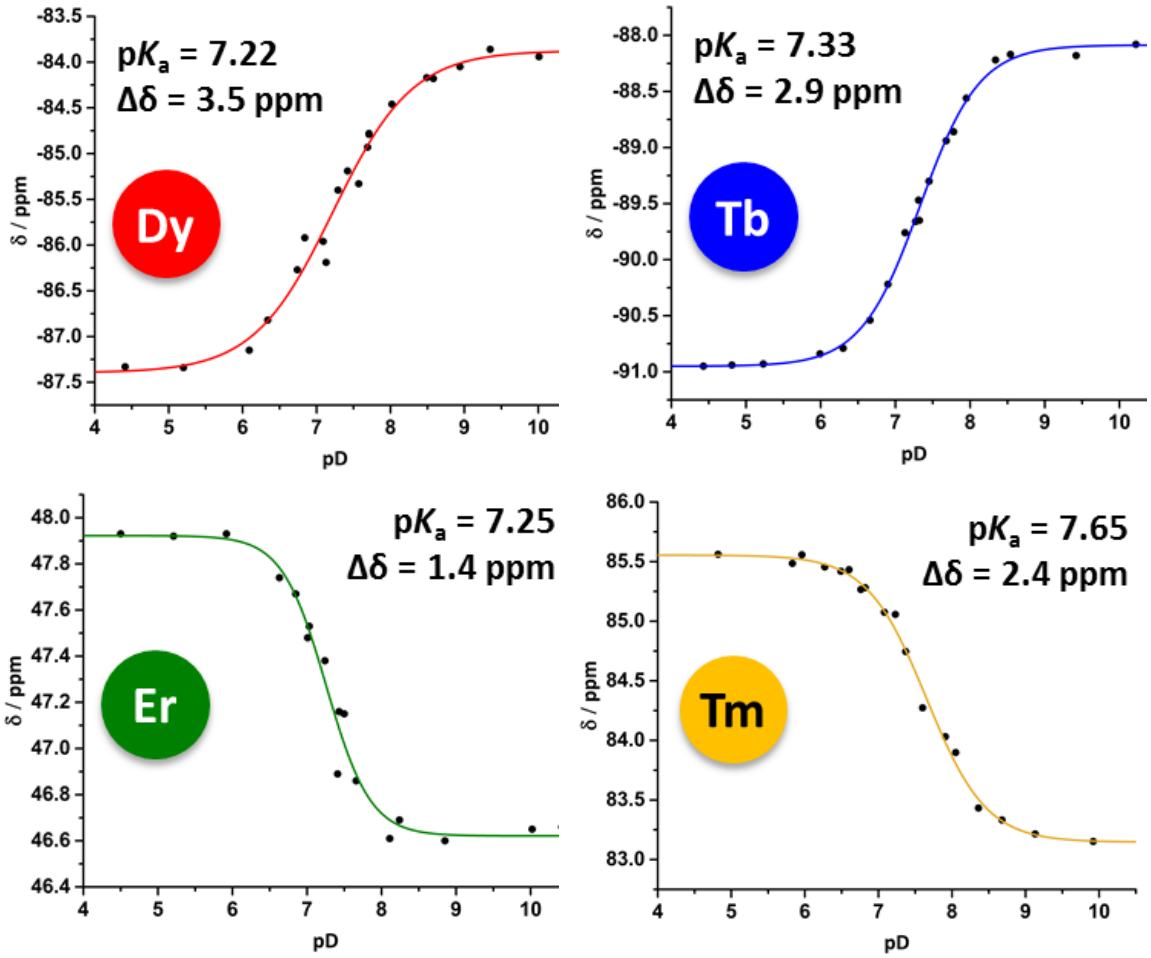

Figure 2.19 Variation in the ^{1}H chemical shift of the major *tert*-butyl resonance of **[LnL^2]**$^-$ as a function of pD (D_2O, 11.7 T, 295 K).

Inspection of the pK_a curves of **[LnL^2]**$^-$ shows that the change from methyl- to benzylphosphinate has increased the pK_a (Table 2.9). The overall solvation of the complex is likely to be affected by the introduction of the more hydrophobic, larger benzylphosphinate groups. Disproportional destabilisation of the doubly negatively charged conjugate base, resulting from reduced overall hydration, would cause an increase in pK_a. The pK_a of **[TmL^2]**$^-$ is also remarkably high, and the explanation for this is not obvious although the same trend is also observed in **[LnL^1]**$^-$. The ionic radius of Tm^{3+} is the smallest of the lanthanide ions studied, which may result in a slight geometric change that alters the Ln-N_{py} bond strength, influencing the polarisability.

Table 2.9 Comparison of the pH sensitivities of the major *tert*-butyl resonance of **[LnL^1]$^-$** and **[LnL^2]$^-$** (D_2O, 11.7 T, 295 K).

Ln^{3+}	pK_a		Δδ / ppm	
	[LnL^1]	**[LnL^2]**	**[LnL^1]**	**[LnL^2]**
Tb	7.20	7.33	1.4	2.9
Dy	7.11	7.22	1.9	3.5
Er	7.11	7.26	0.7	1.3
Tm	7.26	7.65	1.1	2.4

As with **[LnL^1]$^-$**, the values of Δδ were not proportional to the initial chemical shift. Comparison of the pH responses of **[LnL^1]$^-$** and **[LnL^2]$^-$** reveals that the order of Δδ is the same across the Ln^{3+} ions for both series of complexes (Table 2.9). The *tert*-butyl resonance of **[DyL^2]$^-$** shifts most upon the change of pH. However, the magnitude of Δδ in the benzylphosphinate is significantly increased, effectively doubling in the cases of the Tb^{3+}, Er^{3+} and Tm^{3+} complexes. This behaviour may be as a consequence of the differential degree of hydration of the protonated and deprotonated species. As a consequence, the change in solvation, albeit a second sphere effect, may influence the ligand field and hence change anisotropy of the lanthanide ion resulting in a larger chemical shift change. A larger chemical shift range of pH sensitivity, should lead to an increase in accuracy in the measurement of pH.

2.2.5 *In vivo* studies of [LnL^2]$^-$

In order to establish if the modification from methyl to benzyl phosphinates had improved the clearance profile of **[LnL^2]$^-$**, a series of standard contrast enhanced ^{1}H MRI experiments were undertaken using **[GdL^2]$^-$**. These scans revealed no real improvement in the biodistribution profile from **[LnL^1]$^-$** (Figure 2.20); the complex predominantly clears via the kidneys, accumulating rapidly in the bladder. Due to these results further *in vitro* and *in vivo* PARASHIFT imaging experiments were not pursued, and a further modification of the complex was sought in order to increase retention.

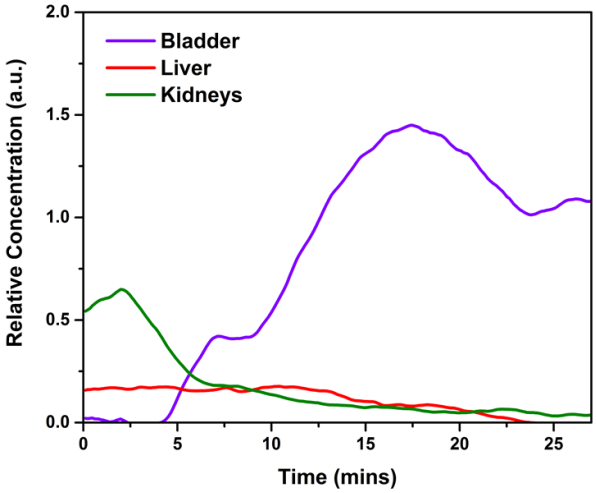

Figure 2.20 Relative concentration of **[GdL^2]$^-$** as a function of time in an intact, healthy mouse following single i.v. injection of 0.05 mmoles/kg.

2.3 Dibenzylphosphinate pH responsive PARASHIFT probe [LnL^3]$^-$

Previous *in vivo* studies by Parker and co-workers on the temperature sensitive PARASHIFT probe dimethylphosphinate probe **[DyL^K]$^-$** showed a slightly more favourable biodistribution (see Section 1.7.1 and 1.73, pages 30-31 and 36-37).[33] It was proposed that modification of the tribenzylphosphinate complex **[LnL^2]$^-$** to a dibenzylphosphinate complex **[LnL^3]$^-$** (Figure 2.21) could result in decreased clearance rates which, when coupled with an increase in the number of magnetically equivalent nuclei as a result of the C_2 symmetry, will increase the observed signal intensity.

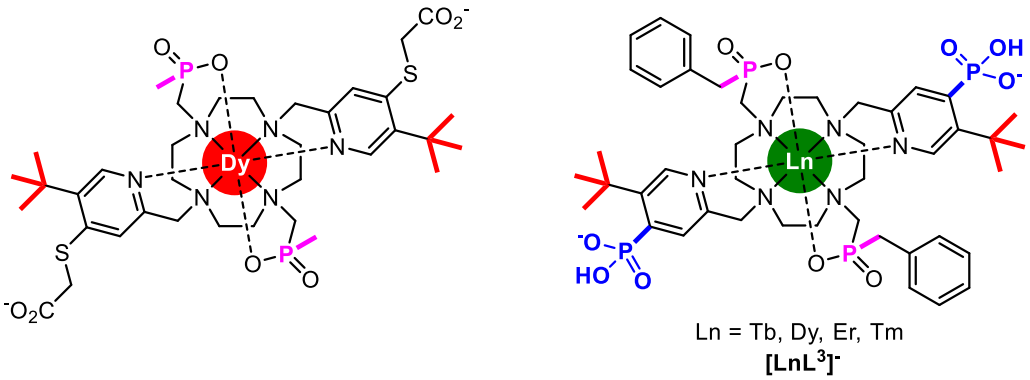

Figure 2.21 Structure of diphosphinate PARASHIFT probes, (*left*) the temperature responsive dimethylphosphinate complex **[DyL^K]$^-$** and (*right*) the pH and temperature responsive dibenzylphosphinate complex **[LnL^3]$^-$.**

The complexes of **[LnL^3]$^-$** (Ln= Tb, Dy, Er, Tm and Gd) were synthesised by Dr P. Kanthi Senanayake and the NMR and relaxation properties of the *tert*-butyl reporter group

were subsequently studied. The metal hydration state of **[TbL^3]**$^-$ was found to be 0, by luminescence lifetime analysis in H_2O and D_2O.

2.3.1 Paramagnetic NMR studies of [LnL^3]$^-$: shift and relaxation

The chemical shift of the major *tert*-butyl resonances of **[LnL^3]**$^-$ are the least shifted of the three classes of probes discussed. However, whilst the shifts are decreased in comparison to **[LnL^2]**$^-$, they remain far beyond the diamagnetic region of water and fat (Figure 2.22). The chemical shift of **[TbL^3]**$^-$ is least affected by the change from tribenzylphosphinate to dibenzylphosphinate (-9%) compared to other lanthanides (-24 to -33%).

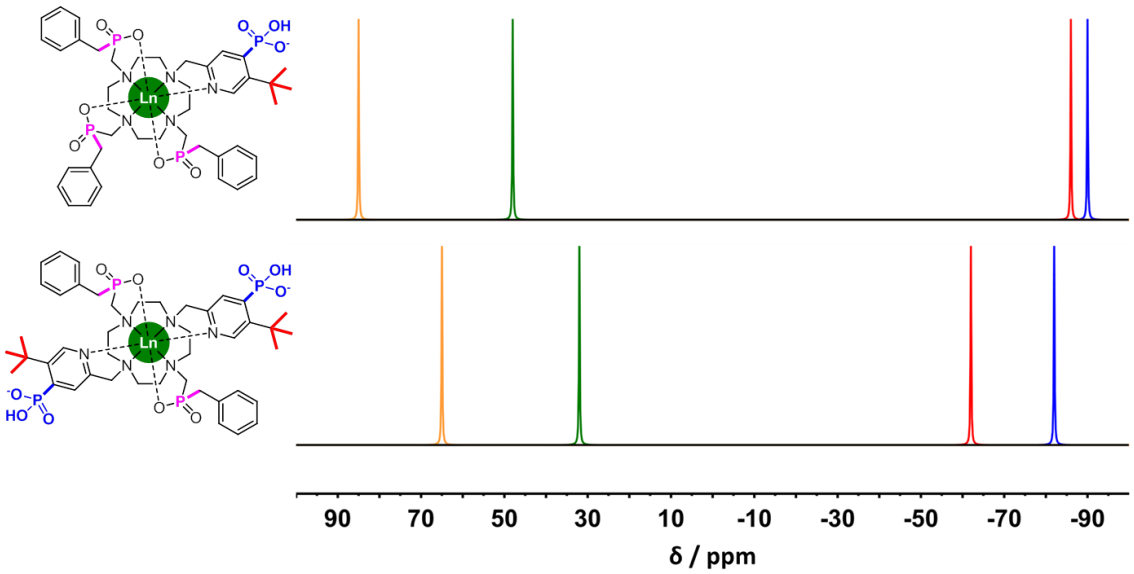

Figure 2.22 Schematic representation of the experimentally measured ^{1}H chemical shifts of the major *tert*-butyl signals in **[LnL^2]**$^-$ (*top*) and **[LnL^3]**$^-$ (*bottom*) (D_2O, 11.7 T, 295 K, pD 7.4) (yellow - Tm, green - Er, red - Dy, blue - Tb).

A single major *tert*-butyl resonance demonstrates the presence of a C_2 symmetric species that renders both reporter groups magnetically equivalent. However, whereas only two diastereoisomers were observed for **[LnL^1]**$^-$ and **[LnL^2]**$^-$, up to four *tert*-butyl resonances were identified for all **[LnL^3]**$^-$ (Figure 2.23). These *tert*-butyl peaks were identified by comparison of integrals, linewidths and their longitudinal relaxation rates.

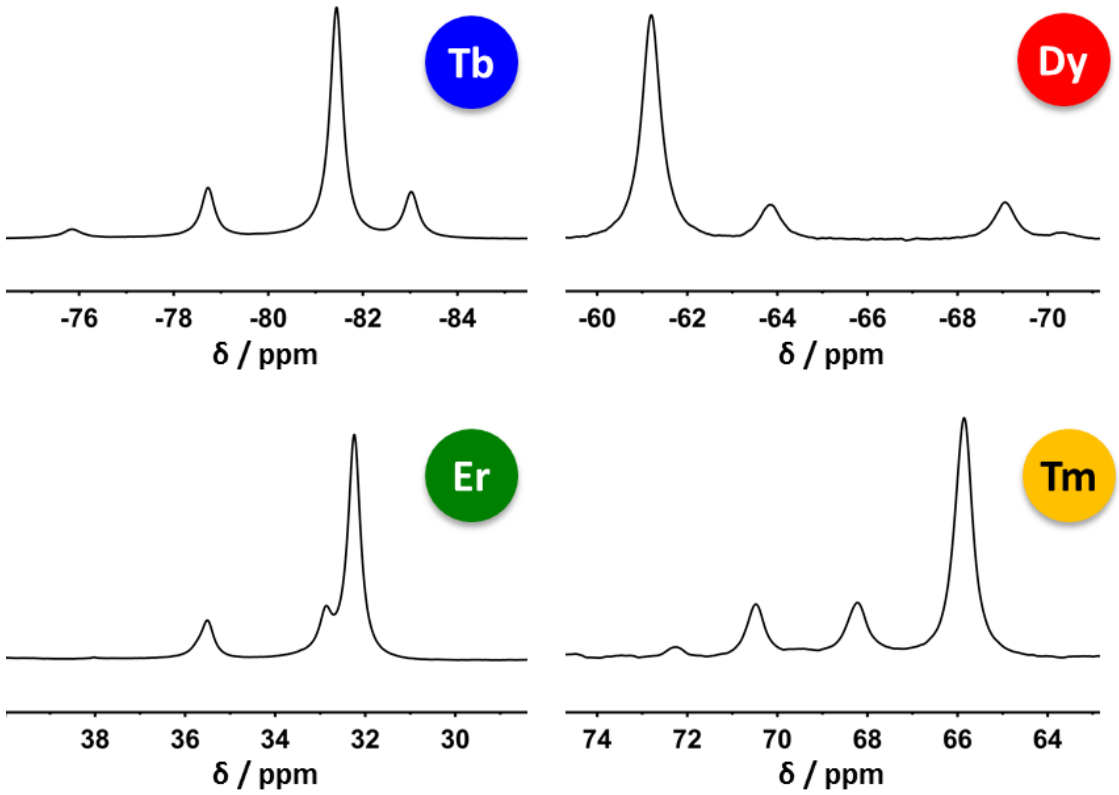

Figure 2.23 ^{1}H NMR spectra of the *tert*-butyl resonances observed for **[LnL^{3}]**$^{-}$ (D_2O, 11.7 T, 295 K, pD 7.4).

For each **[LnL^{3}]**$^{-}$ complex, at least two diastereoisomers were observed and the major *tert*-butyl resonance was the least furthest shifted of these species in every complex except **[TbL^{3}]**$^{-}$. The presence of multiple isomers in slow exchange on the NMR timescale suggests that the dibenzylphosphinate macrocycle is more flexible than in the tri-substituted species. The relative stabilities of the minor diastereoisomers have increased and are now closer in energy to the major conformation. Although the presence of additional minor isomers reduces the signal intensity of the major isomer, in each case the major species accounted for >66% of the *tert*-butyl signal, and thus **[LnL^{3}]**$^{-}$ affords an increase in overall signal intensity in comparison to **[LnL^{2}]**$^{-}$.

The longitudinal relaxation rate of the major *tert*-butyl resonance was measured at six fields over the range 1 to 16.4 T (Table 2.10).

Table 2.10 Longitudinal relaxation rate data for the major *tert*-butyl resonance of **[LnL^3]$^-$** at different magnetic field strengths (D_2O, pD 7.4, 295 K).

Ln^{3+}	**R_1 / s^{-1} (± error)**					
	1.0 T	**4.7 T**	**9.4 T**	**11.7 T**	**14.1 T**	**16.4 T**
Tb	91 (1)	120 (1)	157 (1)	174 (2)	183 (1)	195 (1)
Dy	59 (1)	100 (1)	161 (2)	182 (1)	195 (1)	203 (1)
Er	103 (1)	119 (1)	155 (1)	175 (1)	195 (2)	208 (1)
Tm	16 (1)	61 (1)	112 (4)	127 (2)	129 (1)	150 (1)

Whereas the modification from methyl- to benzylphosphinate resulted in only small changes to longitudinal relaxation rates, the change from tri- to diphosphinate gives rise to a much more marked variation, especially for **[TbL^3]$^-$** and **[TmL^3]$^-$**. The value of R_1 for the Tb^{3+} complex is increased and the rate for the Tm^{3+} complex is dramatically decreased. This effect occurs at all field strengths but is proportionally largest at 1 T. Structural modification from tri- to di- has little impact on the relaxation rate of **[DyL^3]$^-$**; the rates of **[ErL^3]$^-$** decrease, although less notably than **[TmL^3]$^-$**. The longitudinal relaxation rates of **[LnL^3]$^-$** are not all decreased in a similar manner to the chemical shift, and this behaviour indicates that the internuclear distance between reporter protons and lanthanide ion is unlikely to be dramatically changed from **[LnL^2]$^-$**.

Notwithstanding the intrinsic limitations of the approach, the relaxation data were analysed by global minimisation methods assuming classical BRW theory and an *r* of 6.6 Å as previously (Figure 2.24).

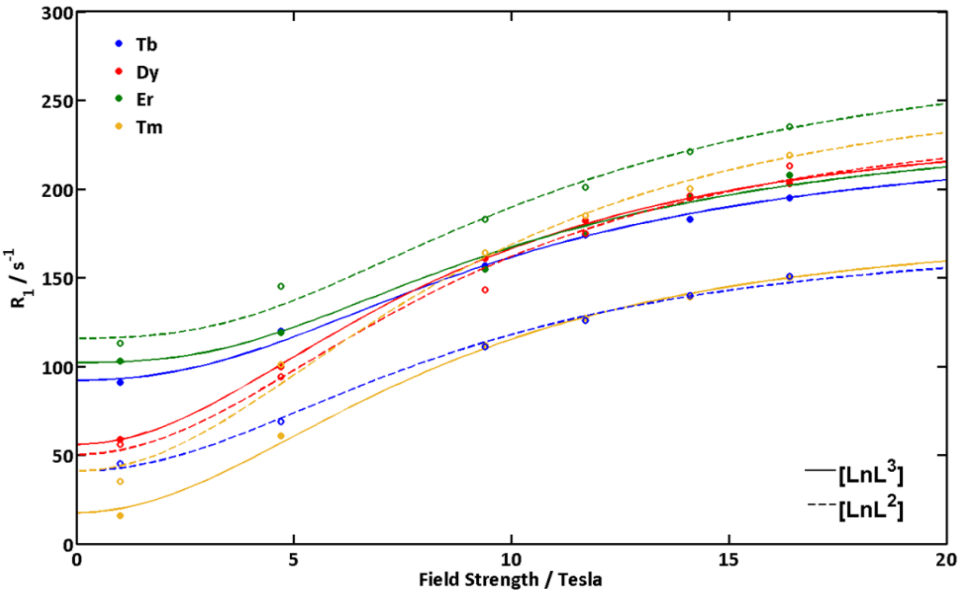

Figure 2.24 ^{1}H NMR relaxation rates (R_1 / s^{-1}) for the major *tert*-butyl resonance of **[LnL^2]$^-$** (dashed) and **[LnL^3]$^-$** (solid) as a function of magnetic field, showing the global fits (line) to the experimental data points (D_2O, 295K, pD 7.4, fixed r = 6.6 Å, minimizes to τ_r = 418 (8) ps).

Similarly to **[LnL^2]$^-$** the fit is least good for **[TmL^3]$^-$** at low fields. The rotational correlation time was estimated to be 418 (±8) ps, and such an increase is in line with the increase in molecular mass. The minimisation process gave 'best-fit' values for μ_{eff} and τ_e, shown in Table 2.11.

Table 2.11 Estimated 'best-fit' values for ^{1}H NMR relaxation parameters of **[LnL^2]$^-$** and **[LnL^3]$^-$** following global fitting with fixed r = 6.6 Å (D_2O, 295 K, pD 7.4)[a].

Ln^{3+}	**τ_e / ps**		**μ_{eff} / BM[a]**	
	[LnL^2]$^-$	**[LnL^3]$^-$**	**[LnL^2]$^-$**	**[LnL^3]$^-$**
Tb	0.43 (5)	0.85 (5)	9.77 (3)	10.45 (2)
Dy	0.44 (6)	0.50 (7)	10.68 (3)	10.72 (1)
Er	0.99 (12)	0.92 (8)	10.89 (4)	10.52 (2)
Tm	0.35 (3)	0.18 (3)	10.90 (5)	10.05 (4)

[a] Theoretical values for the magnetic moments of the lanthanide(III) ions are: Tb, 9.7; Dy, 10.6; Ho, 10.6; Er, 9.6; Tm, 7.6 BM.

Analysis of the magnetic moments and electronic relaxation rates of **[LnL^3]$^-$** shows vast deviation from both the theoretical lanthanide(III) values and from the behaviour of **[LnL^2]$^-$**. A dramatic increase in τ_e for **[TbL^3]$^-$** can tentatively be used to rationalise the increased R_1 rates. The size of the magnetic moment of Tb^{3+} is now significantly higher than the predicted theoretical value. Conversely, the decrease in the measured

relaxation rate of **[TmL^2]$^-$** at low field (<4.7 T) results in large reductions in the estimated values of τ_e.

2.3.2 Paramagnetic NMR studies of [LnL^3]: temperature response

As demonstrated with the earlier series of complexes, the *tert*-butyl chemical shift of **[LnL^3]$^-$** varies linearly with T^{-2} and T, over the measured temperature range (Figure 2.25).

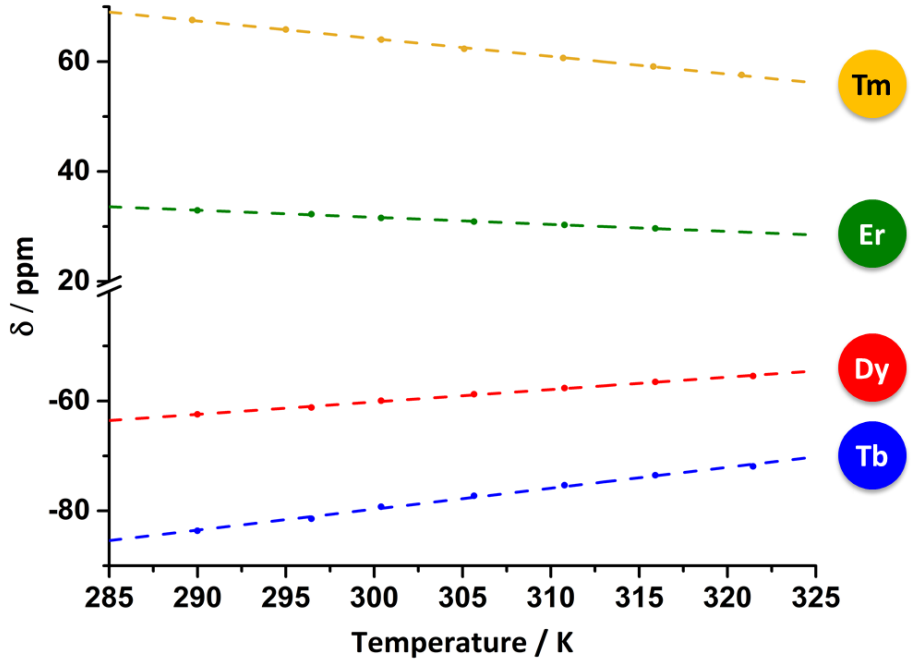

Figure 2.25 Variation in the chemical shift of the major *tert*-butyl resonance of **[LnL^3]$^-$** as a function of temperature (D_2O, 11.7 T, pD 7.4): Tm (*yellow*) R^2 = 0.999; Er (*green*) R^2 = 0.997; Dy (*red*) R^2 = 0.997; Tb (*blue*) R^2 = 0.997.

The temperature sensitivities of **[LnL^3]$^-$** were calculated from the linear fit (Table 2.12).

Table 2.12 Comparison of the temperature sensitivities of the major *tert*-butyl resonance of **[LnL^2]$^-$** and **[LnL^3]$^-$** (D_2O, 11.7 T, pD 7.4).

Ln^{3+}	T sensitivity / ppm/K	
	[LnL^2]$^-$	[LnL^3]$^-$
Tb	+0.45	+0.38
Dy	+0.37	+0.23
Er	-0.24	-0.13
Tm	-0.45	-0.32

The temperature sensitivity of **[LnL^3]$^-$** decreases in comparison to **[LnL^2]$^-$**. The decrease is in line with the reduced chemical shifts of the *tert*-butyl reporter group.

Additionally, to explore the exchange between the additional diastereoisomers of **[LnL^3]$^-$**, the linewidths of the *tert*-butyl resonance were measured as a function of temperature. It is expected that the linewidth of the *tert*-butyl resonance will reduce with increasing temperature as BRW theory predicts a T^{-2} dependence of R_2. However, at higher temperatures (>315 K) the linewidths were observed to increase due to chemical exchange, although no coalescence of the *tert*-butyl resonances was observed.

2.3.3 Paramagnetic NMR studies of [LnL^3]: pH response

The chemical shifts of the *tert*-butyl resonances of **[LnL^3]$^-$** were measured as a function of pH, in order to probe the effect of the structural change from the tri- to the diphosphinate series. Due to the distance between the two phosphonate groups, they were assumed to protonate independently and simultaneously, resulting in a single pK_a value for each *tert*-butyl resonance. As previously observed for **[LnL^1]$^-$** and **[LnL^2]$^-$**, the size of the paramagnetic shift increased at low pD (Figure 2.26).

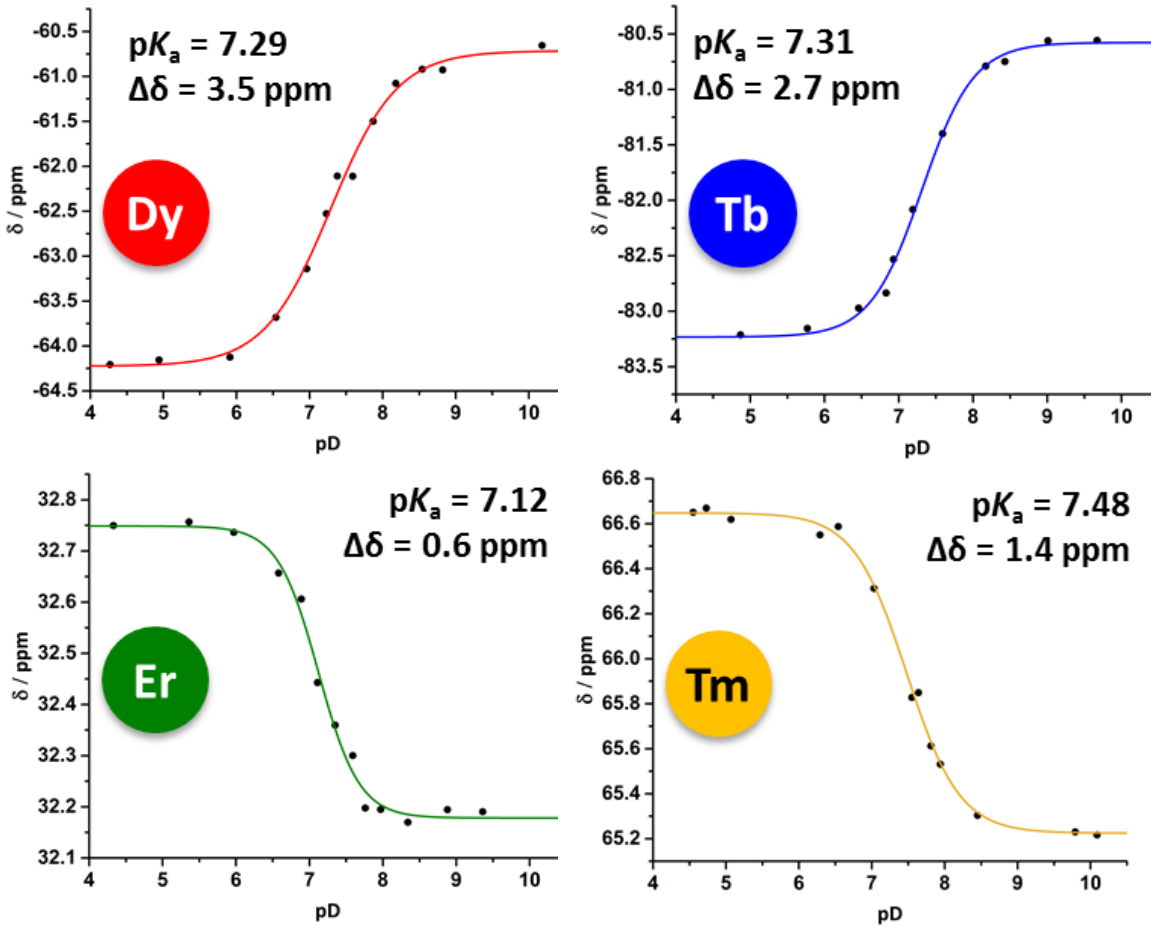

Figure 2.26 Variation in the ^{1}H chemical shift of the major *tert*-butyl resonance of **[LnL^3]$^-$** as a function of pD (D_2O, 11.7 T, 295 K).

Comparison of the fitted pK_a values of **[LnL^3]$^-$** with those of **[LnL^2]$^-$** shows that the protonation equilibrium of the two phosphonates is broadly unchanged (Table 2.13). The average pK_a value (7.30) decreased from that found for **[LnL^2]$^-$** (7.37), although this behaviour can largely be related to the pK_a decreases found for **[TmL^3]$^-$** and **[ErL^3]$^-$**. The total pH sensitivities of the Tb^{3+} and Dy^{3+} complexes of **[LnL^3]$^-$** remained similar to those of the analogous **[LnL^2]$^-$** complexes (Table 2.13). However, the Δδ values of **[ErL^3]$^-$** and **[TmL^3]$^-$** decreased greatly, and this change was not proportional to the decrease in the *tert*-butyl chemical shifts.

Table 2.13 Comparison of the pH sensitivities of the major *tert*-butyl resonance of **[LnL^1]$^-$** and **[LnL^2]$^-$** (D_2O, 11.7 T, 295 K).

Ln^{3+}	pK_a		Δδ / ppm	
	[LnL^2]$^-$	**[LnL^3]$^-$**	**[LnL^2]$^-$**	**[LnL^3]$^-$**
Tb	7.33	7.31	2.9	2.7
Dy	7.22	7.29	3.5	3.5
Er	7.26	7.12	1.3	0.6
Tm	7.65	7.48	2.4	1.4

The pH response of the identified *tert*-butyl resonances of the minor isomers were also analysed (Figure 2.27). Unexpectedly, the different diastereoisomers showed very different sensitivities to pD. The total shift change, Δδ, was particularly different in **[TbL^3]$^-$** and **[DyL^3]$^-$**. For example, one of the minor isomers of the Dy^{3+} complex shifted 5.4 ppm from high to low pD, significantly further than the major isomer (Δδ = 3.5 ppm). Conversely, both minor species of the Tb^{3+} complex were found to shift significantly less (Δδ = 0.4 and 1.0 ppm) compared to that of the major species (Δδ = 2.7 ppm).

The pK_a values were also found to slightly vary between diastereoisomers, each lanthanide complex spanning a similar range. The inclusion of the minor pK_a values also increased the total range of values (7.12 - 7.71) and the order of pK_a values was Tm^{3+}>Tb^{3+}>Dy^{3+}>Er^{3+}. This trend was also observed for the triphosphinate complexes **[LnL^1]$^-$** and **[LnL^2]$^-$**, for which the Tm^{3+} and Tb^{3+} complexes have the highest pK_a values.

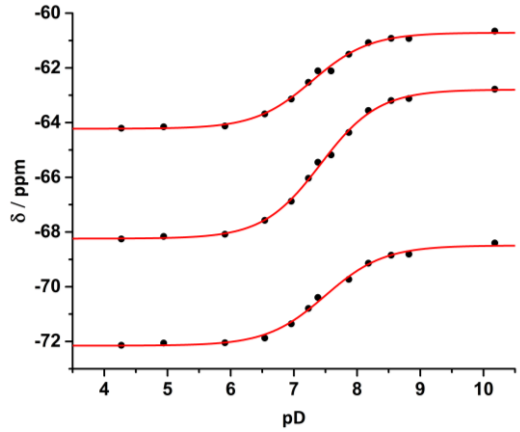

Dy

δ_H ^{t}Bu (pD 7.4) / ppm	Integral	Δδ / ppm	pK_a
-61.5	1	3.51	7.29
-64.4	0.14	5.45	7.42
-69.7	0.14	3.57	7.50

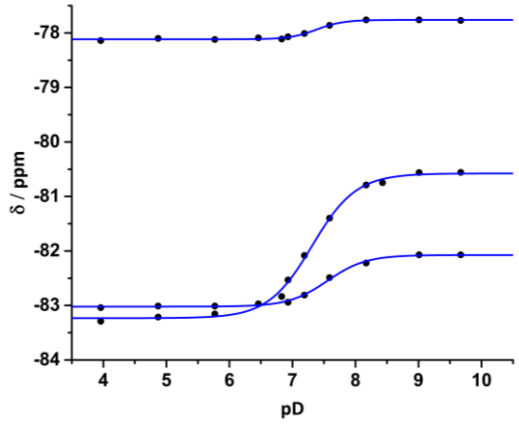

Tb

δ_H ^{t}Bu (pD 7.4) / ppm	Integral	Δδ / ppm	pK_a
-77.9	0.17	0.35	7.38
-81.4	1	2.65	7.31
-82.5	0.17	0.95	7.55

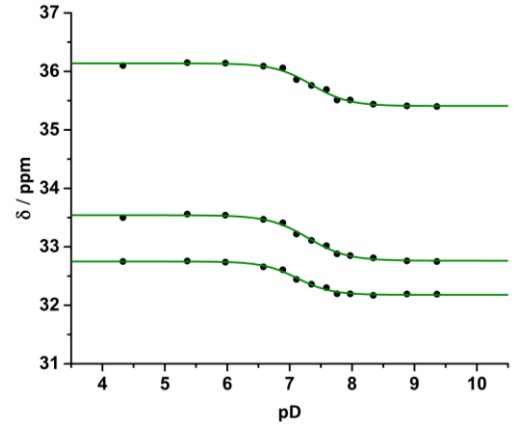

Er

δ_H ^{t}Bu (pD 7.4) / ppm	Integral	Δδ / ppm	pK_a
+35.8	0.19	0.72	7.35
+33.1	0.19	0.78	7.30
+32.4	1	0.57	7.12

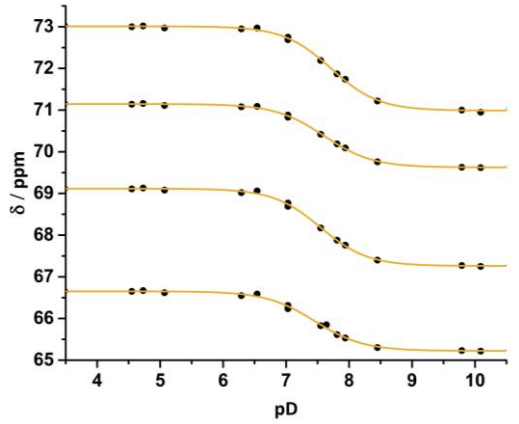

Tm

δ_H ^{t}Bu (pD 7.4) / ppm	Integral	Δδ / ppm	pK_a
+72.2	0.02	2.02	7.71
+70.4	0.17	1.52	7.60
+68.2	0.17	1.85	7.55
+65.8	1	1.43	7.46

Figure 2.27 Variation in the ^{1}H chemical shift of the *tert*-butyl resonances of **[LnL^3]$^-$** as a function of pD (D_2O, 11.7 T, 295 K).

The linewidths of the Dy^{3+} and Tb^{3+} complexes of **L^3** were considered to be rather broad, restricting their use in imaging experiments. Hence, **[TmL^3]$^-$** and **[ErL^3]$^-$** were chosen to be the pair of lanthanides used for the *in vivo* studies. In order to probe the effects of ionic strength on the pK_a and pD response of the diphosphinate complexes, a pD titration was performed in 0.1 M NaCl in D_2O. The titration was performed on a 1:1 mixture of the Er^{3+} and Tm^{3+} complexes. Such an experiment also confirms that the presence of the two different lanthanide complexes in solution has no adverse effect on shift or relaxation behaviour (Figure 2.28).

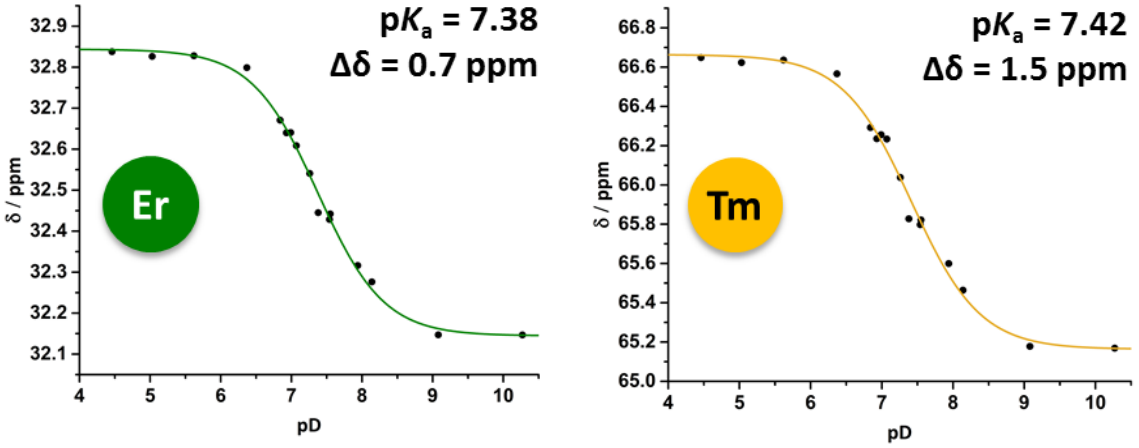

Figure 2.28 Variation in the ^{1}H chemical shift of the major *tert*-butyl resonance of **[ErL^3]$^-$** and **[TmL^3]$^-$** as a function of pD (D_2O, 0.1 M NaCl, 11.7 T, 295 K).

It was expected that an increase in ionic strength would decrease the pK_a, as observed for **[DyL^1]$^-$**. However, whilst the pK_a of major *tert*-butyl resonance of **[TmL^3]$^-$** was found to decrease slightly to 7.42, the pK_a of **[ErL^3]$^-$** actually increased to 7.38, the two pK_a values for the two complexes now lie within the experimental error (Figure 2.28).

The presence of NaCl in solution was found to have no effect on the chemical shift and the longitudinal relaxation rate of the major *tert*-butyl resonance (Table 2.14).

Table 2.14 Overview of the properties the major *tert*-butyl resonance of **[ErL^3]$^-$** and **[TmL^3]$^-$** in an equimolar mixture in 0.1 M NaCl (D_2O, 11.7 T, 295 K).

Ln^{3+}	δ_H ^{t}Bu / ppm	R_1 / s^{-1} (± error) 11.7 T	Δδ / ppm	pK_a
Er	+32	173 (2)	0.7	7.38
Tm	+65	126 (1)	1.5	7.42

The effect of endogenous metal cations (Mg^{2+} and Ca^{2+}) on the chemical shift of **[LnL^3]$^-$** was also explored. It was found that addition of the chloride salts of Mg^{2+} and Ca^{2+} at millimolar concentrations had no discernible effect (Figure 2.29 and Figure 2.30).

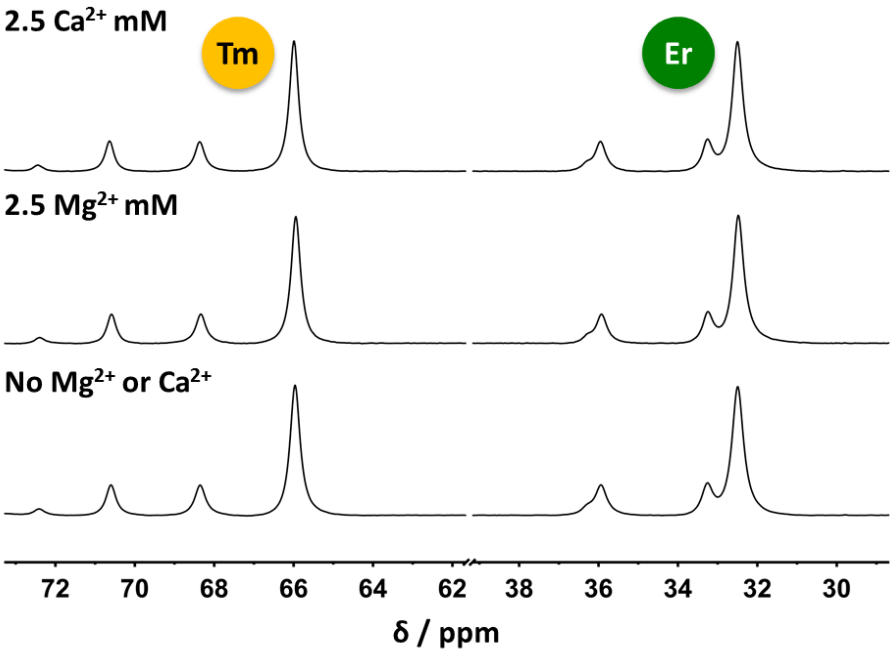

Figure 2.29 Stacked ^{1}H NMR spectra of **[ErL^{3}]**$^{-}$ and **[TmL^{3}]**$^{-}$ (*bottom*) and after addition of excess Mg^{2+} (*centre*) or Ca^{2+} (*top*). (D_2O, pD 7.4, 11.7 T, 295 K).

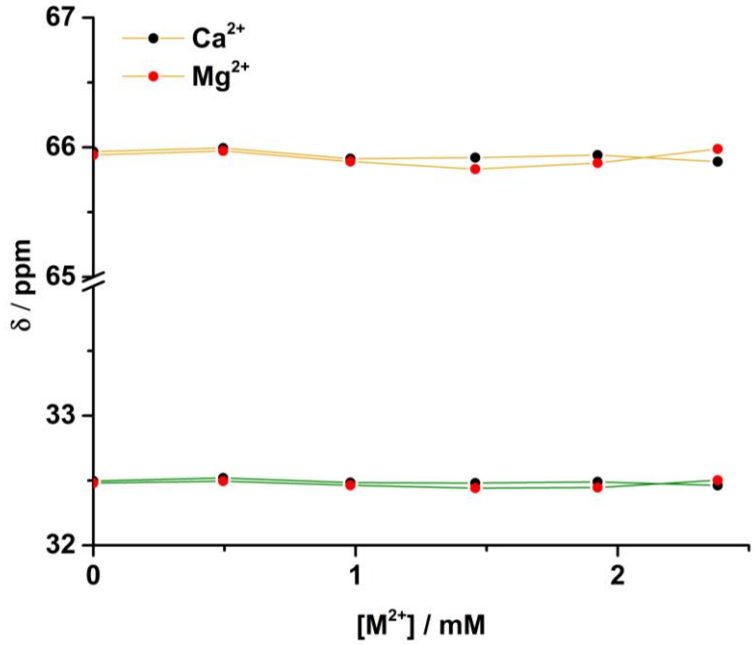

Figure 2.30 Chemical shifts of the *tert*-butyl resonances of **[ErL^{3}]**$^{-}$ (*green*) and **[TmL^{3}]**$^{-}$ (*yellow*) as a function of the number of added equivalents of Ca^{2+} (*black*) and Mg^{2+} (*red*) (D_2O, pD 7.4, 11.7 T, 295 K).

2.3.4 *In vivo* studies of [LnL^{3}]$^{-}$

Standard contrast enhanced ^{1}H MRI was undertaken in intact, healthy mice following tail-vein injection with 0.05 mmol/kg of **[GdL^{3}]**$^{-}$. These scans showed that the dibenzylphosphinate complex was still found to accumulate rapidly in the bladder

(Figure 2.31). However, the relative concentrations in the liver and kidneys within the initial 5 minutes post-injection were improved. The higher local concentration of the probe and increased signal intensity suggest that imaging these organs may be enhanced at early time points.

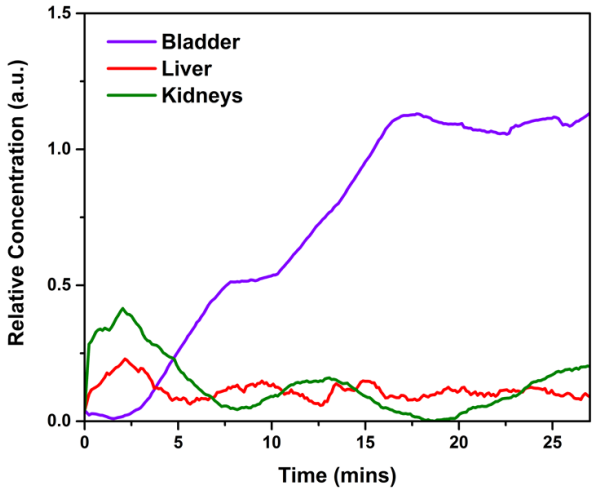

Figure 2.31 Relative average *in vivo* concentration of **[GdL^3]**$^-$ as a function of time in intact, healthy mice (*n* = 3) following single i.v. injection of 0.05 mmol/kg.

^{1}H PARASHIFT experiments were performed on intact, healthy mice following a tail-vein injection with 0.05 mmoles/kg of an equimolar mix of the Er^{3+} and Tm^{3+} complexes in saline. 3DGE triple imaging sequences were utilised, demonstrating that this technique can be used to image simultaneously signals from **[ErL^3]**$^-$, **[TmL^3]**$^-$ and water. Figure 2.32 shows a triple image of a 10 mM phantom of both Tm/Er complexes, and a mouse 120 min post-injection; at this time, renal clearance of the probe results in a strong signal from the bladder only (Figure 2.33). A large spectral width of 60 kHz allowed for the use fast pulse sequences. The frequency offset of the *tert*-butyl signals in the bladder compared to that of the external phantom arises due to the different temperature and pH within the mouse.

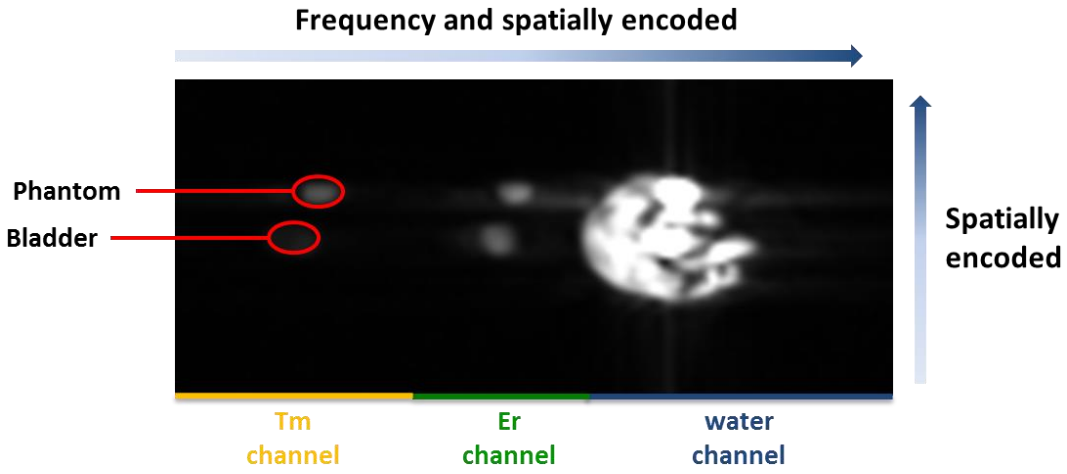

Figure 2.32 A 3DGE triple image taken 120 minutes post-injection of an equimolar 0.05 mmoles/kg solution of **[ErL^3]$^-$** and **[TmL^3]$^-$** in saline. TR = 4.08 ms, TE = 0.77 ms, SW= 60 kHz, 50 averages, scan time = 209 s.

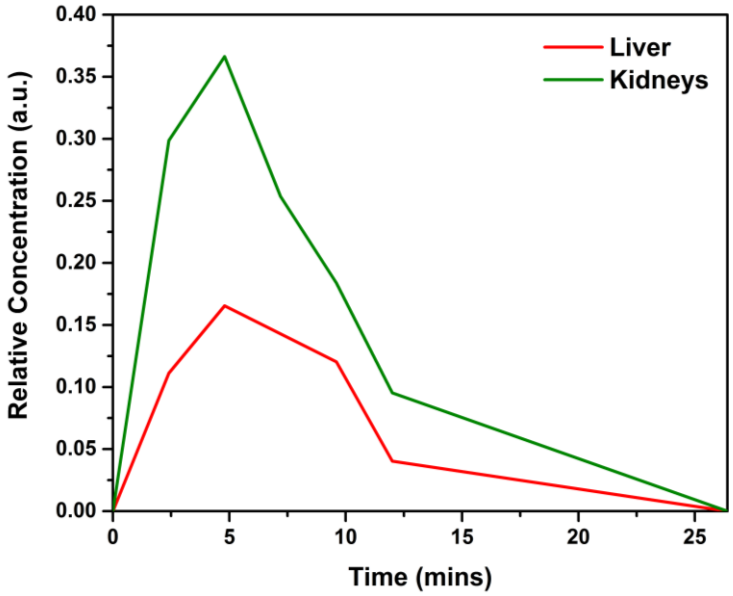

Figure 2.33 Relative average *in vivo* concentration of **[ErL^3]** and **[TmL^3]** as a function of time in an intact, healthy mouse following single i.v. injection of an equimolar 0.05 mmol/kg solution of **[ErL^3]$^-$** and **[TmL^3]$^-$** in saline.

In vivo MRSI acquisitions were also performed and the presence of both complexes was observed within the liver, kidneys (Figure 2.34) and bladder. The linewidths were reduced compared to that of **[DyL^1]$^-$** enabling simpler peak identification.

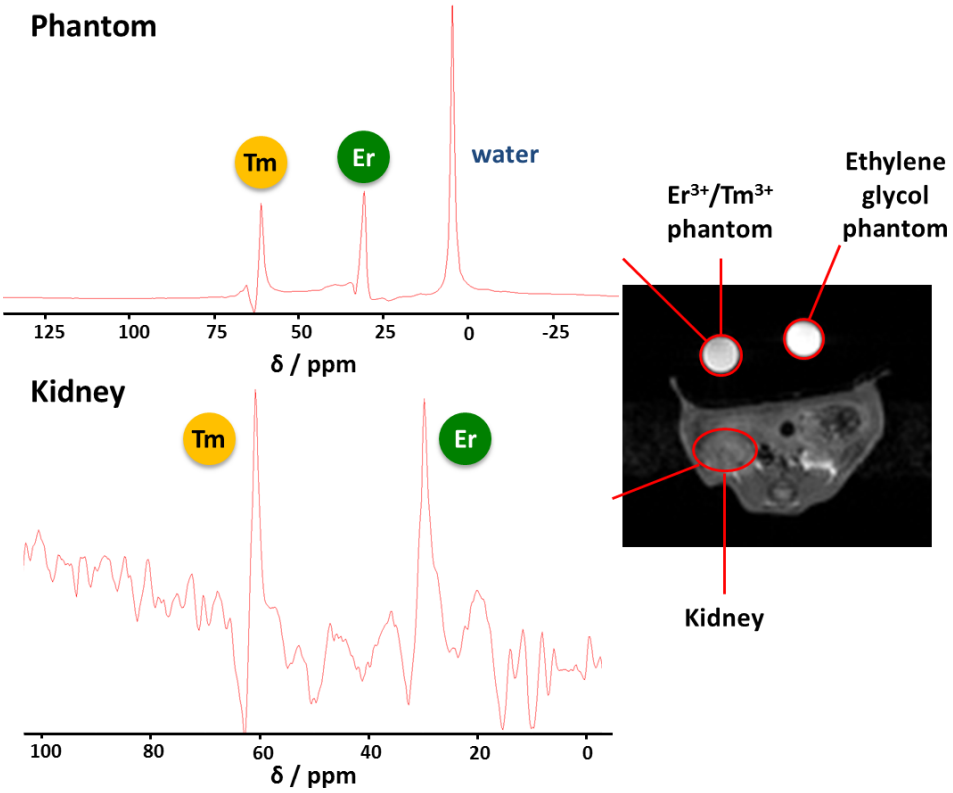

Figure 2.34 (*Right*) T_1-weighted image highlighting kidney of the mouse and two external phantoms containing; a 10 mM equimolar solution of **[ErL^3]**$^-$ and **[TmL^3]**$^-$ in saline for pH calibration and a solution of ethylene glycol for temperature calibration. (*Left*) Selected spectra from 2DSI acquisition of the Er^{3+}/Tm^{3+} containing phantom (*top*) and of the kidney (*bottom*). MRSI acquisition parameters were TR = 14.1 ms, TE = 0.45 ms, SW = 56 kHz.

Further *in vivo* studies are ongoing in order to gain more detailed frequency information from the acquired spectra. This will allow for automation of the processing procedure and enable 2D pH and temperature maps to be readily constructed.

2.4 Conclusions and Future Work

A series of novel pH and temperature responsive ^{1}H PARASHIFT probes, **[LnL$^{1\text{-}3}$]**$^-$, for MRS have been synthesised and characterised. The complexes exist as one major diastereoisomer in aqueous solution so that one major signal of the *tert*-butyl reporter group is observed. The reporter signal of each complex resonates outside the diamagnetic range, well away from the signals of water and fat, allowing for near zero-background imaging. Furthermore, longitudinal relaxation rates of the complexes at clinically relevant fields allow for very short repetition times allowing fast data acquisition per unit time. The highly-shifted signals exhibit large, linear dependence on temperature. The presence of a pH sensitive phosphonate group with a pK_a in a

biologically relevant range (7.16 - 7.37) allows for the measurement of pH by perturbation of the reporter resonance frequency. The dual temperature and pH dependence requires the co-injection of two different lanthanide complexes. A number of parameters must be considered in the selection of these complexes, including their chemical shift and relaxation properties (Figure 2.35).

Initial *in vivo* studies of **[LnL^1]**$^-$ demonstrated that non-invasive measurement of pH and temperature could be achieved using mice with no surgical renal ligation. However, temporal resolution in the liver and kidneys was hindered by the relatively fast clearance and rapid accumulation of the complex into the bladder of the mice studied. It was found that whilst Dy^{3+} and Tb^{3+} complexes demonstrate extremely shifted *tert*-butyl resonances the linewidths of the signals are rather broad, inhibiting imaging *in vivo*.

Structural adaptation was sought in order to increase the lipophilicity of the probe. Modification of the phosphinate R groups from methyl to benzyl resulted in an increase in the chemical shift of the *tert*-butyl resonance. The tribenzylphosphinate complex, **[LnL^2]**$^-$, maintained fast relaxation rates and high temperature sensitivity. The pK_a was found to increase slightly as a result of the increase in hydrophobicity of the complex. Moreover, there was an increase in the total chemical shift of the *tert*-butyl resonance upon pH variation, increasing the potential accuracy of pH measurements. Unfortunately, *in vivo* experiments revealed no improvement in the biodistribution so further structural modification was required.

The change in structure from the tri- to the dibenzylphosphinate resulted in a number of changes to the NMR properties that are not yet well understood. The longitudinal relaxation rate profiles of **[TmL^3]**$^-$ and **[TbL^3]**$^-$ were remarkably different from their related tribenzylphosphinate complexes. Whilst the favourable pH sensitivities were maintained, the paramagnetic shift of the reporter group decreased, but remained well outside the diamagnetic region for all complexes.

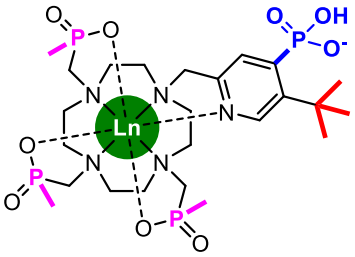

Ln = Tb, Dy, Ho, Er, Tm

[LnL^1]$^-$

Ln^{3+}	δ_H ^{t}Bu / ppm	R_1 / s^{-1} (± error)				T sensitivity / ppm/K	Δδ / ppm	pK_a
		1 T	4.7 T	7 T[a]	9.4 T			
Tb	-83	42 (3)	73 (1)	95	122 (1)	+0.52	1.4	7.20
Dy	-78	54 (5)	88 (3)	121	156 (1)	+0.41	1.9	7.11
Ho	-32	44 (4)	89 (5)	125	160 (2)	+0.17	1.1	7.16
Er	+42	92 (10)	117 (7)	144	173 (3)	-0.24	0.7	7.11
Tm	+74	25 (4)	99 (5)	103	139 (1)	-0.44	1.1	7.26

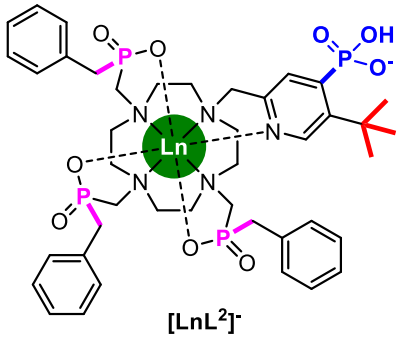

[LnL^2]$^-$

Ln = Tb, Dy, Er, Tm

Ln^{3+}	δ_H ^{t}Bu / ppm	R_1 / s^{-1} (± error)				T sensitivity / ppm/K	Δδ / ppm	pK_a
		1 T	4.7 T	7 T[a]	9.4 T			
Tb	-90	45 (1)	69 (1)	92	111 (1)	+0.44	2.9	7.33
Dy	-86	56 (1)	94 (1)	124	143 (1)	+0.37	3.5	7.22
Er	+48	113 (3)	145 (1)	155	183 (1)	-0.24	1.3	7.26
Tm	+85	35 (1)	101 (1)	133	164 (1)	-0.45	2.4	7.65

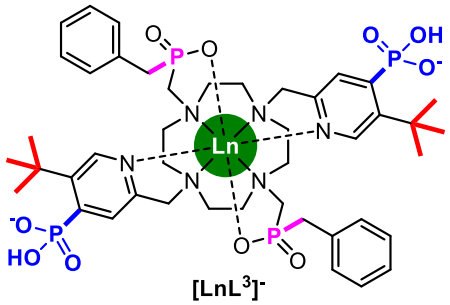

[LnL^3]$^-$

Ln = Tb, Dy, Er, Tm

Ln^{3+}	δ_H ^{t}Bu / ppm	R_1 / s^{-1} (± error)				T sensitivity / ppm/K	Δδ / ppm	pK_a
		1 T	4.7 T	7 T[a]	9.4 T			
Tb	-82	91 (1)	121 (1)	139	157 (1)	+0.38	2.7	7.31
Dy	-62	59 (1)	103 (1)	136	160 (1)	+0.23	3.5	7.29
Er	+32	103 (2)	125 (1)	140	155 (1)	-0.13	0.6	7.12
Tm	+65	16 (1)	61 (1)	87	112 (1)	-0.32	1.4	7.48

Figure 2.35 Overview of selected chemical shift and relaxation properties of the major *tert*-butyl resonances of **[LnL$^{1\text{-}3}$]$^-$**. [a]R_1 at 7 T is estimated using the fits of R_1 against field.

In vivo experiments using an equimolar mixture of **[TmL^3]**$^-$ and **[ErL^3]**$^-$, demonstrated the feasibility of using 3DGE scans to image complexes in which the *tert*-butyl resonance is shifted on the same side of the water resonance. The triple image experiment showed a frequency difference of the reporter resonance between a phantom and the bladder. The offset demonstrates the pH and temperature difference within these locations.

Further *in vivo* work is ongoing in order to construct pH and temperature maps and optimise the sequence parameters to achieve the best quality spectra. Triple imaging experiments should be undertaken on animal models of human disease to assess the change of tissue pH and temperature in these pathologies.

Although development of the dibenzylphosphinate pH probe, **[LnL^3]**$^-$, has resulted in an improved biodistribution, particularly in the liver and kidneys, clearance is still rather fast in a mouse model. Larger animals with reduced metabolic rates will likely have slower clearance rates and may provide better models for temporal imaging of organs such as the liver. Conjugation of the complex to targeting vectors would also reduce clearance rates as the molecular weight of the probe increases. The additional benefit of targeting vectors would increase the local concentration of the probe and allow for non-invasive pH measurement in various pathologies.

In order to design future PARASHIFT probes, the effect of ligand modification should be properly investigated. The vast differences seen in the NMR properties of **[LnL$^{1\text{-}3}$]**$^-$ should be explored, so that the ideal ligand structure can be selected.

2.5 References

1 R. J. Gillies, N. Raghunand, M. L. Garcia-Martin and R. A. Gatenby, *IEEE Eng. Med. Biol. Mag.*, 2004, **23**, 57–64.

2 B. A. Webb, M. Chimenti, M. P. Jacobson and D. L. Barber, *Nat. Rev. Cancer*, 2011, **11**, 671–677.

3 M. Rata, S. L. Giles, N. M. deSouza, M. O. Leach and G. S. Payne, *NMR Biomed.*, 2014, **27**, 158–162.

4 R. J. Gillies, Z. Liu and Z. Bhujwalla, *Am. J. Physiol. Physiol.*, 1994, **267**, C195–C203.

5 S. Aime, M. Botta, L. Milone and E. Terreno, *Chem. Commun.*, 1996, 1265–1266.

6 C. S. Zuo, K. R. Metz, Y. Sun and A. D. Sherry, *J. Magn. Reson.*, 1998, **133**, 53–60.

7 Y. Sun, M. Sugawara, R. V. Mulkern, K. Hynynen, S. Mochizuki, M. Albert and C. S. Zuo, *NMR Biomed.*, 2000, **13**, 460–466.

8 H. K. F. Trübel, P. K. Maciejewski, J. H. Farber and F. Hyder, *J. Appl. Physiol.*, 2003, **94**,

1641–1649.
9 H. K. F. Trubel, P. K. Maciejewski, J. H. Farbe and F. Hyder, *Magn. Reson. Med.*, 2002, **1**, 95173.
10 D. Coman, H. K. Trubel, R. E. Rycyna and F. Hyder, *NMR Biomed.*, 2009, **22**, 229–239.
11 D. Coman, R. A. de Graaf, D. L. Rothman and F. Hyder, *NMR Biomed.*, 2013, **26**, 1589–1595.
12 D. Coman, Y. Huang, J. U. Rao, H. M. De Feyter, D. L. Rothman, C. Juchem and F. Hyder, *NMR Biomed.*, 2016, **29**, 309–319.
13 J. U. Rao, D. Coman, J. J. Walsh, M. M. Ali, Y. Huang and F. Hyder, *Sci. Rep.*, 2017, **7**, 7865.
14 S. Zhang, K. Wu and A. D. Sherry, *Angew. Chem. Int. Ed.*, 1999, **38**, 3192–3194.
15 N. Raghunand, C. Howison, A. D. Sherry, S. Zhang and R. J. Gillies, *Magn. Reson. Med.*, 2003, **49**, 249–257.
16 M. L. Garcia-Martin, G. V. Martinez, N. Raghunand, A. D. Sherry, S. Zhang and R. J. Gillies, *Magn. Reson. Med.*, 2006, **55**, 309–315.
17 Y. Huang, D. Coman, M. M. Ali and F. Hyder, *Contrast Media Mol. Imaging*, 2015, **10**, 51–58.
18 J. Rena and A. D. Sherry, *Inorg Chim. Acta*, 1996, **246**, 331–341.
19 P. K. Senanayake, A. M. Kenwright, D. Parker and S. K. van der Hoorn, *Chem. Commun.*, 2007, 2923–2925.
20 A. M. Kenwright, I. Kuprov, E. De Luca, D. Parker, S. U. Pandya, P. K. Senanayake and D. G. Smith, *Chem. Commun.*, 2008, 2514–6.
21 K. H. Chalmers, E. De Luca, N. H. M. Hogg, A. M. Kenwright, I. Kuprov, D. Parker, M. Botta, J. Ian Wilson and A. M. Blamire, *Chem. A Eur. J.*, 2010, **16**, 134–148.
22 K.-L. N. A. Finney, Durham University, 2016.
23 A. M. Funk, K.-L. N. A. Finney, P. Harvey, A. M. Kenwright, E. R. Neil, N. J. Rogers, P. K. Senanayake and D. Parker, *Chem. Sci.*, 2015, **6**, 1655–1662.
24 T. W. Bell, L. Y. Hu and S. V. Patel, *J. Org. Chem.*, 1987, **52**, 3847–3850.
25 A. Beeby, I. M. Clarkson, R. S. Dickins, S. Faulkner, D. Parker, L. Royle, A. S. de Sousa, J. A. G. Williams and M. Woods, *J. Chem. Soc. Perkin Trans. 2*, 1999, **2**, 493–504.
26 K. Mason, N. J. Rogers, E. A. Suturina, I. Kuprov, J. A. Aguilar, A. S. Batsanov, D. S. Yufit and D. Parker, *Inorg. Chem.*, 2017, **56**, 4028–4038.
27 D. Parker, I. Kuprov, E. Suturina, K. Mason and C. Geraldes, *Angew. Chem. Int. Ed.*, 2017, 12215–12218.
28 N. J. Rogers, K.-L. N. A. Finney, P. K. Senanayake and D. Parker, *Phys. Chem. Chem. Phys.*, 2016, **18**, 4370–4375.
29 K. Mason, A. C. Harnden, C. W. Patrick, A. W. J. Poh, A. S. Batsanov, E. A. Suturina, M. Vonci, E. J. L. McInnes, N. F. Chilton and D. Parker, *Chem. Commun.*, 2018, **54**, 8486–8489.
30 M. E. Boulon, G. Cucinotta, J. Luzon, C. Degl'Innocenti, M. Perfetti, K. Bernot, G. Calvez, A. Caneschi and R. Sessoli, *Angew. Chem. Int. Ed.*, 2013, **52**, 350–354.
31 G. Cucinotta, M. Perfetti, J. Luzon, M. Etienne, P. E. Car, A. Caneschi, G. Calvez, K. Bernot and R. Sessoli, *Angew. Chem. Int. Ed.*, 2012, **51**, 1606–1610.
32 K.-L. N. A. Finney, A. C. Harnden, N. J. Rogers, P. K. Senanayake, A. M. Blamire, D. O'Hogain and D. Parker, *Chem. A Eur. J.*, 2017, **23**, 7976–7989.
33 P. K. Senanayake, N. J. Rogers, K.-L. N. A. Finney, P. Harvey, A. M. Funk, J. I. Wilson, D. O'Hogain, R. Maxwell, D. Parker and A. M. Blamire, *Magn. Reson. Med.*, 2017, **77**, 1307–1317.
34 K. P. Pulukkody, T. J. Norman, D. Parker, L. Royle and C. J. Broan, *J. Chem. Soc. Perkin Trans. 2*, 1993, 605.

3. Comparison of tri- and dibenzylphosphinate complexes

It has been shown previously that small changes to the metal ion coordination sphere can have a dramatic impact on the paramagnetic NMR properties of lanthanide ions, in marked contrast to the behaviour expected from simple ligand field interpretations based on Bleaney's theory of magnetic anisotropy.[1–5]

An in-depth analysis of both the diamagnetic and paramagnetic NMR data of the trimethylphosphinate complexes **[YL^{J}]** and **[YbL^{J}]** and the tricarboxylate complex **[YL^{H}]** and **[YbL^{H}]** (see Section 1.7.1, pages 27-30) revealed that whilst the geometries of the two complexes was generally similar, their NMR behaviour was quite different.[6] It was demonstrated that the markedly different NMR behaviour of the complexes arises from the change in the orientation of the magnetic susceptibility tensor rather than the degree of anisotropy or a change in geometry of the reporter group within the ligand.

Further experimental and theoretical analysis of the isostructural series of paramagnetic complexes, **[LnL^{J}]**, demonstrated that several of the assumptions made in both Bleaney's theory and BRW relaxation theory are incorrect.[7,8] Analysis of the chemical shift data of the trimethylphosphinate complexes (Tb – Yb) enabled the fitting of the individual magnetic susceptibility tensors.[7] Significant variations in the amplitude, shape and orientation of the PCS fields across the series were revealed. The application of Bleaney's theory suggests that only the amplitude and sign should vary between lanthanides and fails to account for changes in ligand field within the series. The implicit assumption that the ligand field splitting is smaller than kT was also demonstrated to fail for **[LnL^{J}]**.

Analysis of the low field (1 T) relaxation rates of the proton resonances for the trimethylphosphinate series (Tb – Yb) demonstrated that both the Curie and dipolar mechanisms should be treated as anisotropic.[8] By measuring the relaxation rates of every proton within the complex, it was found that the relaxation rate depends not only on the distance of the observed nucleus to the lanthanide, but also the angle of Ln-H vector. These results demonstrated that the chemical shift and relaxation

properties of potential PARASHIFT probes are not predictable, as the long-standing theories suggest. To design new probes for MR successfully, the nature of these effects must be better understood.

In order to explore the variations in chemical shift and relaxation described for the pH probes described in Chapter 2, **[LnL$^{1\text{-}3}$]**, it was decided to study the non-phosphonated tri- and di-benzylphosphinate complexes, **[LnL^{4}]** and **[LnL^{5}]$^{+}$** (Figure 3.1). The use of the non-phosphonate substituted pyridine moiety allows for direct comparisons to be made to the trimethylphosphinate complexes, **[LnL^{J}]**, which have been extensively studied.[6–8]

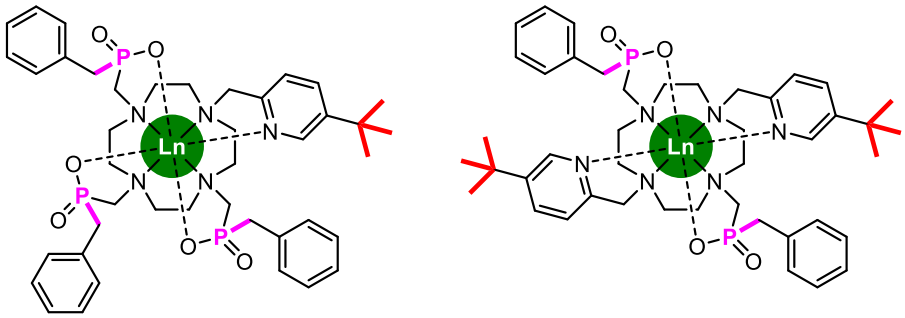

[LnL^{4}] **[LnL^{5}]$^{+}$**

Figure 3.1 Structures of the parent benzylphosphinate complexes **[LnL^{4}]** and **[LnL^{5}]$^{+}$**.

3.1 Synthesis of [LnL^{4}] and [LnL^{5}]$^{+}$

The *tert*-butyl appended pyridine was synthesised using literature procedures (Scheme 3.1).[9] The N-oxide, **7**, was converted to the alcohol, **17**, via a Boekelheide reaction with trifluoroacetic anhydride (TFAA) and subsequent hydrolysis of the resulting trifluoroacetate ester with ethanol and water. Mesylation of the hydroxyl group gave the required mesylate, **18**.

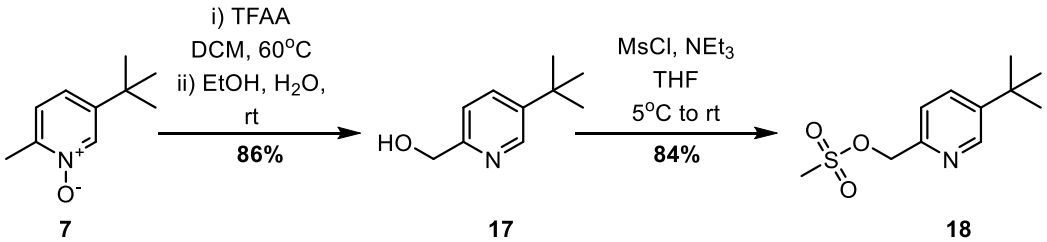

7 **17** **18**

Scheme 3.1 Boekelheide rearrangement reaction followed by mesylation.

The synthesis of the tribenzylphosphinate macrocycle, **16**, was described in Section 2.2.1 (page 68). The dibenzylphosphinate macrocycle was synthesised via an analogous route (Scheme 3.2). Alkylation of cyclen with three equivalents of benzyl chloroformate at pH 2.5 yielded a major product of the *trans*- di-substituted carbamate, **19**, that was purified by recrystallisation. The final amine sites were protected with BOC groups, **20**, before hydrogenation removed the benzyl carbamates to yield the di-BOC macrocycle, **21**. Reaction of **21** with diethyl benzylphosphonite and anhydrous paraformaldehyde yielded the benzylphosphinate ester, **22**, before deprotection of the BOC groups was achieved to give the desired *trans*-substituted dibenzylphosphinate macrocycle, **23**.

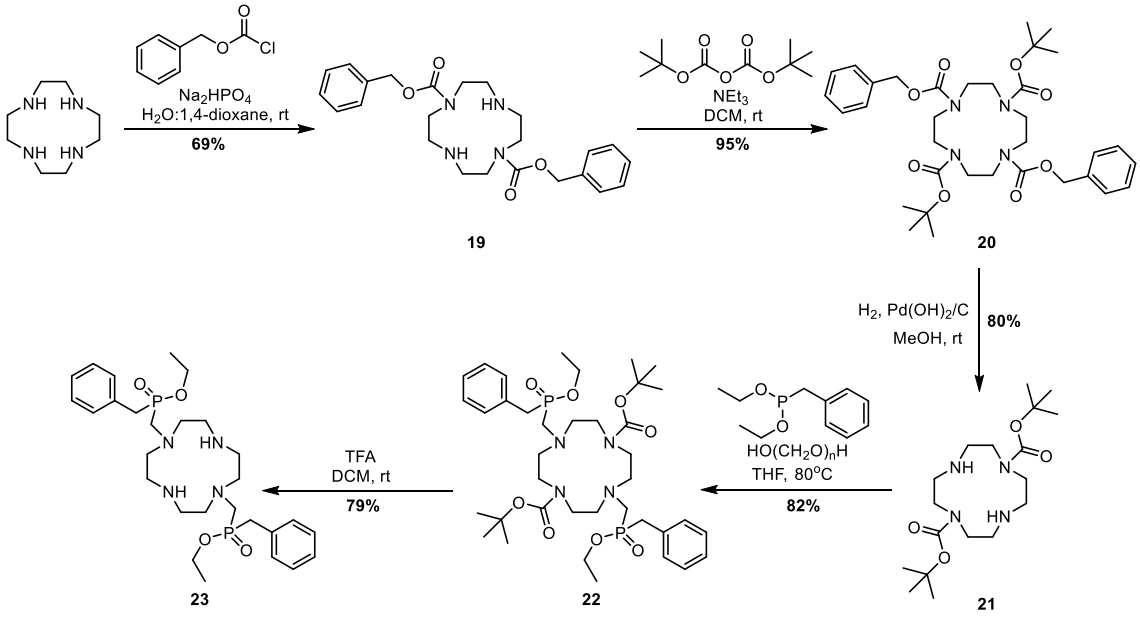

Scheme 3.2 Synthetic route to di-benzylphosphinate cyclen macrocycle, **23**.

The final secondary amines of the tri- and dibenzylphosphinate macrocycles, **16** and **23**, were alkylated with the mesylate, **18**, using caesium carbonate as a base (Scheme 3.3). Deprotection of the phosphinate esters proceeded under acidic conditions, before complexation was achieved using the appropriate lanthanide(III) chloride salt. The complexes **[LnL^4]** and **[LnL^5]$^+$** were purified by reverse-phase HPLC.

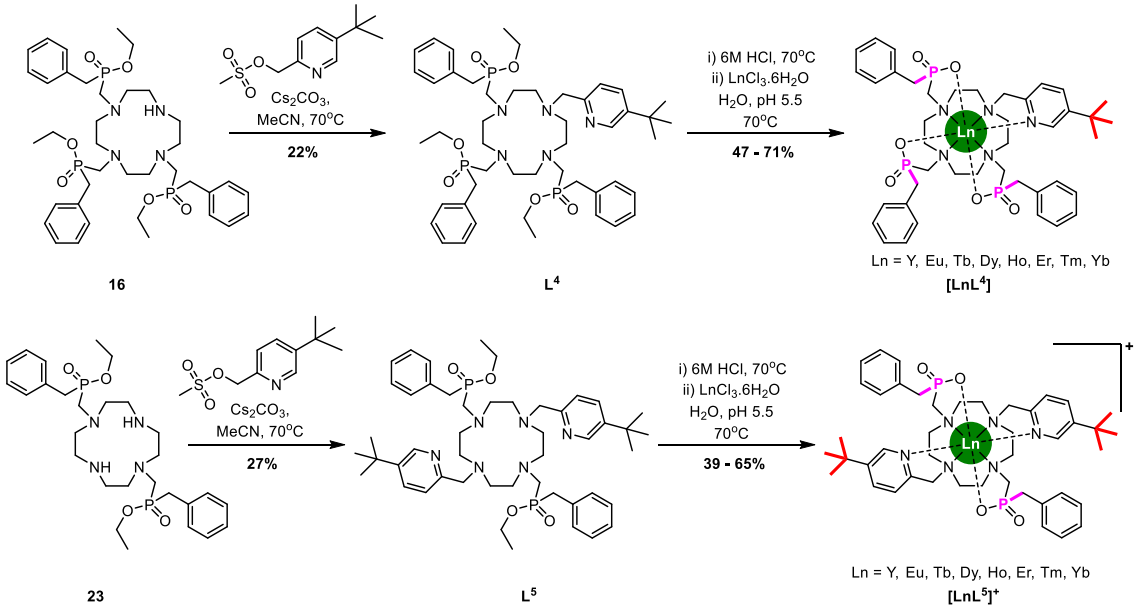

Scheme 3.3 Procedure for the alkylation and complexation of the tribenzylphosphinate complex **[LnL^4]** (*top*) and dibenzylphosphinate complex **[LnL^5]$^+$** (*bottom*).

As **[LnL^5]$^+$** contains only two anionic oxygen donors the overall complex is cationic, the complex exists was isolated as its chloride salt.

The luminescence lifetimes of the Eu^{3+} and Tb^{3+} complexes of **[LnL^4]** and **[LnL^5]Cl** were measured in both H_2O and D_2O and the metal hydration states were calculated (Table 3.1).

Table 3.1 Luminescence lifetime measurements and the calculated *q* values for the Eu^{3+} and Tb^{3+} complexes, **[LnL^4]** and **[LnL^5]Cl** (295 K, λ_{ex} = 270 nm).

[LnL^x]	τ_{H_2O} (ms)	τ_{D_2O} (ms)	*q*
[EuL^4]	1.03	1.67	0.15
[TbL^4]	3.23	3.70	0
[EuL^5]Cl	0.49	0.65	0.30
[TbL^5]Cl	2.56	2.63	0

As expected, both **[LnL^4]** and **[LnL^5]Cl** have no inner sphere water molecule, consistent with the behaviour of the phosphonate-substituted species, **[LnL^2]** and **[LnL^3]** (Sections 2.2.1 and 2.3, pages 69 and 76).

3.2 Structure elucidation

3.2.1 Solid state structure analysis

Crystals of the Yb^{3+} complex of **[LnL^4]** were grown by diffusion of diethyl ether into a methanol solution of the complex (Figure 3.2). The complex crystallised in the centrosymmetric space group $P2_1/c$, both enantiomers were present within the crystal and were symmetry related. The asymmetric unit contained two molecules of the same enantiomer, with four of these within the unit cell (Z = 8). However, only one will be referred to in this thesis, as both exhibited near identical structures. There was no solvent coordinated to the lanthanide ion, however hydrogen bonding was observed between methanol in the lattice and two of the phosphinate oxygen atoms.

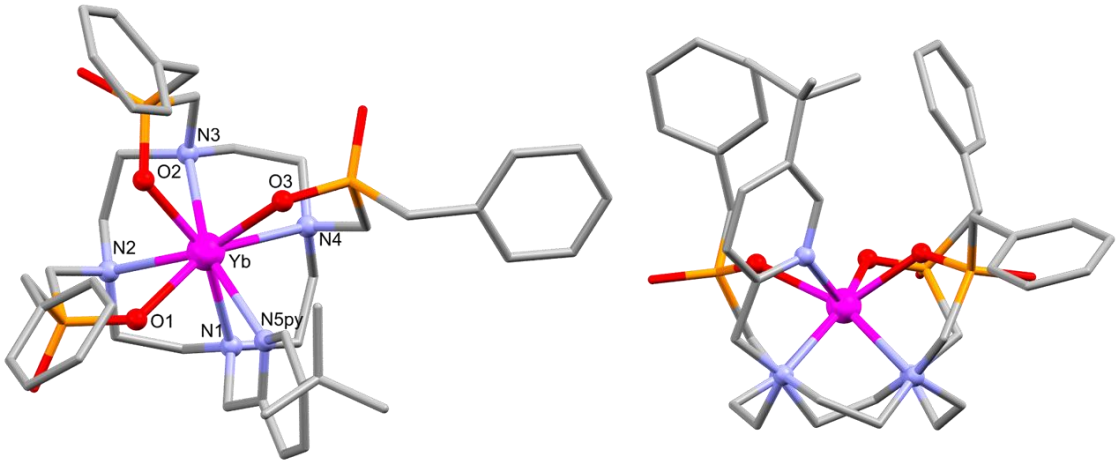

Figure 3.2 Molecular structure of (SSS)-Δ-(δδδδ)-**[YbL^4]**, viewed from the top (*left*) and the side (*right*). H atoms are omitted for clarity.

In order to grow a suitable crystal for X-ray diffraction of **[LnL^5]$^+$** the Cl^- counterion was substituted for the larger PF_6^- anion by salt metathesis. Crystals of **[YbL^5]PF$_6$** were grown using the same method as **[YbL^4]** (Figure 3.3). Similarly to **[YbL^4]**, the dibenzylphosphinate complex crystallised in a centrosymmetric space group, $P\bar{1}$. Only one complex enantiomer was present in the asymmetric unit, and both phosphinate oxygens act as hydrogen bond acceptors to solvent methanol.

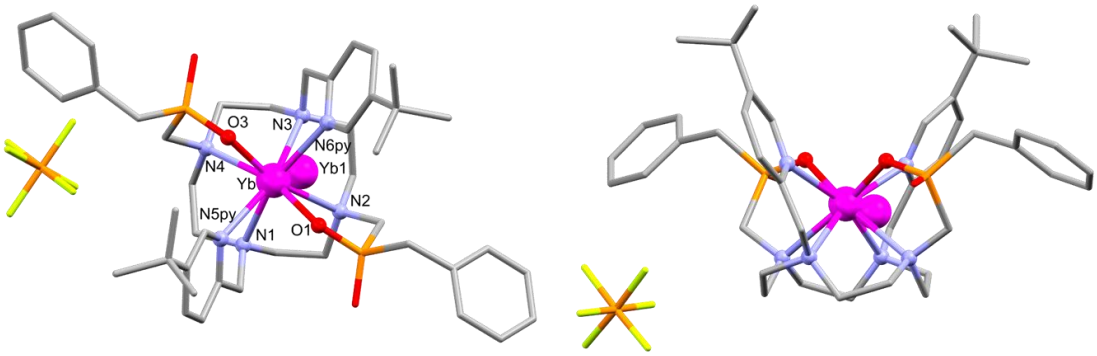

Figure 3.3 Molecular structure of (RR)-Λ-(λλλλ)-**[YbL^5]PF$_6$**, viewed from the top (*left*) and the side (*right*). H atoms are omitted for clarity. The position of the molecule within the unit cell was found to be disordered within 4% of the crystal lattice as indicated by the position of Yb1.

The coordination number of Yb^{3+} was 8 in each complex. Both exhibit a twisted-square-antiprismatic (TSAP) coordination geometry with all phosphinate chiral centres exhibiting the same configuration (SSS-**[YbL^4]** and RR-**[YbL^5]PF$_6$**). The Yb^{3+} ion of **[YbL^4]** was bound to the four ring nitrogen atoms, the pyridine nitrogen atom and the three anionic, phosphinate oxygen atoms, N_5O_3. The coordination sphere of the Yb^{3+} ion of **[YbL^5]$^+$** is N_6O_2, coordinated by the four ring nitrogen atoms as one square plane and the two pyridine nitrogen atoms and two anionic oxygen atoms in a trans arrangement as the other plane. It was expected that **[YbL^5]$^+$** would be C_2 symmetric, however this was not found to be the case in the solid state.

Due to the isomerism observed in the phosphonate-substituted dibenzylphosphinate complex **[LnL^3]**, the solid state structure of **[TbL^5]$^+$** was also sought. The Yb^{3+} ion is the smallest and Tb^{3+} the largest of the later paramagnetic lanthanides discussed in this thesis. Examination and comparison of the crystal structures of both complexes will indicate whether the complexes are isostructural or if large geometry changes occur across the lanthanide series.

Crystals of **[TbL^5]PF$_6$** were grown using the same method as **[YbL^5]PF$_6$** (Figure 3.4). Similarly to **[YbL^5]PF$_6$**, the terbium complex crystallised in the centrosymmetric space group, $P\bar{1}$. In contrast to the Yb^{3+} complex, the asymmetric unit contained the two enantiomeric forms of the Tb^{3+} complex as two different molecules. The two dibenzylphosphinate complexes are comparable, with the same coordination sphere, N_6O_2.

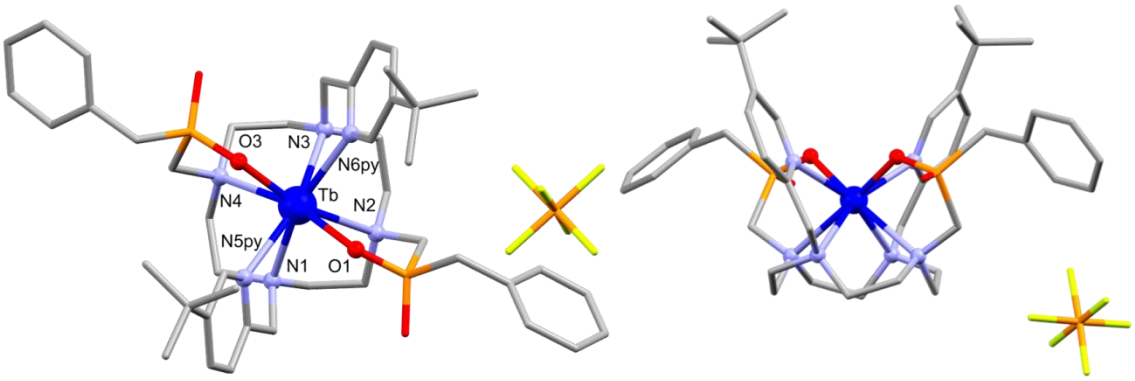

Figure 3.4 Molecular structure of (RR)-Λ-(λλλλ)-**[TbL^5]PF$_6$**, viewed from the top (*left*) and the side (*right*). H atoms are omitted for clarity.

Bond distances between Ln^{3+} and the anionic oxygen donors were shorter than those to the neutral nitrogen donors (Table 3.2). The bond distances of the metal ion to the cyclen nitrogen atoms varied alternatingly in **[LnL^5]PF$_6$**: N1 and N3, which are alkylated with the *tert*-butyl pyridine moiety, had shorter bonds to Ln^{3+} compared to the nitrogen donors alkylated with phosphinates. The Ln-X bond lengths of **[TbL^5]PF$_6$** are longer than those of **[YbL^5]PF$_6$**, as expected due to the larger ionic radius of Tb^{3+}.

The average distance of the two *tert*-butyl reporter group protons to the Yb^{3+} ion of **[YbL^5]PF$_6$** was 6.76 Å, and this was slightly longer than the corresponding distance in **[YbL^4]** which was found to be 6.62 Å in the solid state. The average distance *r* of the *tert*-butyl hydrogen atoms in each enantiomers of **[TbL^5]PF$_6$** was measured to be 6.74 Å, very similar to that of the analogous Yb^{3+} complex. The similarity of the internuclear distance in the solid state suggests that any variations in the NMR properties of the *tert*-butyl reporter group are independent of *r*.

Table 3.2 Bond distances in the N_5O_3 or N_6O_2 coordination sphere of **[YbL^4]** and **[LnL^5]PF$_6$**.

bond	bond lengths (Å)			
	[YbL^4]	**[YbL^5]PF$_6$**	**[TbL^5]PF$_6$ (Λ)**	**[TbL^5]PF$_6$ (Δ)**
Yb-N1	2.549 (3)	2.532 (5)	2.565(2)	2.564(2)
Yb-N2	2.590(3)	2.629 (4)	2.661(2)	2.668(2)
Yb-N3	2.570 (3)	2.524 (4)	2.572(2)	2.588(2)
Yb-N4	2.678 (3)	2.605 (3)	2.646(2)	2.654(2)
Yb-N5py	2.472 (3)	2.515 (5)	2.533(2)	2.541(2)
Yb-O1	2.216 (2)	2.194 (4)	2.226(2)	2.234(2)
Yb-O2/N6py	2.217 (2)	2.508 (4)	2.543(2)	2.535(2)
Yb-O3	2.232 (2)	2.173 (3)	2.242(2)	2.253(2)

The four NCCN torsion angles of the cyclen macrocycle ring, which define the λ/δ configurations, are reported in Table 3.3. They were all found to be the same sign, positive or negative, respectively for the δδδδ and λλλλ enantiomers.

Table 3.3 Torsion angles in the cyclen macrocyclic ring for **[YbL^4]** and **[LnL^5]PF$_6$**.

Torsion Chain	Torsion angle (deg)			
	[YbL^4]	**[YbL^5]PF$_6$**	**[TbL^5]PF$_6$ (Λ)**	**[TbL^5]PF$_6$ (Δ)**
N1-C1-C2-N2	±59.0(4)	±59.0(6)	-58.7(3)	+59.8(3)
N2-C3-C4-N3	±58.6(4)	±57.3(5)	-60.7(3)	+59.9(3)
N3-C5-C6-N4	±56.8(3)	±59.6(6)	-58.3(3)	+57.6(3)
N4-C7-C8-N1	±58.9(4)	±58.8(6)	-59.8(3)	+60.4(3)

The torsion angles of the macrocyclic ring of each complex are similar to each other and also comparable to those found for the analogous trimethylphosphinate complex, **[LnL^J]**.[6]

Similarly, the torsion angles of the exocyclic groups, $NCCN_{py}$ or NCCO, can be either positive or negative (Table 3.4). These angles define the overall Δ or Λ helicity, respectively, of the complex.

Table 3.4 Torsion angles around the exocyclic groups for **[YbL^4]** and **[LnL^5]PF$_6$**.

Torsion Chain	Torsion angle (deg)			
	[YbL^4]	**[YbL^5]PF$_6$**	**[TbL^5]PF$_6$ (Λ)**	**[TbL^5]PF$_6$ (Δ)**
N1-C10-C11-N5py	±28.5(4)	±21.5(7)	-21.8(3)	+22.8(3)
N2-C20-P1-O1	±26.9(3)	±43.6(4)	-43.9(2)	+42.7(2)
N3-C30-P2-O2 or N3-C30-C31-N6py	±30.5(2)	±27.1(6)	-27.1(3)	+29.0(3)
N4-C30-P3-O3	±40.6(2)	±43.3(4)	-44.1(2)	+48.2(2)

The tribenzylphosphinate complex exhibits similar torsion angles to those of the trimethylphosphinate complex.[6] However, the exocyclic torsion angles of the phosphinate chelate arms are larger for **[LnL^5]PF$_6$**.

Cyclen-based, 8-coordinate lanthanide complexes typically exist as a form of square antiprism, with the 4 cyclen nitrogen atoms (N_4) and the arm donor atoms (O_3N or O_2N_2) making up two planar and parallel square bases. The twist angles, α and γ, of the two square planes are 0° for an idealised square prism and 45° for an antiprism. The twist angles for **[YbL^4]**, **[YbL^5]PF$_6$** and **[TbL^5]PF$_6$** are described and shown in Scheme 3.4 and Table 3.5.

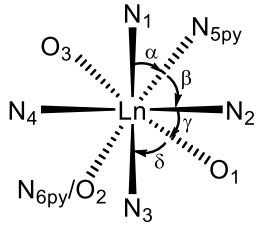

Scheme 3.4 Schematic representation of the twist angles found in octadentate square prismatic lanthanide complexes such as **[YbL^4]** and **[LnL^5]PF$_6$**.

Table 3.5 Twist angles between the N_4 and NO_3/N_2O_2 coordination faces of **[YbL^4]** and **[LnL^5]PF$_6$**.

Plane		Angle (deg)			
		[YbL^4]	**[YbL^5]PF$_6$**	**[TbL^5]PF$_6$ (Λ)**	**[TbL^5]PF$_6$ (Δ)**
N1-Yb-N3 vs O1-Yb-O3	δ	64.1	70.4	70.6	71.3
N1-Yb-N3 vs O2-Yb-N5py or N5py-Yb-N6py	α	24.9	18.1	18.4	17.9
N2-Yb-N4 vs O1-Yb-O3	γ	28.0	18.9	18.5	17.8
N2-Yb-N4 vs O2-Yb-N5py or N5py-Yb-N6py	β	65.4	72.6	72.5	73.0

The average observed twist angle for **[YbL^4]** was 26.4°, near identical to that of **[YbL^J]**.[6] The structural modification from the tri- to the dibenzylphosphinate complex however, has a more significant impact on the twist angle, reducing it to 18.5° and 18.2° for **[YbL^5]Cl** and **[TbL^5]Cl** respectively, indicating the coordination geometry of **[LnL^5]PF$_6$** is somewhat closer to that of an ideal square prism.

3.2.2 DFT studies

In order to probe the solution structures of **[LnL^4]** and **[LnL^5]$^+$**, DFT computational studies, using the Yb^{3+} complex crystal structures as a basis to optimise the geometries, were conducted by Dr Mark A. Fox (Figure 3.5). Paramagnetic Yb^{3+}complexes are difficult to model computationally so the structures were optimised as the diamagnetic Y^{3+} complexes using the hybrid-DFT B3LYP functional and 3-21G* basis set which has been previously demonstrated to be appropriate for such complexes.[10]

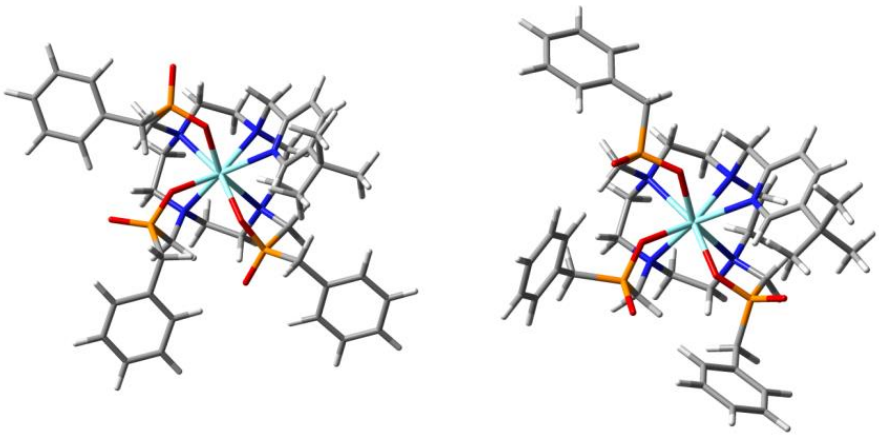

(RRR)-Λ-(λλλλ)-[YL^4] **(RRR)-Δ-(δδδδ)-[YL^4]**

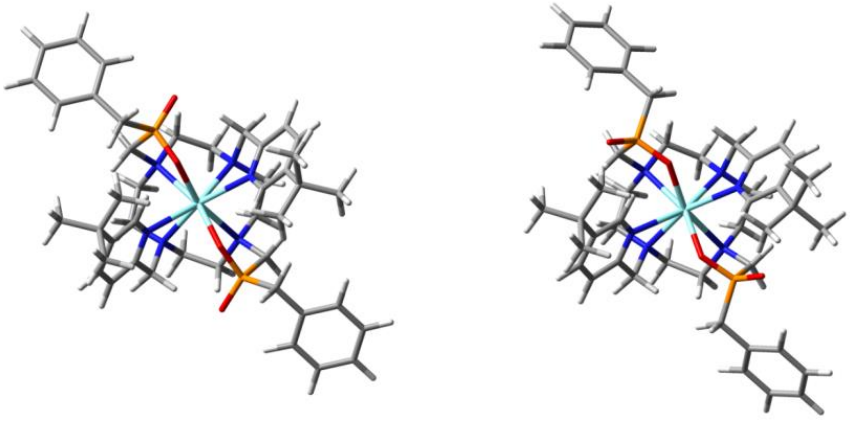

(RR)-Λ-(λλλλ)-[YL^5]$^+$ **(RR)-Δ-(δδδδ)-[YL^5]$^+$**

Figure 3.5 DFT calculated TSAP structures (Λ-(λλλλ) (*left*) and Δ-(δδδδ) (*right*)) of **[YL^4]** (*top*) and **[YL^5]$^+$** (*bottom*).

The relative free energies of the possible isomeric Y^{3+} complexes of **[LnL^4]** and **[LnL^5]$^+$** are shown in Table 3.6. The lowest energy structures for both complexes are both TSAP isomers. In the case of **[YL^4]**, the lowest energy structure was calculated to be (RRR)-Λ-(λλλλ) as observed by crystallography. However, the TSAP isomer (RR)-Δ-(δδδδ) was found to be the lowest energy structure for **[YL^5]$^+$**, although the (RR)-Λ-(λλλλ) TSAP diastereoisomer as found in the solid state is of comparable energy.

Table 3.6 Calculated relative energies for the diastereoisomers of **[YL^4]** and **[YL^5]$^+$**.

Complex Isomer		Relative Energy / kJmol^{-1}	
		[YL^4]	**[YL^5]$^+$**
(R)-Λ-(λλλλ)	**TSAP**	0.0	1.2
(R)-Δ-(δδδδ)	**TSAP**	33.4	0.0
(R)-Λ-(δδδδ)	**SAP**	33.8	25.5
(R)-Δ-(λλλλ)	**SAP**	64.0	13.9

The relative energy of the conformations of the dibenzylphosphinate complex **[YL^5]$^+$**, are smaller compared to those of the tribenzylphosphinate analogue. This suggests

that multiple isomers may be observed in the solution state NMR of **[LnL^5]$^+$**, which is consistent with the multiple *tert*-butyl resonances observed for the phosphonated dibenzylphosphinate complex, **[LnL^3]**.

3.3 Diamagnetic NMR studies of [YL^4] and [YL^5]Cl

The solution ^{1}H, ^{13}C and ^{31}P NMR spectra of the diamagnetic complexes, **[YL^4]** and **[YL^5]Cl**, were analysed in detail. Complexes of **L^4** proved sparingly soluble in D_2O, so all NMR analyses were conducted in CD_3OD for each complex.

Full assignment of the observed ^{1}H, ^{13}C and ^{31}P resonances was achieved for both of the major diastereoisomers of **[YL^4]** and **[YL^5]Cl**. The labelling scheme used for **[LnL^4]** is shown in Figure 3.6 and an analogous scheme was used for **[LnL^5]$^+$**. The assignment of all resonances for the major isomer of both complexes can be found in Section 5.9 (pages 215-216 and 223-224).

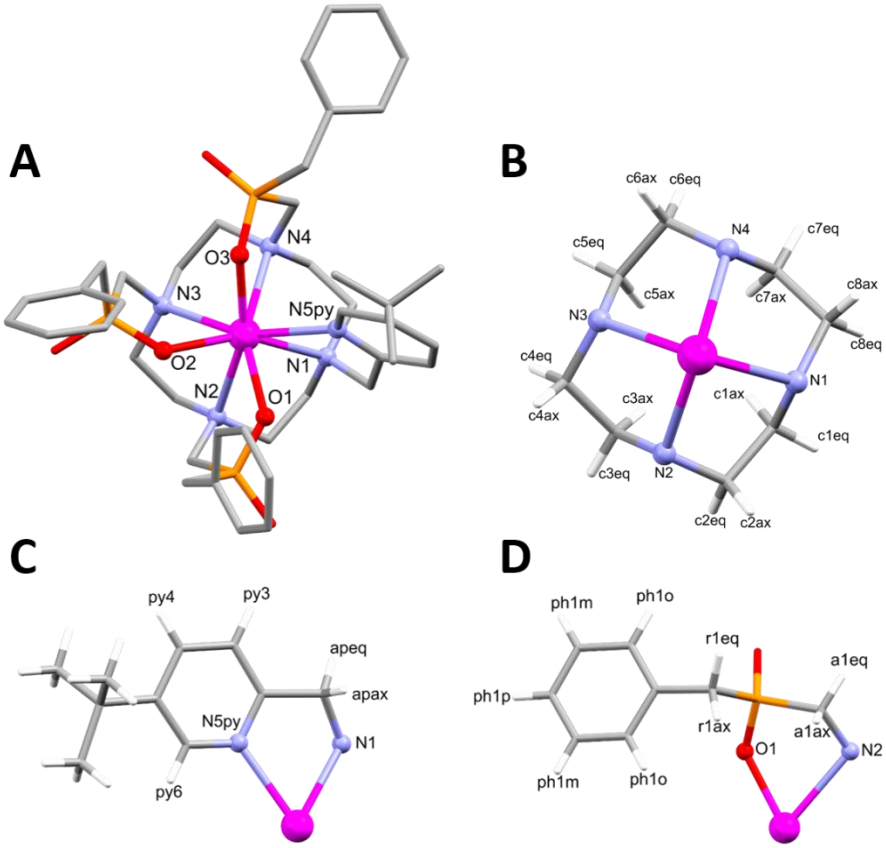

Figure 3.6 Atom labels of **[LnL^4]**: (A) the full structure of **[YbL^4]** showing the donor atoms (B) fragment of the same structure labelling the axial (ax) and equatorial (eq) protons of the cyclen ring; (C) fragment showing the aromatic (py), axial (apax) and equatorial (apeq) protons of the pyridine arm; (D) fragment labelling the axial (a1ax) and equatorial (a1eq) diastereotopic protons of the phosphinate arms, the benzylic axial (r1ax) and equatorial (r1eq) diastereotopic protons and the *ortho*- (ph1o), *meta*- (ph1m) and *para*- (ph1p) benzylic protons.

3.3.1 NMR Assignment of [YL^4]

The ^{31}P NMR spectra of **[YL^4]** showed the presence of three major, distinct phosphorus environments (Figure 3.7). Through-bond *J* coupling to the Y^{3+} ion (^{89}Y, *I* = 1/2) was observed in each case ($^2J_{YP}$ ≈ 6 Hz). The presence of a minor diastereoisomer can also be observed, as previously seen for the analogous trimethylphosphinate complex **[YL^J]**.[6] The ratio of the minor isomer decreased from **[YL^J]** (5:1) to **[YL^4]** (10:1), a trend also observed in the triphosphinate pH probe upon the structural modification from methyl to benzylphosphinate groups.

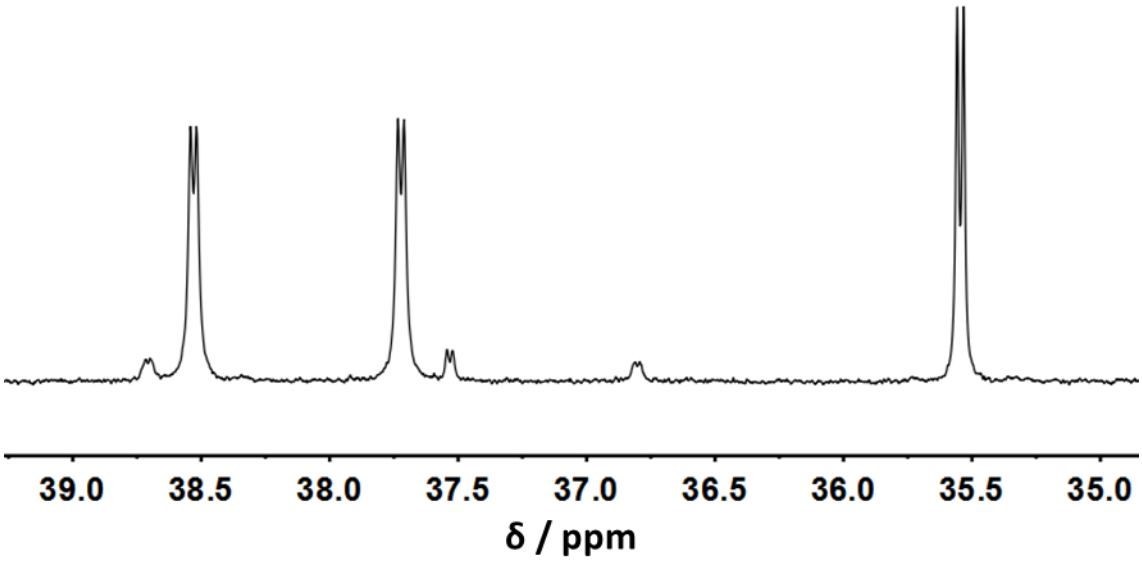

Figure 3.7 ^{31}P NMR spectrum of **[YL^4]** showing the phosphinate resonances of both major and minor isomers, with small ^{89}Y-^{31}P couplings ($^3J_{YP}$ ~ 6 Hz) (14.1 T, 298 K, CD_3OD).

The complex **[YL^4]** contains 43 chemically distinct proton environments and 34 carbon environments. The *tert*-butyl resonance was readily identified from the ^{1}H NMR spectrum and the carbon and proton resonances of the aromatic pyridine were assigned from this resonance using the 2D ^{1}H-^{1}H COSY, ^{1}H-^{13}C HMBC and ^{1}H-^{13}C HSQC spectra. The remaining aromatic signals belong to the phosphinate benzyl groups. Due to the number of overlapping resonances, analysis of the ^{1}H-^{13}C HSQC spectra was required to identify each of the 9 ^{1}H aromatic benzyl resonances. The number of ^{1}H signals means that in solution at room temperature there is fast rotation of the aromatic rings on the NMR timescale. Proton-phosphorus HMBC (Figure 3.8) and ^{1}H-^{1}H COSY spectra were employed to identify the connectivity of the aromatic proton and phosphorus resonances.

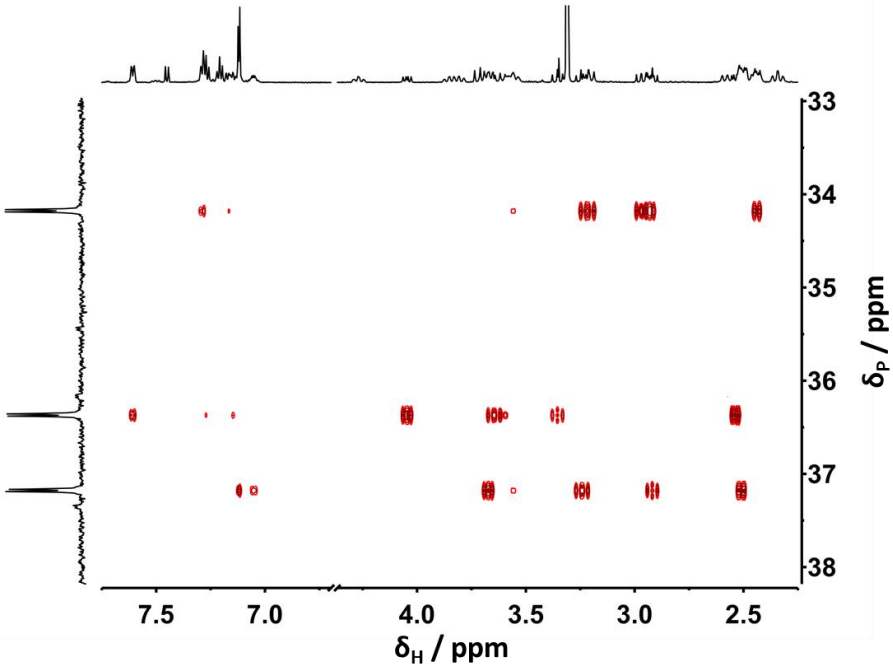

Figure 3.8 ^{1}H-^{31}P HMBC NMR spectrum of **[YL^{4}]** showing the proton-phosphorus correlations in the aromatic and aliphatic regions (14.1 T, 298 K, CD_3OD).

The aliphatic region (4.8 – 2.2 ppm) of the ^{1}H spectra of **[YL^{4}]** contained many overlapping multiplets coupled to phosphorus and/or other protons, which made assignment challenging. Simplification of the spectra was achieved through the use of 'pure shift' ^{1}H NMR techniques (Dr Juan A. Aguilar), which removes both proton and phosphorus coupling. The ^{1}H-^{1}H splitting is removed using the PSYCHE pulse sequence and ^{1}H-^{31}P couplings were removed by standard ^{31}P decoupling methods (Figure 3.9).[11,12]

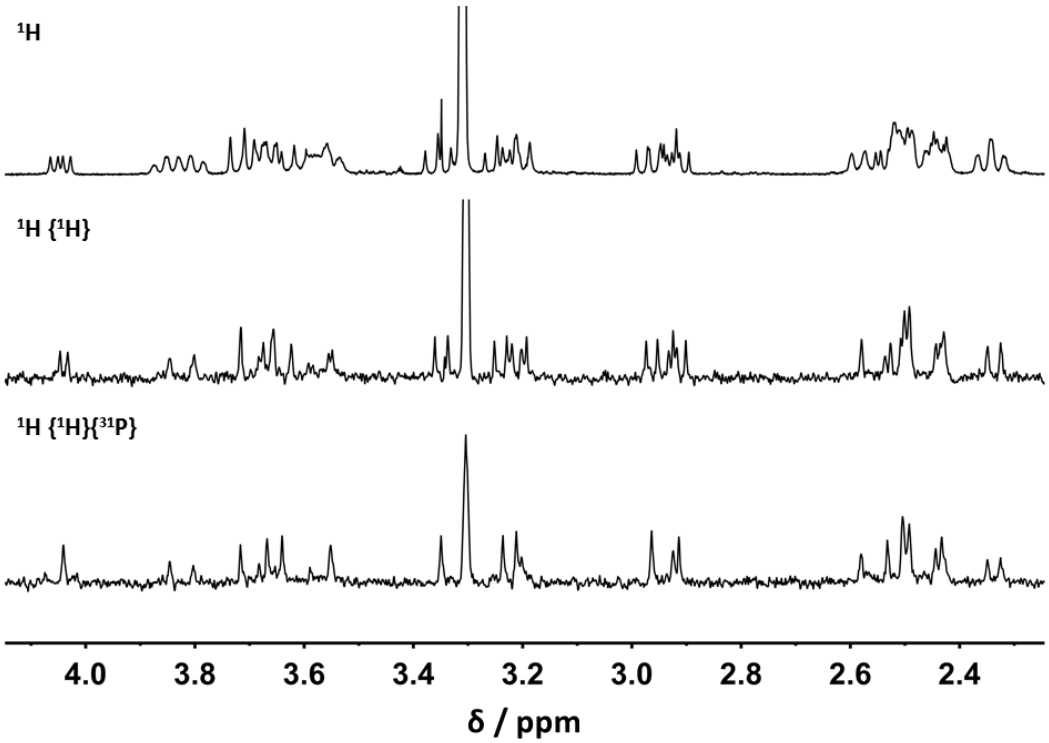

Figure 3.9 ^{1}H (*top*), ^{1}H{^{1}H decoupled} (*centre*) and ^{1}H{^{1}H and ^{31}P decoupled} (*bottom*) NMR spectra of **[YL^{4}]**, in the shift range 2.3 – 4.2 ppm (14.1 T, 298 K, CD_3OD).

In each aliphatic CH_2 group, the protons are diastereotopic. A general assignment was achieved by analysis of the 2D ^{1}H-^{13}C HSQC spectrum, in which the coupled pairs of diastereotopic protons ($^{2}J_{HH}$ ~ 16 Hz) can be readily identified. Proton-proton($^{2}J_{HH}$) and carbon-phosphorus ($^{1}J_{CP}$) *J* coupling can be observed in the ^{1}H-^{13}C HSQC spectrum (Figure 3.10) of the identified benzylic-CH_2 resonances. The complete connectivity of these resonances was aided by inspection of the 2D ^{1}H-^{31}P HMBC spectrum (Figure 3.8) which enabled the resonances to be linked to the correct phosphorus atom and associated aromatic group.

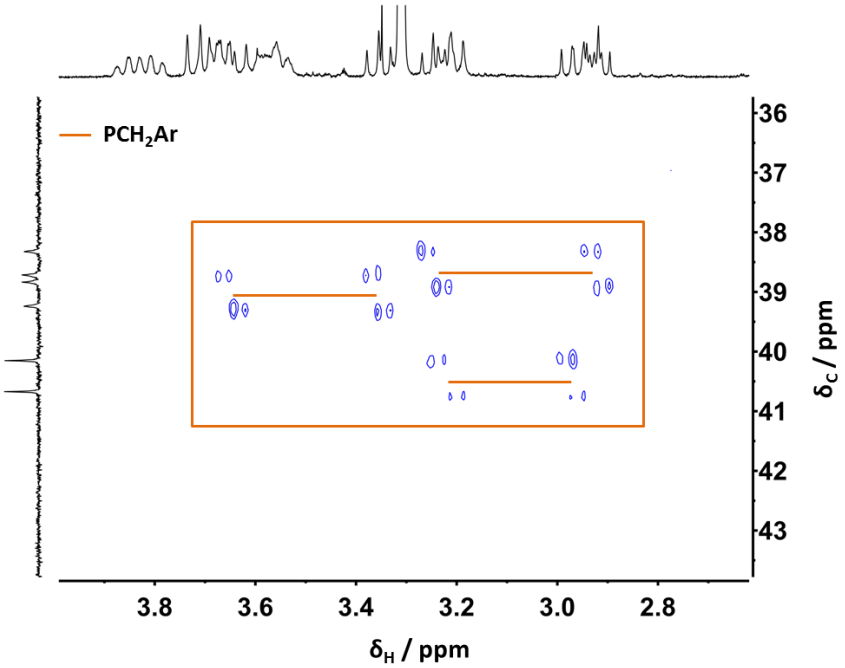

Figure 3.10 ^{1}H-^{13}C HSQC NMR spectrum of the aliphatic region of **[YL^{4}]** showing the PCH_2Ar (*orange*) resonances (14.1 T, 298 K, CD_3OD).

The exocyclic arm CH_2 protons and carbons of the phosphinate groups and pyridine moiety were identified from the ^{1}H-^{13}C HSQC spectrum (Figure 3.11). The phosphinate-CH_2 resonances were correlated to a phosphorus resonance, and therefore the ^{1}H-^{31}P HMBC spectrum was used to connect the exocyclic CH_2 protons to the correct benzylic group (Figure 3.8).

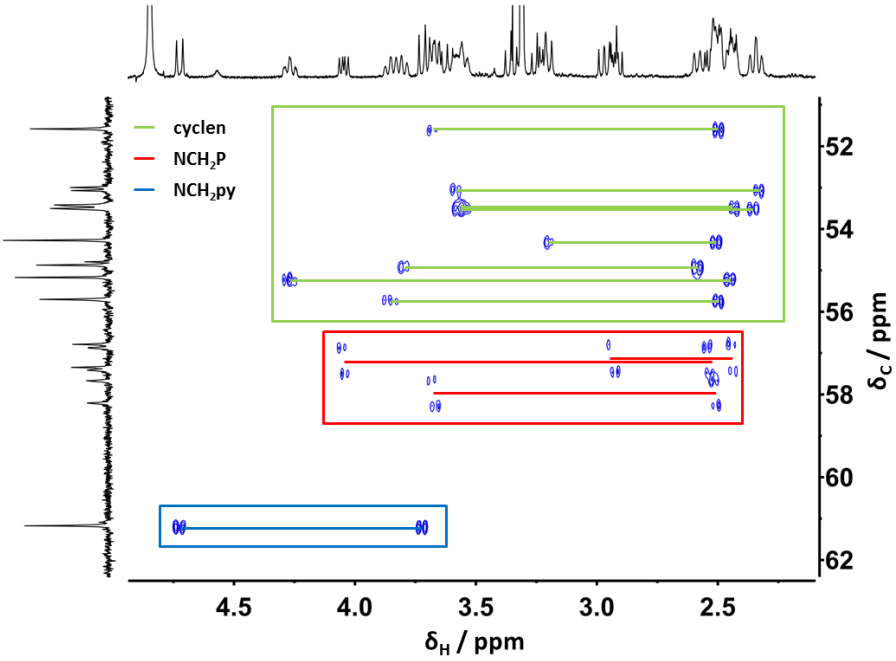

Figure 3.11 ^{1}H-^{13}C HSQC NMR spectrum of the aliphatic region of **[YL^{4}]** showing the cyclen-CH_2 (*green*), NCH_2P (*red*) and NCH_2py (*blue*) resonances (14.1 T, 298 K, CD_3OD).

The ^{1}H-^{13}C HSQC spectrum (Figure 3.11) also allowed for the identification of the cyclen CH_2 protons and carbons. The order of the cyclen carbon resonances around the ring was then determined using ^{1}H-^{13}C HMBC and ^{1}H-^{1}H TOtal Correlated SpectroscopY (TOCSY) (Figure 3.12). TOCSY is similar to ^{1}H-^{1}H COSY; however, correlations are observed for every proton within a given spin system, not just those that are directly coupled. This allowed for each NCH_2CH_2N to be identified and gave the connectivity of carbon resonances, around the macrocyclic ring. Analysis of the ^{1}H-^{13}C HMBC spectra, utilising the known assignment of the exocyclic pyridine CH_2 protons, allowed for the complete assignment of all proton, carbon and phosphorus resonances.

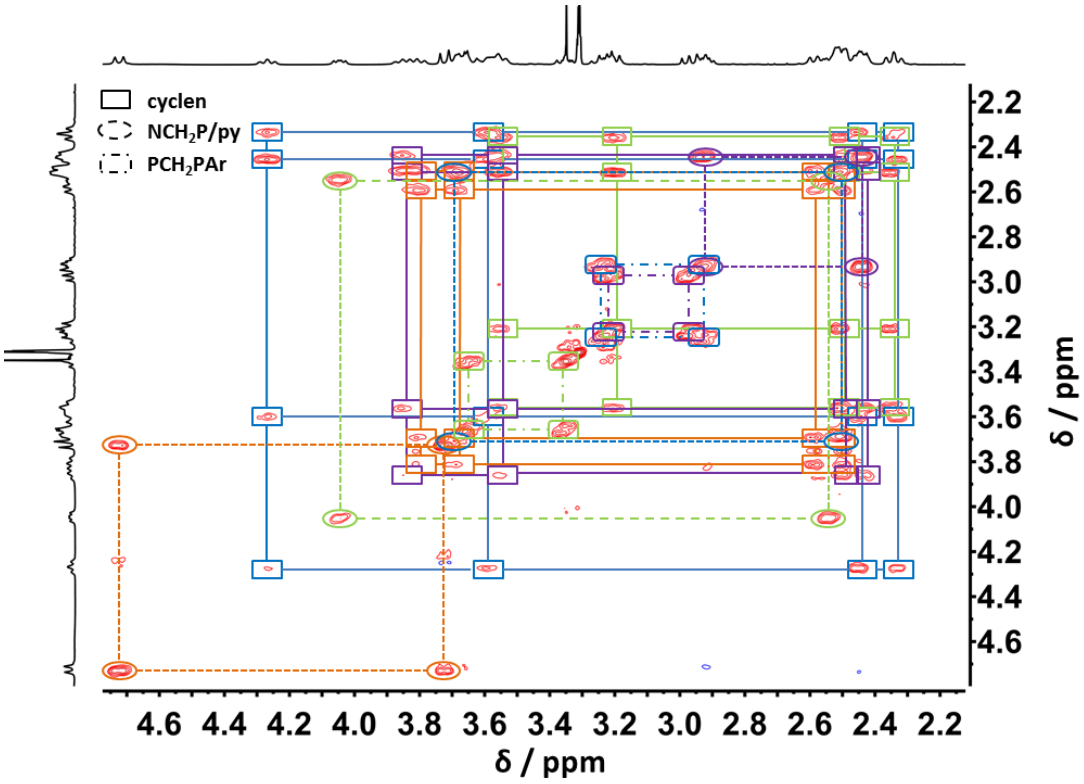

Figure 3.12 Aliphatic region of the ^{1}H-^{1}H TOCSY NMR spectrum of **[YL^{4}]** (14.1 T, 298 K, CD_3OD). The groups of four *J*-coupled cyclen protons are shown with rectangles and solid lines, exocyclic CH_2 pairs are shown with ovals and dashed lines and benzylic pairs are shown with rounded rectangles and dot and dashed lines.

Carbon-phosphorus coupling was seen in three of the cyclen carbon resonances (Figure 3.13).

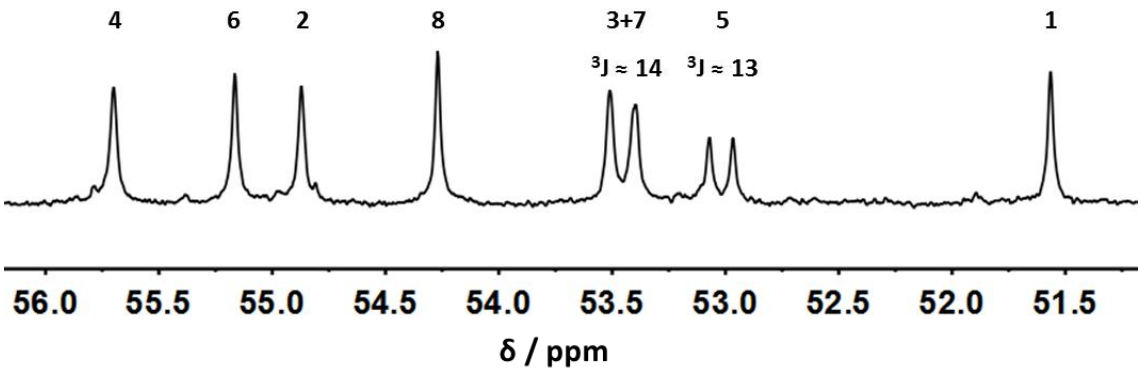

Figure 3.13 ^{13}C NMR spectrum of the cyclen region of **[YL^4]** showing the $^3J_{CP}$ coupling (14.1 T, 298 K, CD_3OD).

Measurement of the torsion angles between the cyclen carbons and the phosphorus atoms of the crystal structure of **[YbL^4]** revealed that the coupling arises in those carbons with a larger torsion angle (Table 3.7). The size of the coupling follows a Karplus-type relationship, so the carbons C2, C4 and C6 exhibit no coupling to phosphorus as the torsion angle (~70°) is close to 90°, where the magnitude of coupling is a minimum.

Table 3.7 Torsion angles between the carbons of the cyclen macrocyclic ring and the phosphinate phosphorus atoms of **[YbL^4]**.

Torsion Chain	Torsion Angle (deg)	$^3J_{CP}$ (Hz)
C2-N2-C20-P1	70.7 (3)	-
C3-N2-C20-P1	169.0 (2)	14
C4-N3-C30-P2	67.7 (3)	-
C5-N3-C30-P2	174.1 (2)	13
C6-N4-C40-P3	75.9 (3)	-
C7-N4-C40-P3	165.8 (2)	14

3.3.2 NMR Assignment of [YL^5]Cl

Although the crystal structures of **[YbL^5]PF$_6$** and **[TbL^5]PF$_6$** did not show C_2 symmetry, analysis of the ^1H and ^{31}P NMR spectra of **[YL^5]Cl** showed that the major isomer exhibits time-averaged C_2 symmetry in solution. The presence of C_2 symmetry meant that assignment of the resonances was simplified, as the number of inequivalent resonances is halved.

The ^{31}P spectrum of **[YL^5]Cl** in CD_3OD showed one major isomer, that revealed a through-bond *J* coupling to the Y^{3+} ion of the same magnitude as seen in **[YL^4]** ($^2J_{YP} \approx 6$ Hz) (Figure 3.14).

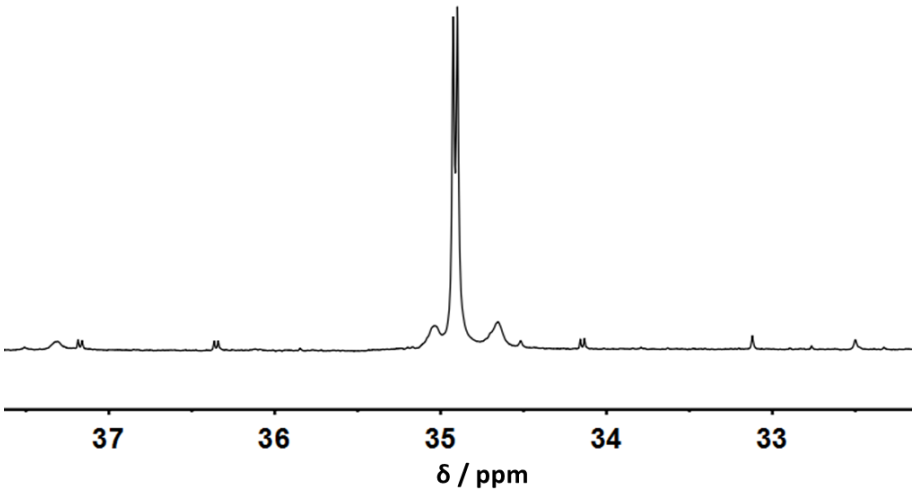

Figure 3.14 ^{31}P NMR spectrum of **[YL^5]Cl** showing the phosphinate resonances of the major and minor isomers and the small ^{89}Y-^{31}P couplings (14.1 T, 298 K, CD_3OD).

Unlike **[YL^4]**, in which only phosphorus resonances arising from a major and a single minor isomer were observed, the ^{31}P spectrum of **[YL^5]Cl** showed the presence of multiple smaller phosphorus signals. Some of the minor resonances displayed Y^{3+} coupling, although other signals were broader and did not show any splitting.

The 1- and 2-dimensional ^1H NMR spectra confirmed the presence of multiple diastereoisomers and their presence was best visualised in the aromatic region of the ^1H-^{13}C HSQC spectrum (Figure 3.15). At least three minor isomers were seen for each of the three pyridine resonances. However, the major diastereoisomer accounted for ~70% of the signal, as calculated by integration.

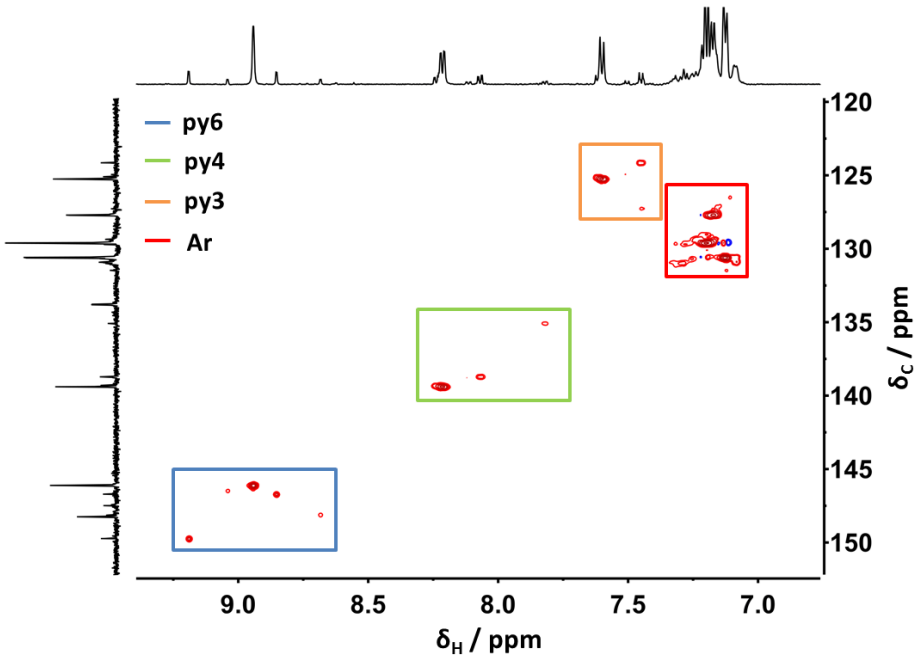

Figure 3.15 ^{1}H-^{13}C HSQC NMR spectrum of the aromatic region of **[YL^{5}]Cl** highlighting the major and minor pyridine ((py6 – *blue*), (py4 – *green*) and (py3 – *orange*)) and aromatic benzyl (*red*) resonances (14.1 T, 298 K, CD_3OD).

The ^{1}H-^{1}H COSY spectrum of the aromatic pyridine region was used to assign the minor pyridine resonances (Figure 3.16). However, the pyridine proton resonances were the only minor signals that could be identified, and only the assignment of the major isomer will be discussed henceforth.

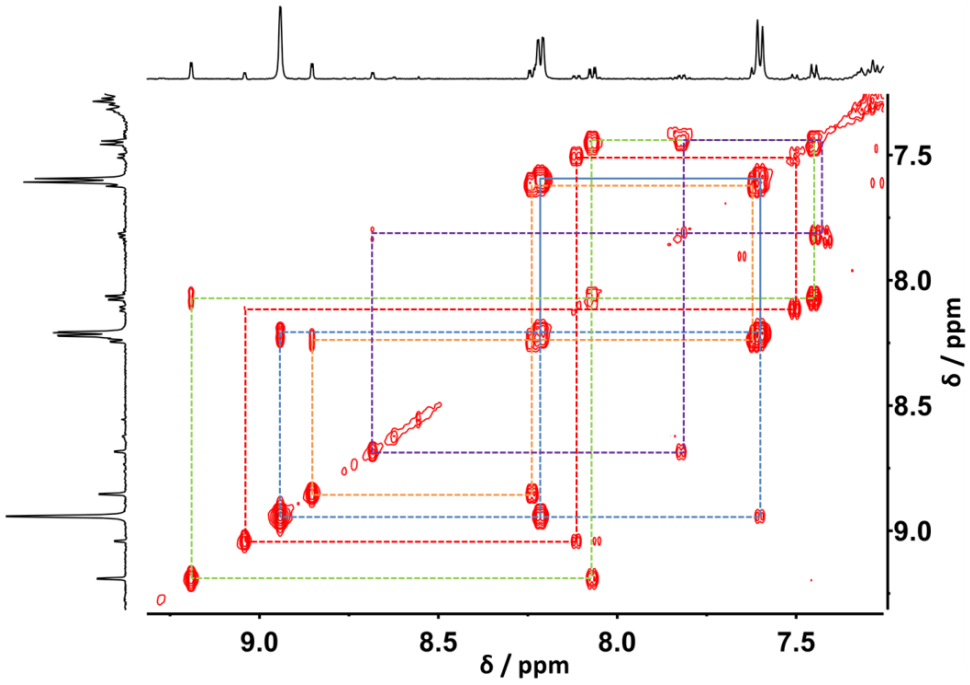

Figure 3.16 ^{1}H-^{1}H COSY NMR spectrum of the aromatic region of **[YL^{5}]Cl** highlighting the correlations between pyridine resonances (14.1 T, 298 K, CD_3OD). Each colour highlights a different spin system and stereoisomer.

The major *tert*-butyl and pyridine resonances were assigned similarly to those of **[YL^4]**, utilising 2D ^{1}H-^{1}H COSY, ^{1}H-^{13}C HMBC and ^{1}H-^{13}C HSQC spectra.

Proton-phosphorus HMBC (Figure 3.17) was used to identify the major benzylic and exocyclic phosphinate CH_2 protons. The 2D spectrum also showed the presence of phosphorus-proton correlations for the minor isomers.

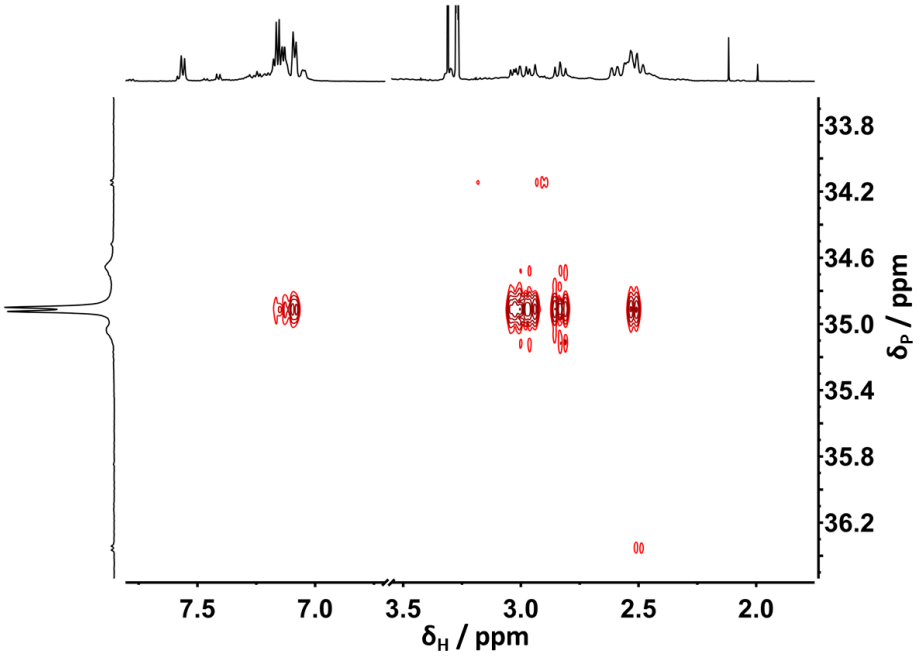

Figure 3.17 ^{1}H-^{31}P HMBC NMR spectrum of **[YL^5]Cl** (14.1 T, 298 K, CD_3OD).

Although the aliphatic region of the ^{1}H spectrum of **[YL^5]Cl** was generally simpler than that of **[YL^4]**, due to the reduced number of major resonances, decoupling techniques still aided assignment (Figure 3.18).

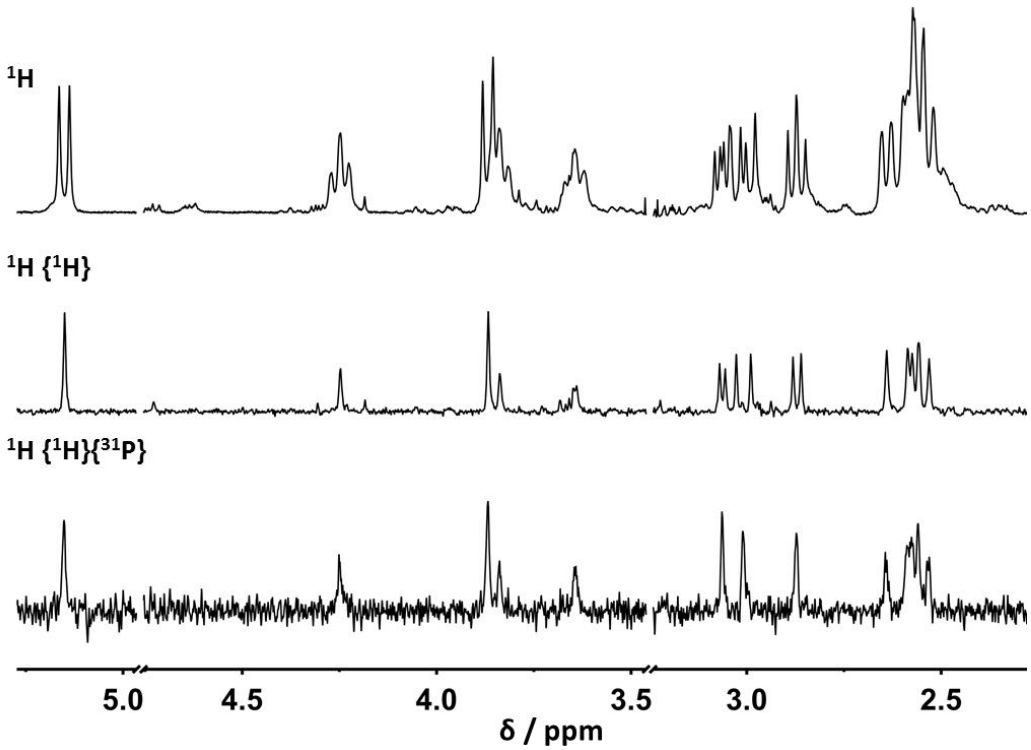

Figure 3.18 ^{1}H (*top*), ^{1}H{^{1}H decoupled} (*centre*) and ^{1}H{^{1}H and ^{31}P decoupled} (*bottom*) NMR spectra of **[YL^5]Cl**, in the shift range 2.3 – 5.3 ppm (14.1 T, 298 K, CD_3OD).

The aliphatic diastereotopic proton pairs were identified using the corresponding 2D ^{1}H-^{13}C HSQC spectrum (Figure 3.19).

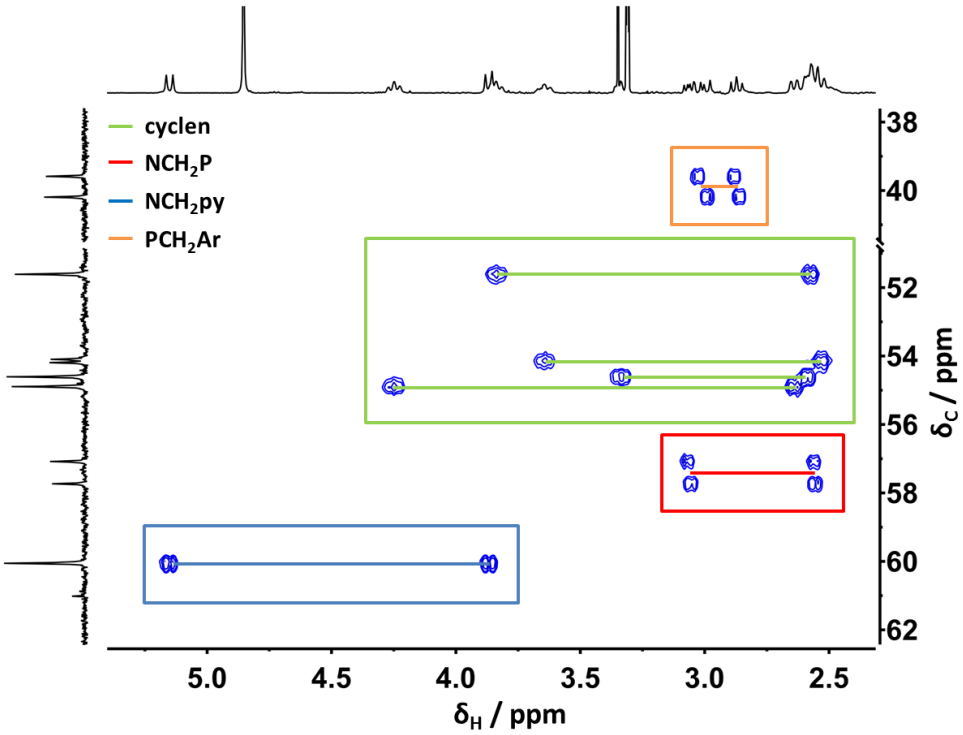

Figure 3.19 ^{1}H-^{13}C HSQC NMR spectrum of the aliphatic region of **[YL^4]** showing the cyclen-CH_2 (*green*), NCH_2P (*red*), NCH_2py (*blue*) and PCH_2Ar (*orange*) resonances (14.1 T, 298 K, CD_3OD).

Full assignment of the cyclen protons was achieved using the ^{1}H-^{1}H TOCSY spectrum (Figure 3.20) and ^{1}H-^{13}C HMBC spectra. Similarly to **[YL^{4}]**, carbon phosphorus splitting was observed for C3 of the cyclen ring (~14 Hz). Analysis of the crystal structure of **[YbL^{5}]PF$_{6}$** showed that the torsion angle between this carbon and the phosphorus atom was ~163.5°.

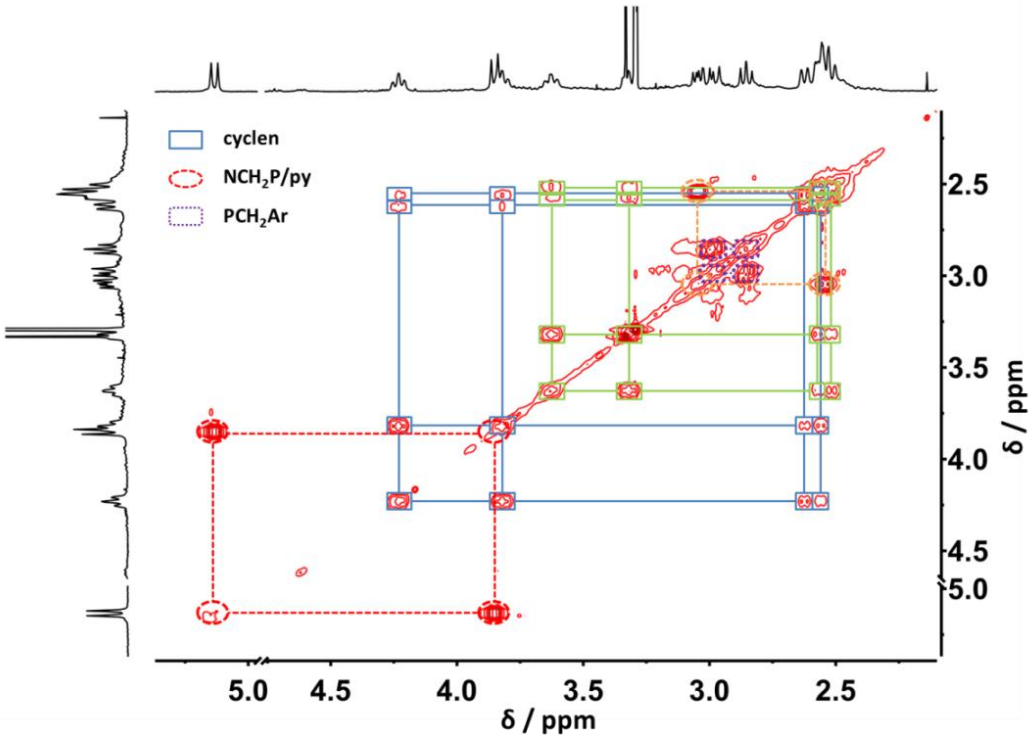

Figure 3.20 Aliphatic region of the ^{1}H-^{1}H TOCSY NMR spectrum of **[YL^{4}]** (14.1 T, 298 K, CD_3OD). The two groups of four *J*-coupled cyclen protons are shown with rectangles and solid lines (*blue* and *green*), exocyclic CH_2 pairs (NCH_2P/py) are shown with ovals and dashed lines (*orange* and *red*) and the benzylic pair (PCH_2Ar) are shown with rounded rectangles and dotted lines (*purple*).

3.3.3 Dynamic NMR analysis of [YL^{4}] and [YL^{5}]Cl

Whilst the full assignment reveals the connectivity of the complexes, determination of the solution structure of **[YL^{4}]** and **[YL^{5}]Cl** has not yet been achieved. In the case of the trimethylphosphinate complex, **[YL^{J}]**, ^{1}H-^{1}H NOESY/EXSY NMR was utilised to investigate the structure and dynamics of the major isomer.[6] The presence of certain observed NOE signals was used to identify the TSAP isomer (RRR)-Λ-(λλλλ). Previous work has demonstrated that octadentate SAP structures will show two strong NOE correlations between exocyclic NCH_2P/py protons and the endocyclic, cyclen ring protons; whereas only one cross-peak will be present for a TSAP structure.[13] In the case of **[YL^{4}]** only one strong NOE correlation with the ring protons was observed, as

shown in Figure 3.21. Additionally, the cross-peak observed is between the axial exocyclic pyridyl CH_2 proton (apax) with the axial endocyclic, cyclen proton of C2 (c2ax). This correlation is only possible in a TSAP structure indicating that the major isomer in solution has a TSAP geometry, in agreement with the outcome of the DFT calculations and in accordance with the crystal structure of **[YbL^4]**.

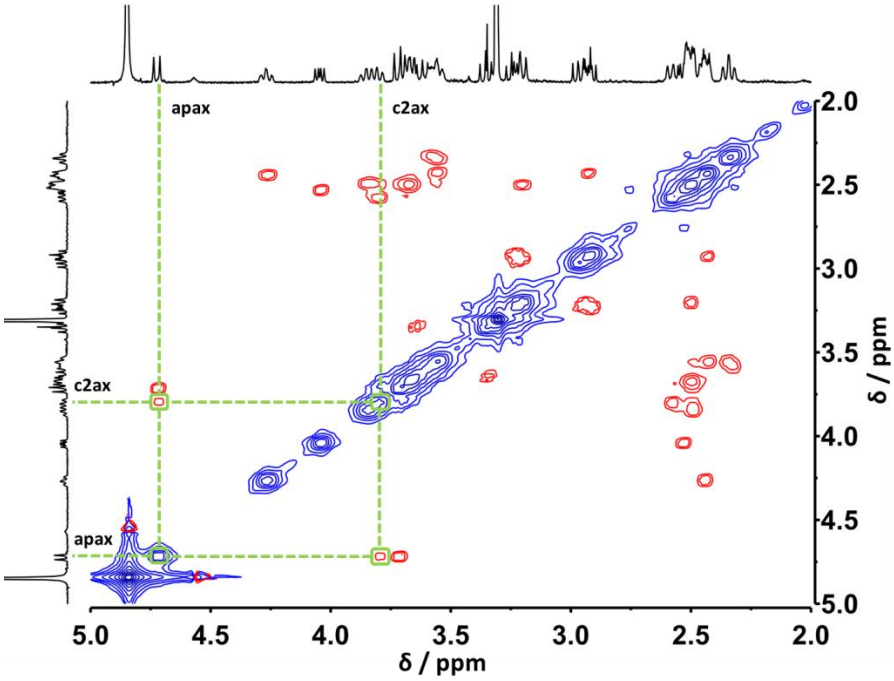

Figure 3.21 Aliphatic region of the ^{1}H-^{1}H NOESY NMR spectrum of **[YL^4]** (14.1 T, 298 K, CD_3OD, 300 ms mixing time). The NOE cross-peak highlighted is that of the axial exocyclic pyridyl CH_2 proton (apax) with the axial endocyclic, cyclen proton of C2 (c2ax). This correlation is only possible in a TSAP structure. The other NOE cross peak observed for apax is to its diastereotopic proton apeq.

Distinguishing between the two possible TSAP isomers (RRR)-Λ-(λλλλ) and (RRR)-Δ-(δδδδ) of the trimethylphosphinate complex **[YL^J]** relied on the presence of correlations between the phosphinate methyl resonances and the exocyclic CH_2 phosphinate protons.[6] The absence of cross-peaks between the phosphinate methyl groups and the endocyclic ring protons eliminated the possibility of the TSAP structure (RRR)-Δ-(δδδδ), as in this conformer the methyl protons would be in closer proximity to the cyclen protons than to the exocyclic CH_2 protons. Analysis of the DFT structures of both TSAP isomers of **[YL^4]** shows that in the minimum energy structure of the (RRR)-Δ-(δδδδ) diastereoisomer, the ^{1}H-^{1}H distance between the benzylic CH_2 (rax and req) and cyclen protons should be ~2 Å. Protons in such close proximity should give strong NOE signals. The distance between the benzylic CH_2 and the exocyclic

phosphinate CH_2 protons in the DFT lowest energy structure of the (RRR)-Λ-(λλλλ) conformer is much longer at ~2.7 Å. At such an internuclear distance, no or an extremely weak NOE signal would be observed. In the NOESY spectrum of **[YL^4]**, no NOE correlations were observed between the benzylic protons and either the endocyclic or exocyclic CH_2 resonances (Figure 3.21). Initially, it was thought that neither TSAP structure would be able to be conclusively assigned.

However, upon further inspection, the two benzyl CH_2 resonances of phosphinate P3 do show weak correlations between both the *tert*-butyl (tBu) and H^6 resonance of the pyridine, py6, (Figure 3.22). Analysis of the DFT structures showed that this interaction between the adjacent phosphinate group and the pyridine resonances can only occur in (RRR)-Λ structures. The major solution isomer of **[YL^4]** must be (RRR)-Λ-(λλλλ), as expected from the DFT calculations and from the crystal structure of **[YbL^4]**.

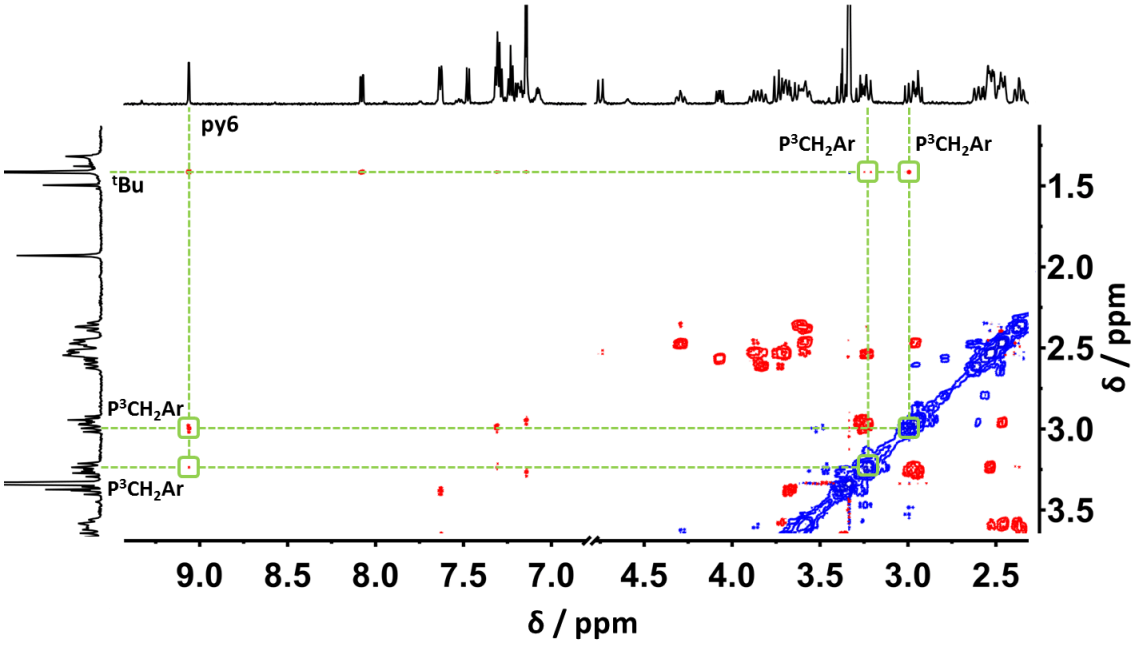

Figure 3.22 ^{1}H-^{1}H NOESY NMR spectrum of **[YL^4]** (14.1 T, 298 K, CD_3OD, 300 ms mixing time). The NOE cross-peaks highlighted are those of the P^3 phosphinate benzylic CH_2 protons with the pyridine H^6 (py6) and *tert*-butyl resonance (tBu).

The aromatic region of the NOESY spectra of **[YL^4]** and **[YL^5]** also revealed chemical exchange, as cross-peaks with the same phase as the diagonal were also present, consistent with the occurrence of such an exchange process. The major pyridine resonances of **[YL^4]** were observed to exchange with the equivalent minor resonances (Figure 3.23). Exchange spectroscopy calculations were performed using the MestreNova EXSYCalc program using intensity data obtained from two EXSY spectra.

The first has a mixing time of 0 ms, which allows for thermal equilibrium, with no chemical exchange to be observed. The amplitudes of the diagonal resonance are then compared with the diagonals and cross peaks of the second EXSY spectrum. In this latter experiment, a mixing time must be chosen that is large enough for magnetisation transfer to occur; in this work, that mixing time was found to be 300 ms (Figure 3.23).

Using the H^6 pyridine resonance (py6), the rate of exchange between the minor and major isomer of **[YL^4]** was found to be 1.27 s^{-1}. The reverse rate was slower (0.12 s^{-1}), and the equilibrium constant calculated from these rates (K_{eq} = 10.9) was found to be in reasonable agreement with that calculated by integration of the fully relaxed ^{31}P NMR spectrum (10:1) (Figure 3.7). Similar exchange rates were found for the behaviour of related trimethylphosphinate complexes, **[YL^J]** and **[YL^1]**.[6]

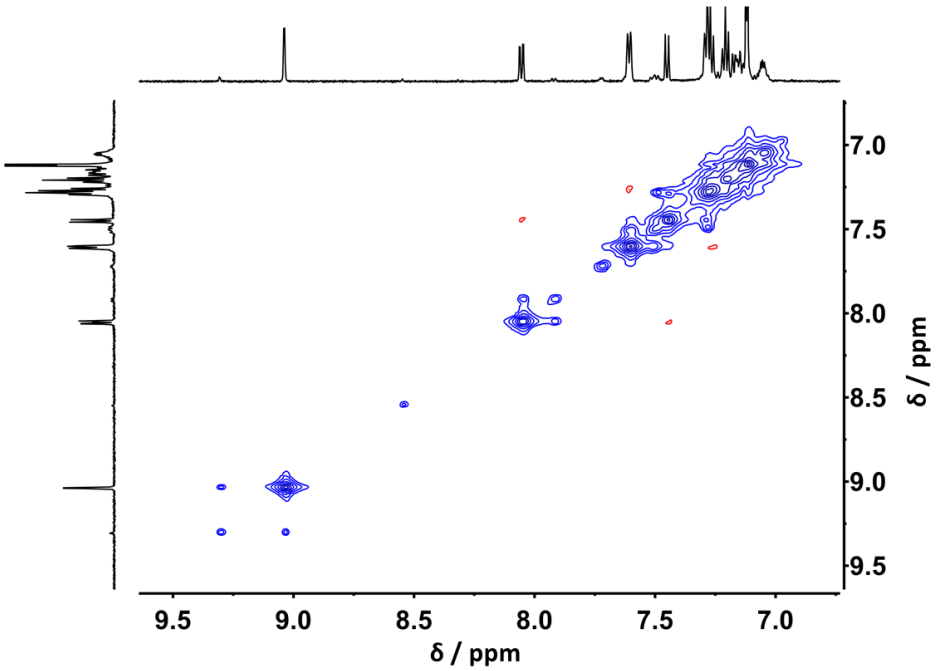

Figure 3.23 Aromatic region of the ^1H-^1H NOESY NMR spectrum of **[YL^4]** (14.1 T, 298 K, CD_3OD, 300 ms mixing time). The out of phase (*red*) cross-peaks indicate through-space NOE correlations and the in phase (*blue*) cross-peaks indicate chemical exchange.

As with to **[YL^4]**, the structure of **[YL^5]Cl** must also be a TSAP, as only one strong NOE signal was observed between the exocyclic pyridyl CH_2 and the cyclen CH_2 protons (Figure 3.24). Again, the only NOE correlation seen is between the axial proton on the C2 carbon of the cyclen ring (c2ax) and the axial exocyclic pyridyl proton (apax).

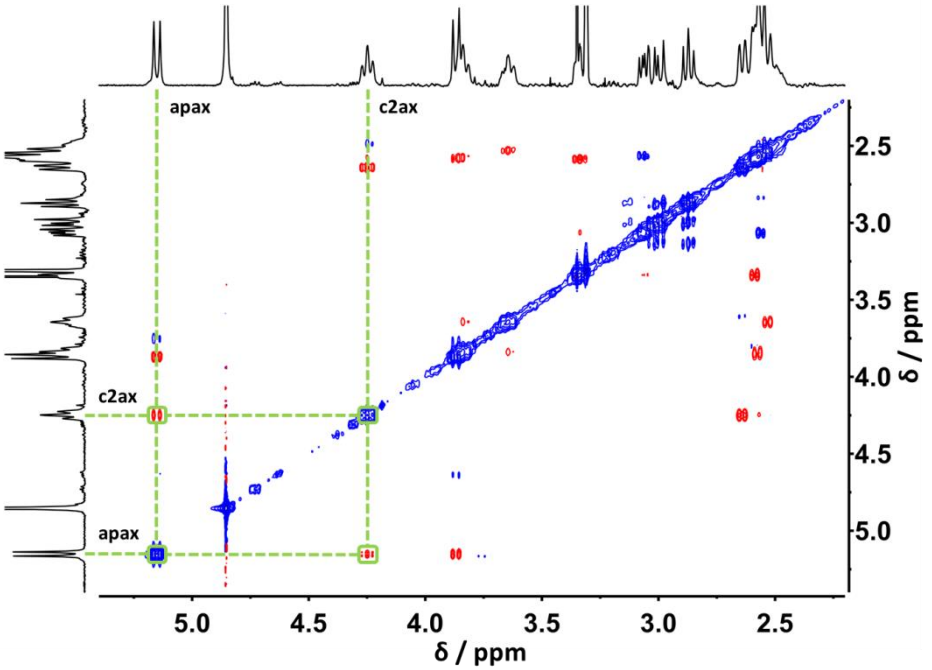

Figure 3.24 Aliphatic region of the ^{1}H-^{1}H NOESY NMR spectrum of **[YL^{5}]Cl** (14.1 T, 298 K, CD_3OD, 300 ms mixing time). The NOE cross-peak highlighted is that of the axial exocyclic pyridyl CH_2 proton (apax) with the axial, endocyclic proton of C2 (c2ax). This correlation is only possible in a TSAP structure. The other NOE cross peak observed for apax is to its diastereotopic proton apeq.

Through-space correlations were also observed between the benzylic protons and both H^{6} of the pyridine (py6) and the *tert*-butyl resonance (Figure 3.25). As with **[YL^{4}]**, the solution structure of the major diastereoisomer of **[YL^{5}]Cl** must be (RR)-Λ-(λλλλ), as revealed in the crystal structure analysis of **[YbL^{5}]PF$_6$**. DFT calculations predicted that the most stable solution structure was the other TSAP diasteroisomer (RR)-Δ-(δδδδ). However, the NOE signals observed in the solution NMR spectrum preclude this possibility. The DFT calculated relative energy between the two TSAP isomers was small (1.2 kJmol^{-1}).

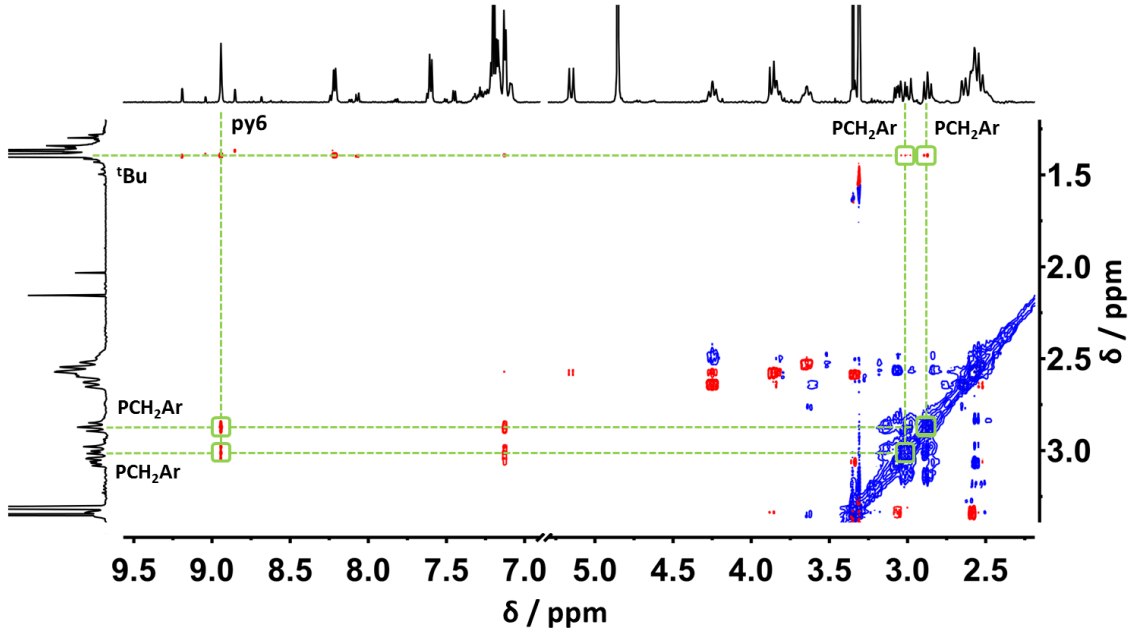

Figure 3.25 ^{1}H-^{1}H NOESY NMR spectrum of **[YL^{5}]Cl** (14.1 T, 298 K, CD_3OD, 300 ms mixing time). The NOE cross-peaks highlighted are those of the phosphinate benzylic CH_2 protons with the pyridine H^{6} (py6) and *tert*-butyl (tBu) resonance.

The previous ^{1}H NMR experiments of **[YL^{5}]Cl** revealed the presence of multiple diastereoisomers within the aromatic pyridine region. The H^{6} pyridine resonances overlapped least, and that enabled at least seven signals to be identified from the ^{1}H (Figure 3.26) and ^{1}H-^{1}H COSY spectra (Figure 3.16, page 113).

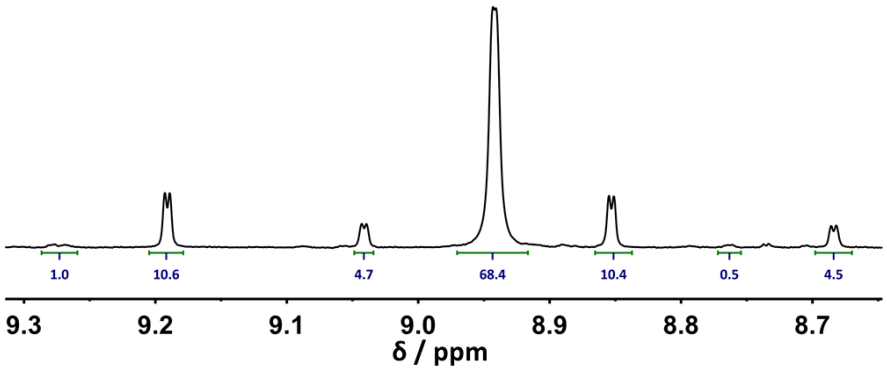

Figure 3.26 ^{1}H NMR spectrum of the pyridine H^{6} resonances of **[YL^{5}]Cl** (14.1 T, 298 K, CD_3OD). The integrals of each peak is shown as a % value.

^{1}H-^{1}H EXSY spectroscopy at two different mixing times was used to investigate the exchange between the observed resonances (Figure 3.27). The experiment showed that interconversion between all isomers does not occur on this timescale at 298 K.

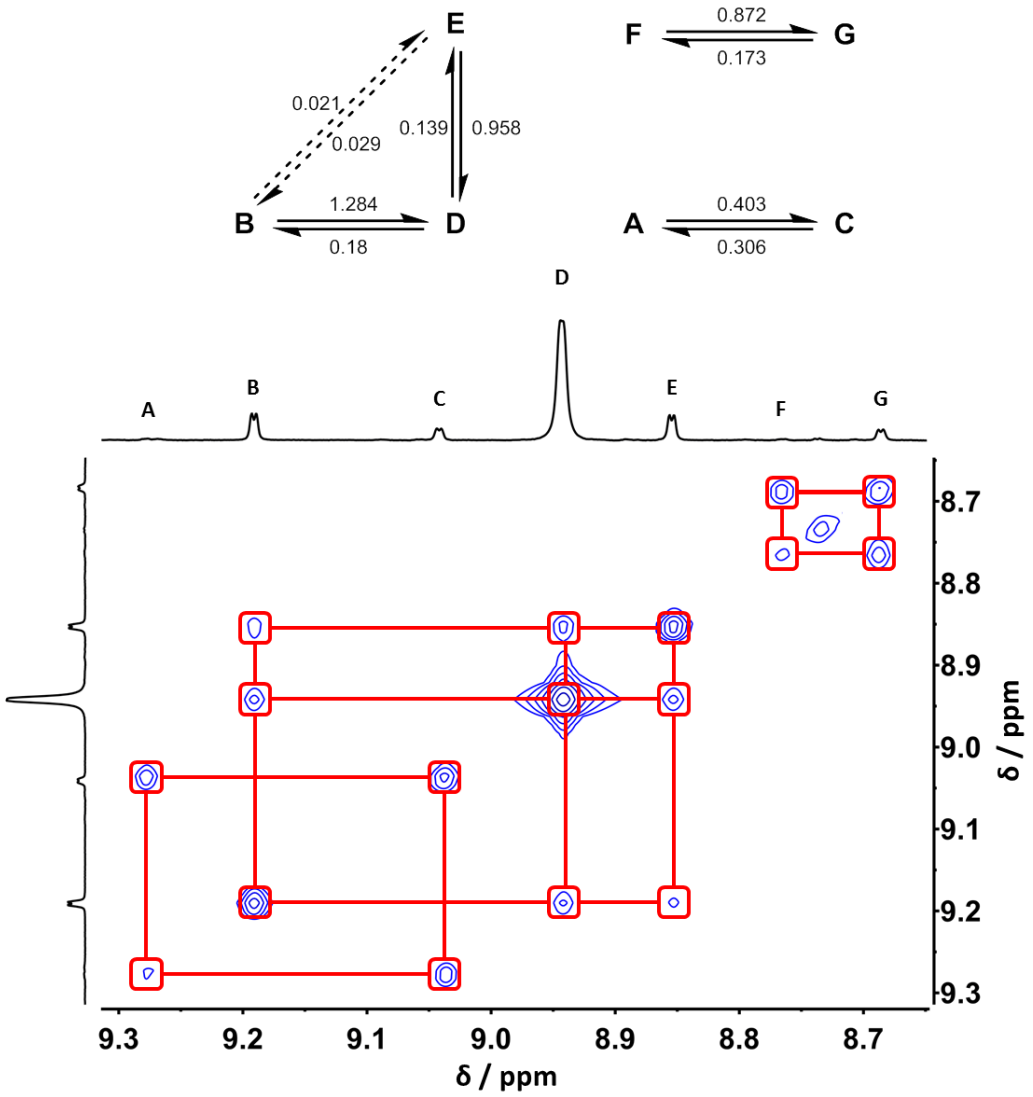

Figure 3.27 (*Top*) Forward and reverse reaction rates in s^{-1} for the isomers of py6 as calculated with EXSYCalc. (*Bottom*) Aromatic region of the ^{1}H-^{1}H NOESY NMR spectrum of **[YL^{5}]Cl** showing the H^{6} pyridine resonances (14.1 T, 298 K, CD_3OD, 300 ms mixing time).

Analysis of the 2D spectra using EXSYCalc quantified the rate of exchange between the diastereoisomers. The forward and reverse rates of the exchange of the isomers were broadly similar (k = 0.87 – 1.28 s^{-1}, k^{-1} = 0.14 – 0.18 s^{-1}) except for the pair A and C. Indeed, rates of these exchange processes are similar to those found for both **[YL^{4}]** and **[YL^{J}]**.

The major isomer, D, was found to exchange with both resonances B and E (Figure 3.27), which are of similar intensities in the ^{1}H NMR spectrum. A very weak correlation was seen between B and E, which may arise via indirect exchange involving the major isomer D.

3.4 Paramagnetic NMR studies of [YbL^4] and [YbL^5]Cl

3.4.1 Pseudocontact shift analysis of [YbL^4] and [YbL^5]Cl

The ^{1}H NMR spectrum of **[YbL^4]** revealed the presence of a major and minor isomer in a ratio of 13:1 (Figure 3.28). The proton resonances of the major isomer were observed between +150 to -75 ppm, with the *tert*-butyl group resonating at +20 ppm. Compared to the chemical shifts of the trimethylphosphinate complex **[YbL^J]** the benzylphosphinate pseudocontact shifts are slightly increased.[6] The *tert*-butyl chemical shift of the trimethylphosphinate analogue was observed at +16 ppm.

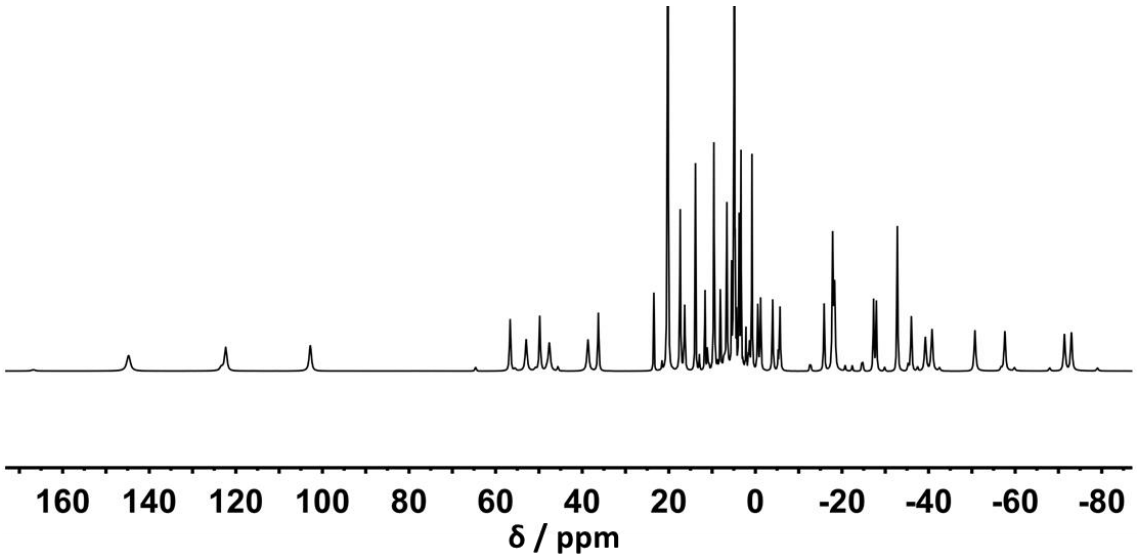

Figure 3.28 ^{1}H NMR spectrum of **[YbL^4]** (4.7 T, 295 K, CD_3OD).

Three major phosphorus resonances were observed in the ^{31}P spectrum of **[YbL^4]** found to be shifted to lower frequency (-30, -63 and -65 ppm) relative to the diamagnetic analogue **[YL^4]** (Figure 3.29). The minor isomer resonances were shifted similarly, in a ratio of 12:1, in close agreement with the value obtained from the integration of the fully relaxed ^{1}H NMR spectrum.

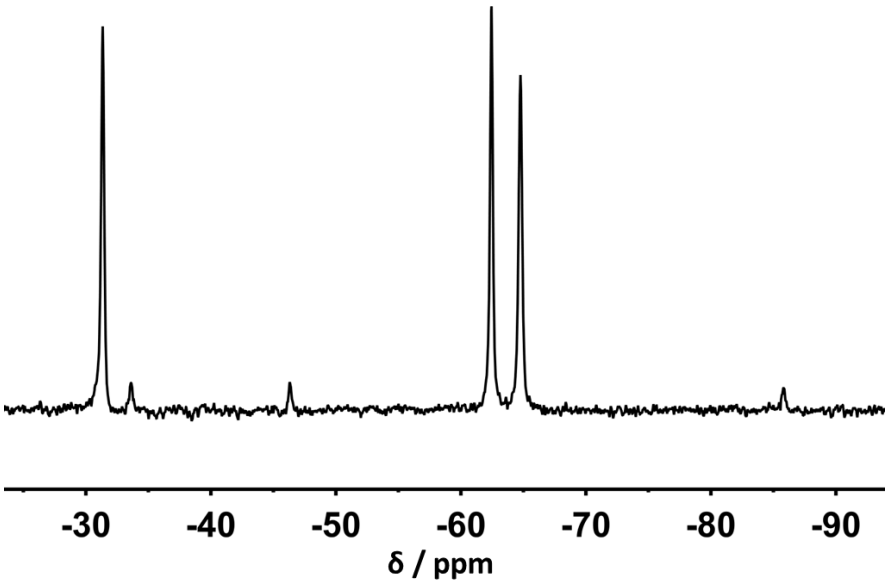

Figure 3.29 ^{31}P NMR spectrum of **[YbL^4]** (4.7 T, 295 K, CD_3OD).

The spectral range of the ^{1}H chemical shifts of the major isomer of **[YbL^5]Cl** (+65 to -50 ppm) was significantly decreased compared to that of **[YbL^4]** (Figure 3.30). The *tert*-butyl chemical shift (+9 ppm) has also decreased from the tri- to the dibenzylphosphinate complex. Analysis of the crystal and DFT optimised structures does not readily account for the large changes in the pseudocontact shifts as there is minimal structural variation between the complexes.

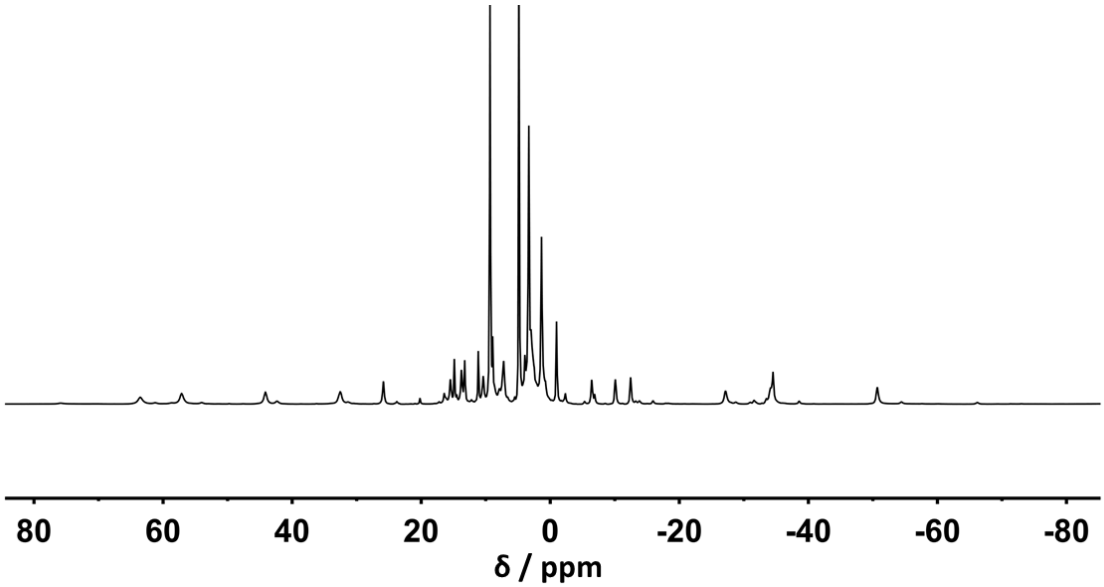

Figure 3.30 ^{1}H NMR spectrum of **[YbL^5]Cl** (4.7 T, 295 K, CD_3OD).

Quantifying the proportion of the major isomer from the ^{1}H spectrum was challenging. Analysis of the ^{31}P spectrum was simpler, as only five resonances were observed

(Figure 3.31). The major resonance represented around 80% of the signal. The two largest minor resonances were of equal intensity, as seen previously for py6 in the ^{1}H spectrum of **[YL^{5}]Cl**. Two equal intensity phosphorus resonances will arise from a diastereoisomer if it is asymmetric in solution. The phosphorus chemical shifts were all negatively shifted, with similar magnitudes to those seen for **[YbL^{4}]**.

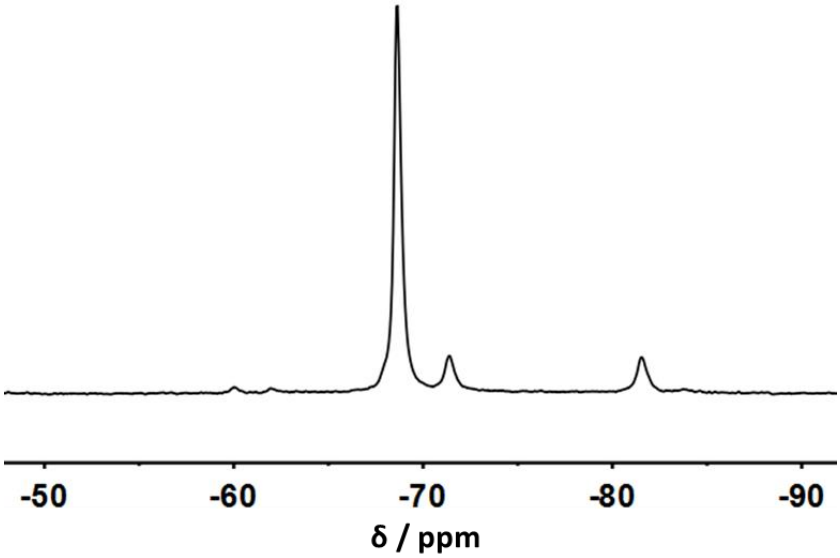

Figure 3.31 ^{31}P NMR spectrum of **[YbL^{4}]** (4.7 T, 295 K, CD_3OD).

In order to construct the PCS fields of **[YbL^{4}]** and **[YbL^{5}]Cl**, the chemical shifts, linewidths and longitudinal relaxation rates of every proton in each of the Yb^{3+} complexes were measured (4.7 T). A combinatorial assignment and fitting of the NMR data, excluding the benzyl resonances was achieved via a semi-automated procedure in Spinach 1.9, carried out by Dr Elizaveta A. Suturina (Bath University) using the DFT optimised structures of the (RRR)-Λ-(λλλλ) and (RR)-Λ-(λλλλ) complexes (Figure 3.32) (See Appendix, Tables S1 and S2).

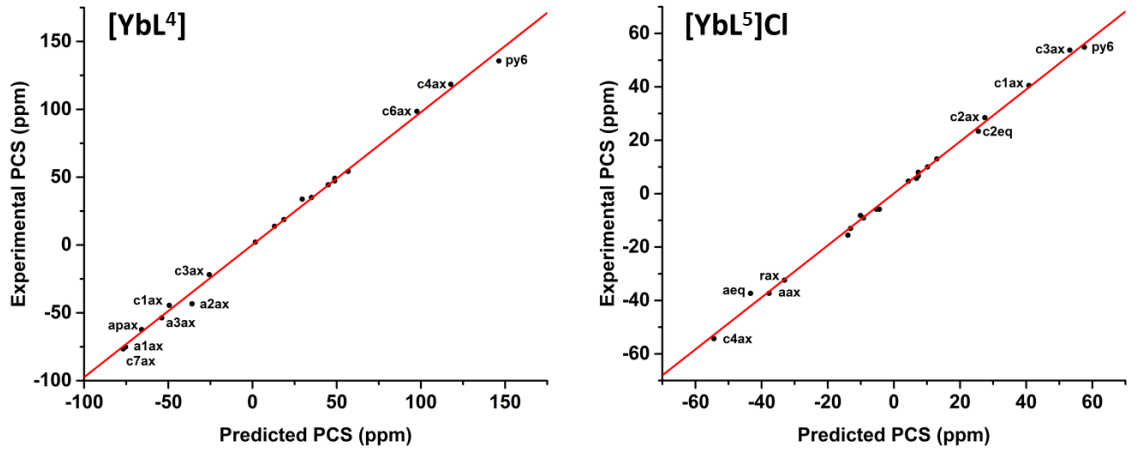

Figure 3.32 Comparison of the observed and 'best- fit' PCS values for **[YbL^4]** (*left*) (R^2 = 0.997) and **[YbL^5]Cl** (*right*) (R^2 = 0.997). Assignments of selected resonances have been highlighted; a full assignment can be found in the Appendix (Tables S1 and S2).

The 'best-fit' susceptibility tensors can be converted to axiality and rhombicity parameters together with three Euler angles, with respect to the molecular frame (Table 3.8). For each complex, the z axis of the molecular frame goes through the Yb^{3+} ion and the centre of the four nitrogen atoms of cyclen, the x axis points towards nitrogen N1 (a more detailed description of this method can be found in Section 5.7, pages 193-194).

Table 3.8 Magnetic susceptibility tensors for **[YbL^J]**, **[YbL^4]** and **[YbL^5]Cl** expressed in terms of axiality (χ_{ax}), rhombicity (χ_{rh}) and Euler angles.

Complex	χ_{ax} (Å^3)	χ_{rh} / χ_{ax}	α (deg)	β (deg)	γ (deg)
[YbL^J][a]	0.11	0.14	185	23	300
[YbL^4]	0.13	0.11	168	22	171
[YbL^5]Cl	-0.087	0.10	70	90	269

[a] In D_2O From reference[6]

The pseudocontact shift fields that were constructed from these values are shown in Figure 3.33. Comparing the susceptibility tensor fitting results of **[YbL^4]** to the trimethylphosphinate complex, **[YbL^J]**, reveals that the structural modification from methyl- to benzyl- phosphinates has minimal impact on the amplitude, shape and orientation of the PCS fields. The magnitude of the **[YbL^4]** PCS field is slightly increased from that of **[YbL^J]**. The tilt angle of the main anisotropy axis (angle β in Table 3.8) is near identical for both of the triphosphinate complexes (22° and 23°). The shape of the magnetic susceptibility tensor varies minimally between the complexes, and can be described to be between fully axial (χ_{rh} / χ_{ax} = 0) and fully rhombic (χ_{rh} / χ_{ax} = 0.33).

However, comparisons between **[YbL^4]** and **[YbL^5]Cl** reveal very large variations in the PCS fields. The magnetic anisotropy has changed sign, resulting in the negative PCS lobe being larger than the positive one. It would be expected from this result that the chemical shifts of the proton resonances in **[YbL^5]Cl** will be opposite in sign to those of **[YbL^4]**. However, the change in sign is also accompanied by an extremely large tilt angle, β (90°), which results in the negative PCS lobe being orientated in the equatorial plane of the molecule, as in **[YbL^4]**. This cooperative effect of the change in sign and angle begins to explain the large changes seen between the tri- and dibenzylphosphinate species.

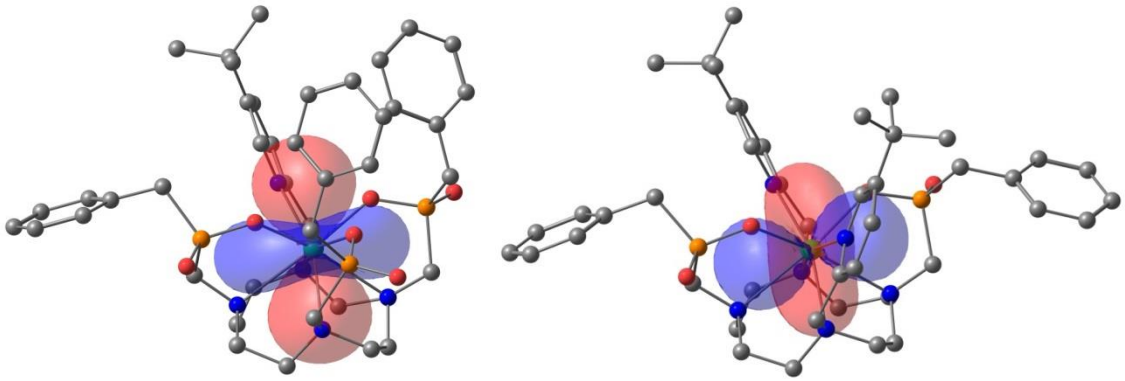

Figure 3.33 Pseudocontact shift (PCS) field reconstructed using the best fit susceptibility tensor for **[YbL^4]** (*left*) and **[YbL^5]$^+$** (*right*) created in Spinach by Dr Elizaveta A. Suturina. Positive PCS is shown in red, negative in blue.

Comparisons of the fitted magnetic susceptibility tensors of **[YbL^4]** and **[YbL^5]Cl** with that of **[YbL^J]** must regarded with some caution as the NMR data were measured in different solvents (D_2O vs CD_3OD).

3.5 Luminescence of [EuL^4] and [EuL^5]Cl in solution

The emission spectra of the complexes **[EuL^4]** and **[EuL^5]Cl** were measured in methanol at room temperature (Figure 3.34).

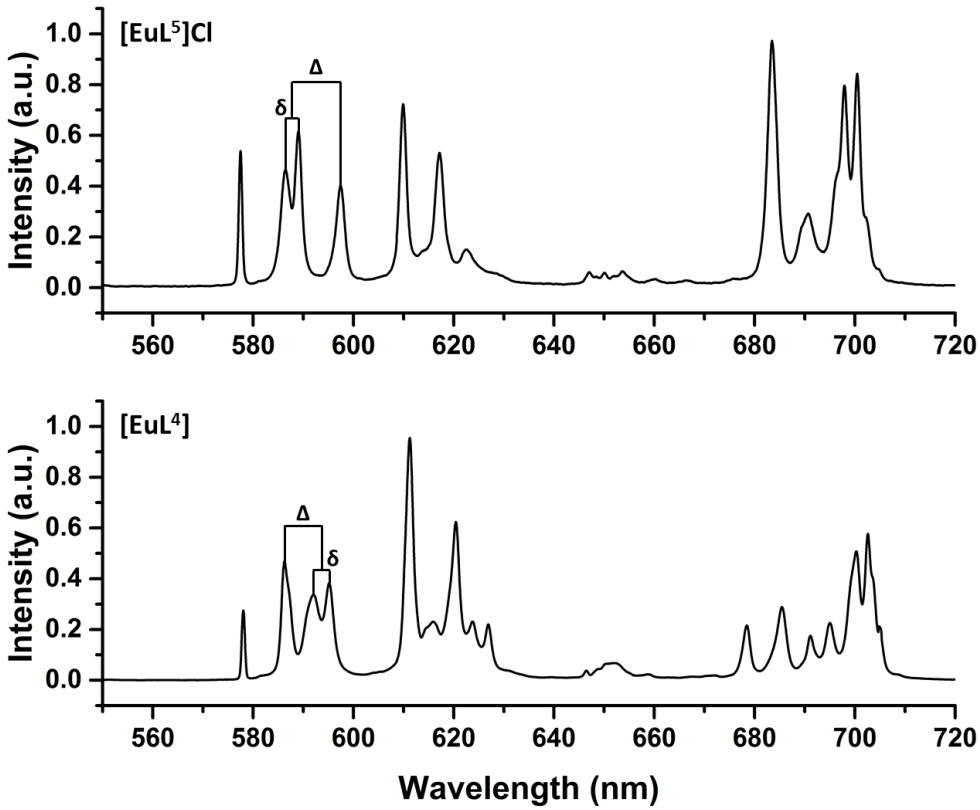

Figure 3.34 Emission spectra of **[EuL^4]** (*bottom*) and **[EuL^5]Cl** (*top*) with the splittings (Δ and δ) of the Δ*J* = 1 manifold highlighted (295 K, λ_{ex} = 276 nm, CH_3OH).

The fine structure of the Δ*J* = 1 band is controlled by the crystal field splitting of the excited $^7F_1$ level, as defined by the nature of the ligand.[14] In complexes with C_1 or C_2 symmetry the splitting Δ (cm^{-1}) = $-\frac{3}{5}B_0^2$ and δ (cm^{-1}) = $-\frac{2}{5}B_2^2$, in which the ligand field parameters are based on Stevens operators (Figure 3.34). The sign of Δ is positive if the singlet component is higher in energy than the doublet component (e.g. **[EuL^4]**). Generally, the analysis of emission spectra uses a different formulation of ligand field theory, and is described by spherical tensors. Conversion between the two formalisms is described by Equations 3.1 and 3.2.[14]

$$B_0^2[\text{Spherical Tensors}] = 2B_0^2[\text{Stevens Operators}] \quad (3.1)$$

$$B_2^2[\text{Spherical Tensors}] = \frac{2}{\sqrt{6}}B_2^2[\text{Stevens Operators}] \quad (3.1)$$

The ligand field parameters are given in terms of irreducible spherical tensors in Table 3.9. The B_0^2 value of **[EuL^4]** and B_2^2 values of both complexes are in good agreement with similar complexes previously reported, including that of the trimethylphosphinate species (-660 cm^{-1}, H_2O).[7,9] The very large positive value of the B_0^2 value of **[EuL^5]Cl** is

rather unusual but the change in sign is consistent with that seen from the analysis of the pseudocontact shift data of **[YbL^5]Cl** (Table 3.8, page 126).

Table 3.9 Ligand field parameters of **[EuL^4]** and **[EuL^5]Cl** in the spherical operator formalism.

Complex	Δ (cm^{-1})	δ (cm^{-1})	B_0^2 (cm^{-1})	B_2^2 (cm^{-1})
[EuL^4]	211	82	-703	-167
[EuL^5]Cl	-277	75	+923	-153

3.6 Paramagnetic NMR studies of [LnL^4] and [LnL^5]Cl

3.6.1 Pseudocontact shift analysis of [LnL^4] and [LnL^5]Cl

After the initial studies on the Yb^{3+} and Eu^{3+} complexes of **[LnL^4]** and **[LnL^5]Cl**, the investigation was extended to the remaining paramagnetic complexes (where Ln = Tm, Dy, Er, Ho, Tm and Yb). The shift and relaxation properties of the *tert*-butyl resonances of each complex were measured in CD_3OD. It has been previously shown that changes in the solvation of lanthanide complexes can have significant effects on the paramagnetic NMR behaviour[4] and hence direct comparisons to **[LnL^J]** must be cautious as these measurements were undertaken in D_2O. Chemical shift data of the major *tert*-butyl ^1H resonances of **[LnL^4]** and **[LnL^5]Cl** (Figure 3.35) showed that the change from tri- to dibenzyl phosphinate results in decreased pseudocontact shifts, as seen in the pH responsive complexes **[LnL^2]** and **[LnL^3]** (Figure 2.22, page 76). The *tert*-butyl reporter resonance is still found outside the diamagnetic region in each complex, except **[YbL^5]Cl** (+9.3 ppm).

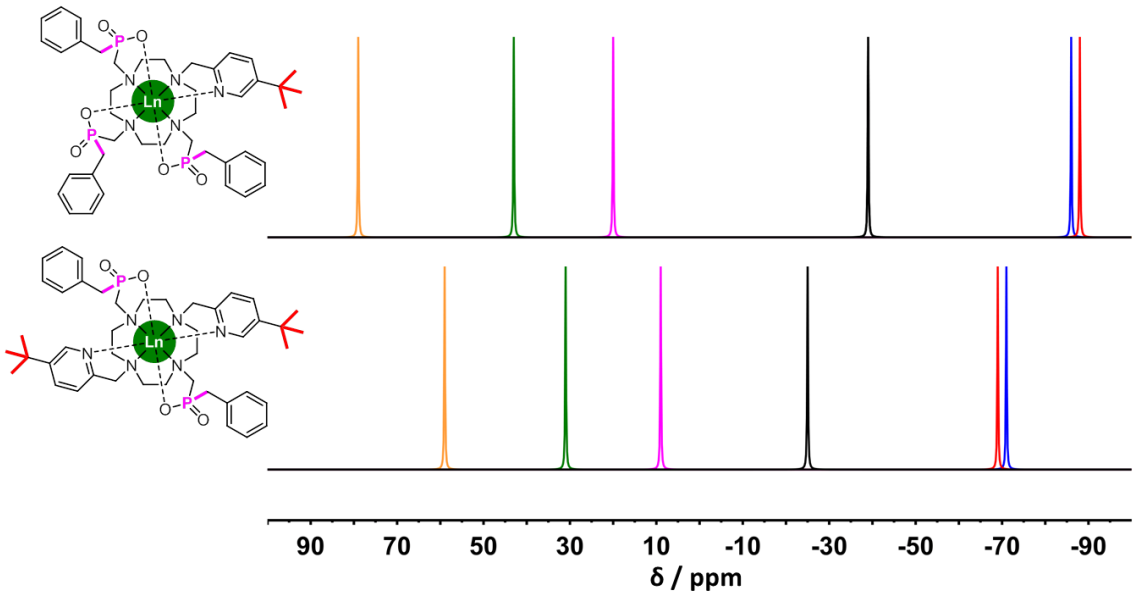

Figure 3.35 Schematic representation of the experimentally measured ^{1}H chemical shifts of the major *tert*-butyl signals in **[LnL^{4}]** (*top*) and **[LnL^{5}]Cl** (*bottom*) (MeOD, 11.7 T, 295 K, pD 7.4) (yellow - Tm, green - Er, magenta - Yb, black – Ho, red - Dy, blue - Tb).

As observed in the diamagnetic complex **[YL^{4}]**, the paramagnetic complexes of **L^{4}** exist in solution as two diastereoisomers in slow exchange on the NMR timescale. In each case the major isomer represented over 90% of the signal intensity in both the ^{1}H and ^{31}P spectra, suggesting that the sterically bulky benzyl groups destabilise the minor isomer in comparison to the smaller methyl groups of **[LnL^{J}]** (See Appendix, Figures S1 and S2). Similarly to the behaviour of the pH responsive dibenzylphosphinate complex **[LnL^{3}]**, multiple diastereoisomers were present in the ^{1}H spectra of **[LnL^{5}]Cl** (see Appendix, Figure S3), as identified by integration, linewidth analysis and longitudinal relaxation rates. However, due to the large number of proton resonances, the isomers of **[LnL^{5}]Cl** were best distinguished in the ^{31}P spectra (Figure 3.36). The phosphinate ^{31}P resonances for each **[LnL^{5}]Cl** complex are extremely broad and far shifted, ranging from +1350 ppm (Dy^{3+}) to -400 ppm (Tm^{3+}). A major single phosphinate resonance was seen for each complex, meaning that the major conformation possesses time-averaged C_2 symmetry. At least two minor phosphinate resonances were observed for each complex. In each case, except **[TbL^{5}]Cl**, the major diastereoisomer accounted for >50% of the phosphorus resonances as calculated by integration.

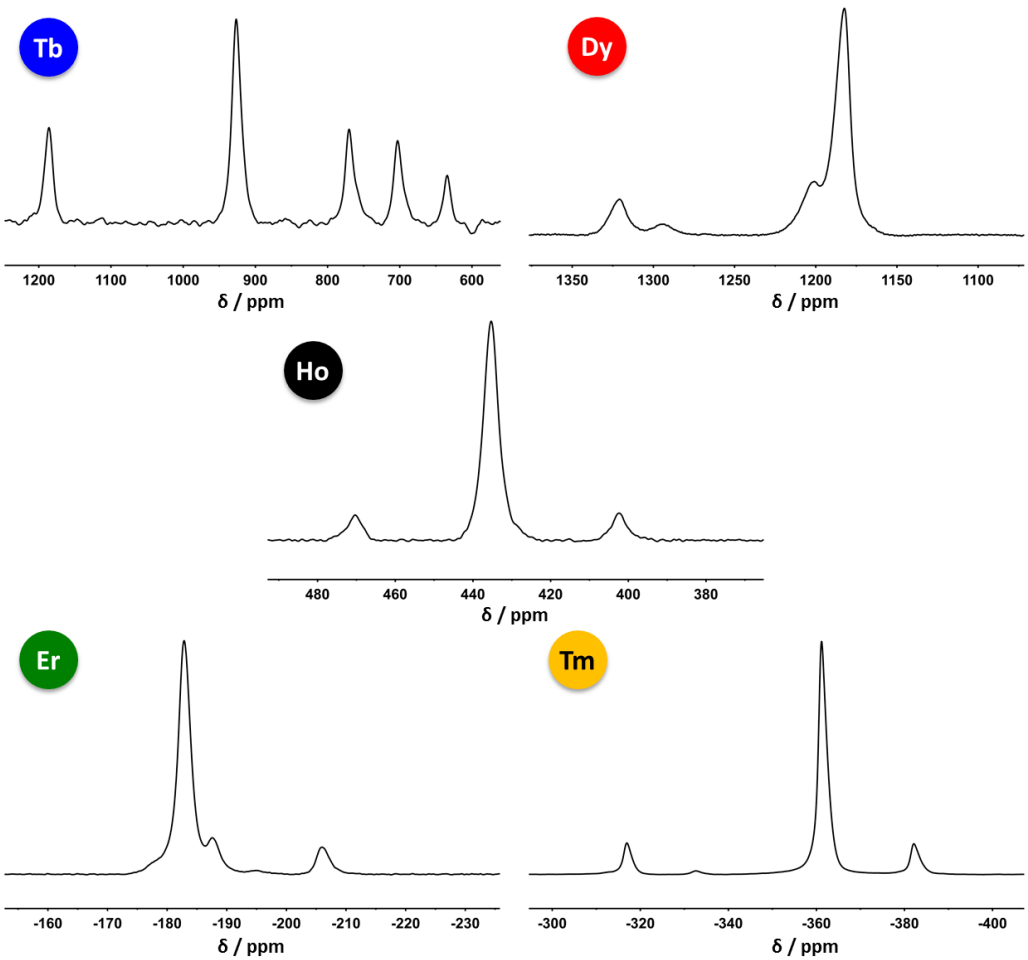

Figure 3.36 ^{31}P NMR spectra of the phosphinate resonances observed for **[LnL^5]Cl** (CD_3OD, 4.7 T, 295 K).

Analysis of the minor isomers found that the two largest of the minor phosphinate resonances gave similar integration values in each complex, as found previously in both **[YL^5]Cl** and **[YbL^5]Cl**. In the ^{31}P and ^{1}H spectra of **[TbL^5]Cl** the major isomer was proportionally smaller. Integration of the fully relaxed ^{31}P and ^{1}H spectra revealed a general trend that as the size of the complexed lanthanide(III) ion increases, the proportion of minor isomers increases with respect to the major diastereoisomer (Figure 3.37).

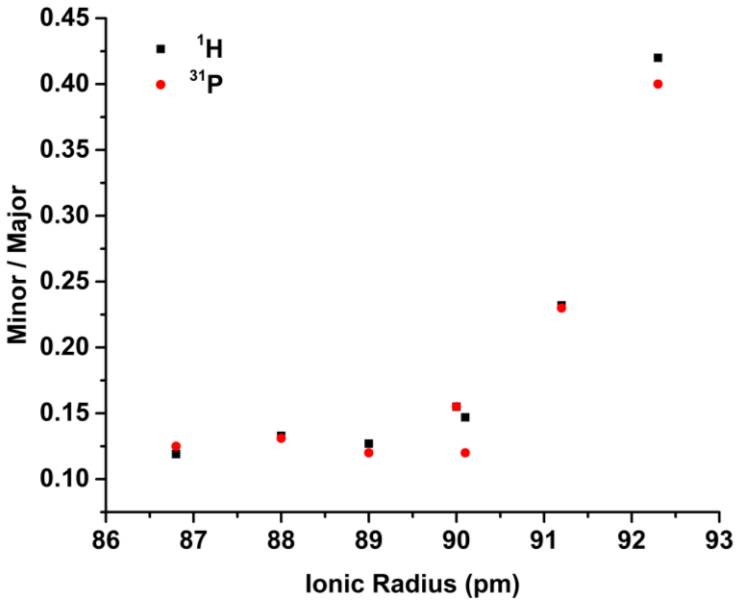

Figure 3.37 Variation in the ratio of the intensities of the ^{1}H *tert*-butyl and ^{31}P phosphinate resonances of the minor and major species of **[LnL^{5}]Cl** as a function of the lanthanide ionic radius (CD_3OD, 4.7 T).

Assignment and fitting of the ^{1}H shift data of the paramagnetic complexes of **[LnL^{4}]** and **[LnL^{5}]Cl** (excluding Ho^{3+}) with Spinach 1.9 was carried out by Dr Elizaveta A. Suturina (Bath University) (See Appendix, Tables S1 and S2). Susceptibility tensor fitting results revealed a significant variation in the amplitude, shape and orientation of the PCS fields across the series for each complex (Figure 3.38).

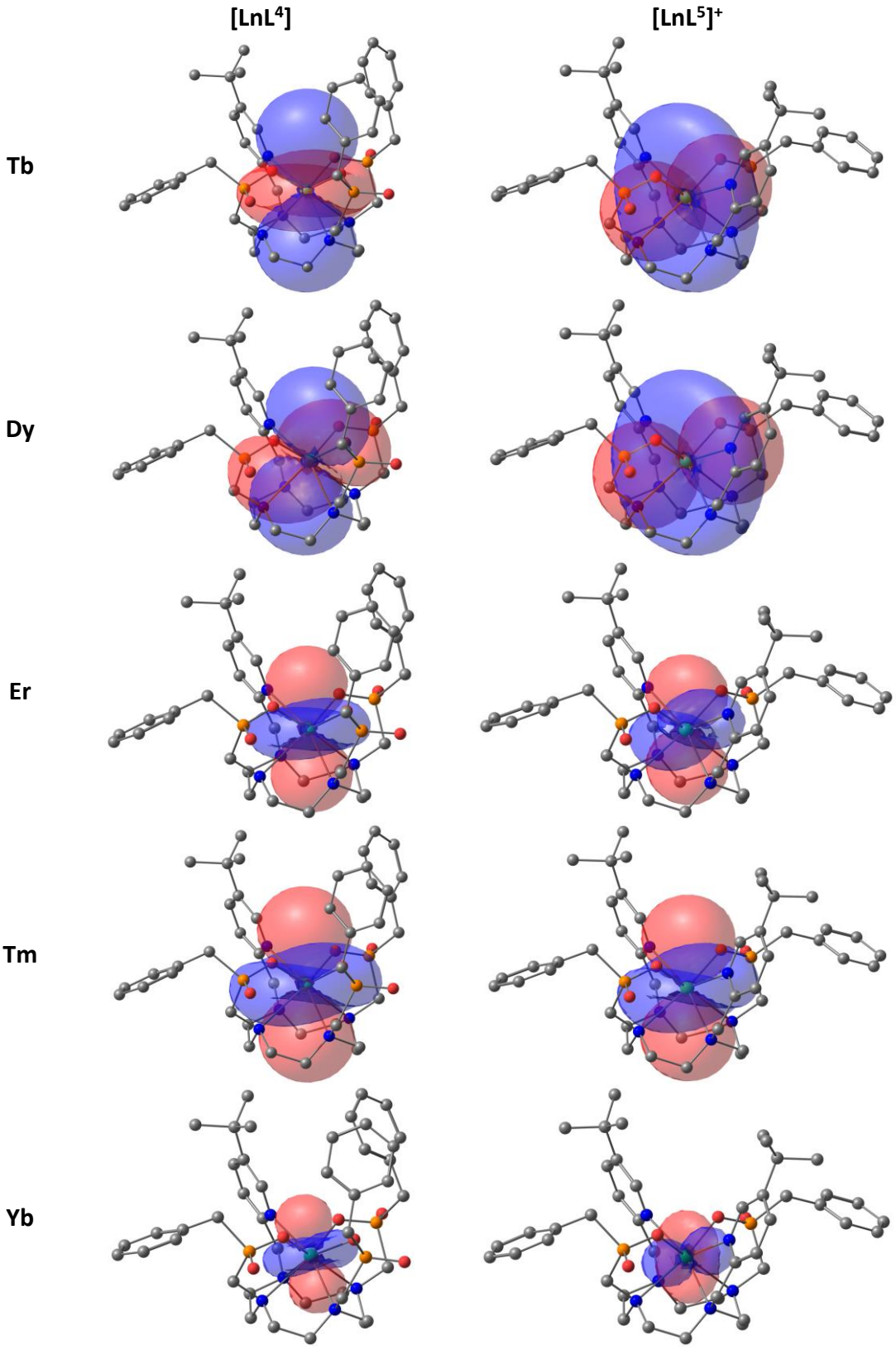

Figure 3.38 Pseudocontact shift (PCS) field reconstructed using the best fit susceptibility tensor for **[LnL^4]** (*left*) and **[LnL^5]$^+$** (*right*) created in Spinach by Dr Elizaveta A. Suturina. Positive PCS is shown in red, negative in blue.

The orientations of the major component of the magnetic susceptibility tensors, β, of the tribenzylphosphinate complex, **[LnL^4]**, were found to be generally similar to those

of the trimethylphosphinate complex, **[LnL^J]** (Table 3.10).[7] The negative lobe of the PCS field of **[TbL^4]** points much more directly at the *tert*-butyl reporter group compared to that of **[DyL^4]**. It is this orientation that explains why the chemical shift of the reporter group of the Tb^{3+} complex is as large as the Dy^{3+} complex despite having a lower Bleaney constant. The shape of the magnetic susceptibility tensors of the **[LnL^4]** varied compared to **[LnL^J]**.[7] **[TbL^4]** is found to be significantly less rhombic and **[TmL^4]** is less axial than their trimethylphosphinate analogues. However, **[DyL^4]** was calculated to be almost fully rhombic as found previously with **[DyL^J]**.

Table 3.10 Magnetic susceptibility tensors for **[LnL^4]** expressed in terms of axiality (χ_{ax}), rhombicity (χ_{rh}) and Euler angles.

Ln^{3+}	χ_{ax} (Å^3)	χ_{rh} / χ_{ax}	α (deg)	β (deg)	γ (deg)
Tb	-0.83	0.14	30	10	278
Dy	-0.70	0.29	174	16	338
Er	0.35	0.11	181	13	317
Tm	0.66	0.11	169	6	162
Yb	0.13	0.11	168	22	171

Table 3.11 Magnetic susceptibility tensors for **[LnL^5]$^+$** expressed in terms of axiality (χ_{ax}), rhombicity (χ_{rh}) and Euler angles.

Ln^{3+}	χ_{ax} (Å^3)	χ_{rh} / χ_{ax}	α (deg)	β (deg)	γ (deg)
Tb	0.84	0.088	242	90	101
Dy	0.95	0.015	249	90	76
Er	0.25	0.30	146	4	178
Tm	0.53	0.16	140	2	184
Yb	-0.087	0.10	70	90	269

The shape, amplitude and orientation of the PCS fields of **[LnL^5]$^+$** vary significantly from the tribenzylphosphinate complex (Table 3.11). The complexes **[DyL^5]$^+$** and **[TbL^5]$^+$** are almost ideally axial whilst **[ErL^5]$^+$** is almost fully rhombic.

Additionally, the sign of the PCS field is the opposite of that found with **[LnL^J]** and **[LnL^4]** for the Tb^{3+}, Dy^{3+} and Yb^{3+} complexes of **L^5**. In these complexes, the reversal in sign is accompanied by a 90° change in the orientation of the major component of the susceptibility tensor, β. The result of both of these effects is that the pseudocontact chemical shifts of these complexes remain the same sign as those in the triphosphinate complexes. These vast changes may be crudely ascribed to the change in symmetry from the triphosphinate (C_1) to the diphosphinate (C_2) complexes,

3.6.2 Relaxation rate analysis of [LnL^4] and [LnL^5]Cl

The longitudinal relaxation rates of the major *tert*-butyl resonances of **[LnL^4]** and **[LnL^5]Cl** were measured at six fields over the range 1 to 16.4 T (Tables 3.12 and 3.13).

Table 3.12 ^{1}H NMR longitudinal relaxation rate data for the *tert*-butyl resonance of **[LnL^4]** as a function of magnetic field (CD_3OD, 295 K).

Ln^{3+}	R_1 / Hz (± error)					
	1 T	**4.7 T**	**9.4 T**	**11.7 T**	**14.1 T**	**16.4 T**
Tb	37 (1)	49 (1)	73 (1)	85 (1)	98 (1)	109 (1)
Dy	42 (1)	58 (1)	90(1)	106 (1)	123 (1)	140 (1)
Ho	34 (2)	55 (1)	95 (1)	116 (1)	137 (1)	157 (1)
Er	83 (3)	93 (2)	119 (2)	136 (1)	153 (1)	170 (1)
Tm	24 (1)	70 (1)	113 (1)	130 (1)	146 (1)	160 (2)
Yb	12.2 (0.9)	11.7 (0.3)	12.4 (0.7)	12.7 (0.1)	13.1 (0.1)	13.5 (0.1)

Table 3.13 ^{1}H NMR longitudinal relaxation rate data for the *tert*-butyl resonance of **[LnL^5]Cl** as a function of magnetic field (CD_3OD, 295 K).

Ln^{3+}	R_1 / Hz (± error)					
	1 T	**4.7 T**	**9.4 T**	**11.7 T**	**14.1 T**	**16.4 T**
Tb	78 (1)	90 (1)	113 (1)	129 (1)	141 (1)	153 (1)
Dy	63 (1)	80 (1)	111 (1)	135 (1)	153 (1)	171 (1)
Ho	28 (1)	49 (1)	89 (1)	115 (1)	139 (1)	162 (1)
Er	71 (3)	66 (1)	87 (2)	111 (1)	133 (1)	153 (1)
Tm	11.4 (1)	35 (1)	67 (1)	85 (1)	98 (1)	111 (2)
Yb	10.4 (0.4)	10.3 (0.1)	9.2 (0.2)	9.7 (0.1)	9.7 (0.1)	10.9 (0.1)

Comparison of these rates showed that the structural change from tri- to dibenzylphosphinate induces very large changes in the relaxation behaviour (Figure 3.39). The longitudinal relaxation rates of **[TbL^5]Cl** are increased dramatically compared to its tribenzylphosphinate analogue, **[TbL^4]**. The effect is largest at lower magnetic fields, at 1 and 4.7 T the relaxation rate is increased by 110% and 84% respectively. Conversely, the opposite effect is seen for **[TmL^5]Cl**, in which the longitudinal relaxation rates are significantly slower, especially at lower fields.

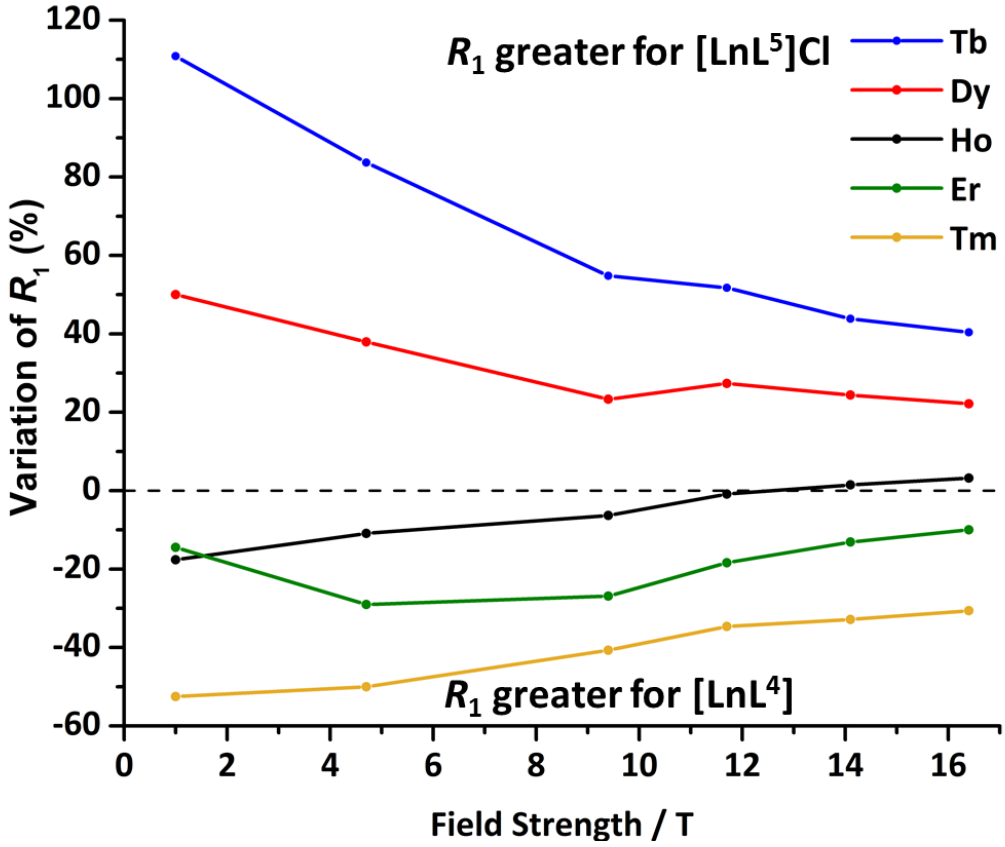

Figure 3.39 Variation of the longitudinal rates (R_1 / s^{-1}) of the major *tert*-butyl resonance from **[LnL^4]** to **[LnL^5]Cl** expressed as a percentage against the magnetic field for each lanthanide (CD_3OD, 295 K) (yellow - Tm, green - Er, black – Ho, red - Dy, blue - Tb).

The dipolar term of the SBM equation, for describing longitudinal relaxation rates (Equation 1.9, page 20), dominates the relaxation rate at low fields, and the dramatic changes seen at lower fields suggest that it is this term that is most affected by the structural change. In order to probe this issue further, the relaxation data were analysed by global minimisation methods assuming classical BRW theory (Figure 3.40 and Figure 3.41), and an average internuclear distance of 6.6 Å was used, as previously used in Chapter 1.

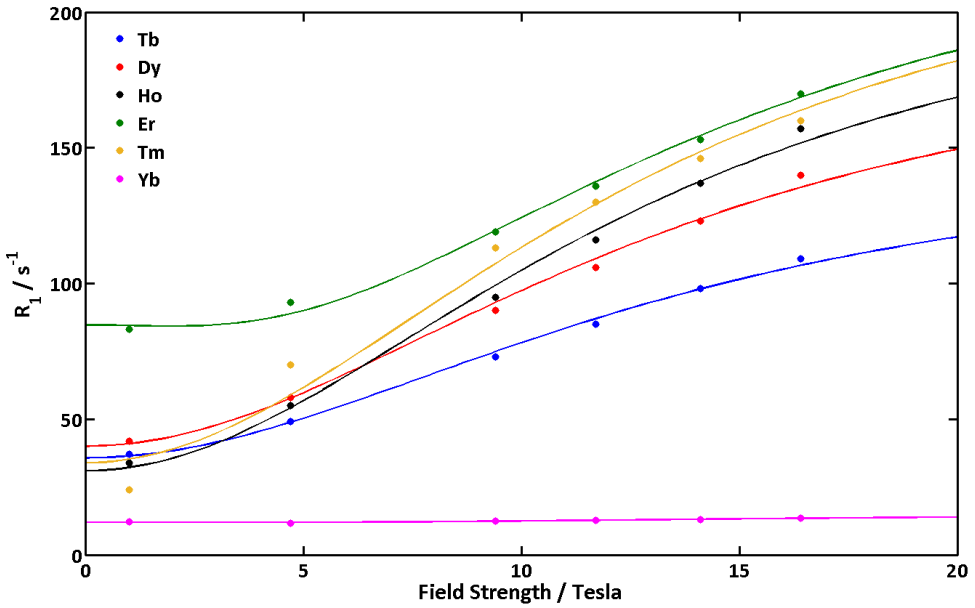

Figure 3.40 ^{1}H NMR relaxation rates (R_1 / s^{-1}) for the major *tert*-butyl resonance of **[LnL^4]** as a function of magnetic field, showing the global fits (line) to the experimental data points (CD_3OD, 295K, pD 7.4, fixed r = 6.6 Å, minimizes to τ_r = 286 (13) ps).

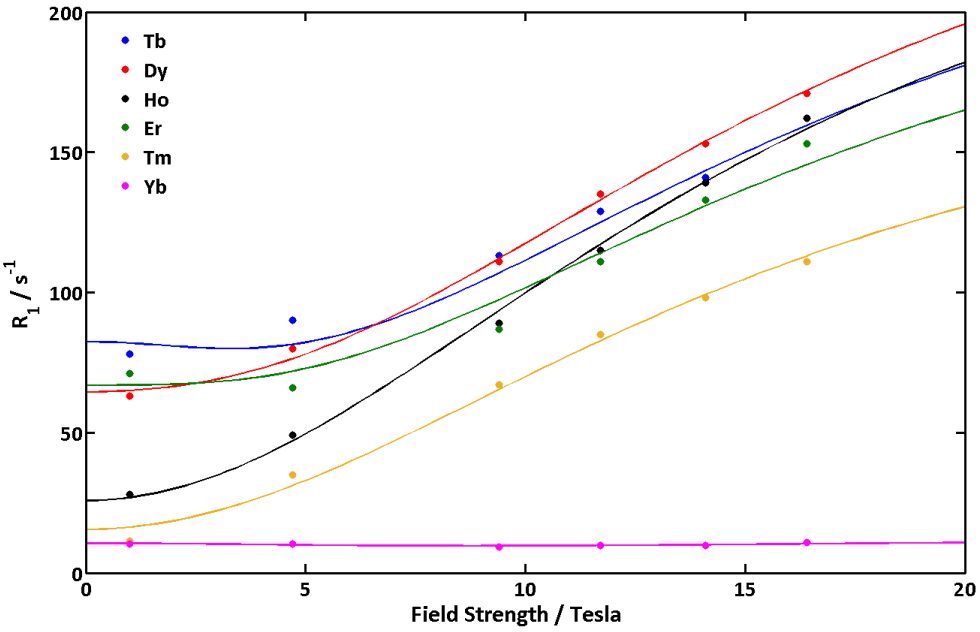

Figure 3.41 ^{1}H NMR relaxation rates (R_1 / s^{-1}) for the major *tert*-butyl resonance of **[LnL^5]Cl** as a function of magnetic field, showing the global fits (line) to the experimental data points (CD_3OD, 295K, pD 7.4, fixed r = 6.6 Å, minimizes to τ_r = 240 (19) ps).

The global fits of **[LnL^4]** and **[LnL^5]Cl** were generally reasonable. However, the data for the tribenzylphosphinate complex **[TmL^4]** did not fit well, especially at lower fields. In the case of the dibenzylphosphinate complexes, **[TbL^5]Cl** and **[ErL^5]Cl** were found to fit poorly; this effect was, yet again, most apparent at lower fields. These results suggest that there is an additional factor determining the relaxation rates at lower fields that BRW theory fails to account for.

The fitting process gave rotational correlation times for **[LnL^4]** and **[LnL^5]Cl**, of 286 (±13) and 240 (±19) ps respectively. The value of τ_r is decreased from the analogous phosphonated complexes, **[LnL^2]** and **[LnL^3]** (400 (±15) and 418 (±8)). The decrease can be rationalised by the reduced mass and smaller solution solvation shell of **[LnL^4]** and **[LnL^5]Cl** and the significant reduction in solvent viscosity from water to methanol.

The electronic relaxation times, τ_e, and effective magnetic moments, μ_{eff}, were also fitted individually for each lanthanide(III) complex (Table 3.14). The values of μ_{eff} for **[DyL^5]Cl**, **[TbL^5]Cl** and **[HoL^5]Cl** increase compared to the analogous complexes of **[LnL^4]**. In contrast the dibenzylphosphinate complexes of Er^{3+}, Tm^{3+} and Yb^{3+}, have decreased μ_{eff} values. As demonstrated by Figure 3.39 the structural change has the largest effect at lower fields (> 4.7 T), suggesting the dipolar term and therefore the electronic relaxation time is most impacted. The fitted values of τ_e show this clearly, with the estimated values for **[TbL^5]Cl** and **[DyL^5]Cl** increasing, by 94% and 44% respectively, compared to the tribenzylphosphinate complex. The decrease in relaxation of **[ErL^5]Cl** and **[TmL^5]Cl** is reflected in the decreased τ_e values. As seen in Figure 3.39, the relaxation rate of **[HoL^4]** is faster at fields below 12 T, and this can be associated with the modest (-17%) decrease in the value of τ_e of **[HoL^5]Cl**. However, above 12 T this trend is reversed as the increase in μ_{eff} becomes dominant.

Table 3.14 Estimated 'best-fit' values for ^{1}H NMR relaxation parameters of **[LnL^4]** and **[LnL^5]Cl** following global fitting with fixed r = 6.6 Å (CD_3OD, 295 K, pD 7.4).[a]

Ln^{3+}	τ_e / ps		μ_{eff} / BM[a]	
	[LnL^4]	[LnL^5]Cl	[LnL^4]	[LnL^5]Cl
Tb	0.48	0.93	8.68	9.49
Dy	0.47	0.68	9.27	9.77
Ho	0.34	0.28	9.61	9.70
Er	0.91	0.78	9.70	9.30
Tm	0.36	0.20	9.80	8.93
Yb	0.55	0.58	4.69	4.27

[a] Theoretical values for the magnetic moments of the lanthanide(III) ions are: Tb, 9.7; Dy, 10.6; Ho, 10.6; Er, 9.6; Tm, 7.6; Yb, 4.3 BM.

3.7 Conclusions and Future Work

In order to develop and optimise ^{1}H PARASHIFT probes for MRSI *in vivo*, an understanding of the structure, solution dynamics and magnetic anisotropy of existing probes is required. The novel lanthanide complexes of the benzylphosphinate macrocycles **L^{4}** and **L^{5}** are prototypical examples of agents that are being developed.

The solution structure of the major isomers of each complex have been identified by studies of the related diamagnetic Y^{3+} complexes. The major species of complexes **[YL^{4}]** and **[YL^{5}]Cl** is observed to be the same eight-coordinate TSAP conformation (R)-Λ-(λλλλ) in both solution and the solid state. As seen with similar triphosphinate complexes,[6] **[LnL^{4}]** undergoes a chemical exchange process with a single minor isomer in solution. NMR exchange spectroscopy revealed similar exchange rates compared with the previously published trimethylphosphinate complex **[LnL^{J}]**. Due to the different isomer ratios, **[YL^{4}]** represents a SNR improvement as the equilibrium constant of the major isomer is larger for the benzyl appended complex. The behaviour of the dibenzylphosphinate complex **[YL^{5}]Cl** is different, and multiple isomers are observed in both the ^{1}H and ^{31}P spectra. DFT calculations suggest that the different isomers of **[LnL^{5}]$^{+}$** are closer in energy and the overall conformational flexibility of the ligand is greater.

Analysis of the pseudocontact chemical shift behaviour of the *tert*-butyl resonances of the paramagnetic species of **L^{4}** and **L^{5}** demonstrated that whilst the sign of the shift remains the same, the magnitude decreases from tri- to dibenzylphosphinate. The reduction in pseudocontact shift was not consistent across the lanthanide series, evidence that the degree of anisotropy and orientation of its major component varies for the isostructural complexes.

The paramagnetic ^{1}H NMR spectra of **[YbL^{4}]** and **[YbL^{5}]Cl** have been analysed and assigned allowing the fitting of the magnetic susceptibility tensors. In the case of the tribenzylphosphinate complex, the magnetic anisotropy was observed to be quite similar to the trimethylphosphinate complex. In contrast, the magnetic anisotropy of the dibenzylphosphinate Yb^{3+} complex changes sign. However, this dramatic change is balanced out by the orientation of the susceptibility rotating by 90°. The result of this

is that whilst the negative PCS lobe is now bigger than the positive, it remains orientated in the equatorial plane of the molecule. Evidence of the change in sign of the magnetic anisotropy of **[LnL^5]Cl** was found from analysis of corresponding Eu^{3+} complex emission spectra. Analysis of the $\Delta J = 1$ band reveals that the crystal field parameter B_0^2 indeed changes sign from the tri- to dibenzylphosphinate complex.

The fitting procedure was continued for the remaining paramagnetic Ln^{3+} complexes of **L^4** and **L^5** (excluding Ho^{3+}), which demonstrated that the shape, sign, orientation and magnitude of the magnetic susceptibility tensor varies unpredictably even within an isostructural series of complexes. Similarly to **[YbL^5]Cl**, the magnetic anisotropy of the dibenzylphosphinate complexes of Dy^{3+} and Tb^{3+} were found to be of the opposite sign, but orientated by 90° to that fitted for the analogous tribenzylphosphinate species. The vast differences between the PCS fields of **[LnL^4]** and **[LnL^5]Cl** could possibly arise from the change in symmetry between the complexes. Assignment and fitting of the proton resonances of the paramagnetic complexes **[HoL^4]** and **[HoL^5]Cl** would enable the construction of the PCS fields across the complete series. The large changes to the PCS fields of **[LnL^4]** and **[LnL^5]Cl**, induced by modification from tri- to dibenzylphosphinate, were not readily predicted. Similar analysis on a variety of complexes, with different geometries and symmetries may enable trends to be identified.

The structural change also induced relaxation rate changes, the longitudinal relaxation rates of the Tb^{3+} and Dy^{3+} complexes of **L^5** were observed to be faster than those of **L^4**. Conversely, the R_1 values of **[HoL^5]Cl, [ErL^5]Cl** and **[TmL^5]Cl**, were found to be lower than those of the analogous tribenzylphosphinate complexes. In both cases this effect was found to be largest at lower fields (< 4.7 T), suggesting that the change in structure has a larger impact on the electronic relaxation time, rather than the magnetic moment, of the lanthanide ion. More in-depth analysis of the relaxation rates of all the proton resonances of **[LnL^4]** and **[LnL^5]Cl** should be explored in order to further examine the anisotropy of the paramagnetically induced relaxation rate of different lanthanide complexes. This may explain the significant variations of longitudinal relaxation rates in the Tb^{3+} and Tm^{3+} complexes of **[LnL^4]** and **[LnL^5]Cl**.

The results shown in this thesis demonstrate the difficulty in predicting the NMR properties of a particular PARASHIFT probe, even when making seemingly minor ligand modifications. In the example of modification from a tri- to diphosphinate complex, initial analysis of the *tert*-butyl reporter chemical shifts suggests only a minor change in the lanthanide anisotropy. However, in-depth analysis demonstrates that both a change in sign and orientation of the PCS field is occurring. When looking only at the chemical shift of the reporter resonance these two variations mostly cancel each other out but may be causing the dramatic changes in relaxation.

3.8 References

1 O. A. Blackburn, N. F. Chilton, K. Keller, C. E. Tait, W. K. Myers, E. J. L. McInnes, A. M. Kenwright, P. D. Beer, C. R. Timmel and S. Faulkner, *Angew. Chem. Int. Ed.*, 2015, **54**, 10783–10786.

2 N. J. Rogers, K.-L. N. A. Finney, P. K. Senanayake and D. Parker, *Phys. Chem. Chem. Phys.*, 2016, **18**, 4370–4375.

3 G. Castro, M. Regueiro-Figueroa, D. Esteban-Gómez, P. Pérez-Lourido, C. Platas-Iglesias and L. Valencia, *Inorg. Chem.*, 2016, **55**, 3490–3497.

4 M. Vonci, K. Mason, E. A. Suturina, A. T. Frawley, S. G. Worswick, I. Kuprov, D. Parker, E. J. L. Mcinnes and N. F. Chilton, *J. Am. Chem. Soc.*, 2017, **139**, 14166-14172

5 K. Mason, A. C. Harnden, C. W. Patrick, A. W. J. Poh, A. S. Batsanov, E. A. Suturina, M. Vonci, E. J. L. McInnes, N. F. Chilton and D. Parker, *Chem. Commun.*, 2018, **54**, 8486–8489.

6 K. Mason, N. J. Rogers, E. A. Suturina, I. Kuprov, J. A. Aguilar, A. S. Batsanov, D. S. Yufit and D. Parker, *Inorg. Chem.*, 2017, **56**, 4028–4038.

7 D. Parker, I. Kuprov, E. Suturina, K. Mason and C. Geraldes, *Angew. Chem. Int. Ed.*, 2017, 12215–12218.

8 E. A. Suturina, K. Mason, C. F. G. C. Geraldes, N. F. Chilton, D. Parker and I. Kuprov, *Phys. Chem. Chem. Phys.*, 2018, **20**, 17676–17686.

9 A. M. Funk, K.-L. N. A. Finney, P. Harvey, A. M. Kenwright, E. R. Neil, N. J. Rogers, P. K. Senanayake and D. Parker, *Chem. Sci.*, 2015, **6**, 1655–1662.

10 E. R. Neil, M. A. Fox, R. Pal, L.-O. O. Pålsson, B. A. O'Sullivan and D. Parker, *Dalton Trans.*, 2015, **44**, 14937–14951.

11 M. Foroozandeh, R. W. Adams, N. J. Meharry, D. Jeannerat, M. Nilsson and G. A. Morris, *Angew. Chem. Int. Ed.*, 2014, **53**, 6990–6992.

12 J. A. Aguilar, J. Cassani, M. Delbianco, R. W. Adams, M. Nilsson and G. A. Morris, *Chem. A Eur. J.*, 2015, **21**, 6623–6630.

13 L. Di Bari, G. Pintacuda, P. Salvadori, R. S. Dickins and D. Parker, *J. Am. Chem. Soc.*, 2000, **122**, 9257–9264.

14 C. Görller-Walrand and K. Binnemans, in *Handbook on the Physics and Chemistry of Rare Earths 23*, 1996, pp. 121–283.

4. Development of zinc responsive PARASHIFT probes

Metal cations are essential for life, are associated with numerous biological signalling pathways and are found in countless enzymes and proteins. Zinc (Zn^{2+}) is the second most abundant transition metal ion, after iron, in the body. Most biological Zn^{2+} is tightly bound within metalloproteins and plays a key role in enzymatic catalysis and structural organisation. However, Zn^{2+} has also been found to be an important signalling ion and relatively high concentrations of free Zn^{2+} (μM) can be present extracellularly in several organs (e.g. the pancreas and prostate gland) in the body.[1] Disruption of normal Zn^{2+} homeostasis is associated with many diseases, such as diabetes and prostate disease. Elevated levels of zinc in the brain have been linked to certain neurodegenerative disorders, including Alzheimer's disease.

The abundance and importance of Zn^{2+} in biology has led to the development of many chemical sensors, most commonly based on fluorescence detection.[2,3] Typically these sensors are small molecular probes, such as the cell-permeable probe Zinpyr-1 described by Lippard and Tsien (Figure 4.1),[4] and contain a fluorescent reporting group appended with selective Zn^{2+} chelators. The most frequently used chelator incorporated into Zn^{2+} sensors is bis(2-pyridylmethyl)amine, also known as dipicolyamine (DPA). DPA forms an extremely stable complex with Zn^{2+} (K_d = 158 nM)[5] and has no measurable affinity for other biological, divalent cations, such as Ca^{2+} and Mg^{2+}.[6]

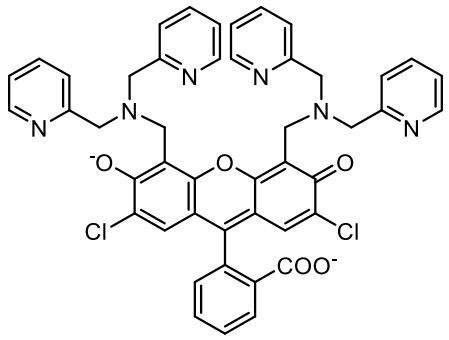

Figure 4.1 Structure of the fluorescent Zn^{2+} sensor Zinpyr-1.

Zn^{2+} sensors for MRI have also been designed. Typically they are Gd^{3+}-based complexes with relaxivity values that vary as a function of Zn^{2+} concentration.[7,8]

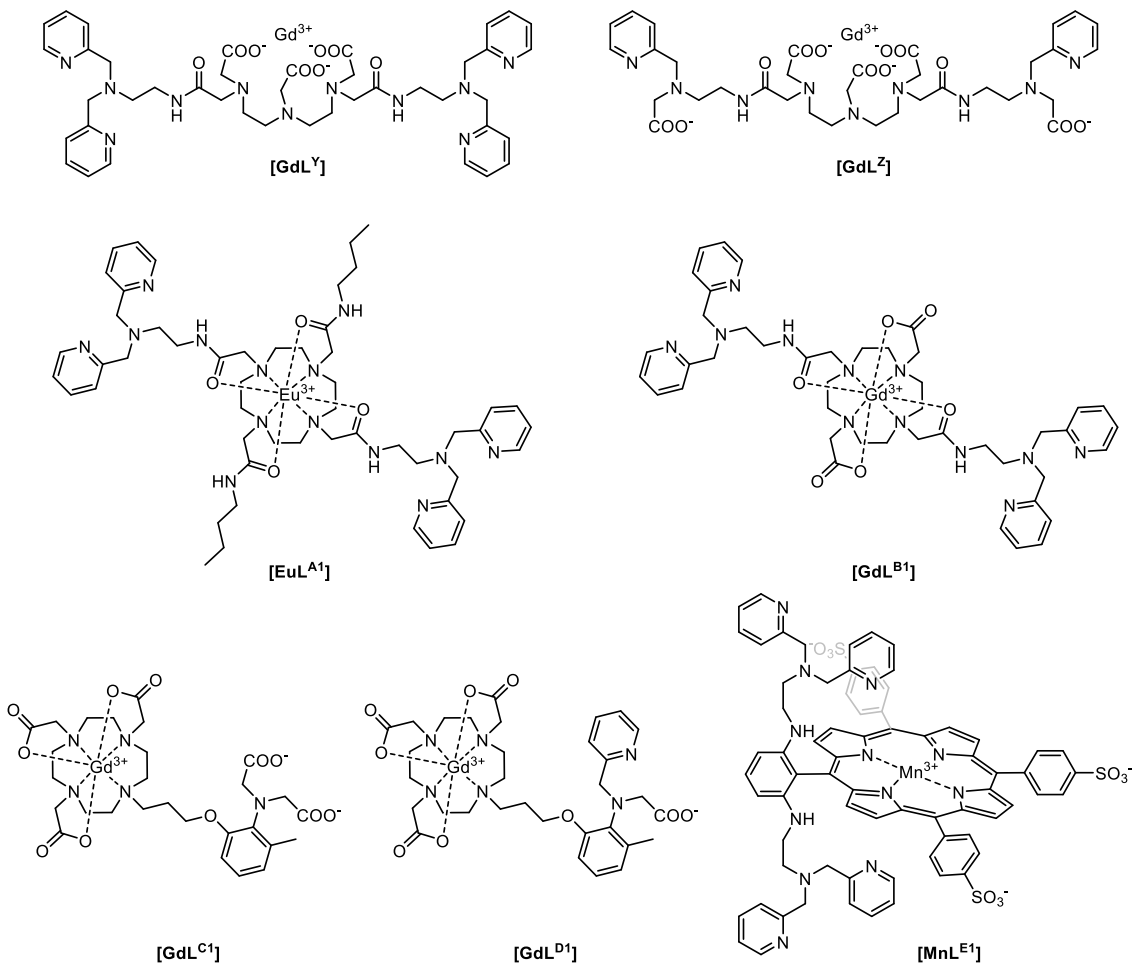

Figure 4.2 Examples of MRI-based Zn^{2+} sensors.

Nagano and co-workers designed the first Zn^{2+} sensing MRI probe, based on a Gd-DTPA backbone appended with two DPA moieties, **[GdL^{Y}]** (Figure 4.2).[9] Upon addition of up to 1 equivalent of Zn^{2+}, the relaxivity of the complex decreased by 33%. In the resulting 1:1 complex, Zn^{2+} is coordinated by both DPA units. The hydrophobic pyridine moieties sterically limit the access of water to the Gd^{3+} ion, resulting in a decrease in relaxivity. However, this change is reversed upon the further addition of Zn^{2+} as a less sterically demanding 2:1 complex forms at higher concentrations. The replacement of one pyridine unit of each DPA moiety by a carboxylate group, **[GdL^{Z}]** (Figure 4.2) circumvented this problem as the 2:1 complex was no longer favoured, meaning the 30% relaxivity decrease was maintained, even after addition of excess Zn^{2+}.[10] Both of these sensors displayed high selectivity for Zn^{2+} as no relaxivity changes were induced upon addition of Mg^{2+} or Ca^{2+}.

Sherry and co-workers developed an Eu^{3+} PARACEST probe for the selective sensing of Zn^{2+}, based upon a cyclen-tetraamide macrocycle appended with two DPA moieties,

[EuL^{A1}] (Figure 4.2).[11] Following addition of Zn^{2+}, the CEST magnitude of the exchanging inner sphere water molecule decreased and this behaviour was attributed to a faster exchange rate. Phantom imaging demonstrated selectivity against Mg^{2+} and Ca^{2+}. However, the loss of the CEST signal was also found to be pH dependent, and a marked temperature dependence of the chemical shift of this resonance was also observed.

The PARACEST probe, **[EuL^{A1}]**, was modified to create a Gd^{3+}-based relaxivity probe, in which two of the amides were replaced with carboxylates, **[GdL^{B1}]** (Figure 4.2).[12] A modest increase (20%) in relaxivity was observed with the addition of Zn^{2+} until 2 equivalents had been added. The increase in relaxivity was suggested be due to the presence of the Zn^{2+} cation promoting faster water exchange rates at the Gd^{3+} ion. When the same addition of Zn^{2+} was performed in the presence of human serum albumin (HSA), a significantly larger increase (165%) in the relaxivity was observed. Fluorescent displacement experiments indicated that the 2:1 Zn^{2+}_2:**[GdL^{B1}]** complex binds strongly to HSA, whereas the **[GdL^{B1}]** complex alone binds weakly. The increase in relaxivity in the presence of HSA was therefore attributed to an increase in the rotational correlation time for the complex when bound to the large protein. *In vivo* studies demonstrated that the complex could be used to monitor the glucose-stimulated co-release of Zn^{2+} with insulin from pancreatic β-cells.[13] It was shown that mice on high-fat diets displayed higher contrast enhancement upon injection of glucose and **[GdL^{B1}]**, consistent with pancreatic expansion and concomitant increase in β-cell function. More recently the same complex was investigated for the detection of the release of Zn^{2+} in the prostate.[14]

GdDO3A-based Zn^{2+} sensors were investigated by Meade and co-workers, **[GdL^{C1}]** and **[GdL^{D1}]** (Figure 4.2), in which the relaxivity increased upon the binding of Zn^{2+}.[15,16] The aminoacetate groups in **[GdL^{C1}]** were ^{13}C-labeled providing direct evidence of carboxylate binding to the paramagnetic centre, in the absence of Zn^{2+}. In the free complex, Gd^{3+} is coordinatively saturated and thus has a low relaxivity. Upon addition of Zn^{2+}, the relaxivity increases by over 100%. *In vitro* phantom images, obtained at 4.7 T, demonstrated selectivity for Zn^{2+} over Ca^{2+} and Mg^{2+}.

Lippard and co-workers designed a dual-function Mn^{2+}-based probe for MRI and fluorescence, **[MnL^{E1}]** (Figure 4.2).[17] The fluorescence and relaxivity of the porphyrin

complex was modulated by the presence of Zn^{2+}. The probe shows a 24% decrease in relaxivity upon the addition of 1 equivalent of Zn^{2+} and the near infrared (NIR) fluorescence increased by a factor of 10. The water-soluble porphyrin probe was able to permeate cell membranes and MR experiments demonstrated that the probe could induce lower relaxivity values in cells incubated with Zn^{2+}. The contrast agent was shown to effectively penetrate and stain cells *in vivo* using intracranially injected rats.[18] However, in the regions of the brain with known higher concentrations of Zn^{2+}, the contrast enhancement was found to be greater than for regions with lower concentration of Zn^{2+}, the opposite of the dependence found with *in vitro* and cellular experiments.

Unfortunately, all of the contrast agents described above rely on indirect methods of detection, which measure the properties of the bulk water, to quantify the Zn^{2+} concentration. It is not possible to determine the Zn^{2+} concentration without knowing the concentration of the probe in each voxel studied. Local concentrations cannot be known *in vivo* without additional efforts or scans to calculate contrast agent concentration. The use of PARASHIFT probes provides the opportunity to remove this limiting requirement, as the probe itself reports the presence of Zn^{2+} by modulation of a concentration independent parameter.

A Eu^{3+}-based Zn^{2+} luminescence sensor has been previously reported by Pope and co-workers, which contained a pyridine group appended with a DPA moiety, on a DO3A macrocycle, **[EuL^{F1}]** (Figure 4.3).[19] Upon addition of 1 equivalent of $ZnCl_2$, the observed europium luminescence emission was quenched. A 1:1 complex formed with Zn^{2+}, and the changes to the luminescence spectrum occurred as a result of the modulation of the Eu^{3+} coordination environment.

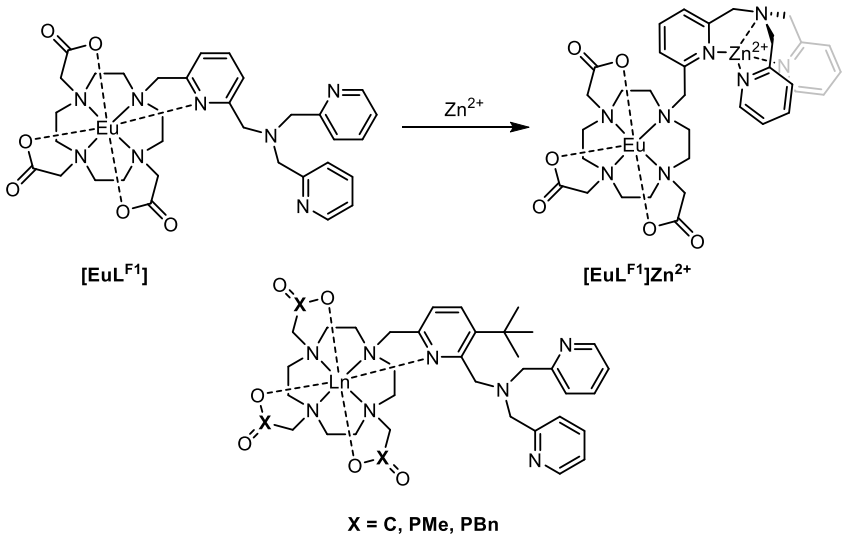

Figure 4.3 Structure of existing luminescent Eu^{3+}-based Zn^{2+} probe and proposed conformational change upon Zn^{2+} binding (*top*) and proposed structure of PARASHIFT Zn^{2+} probe (*bottom*).

It is proposed in this thesis to modify **[EuL^{F1}]** by adding a *tert*-butyl reporter group adjacent to the DPA Zn^{2+} sensing moiety, thereby creating the first metal responsive PARASHIFT probe (Figure 4.3).

4.1 Synthesis of [LnL^{7}]

The initially proposed synthetic pathway to the *tert*-butyl and DPA appended Zn^{2+} sensing moiety is shown below in Scheme 4.1.

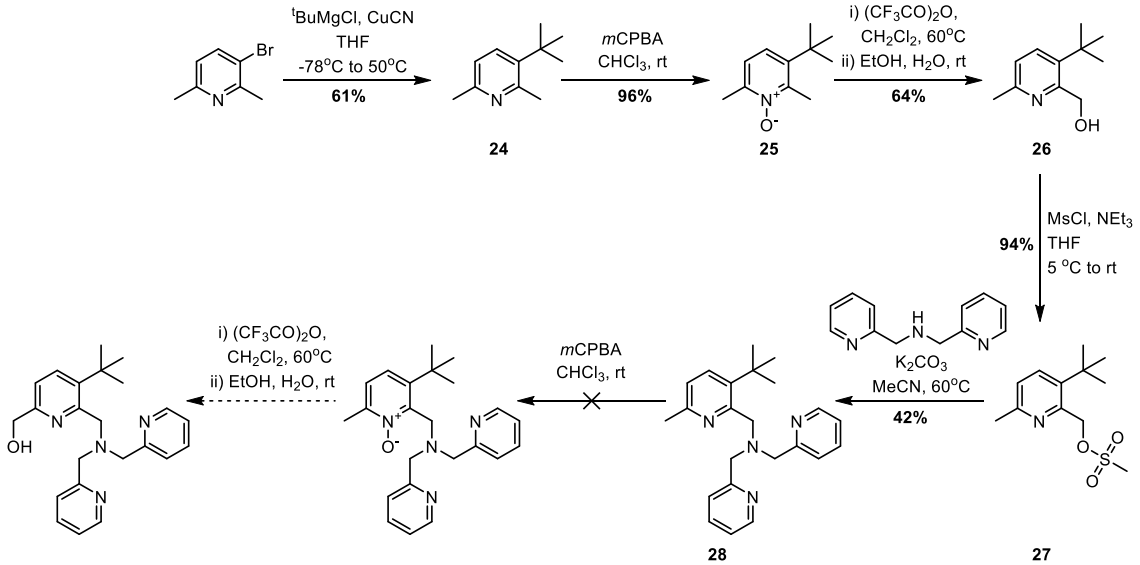

Scheme 4.1 Attempted synthetic pathway to the desired *tert*-butyl and DPA appended pyridine intermediate.

The *tert*-butyl reporter group was installed first, onto 3-bromo-2,6-dimethylpyridine, using a Grignard reaction, by an analogous method to that described previously in Section 2.1.1 (pages 52 and 53). The reaction was found to be extremely slow, yielding <20% of the desired product after a week of stirring at room temperature. The solvent system of the reaction was changed from diethyl ether to tetrahydrofuran, allowing heating of the reaction to 50°C and under these conditions completion of the reaction was achieved overnight. The desired product, **24**, was not volatile, unlike 5-*tert*-butyl-2-methylpyridine (**6**), which allowed purification to be undertaken by silica gel column chromatography. The conversion to the corresponding N-oxide, **25**, was achieved by reaction with *m*CPBA, before a Boekelheide rearrangement using trifluoroacetic anhydride activated the proximate CH bond of the methyl group. It was expected that a mixture of both possible trifluoroacetic ester regioisomers from the rearrangement (Figure 4.4) would be present.

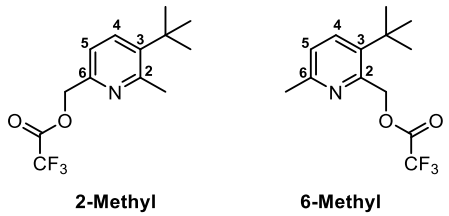

Figure 4.4 Structures of the two possible trifluoroacetic ester regioisomers from the Boekelheide rearrangement of **25**.

However, the crude ^{1}H NMR spectrum of the trifluoroacetic ester indicated only a single product was present. After room temperature hydrolysis, the alcohol product, **26**, was purified by silica gel column chromatography. The NOESY 2D NMR spectrum was utilised to characterise **26** (Figure 4.5) and two indicative correlations confirmed the presence of only the 6-methyl product. Cross-peaks revealed a close spatial proximity of the *tert*-butyl protons and the allylic alcohol protons and also between the pyridine H^{5} and the remaining methyl protons that can only occur in the 6-methyl regioisomer.

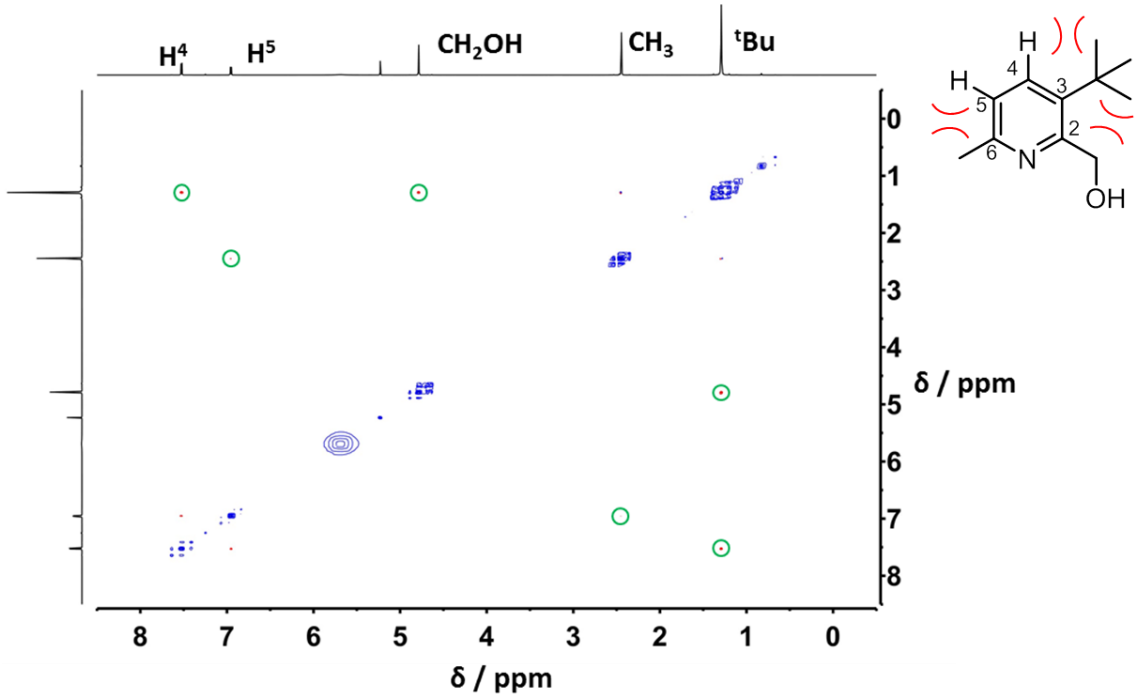

Figure 4.5 ^{1}H-^{1}H NOESY NMR spectrum of **26**. The NOE correlations of importance are circled in green.

Mesylation of **26** with methanesulfonyl chloride and triethylamine led to the mesylate ester **27**, before alkylation of DPA was carried out using potassium carbonate as the base. The tripicolyl product, **28**, was purified using reverse phase HPLC. In order to introduce the alcohol functionality, it was necessary to re-oxidise the pyridine nitrogen. However, due to the presence of multiple pyridine rings, reaction of **28** with one equivalent of *m*CPBA yielded a mixture of N-oxide products that could not be separated or purified.

Alternative methods to reach the hydroxyl group required in the final pyridine were therefore explored. Oxidation of the 6-methyl group of **28** was attempted with selenium dioxide, but similarly this could not yield a selective reaction. Bromination, via a radical reaction with N-bromosuccinimide also gave a mixture of products. The lack of selectivity is due to the presence of multiple picolyl environments at which reaction can occur.

A new synthetic pathway (Scheme 4.2) was proposed in which the N-oxide was installed before the alkylation of the DPA moiety.

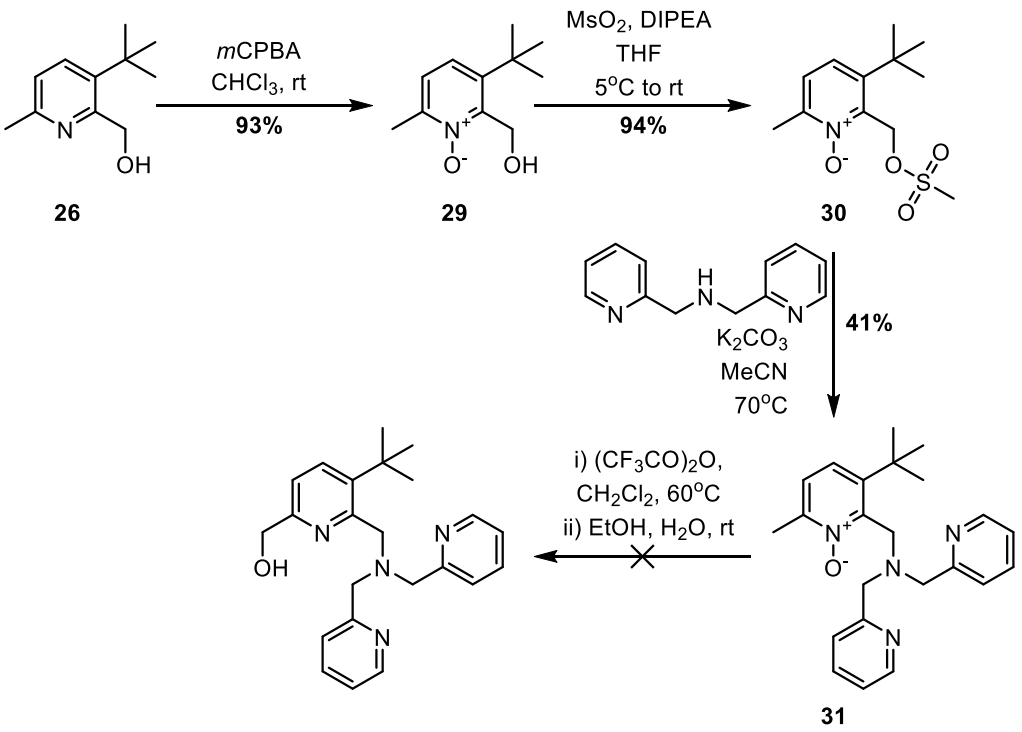

Scheme 4.2 Alternate synthetic pathway to the *tert*-butyl and DPA appended pyridine intermediate.

The 6-methyl alcohol product, **26**, was converted to the N-oxide, **29**, with *m*CPBA and the subsequent mesylation of the alcohol was initially attempted with methanesulfonyl chloride and triethylamine. Mass spectrometry of the crude reaction mixture revealed that, whilst full conversion of the alcohol to the mesylate had occurred, the major species had also undergone reduction of the N-oxide. A literature search revealed that methanesulfonyl chloride and triethylamine may be used as reagents for the reduction for N-oxides, thought to be through the formation of SO_2.[20,21] A change of base from triethylamine to N,N-diisopropylethylamine (DIPEA) afforded the mesylated product, **30**, in reactions with both methanesulfonyl chloride and anhydride, suggesting that a more sterically hindered base prevents the production of SO_2. The alkylation of DPA proceeded similarly to that previously described, and the tripicolyl product, **31**, was purified using HPLC. Unfortunately, upon reaction with TFAA no desired product was seen to be formed by the either crude NMR spectrum or mass spectrometry. It is likely that the deprotonation step of the Boekelheide rearrangement occurred on the more acidic 2-picolyl protons, instead of the 6-methyl as desired.

The conversion of the 6-methyl group to an alcohol was deemed unfeasible after the addition of the DPA moiety. Accordingly, a new synthetic route was developed in which both methyl groups of **24** are oxidised before the introduction of the Zn^{2+} sensing amine (Scheme 4.3). Oxidation and subsequent esterification of both methyl groups of **24** should yield a diester, which may be carefully reduced to two potential regioisomers of the monoester, both of which can be intermediates to the desired Zn^{2+} sensing arm.

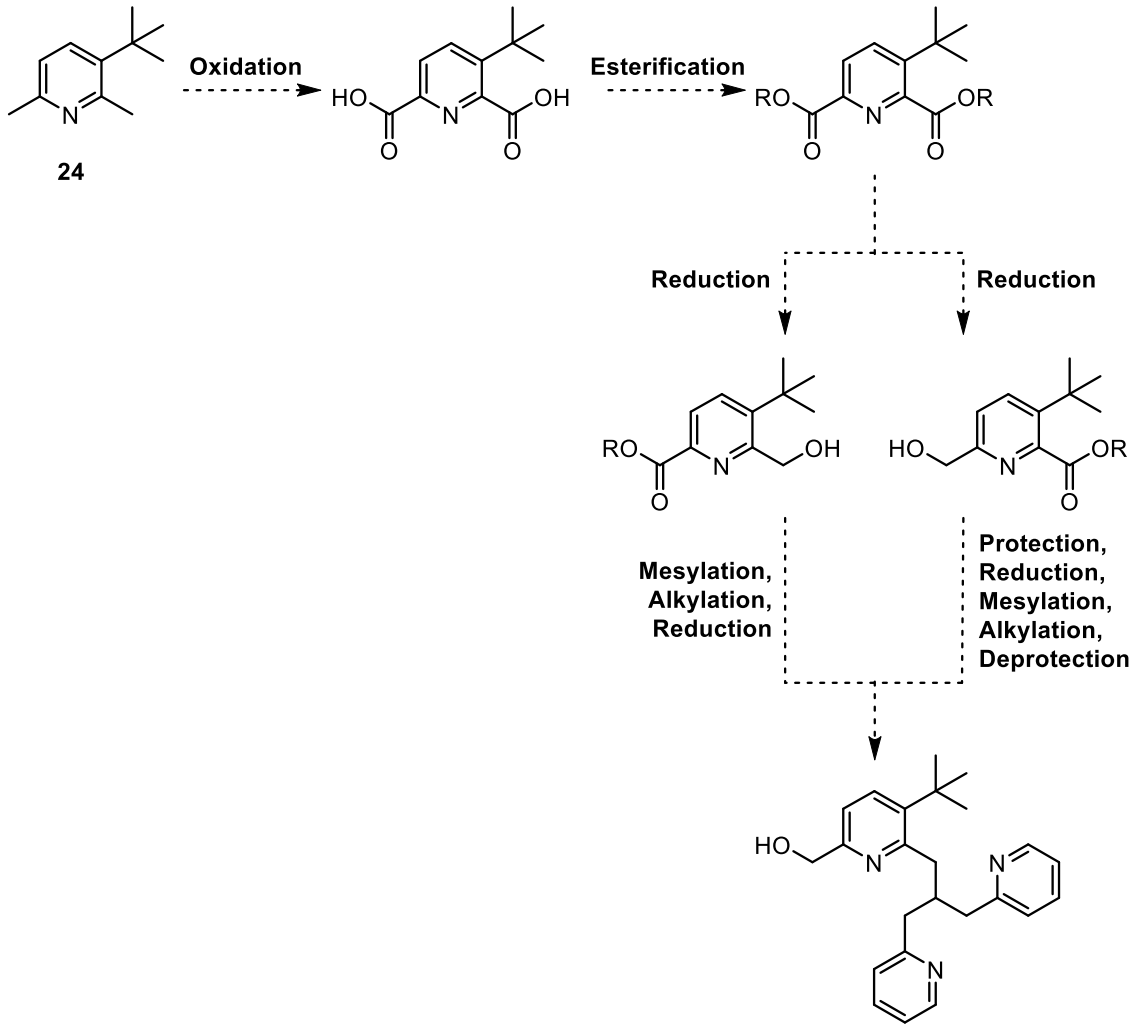

Scheme 4.3 General strategy for the synthesis of *tert*-butyl and DPA appended pyridine intermediate from 3-*tert*-butyl-2,6-dimethylpyridine, **24**.

The dimethyl pyridine precursor, **24**, was oxidised to the dicarboxylate salt with $KMnO_4$ (Scheme 4.4). The dicarboxylic acid could not be isolated, so the esterification step was performed on the crude dicarboxylate salt. Initial attempts to install methyl esters with methanol and catalytic H_2SO_4 were unsuccessful. The esterification was reattempted, similarly on the crude salt, with thionyl chloride and methanol to first form the reactive acyl chloride. The ^1H NMR spectrum of the reaction mixture revealed two major

products which were separated by silica gel column chromatography to yield the desired diester, **33**, as the minor product (23%) and the monoester, **32**, as the major product (35%). Only one mono-ester regioisomer was observed. Analysis of the 2D ^{1}H-^{13}C HMBC NMR spectrum established this to be the 6-ester. Formation of the 2-ester is expected to be inhibited due to the increased steric hindrance from the presence of the adjacent, bulky *tert*-butyl group. An esterification with the same conditions was repeated on the pure monoester product, **32**, however no second esterification was observed. A Steglich esterification using the carbodiimide N,N'-dicyclohexylcarbodiimide (DCC) with 4-dimethylaminopyridine (DMAP) as a catalyst yielded the diester, **33**, although separation of the product from the excess dicyclohexylurea by-product proved challenging. The reaction was repeated with 1-ethyl-3-(3-dimethylaminopropyl)carbodiimide (EDC), the aqueous soluble urea by-products of which were easily removed through aqueous washing before further purification on silica gel.

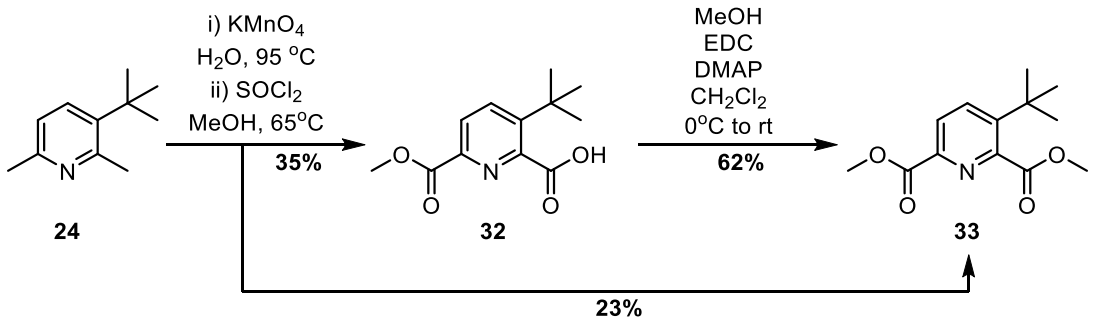

Scheme 4.4 The synthetic route to dimethyl 3-*tert*-butyl-2,6-pyridinecarboxylate, **33**.

A test reaction of the mono-reduction of diester, **33**, was attempted using sodium borohydride at 0°C (Scheme 4.5 and 4.6). The reaction was monitored regularly by thin layer chromatography (TLC) to ensure consumption of the starting material and limit over reduction to the diol, (2,6-dihydroxymethyl, Scheme 4.5).

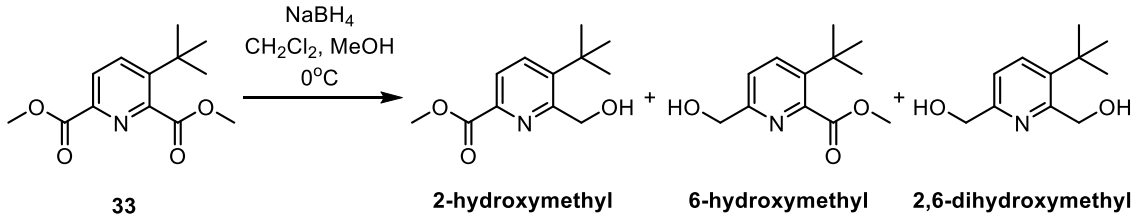

Scheme 4.5 The reduction of 3-*tert*-butyl-2,6-pyridinecarboxylate, **33**, and the possible products.

However TLC analysis showed complete loss of starting material immediately (<5 min) and only a single spot was visible under UV, even after stirring the reaction at room temperature for several hours. NMR analysis of the reaction mixture confirmed the presence of only one product, indicating the complete regioselectivity of the reduction. Purification by silica gel column chromatography yielded a single mono-reduced regioisomer in near quantitative yield. The 2D NOESY NMR spectrum was employed to determine the constitution of this regioisomer (Figure 4.6). Through-space correlations were found between the *tert*-butyl group and the methyl protons of the ester. The reduction reaction therefore occurred selectively to produce the 6-hydroxylmethyl pyridine, **34**, which was further corroborated by the presence of a cross peak between the pyridine H^5 and the hydroxymethyl protons.

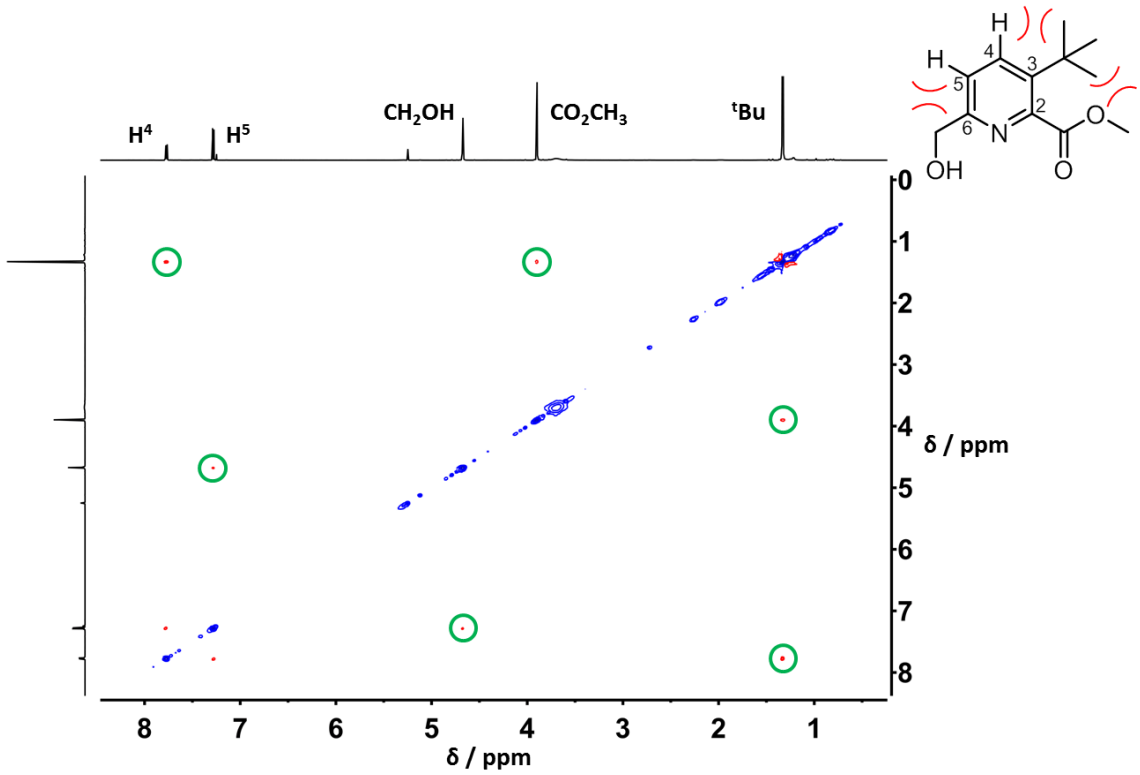

Figure 4.6 ^{1}H-^{1}H NOESY NMR spectrum of **34**. The NOE correlations of importance are circled in green.

As indicated in Scheme 4.3, the 6-hydroxylmethyl group must be protected before the second ester is reduced so that the DPA group can be alkylated regioselectively. A tetrahydropyran (THP) ether was chosen due to the ease of protection and deprotection and their known stability under reductive and basic conditions. The protection step was achieved by reaction of **34** with 3,4-dihydro-2H-pyran and catalytic *p*-toluenesulfonic acid to yield **35** (Scheme 4.6). The remaining ester was reduced with

lithium aluminium hydride to give the alcohol **36**. Conversion to the mesylate, **37**, succeeded using methanesulfonyl chloride and triethylamine, prior to alkylation of DPA. Purification of the alkylated product, **38**, was achieved with column chromatography on alumina.

The THP ether was then hydrolysed under acidic conditions with *p*-toluenesulfonic acid to yield the desired novel *tert*-butyl and DPA appended pyridine, **39**. Mesylation of the hydroxyl group provided the required reactive pyridine moiety, **40**, for alkylation of the cyclen macrocycle.

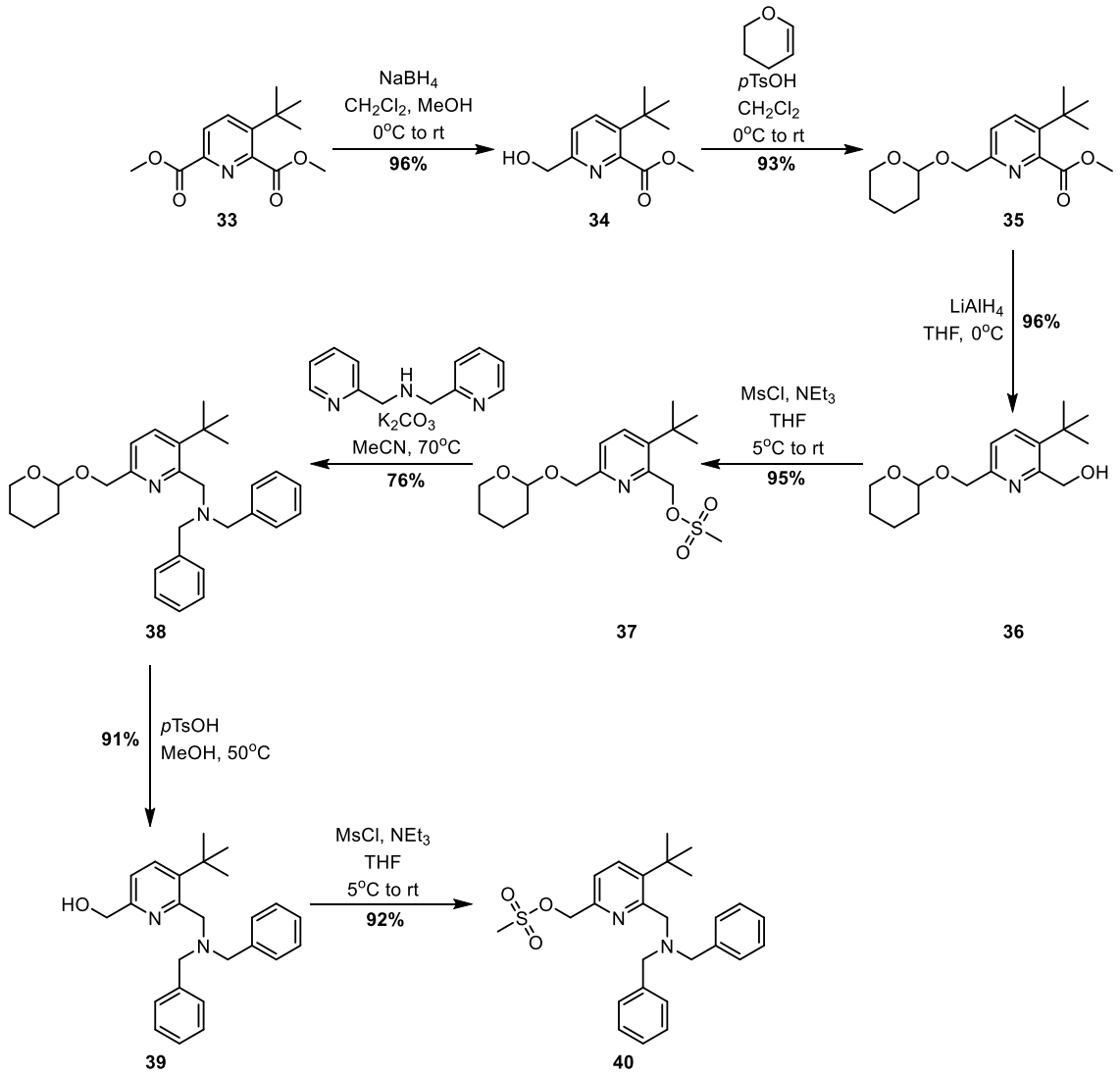

Scheme 4.6 Synthesis of the *tert*-butyl and DPA appended pyridine intermediate, **40**, from the diester, **33**.

The previous work described in Chapter 3 indicated that neutral tribenzylphosphinate Ln^{3+} complexes may have limited water solubility. However, neutral

trimethylphosphinate complexes, such as **[LnL^J]**, have demonstrated sufficient solubility in water. Hence the macrocycle, **5**, was chosen as the ligand backbone of the Zn^{2+} probe. The alkylation step was carried out in anhydrous acetonitrile using caesium carbonate as the base (Scheme 4.7), and the crude ligand purified by alumina column chromatography.

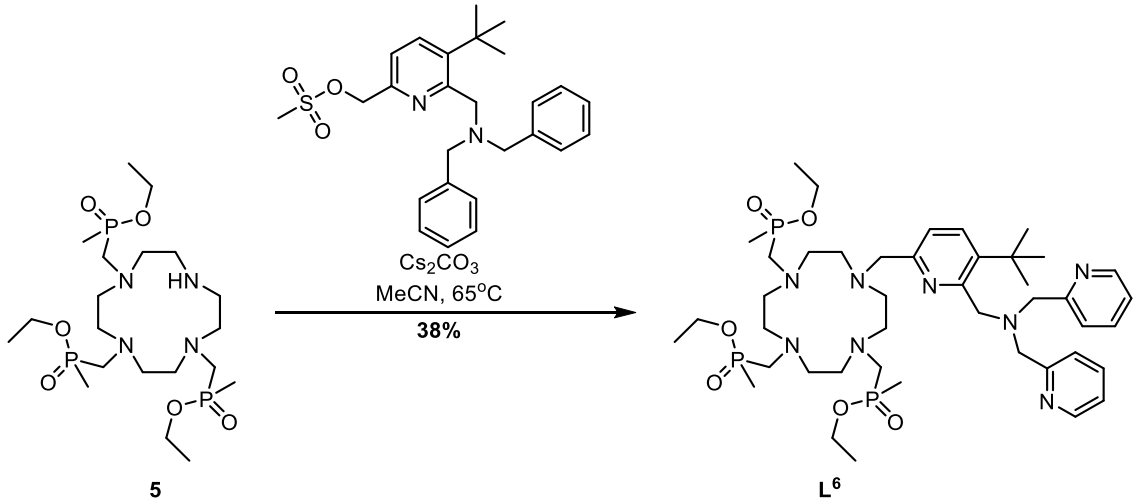

Scheme 4.7 The alkylation of trimethylphosphinate **5** with mesylate **40** to afford the ligand **L^6**.

Phosphinate ester hydrolysis of **L^6** was carried out in aqueous 6 M HCl solution at 70°C (Scheme 4.8), and reaction progress was monitored by mass spectrometry. Once the ester hydrolysis was complete, the pH of the solution was adjusted to 5.5 and dysprosium(III) chloride was added. The reaction was stirred for 7 days at 70°C. However, after HPLC, only uncoordinated ligand was observed and no complex could be isolated. Several attempts at the complexation reaction yielded similar results regardless of solvent and pH. The additional steric bulk of the Zn^{2+} sensing pyridine moiety may have inhibited complex formation in the triphosphinate macrocycle.

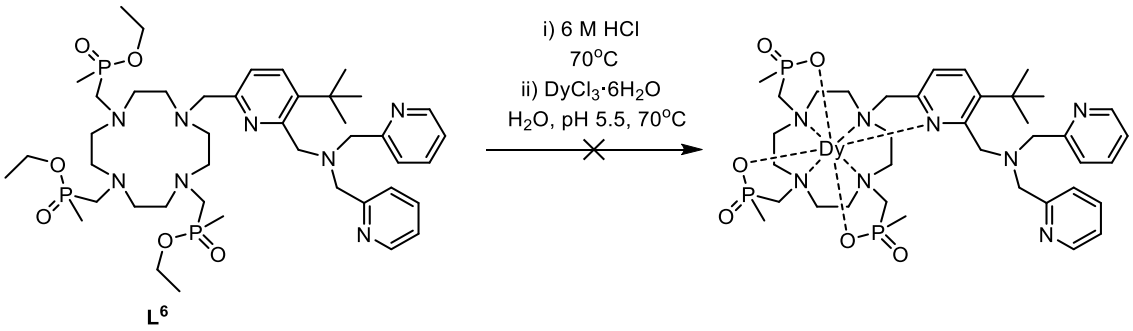

Scheme 4.8 Attempted hydrolysis and complexation of ligand **L^6.**

In order to achieve complexation a less sterically hindered macrocyclic derivative was sought. The *tert*-butyl tri-ester of DO3A, **41**, was therefore prepared using a literature procedure (Scheme 4.9).[22]

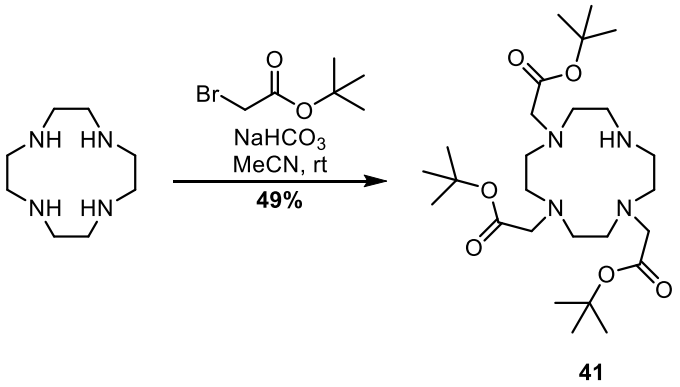

Scheme 4.9 Synthesis of the *tert*-butyl tri-ester of DO3A.

Alkylation of the macrocycle, **41**, with the mesylate, **40**, was achieved in acetonitrile using caesium carbonate as the base (Scheme 4.10). Hydrolysis of the *tert*-butyl esters was carried out in trifluoroacetic acid (TFA) and dichloromethane at room temperature before complexation in aqueous solution with the appropriate lanthanide(III) chloride hexahydrate. The crude complexes were purified by reverse phase HPLC.

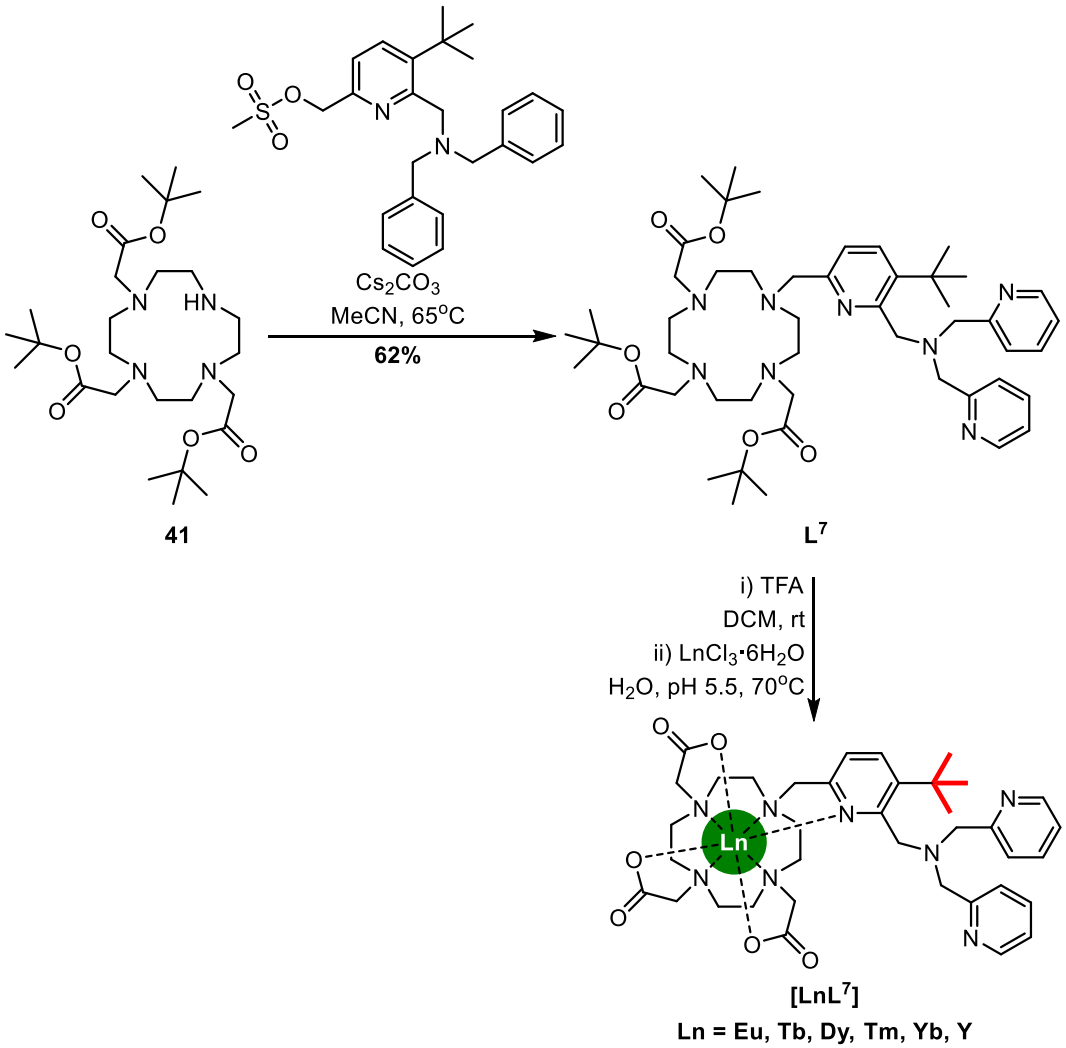

Scheme 4.10 General procedure for the alkylation, hydrolysis and complexation of **[LnL^7]**.

The inner sphere hydration state, *q*, for **[LnL^7],** was calculated by measuring the luminescence lifetimes of **[EuL^7]** and **[TbL^7]** in both H_2O and D_2O (Table 4.1).

Table 4.1 Luminescence lifetime measurements of **[EuL^7]** and **[TbL^7]** (295 K, λ_{ex} = 276 nm, pH/pD = 7.3).

Ln	τ_{H_2O} (ms)	τ_{D_2O} (ms)	*q*
Eu	1.61	1.15	0.00
Tb	2.78	2.55	-0.14

A *q* value of 0 was expected, as the lanthanide has a coordination number of at least 8 and there is an additional shielding effect from the hydrophobic DPA. The *q* value of zero was observed experimentally, in agreement with the results of Pope and co-workers.[19]

4.2 NMR studies of [LnL^7]: shift and relaxation

4.2.1 Diamagnetic NMR studies of [YL^7]: shift and relaxation

The diamagnetic complex **[YL^7]** was synthesised in order to compare the NMR behaviour with the analogous paramagnetic complexes. ^{1}H NMR analysis revealed a mixture of broad and sharp resonances within the aromatic pyridine region (Figure 4.7).

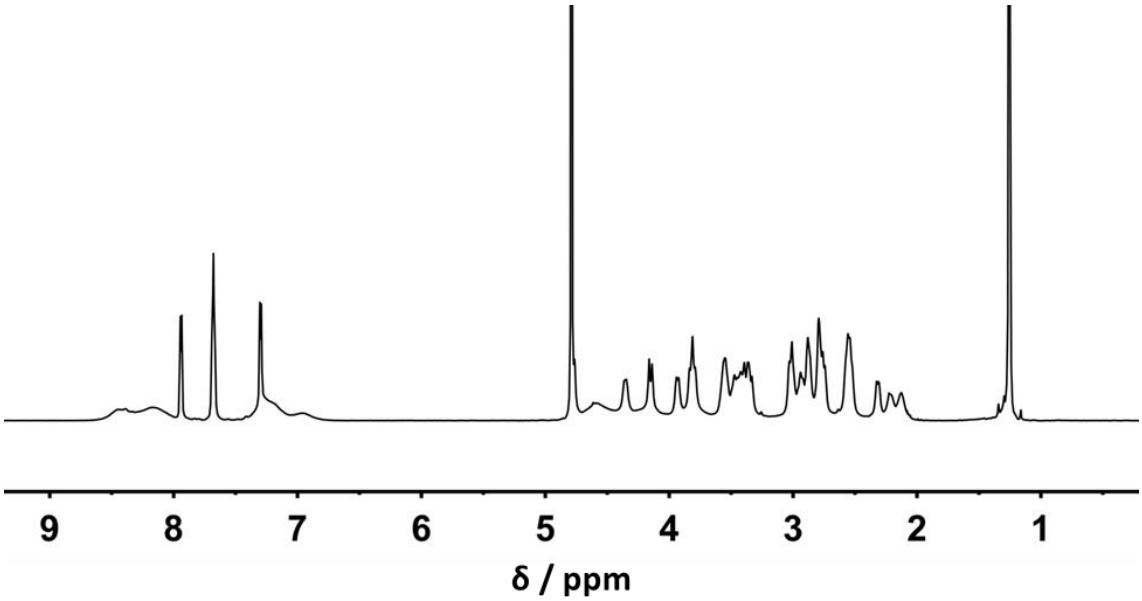

Figure 4.7 ^{1}H NMR spectrum of **[YL^7]** (D_2O, 16.4 T, 295 K, pD 7.3).

A general assignment was attempted using the HSQC, COSY and NOESY 2D NMR spectra. However, no resonances corresponding to the aromatic or picolyl DPA protons could be assigned unequivocally. Whilst the two aromatic proton resonances of the *tert*-butyl pyridine moiety are sharp and readily assignable, several of the aromatic DPA resonances are exchange broadened. Such exchange broadening is consistent with the presence of more than one conformation or species of the DPA moiety.

Variable temperature NMR was undertaken in an attempt to explore the origins of the broadening of the aromatic resonances (Figure 4.8). Upon cooling, multiple resonances appeared within the aromatic region. Above 305 K, these resonances sharpened and coalesced to reveal four distinct picolyl environments. The macrocyclic ring protons also sharpened at lower temperature but no additional resonances were seen.

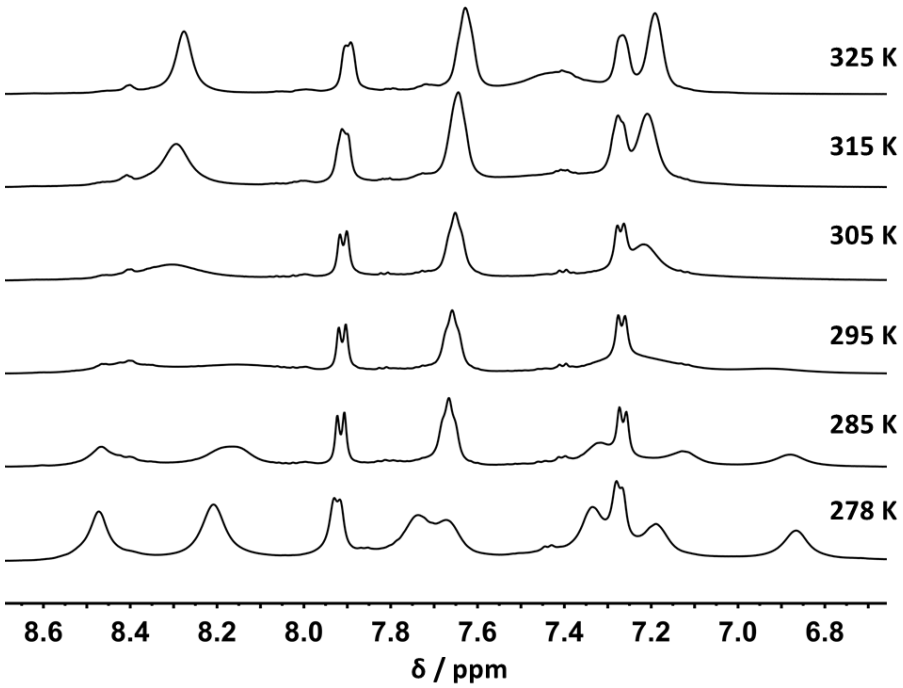

Figure 4.8 Stacked variable temperature ^{1}H NMR spectra of the aromatic region of **[YL^{7}]** (D_2O, 11.7 T, pD 7.3), showing a coalescence phenomenon around 300 K.

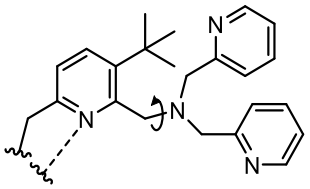

Figure 4.9 Partial structure of the Zn^{2+} sensing DPA moiety highlighting C-N_{amine} rotation.

The variable temperature NMR study demonstrates that at temperatures above 285 K the C-N_{amine} bond (Figure 4.9) must be free to rotate sufficiently quickly that the two picolyl rings are rendered equivalent on the NMR timescale. As the temperature decreases, bond rotation slows and the picolyl rings are inequivalent, which may be associated with a weak interaction between the tertiary amine lone pair and the lanthanide(III) ion, perhaps mediated by a bridging solvent interaction.

4.2.2 Paramagnetic NMR studies of [LnL^{7}]: shift and relaxation

The chemical shifts of the *tert*-butyl reporter group of the paramagnetic **[LnL^{7}]** complexes were measured in D_2O (Figure 4.10). The resonances are significantly less shifted than the phosphinate-based complexes described in the previous chapters. However, the *tert*-butyl resonance for the Tm^{3+}, Tb^{3+} and Dy^{3+} complexes lies well outside the diamagnetic region.

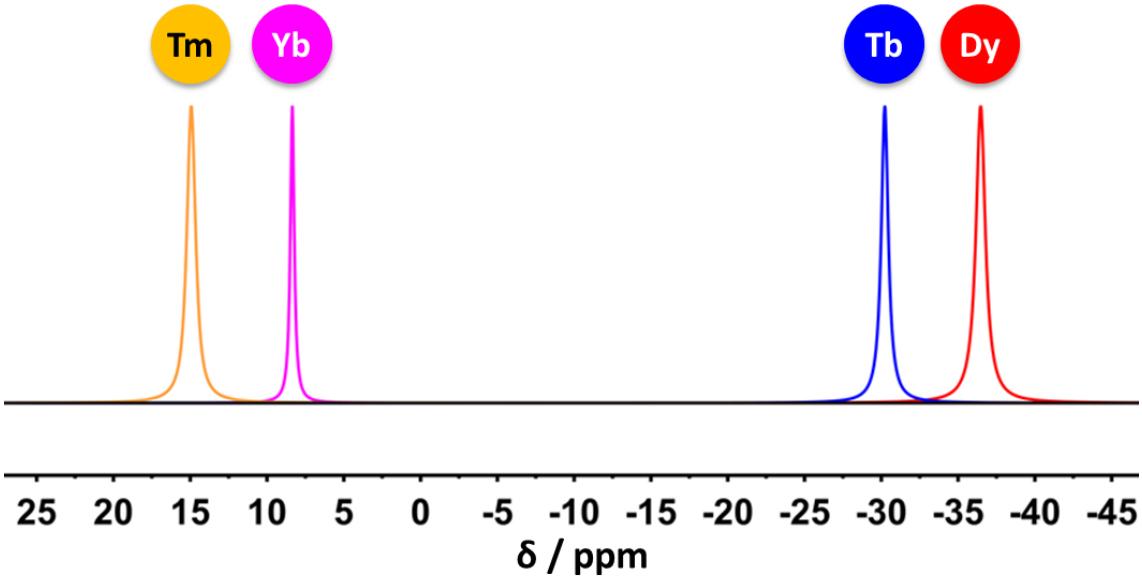

Figure 4.10 Schematic showing the superimposed partial ^{1}H NMR spectra of the *tert*-butyl resonance of **[LnL^{7}]** (D_2O, 4.7 T, 295 K, pD 7.3): Tm (yellow); Yb (magenta); Tb (blue); Dy (red).

When compared to the analogous carboxylate complex without the Zn^{2+} sensing moiety, **[LnL^{H}]** (see Section 1.7.1, page 27-29), the *tert*-butyl pseudocontact chemical shifts are increased. The increase is most significant for the negatively shifting *tert*-butyl resonances. Thus, in **[TbL^{H}]** and **[DyL^{H}]** chemical shifts of -10.6 and -20.1 ppm respectively are observed, compared to -30.2 and -36.5 ppm in **[TbL^{7}]** and **[DyL^{7}]**. It has been found previously that the presence of an axially coordinated water molecule can have a significant impact on the paramagnetic shift of lanthanide complexes in structurally related ligands (see Section 1.7.1, page 27-31), as the orientation and size of the principal component of the magnetic susceptibility tensor (the axial component) are sensitive to structural perturbation. The larger chemical shifts in **[LnL^{7}]** are also consistent with the loss of the inner sphere water molecule, as established from the lifetime analysis of the Eu^{3+} and Tb^{3+} complexes (Table 4.1).

Unlike **[LnL^{H}]**, in which two diastereoisomers are observed, only one *tert*-butyl resonance was present for every **[LnL^{7}]**. The weak interaction postulated between the DPA amine and lanthanide(III) ion is likely to stabilise the complex and reduce the flexibility of the macrocyclic backbone.

The longitudinal relaxation rate, R_1, of the *tert*-butyl resonance of **[LnL^{7}]** was measured at six different field strengths (Table 4.2). The rates are comparable with those of

[LnL^{H}],[23] indicating that there is no large structural change in the complex that causes the increase in the pseudocontact shift of the *tert*-butyl resonances.

Table 4.2 ^{1}H NMR longitudinal relaxation rates for the *tert*-butyl resonance of **[LnL^{7}]** as a function of magnetic field (D_2O, 295 K, pD 7.3).

Ln^{3+}	R_1 / s^{-1} (± error)					
	1 T	**4.7 T**	**9.4 T**	**11.7 T**	**14.1 T**	**16.4 T**
Tb	43 (1)	61 (1)	95 (1)	118 (1)	133 (1)	150 (1)
Dy	72 (1)	103 (1)	146 (1)	181 (1)	217 (1)	243 (1)
Tm	20 (1)	38 (1)	55 (1)	72 (1)	77 (1)	88 (1)
Yb	8.8 (0.3)	9.1 (0.1)	8.1 (0.1)	10.7 (0.1)	11.0 (0.3)	11.2 (0.3)

The relaxation data of the four complexes were analysed by global minimisation methods assuming the internuclear distance, *r*, was 6.6 Å (Figure 4.11). The fitting yielded generally good results, although both **[DyL^{7}]** and **[TmL^{7}]** were less well fitted at low fields.

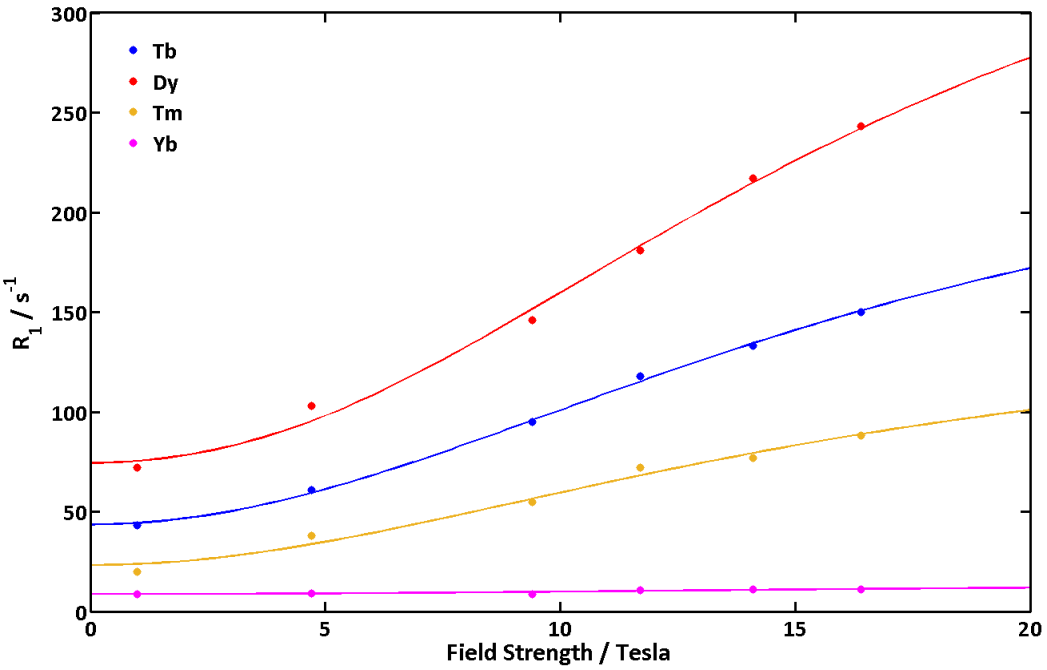

Figure 4.11 ^{1}H NMR relaxation rates (R_1 / s^{-1}) for the major *tert*-butyl resonance of **[LnL^{7}]** as a function of magnetic field, showing the global fits (line) to the experimental data points (D_2O, 295K, pD 7.3, fixed *r* = 6.6 Å, minimizes to τ_r = 237 (7) ps).

This minimisation process gave a common rotational correlation time, τ_r, of 237 (±7) ps, and also predicted values of μ_{eff} and τ_e for each lanthanide ion (Table 4.3). The calculated value of τ_r is slightly increased from the value of the similar tricarboxylate complex, **[LnL^{H}]** (197 (±7) ps), which is consistent with the increase in

molecular volume arising from the additional DPA moiety. The predicted μ_{eff} values are in relatively close agreement to those theoretically calculated.

Table 4.3 Estimated 'best-fit' values for ^{1}H NMR relaxation parameters of **[LnL^7]** following global fitting with fixed r = 6.6 Å (D_2O, 295 K, pD 7.4)[a]

Ln^{3+}	τ_e / ps	μ_{eff} / BM[a]
Tb	0.49 (5)	9.48 (2)
Dy	0.65 (6)	10.72 (4)
Tm	0.34 (12)	8.26 (5)
Yb	0.44 (3)	4.47 (6)

[a] Theoretical values for the magnetic moments of lanthanide(III) ions are: Tb, 9.7; Dy, 10.6; Tm, 7.6; Yb 4.3 BM.

The chemical shift of the reporter *tert*-butyl group was investigated over the temperature range 290 K to 325 K and showed a linear dependence (Figure 4.12). The magnitudes of the linear sensitivities are significantly decreased in comparison to the previously discussed phosphinate complexes; **[TbL^7]** and **[DyL^7]** have the largest dependences, 0.25 and 0.27 ppm/K respectively.

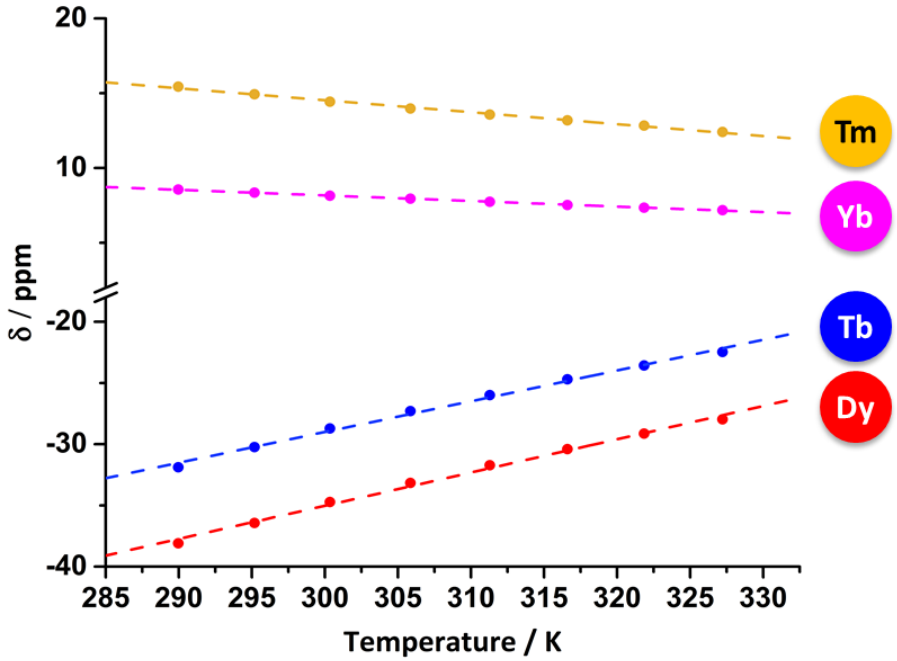

Figure 4.12 Variation in the chemical shift of the *tert*-butyl resonance of **[LnL^7]** as a function of temperature (D_2O, 11.7 T, pD 7.3): Tm (yellow) R^2 = 0.996; Yb (magenta) R^2 = 0.998; Tb (blue) R^2 = 0.994; Dy (red) R^2 = 0.995.

4.3 pH Responsive behaviour of [LnL^7]

4.3.1 Luminescence studies of [EuL^7] and[TbL^7]: pH response

In order to study the pH sensitivity of **[LnL^7]** a pH titration with **[EuL^7]** was carried out. The emission spectrum and emission lifetime were recorded as a function of pH. The emission spectra showed that the luminescence generally decreases upon decreasing pH (Figure 4.13). A sigmoidal fit of the intensity ratio of the largest ΔJ = 2 band against a ΔJ = 0 band gave a pK_a of 5.70(05).

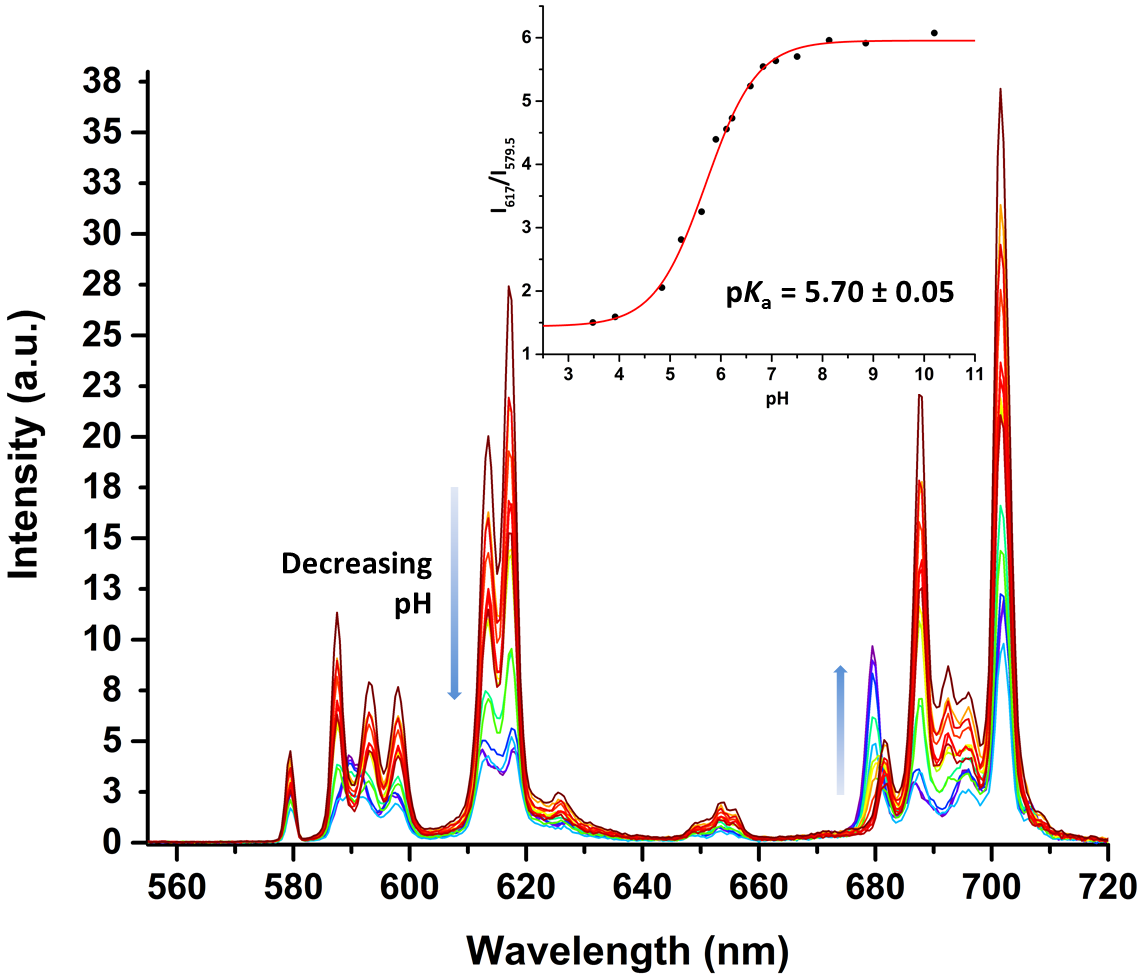

Figure 4.13 Variation of the emission spectra of **[EuL^7]** (20 μM) as a function of pH (H_2O, 295 K, λ_{ex} = 276 nm). (*Inset*) The ratio of emission intensities at 617 nm (ΔJ = 2) / 579.5 nm (ΔJ = 0) as a function of pH.

The luminescence lifetimes of ΔJ = 2 was also measured in D_2O and H_2O at varying pH (Figure 4.14). Interestingly, whilst the lifetime in H_2O decreased with decreasing pH, the lifetime in D_2O increased at lower pH.

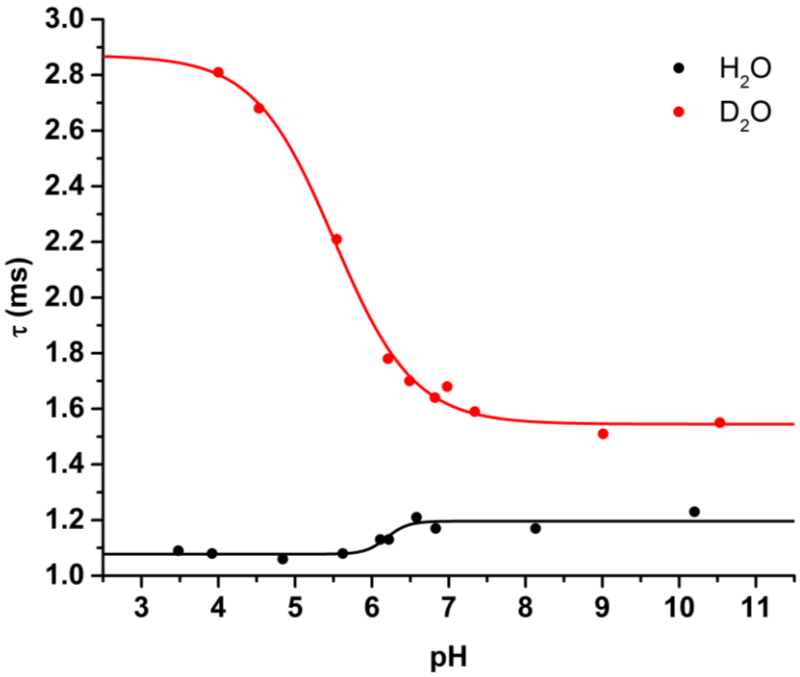

Figure 4.14 Variation of the lifetime of **[EuL^7]** as a function of pH in H_2O and D_2O (295 K, λ_{ex} = 276 nm, λ_{em} = 617 nm).

The hydration state of **[EuL^7]** was estimated, from the sigmoidal fit of the variation of the observed lifetimes with pH/pD. At high pH q = 0, and at low pH, the apparent q value was 0.4. Lifetime measurements of **[TbL^7]** revealed similar q values at high and low pH/pD, 0 and 0.3 respectively. Such a variation is most simply explained by the quenching effect of the proximate NH vs ND oscillator of the protonated tertiary amine nitrogen. It has previously been established that amine NH oscillators are twice as effective as OH oscillators at quenching Eu^{3+} excited states.[24] In the complex, **[LnL^7]**, there may be a bifurcated hydrogen bond shared between the sp^3 N atom and the pyridyl sp^2 N atom that would be within 4Å of the Eu ion and hence able to quench by through-space vibrational energy transfer, for which the distance dependence is r^{-6}.

A pK_a value of 5.7, accompanied by the small change in spectral form, suggests that protonation is occurring on the dipicolyl amine nitrogen atom. The observed pK_a value is only slightly lower than that reported for the model compound trispicolylamine (TPA), for which a value of 6.2 has been found.[25] The presence of the sterically bulky *tert*-butyl group and the shielding provided by the three proximate aromatic rings will tend to inhibit local solvation and so will not stabilise the protonated form (i.e. the conjugate acid), as effectively as normal.

4.3.2 Diamagnetic NMR studies of [YL^7]: pH response

The ^{1}H NMR spectra of **[YL^7]** above and below the pK_a were acquired (Figure 4.15). At low pD (4.5) the aromatic DPA proton resonances are shifted to higher frequency, indicative of protonation of the pyridine N. The aromatic resonances are significantly sharper at low pD, whilst the macrocyclic region is broader. As there are only 6 distinct pyridine environments upon addition of acid, the DPA pyridine protons must be equivalent, as was observed at high temperature. The C-N_{amine} must have freedom of rotation on an intermediate NMR timescale. The increasing broadness of the macrocyclic proton resonances suggests that the rate of exchange between low energy conformations of the ligand backbone is accelerated at low pD. This is consistent with the luminescence pK_a data that suggests it is the DPA amine which becomes protonated, as upon protonation the interaction between the metal ion and amine lone pair will be lost. The change from 9- to 8- coordination of the metal would result in increased flexibility of the macrocyclic backbone.

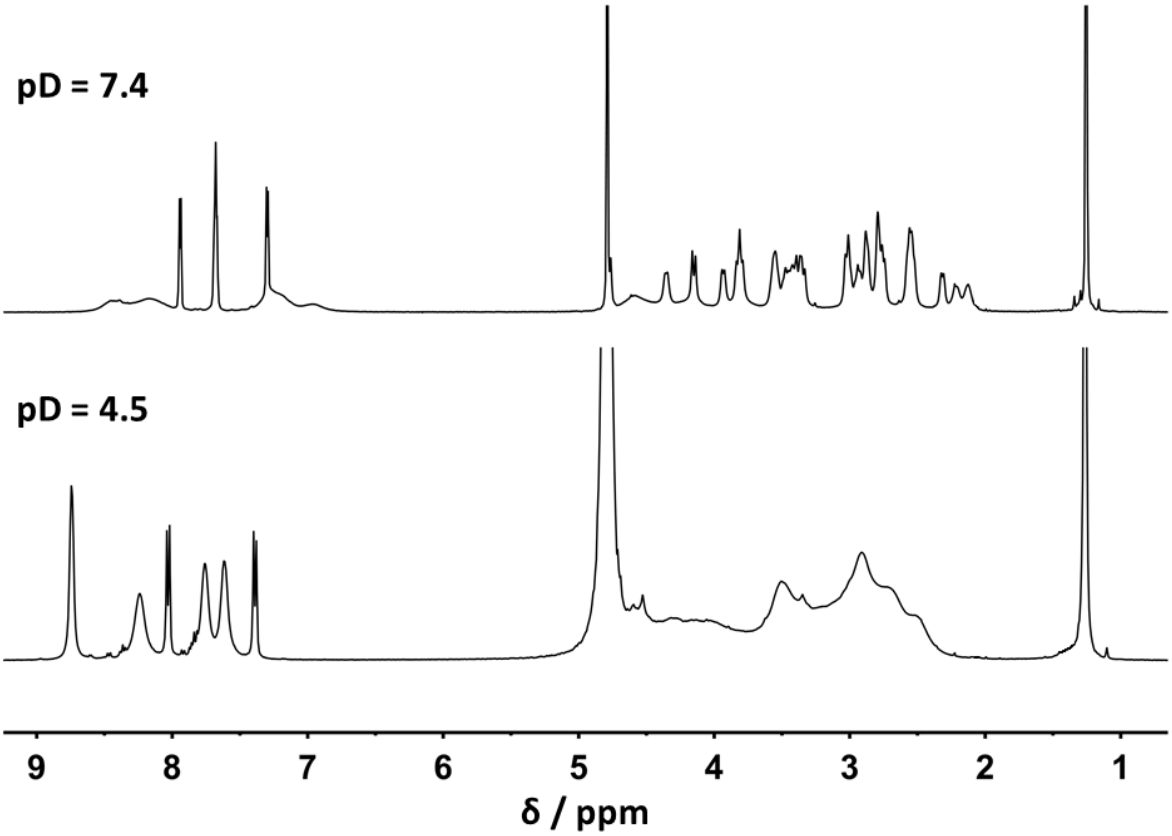

Figure 4.15 Stacked ^{1}H NMR spectra of **[YL^7]** at different pD values, above (*top*) and below (*bottom*) the pK_a (5.7) (D_2O, 9.4 T, 295 K).

4.3.3 Paramagnetic NMR studies of [DyL^7]: pH response

A pD titration was carried out on the paramagnetic complex **[DyL^7]** (Figure 4.16). From high pD to low pD, the *tert*-butyl resonance (-36 ppm) broadens and the pseudocontact shift increases (chemical shift becomes more negative) before sharpening (-47 ppm), whilst there is an additional *tert*-butyl peak that appears (-60 ppm) and sharpens as pD decreases. The presence of two *tert*-butyl resonances below the pK_a demonstrates there are two different forms of the protonated complex that are in slow exchange.

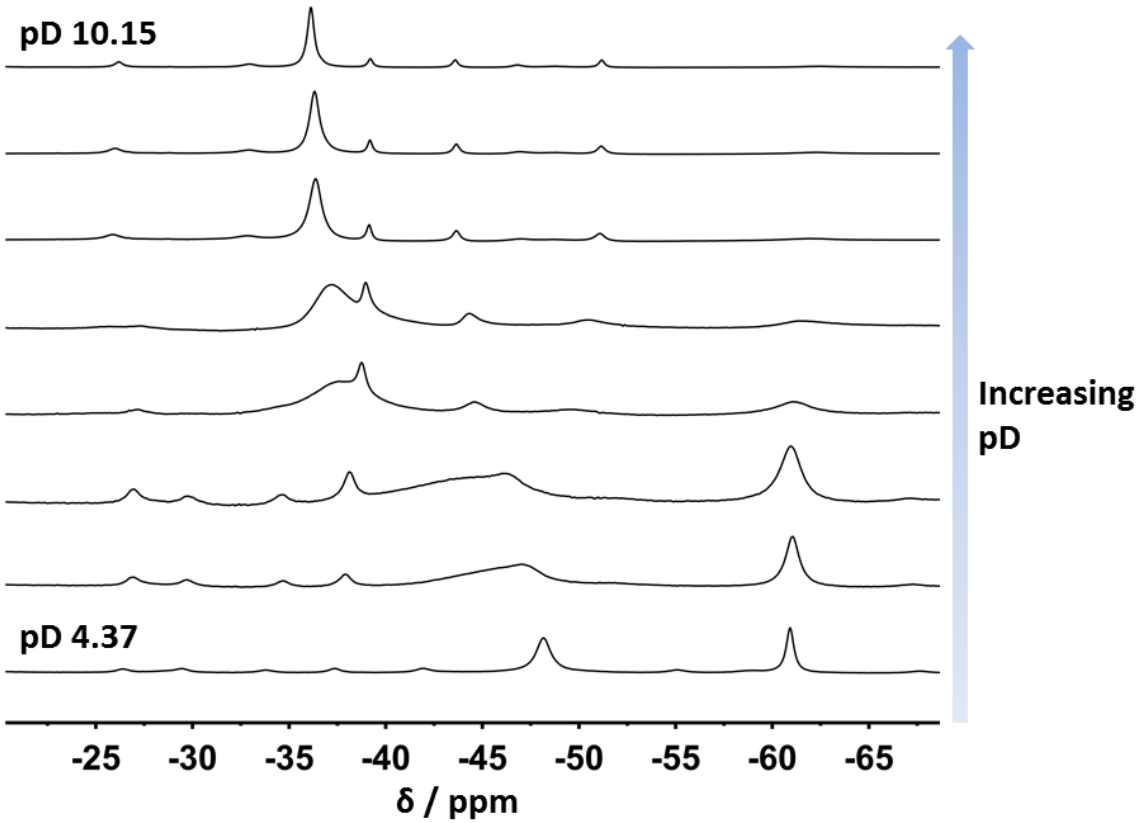

Figure 4.16 Stacked ^{1}H NMR spectra of the *tert*-butyl resonances of **[DyL^7]** as a function of pD (D_2O, 11.7 T, 295 K).

The longitudinal relaxation rates of the two new *tert*-butyl peaks at -47 and -60 ppm were measured at low pD (295 K, 11.7 T) and were found to be 164 and 163 Hz respectively, compared to the high pD rate of 181 Hz. The increase in chemical shift, which was also accompanied by an increase in linewidth and hence R_2, indicates that there is a change in the anisotropy of the pseudocontact shift field. Or, the change may arise from a structural change of the complex that brings the Dy^{3+} centre either closer in space to the *tert*-butyl group, or at a different angle with respect to the main

component of the magnetic susceptibility tensor. As the longitudinal relaxation actually decreases at higher pD, the change is unlikely to be the result of a decreased internuclear distance. The loss of the postulated weak interaction of the DPA amine is likely to induce a change in the anisotropy of the pseudocontact shift field as ligand changes in the axial position have previously been shown to have drastic effects on the ligand field and therefore the anisotropy of lanthanide complexes.[26,27]

The presence of two *tert*-butyl resonances is indicative of the complex exchanging between low energy conformations of the macrocyclic ring. In the diamagnetic species **[YL^7]** this led to broadening of the macrocyclic region. However, the frequency difference of the two species of the paramagnetic complex results in the exchange being slower on the NMR timescale.

4.4 Zn^{2+} responsive behaviour of [LnL^7]

As **[LnL^7]** has demonstrated pH dependence, it is crucial that any metal ion titrations be buffered in order to keep the pH or pD constant within a physiological range above the pK_a. In order to maintain consistency between luminescence and NMR titrations, it was decided that the same buffer system should be used throughout. The buffer 'TRIS' was selected due to the useful pH range (7-9) and the commercial availability of the deuterated analogue.

4.4.1 Luminescence studies of [EuL^7] and[TbL^7]: Zn^{2+} response

The addition of $ZnCl_2$ to **[EuL^7]** resulted in a significant emission intensity decrease and changes to spectral form in the ΔJ = 1, 2 and 4 manifolds (Figure 4.17). Such significant changes in spectral form indicate a change in the coordination environment of the Eu^{3+} ion. Analysis of the ΔJ = 2 transitions suggested an extremely strong interaction between the complex and Zn^{2+} (Figure 4.17). The binding curve indicates a 1:1 binding stoichiometry with very high affinity. Attempts to fit the binding curves failed, suggesting a dissociation constant, K_d, of less than 1 μM.

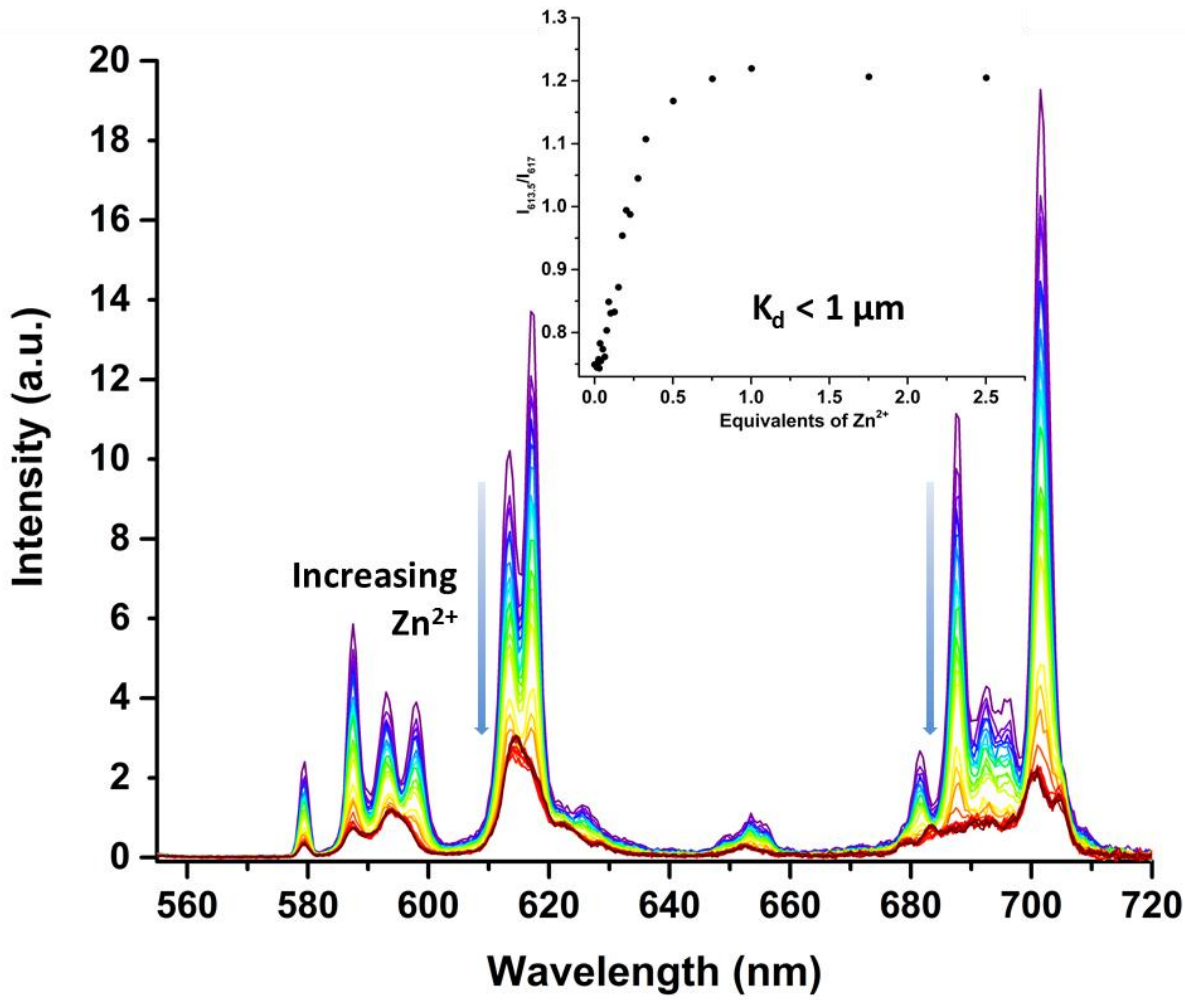

Figure 4.17 Variation of the emission spectra of **[EuL^7]** (20 µM) as a function of equivalents of Zn^{2+}. (*Inset*) Intensity ratio of 613.5 nm / 617 nm as a function of equivalents of Zn^{2+} (295 K, H_2O, 0.1 M TRIS, pH/pD = 7.3, λ_{ex} = 276 nm).

The europium luminescence lifetime was monitored as a function of the number of equivalents of Zn^{2+} added, both in D_2O and H_2O (Table 4.4 and Figure 4.18). Upon addition of $ZnCl_2$ the lifetime of the lanthanide excited state increased in D_2O. However, it decreased in H_2O. The same result was obtained with **[TbL^7]** (Table 4.4).

Table 4.4 Luminescence lifetime measurements of **[EuL^7]** and **[TbL^7]** with and without an excess of Zn^{2+} (295 K, λ_{ex} = 276 nm, pH/pD = 7.3).

Ln	Zn^{2+} equivalents	τ_{H_2O} (ms)	τ_{D_2O} (ms)	q
Eu	0	1.15	1.61	0.00
	5	0.61	1.96	1.06
Tb	0	2.55	2.78	-0.14
	5	1.94	3.19	0.75

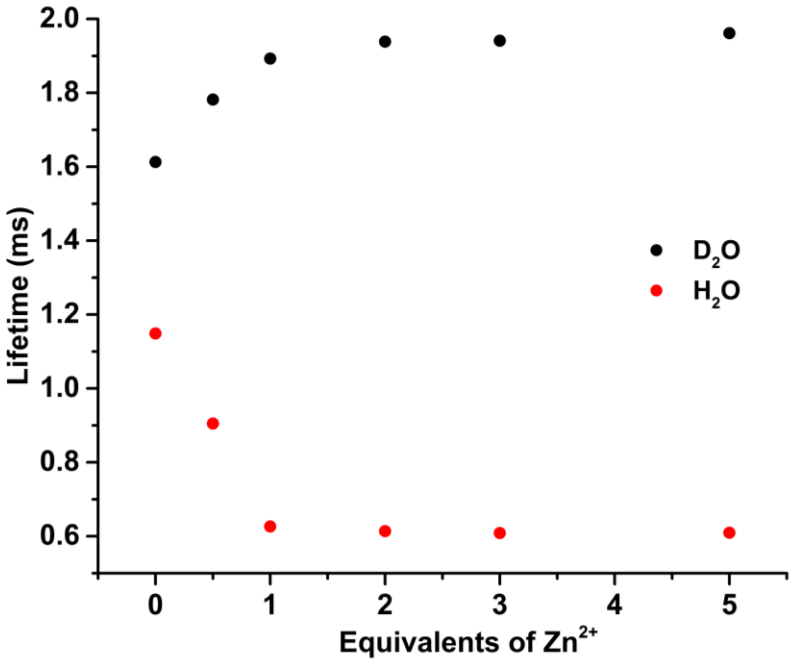

Figure 4.18 Variation of the lifetime of **[EuL^7]** as a function of equivalents of Zn^{2+} in H_2O and D_2O (295 K, 0.1 M TRIS/TRIS-d_{11}, pH/pD = 7.3, λ_{ex} = 276 nm, λ_{em} = 617 nm).

The hydration states of the europium and terbium ions following binding of Zn^{2+} were calculated to be q = 1 (Table 4.4). The coordination of an inner sphere water molecule and the observation of the lifetime variation are consistent with a 1:1 binding stoichiometry, in which the binding mode is analogous to that originally proposed by Pope and co-workers (Figure 4.3). The *tert*-butyl pyridine is no longer coordinated to the lanthanide ion, and the zinc ion is coordinated to all three pyridine nitrogen atoms and the tertiary amine N atom (Scheme 4.11).

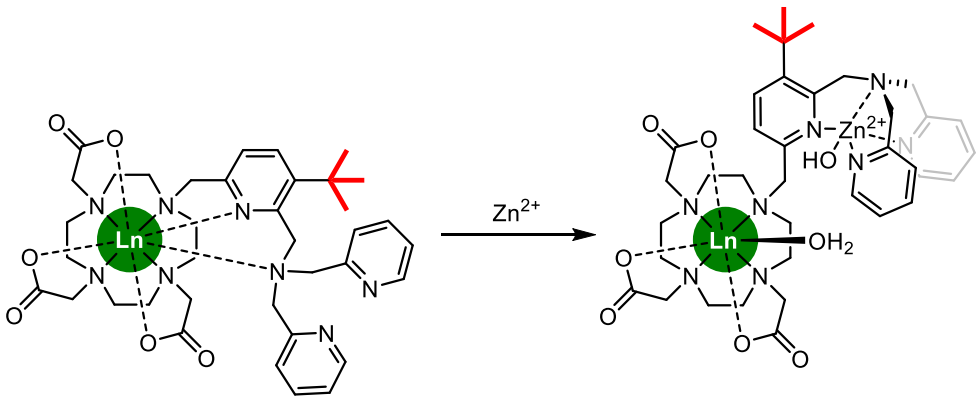

Scheme 4.11 Proposed structures of **[LnL^7]** without (*left*) and with Zn^{2+} (*right*). It is assumed that the Zn^{2+} ion will be 5-coordinate and that at pH 7.3 the coordination is completed by OH^-.

The selectivity of this probe towards Zn^{2+} with respect to other biologically relevant, divalent cations was explored through titrations of $CaCl_2$ and $MgCl_2$ with **[EuL^7]**. No

change in spectral form was observed upon addition of up to 10 equivalents (200 µM) of the cations in each case, indicating that no significant interaction was occurring with the complex (Figure 4.19).

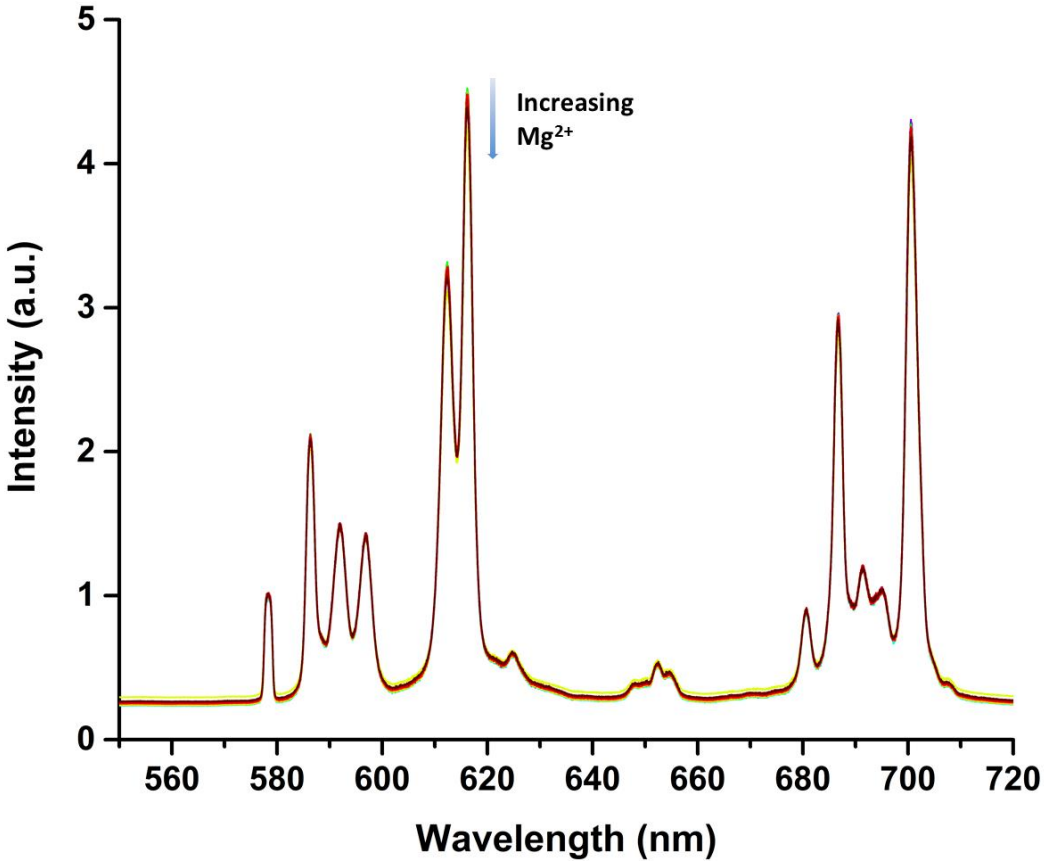

Figure 4.19 Variation of emission spectral form for **[EuL^7]** (20 µM) as a function of [Mg^{2+}] (295 K, H_2O, 0.1 M TRIS, pH/pD = 7.3, λ_{ex} = 276 nm).

In order to prove that Zn^{2+} binding is reversible, ligands with a high affinity for Zn^{2+} (ethylenediaminetetraacetic acid (EDTA) and diethylenetriaminepentaacetic acid (DTPA)) were titrated into a 1:1 solution of **[EuL^7]** and $ZnCl_2$ (Figure 4.20).

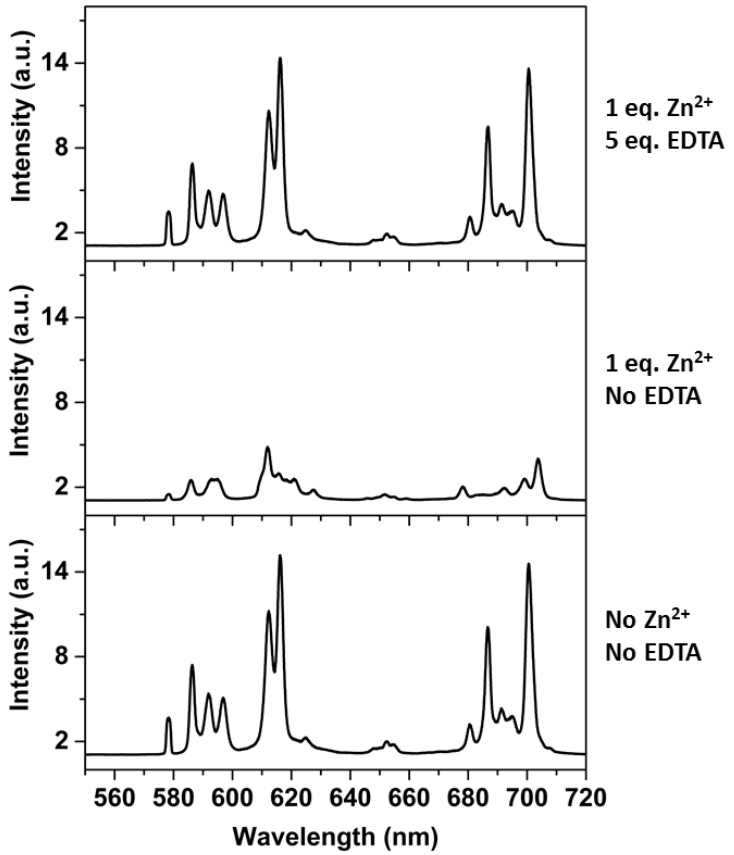

Figure 4.20 Stacked emission spectra of **[EuL^7]** (20 μM) (*bottom*) alone, with one equivalent of Zn^{2+} (*centre*) and with one equivalent of Zn^{2+} and 5 equivalents of EDTA (*top*) (295 K, H_2O, 0.1 M TRIS, pH/pD = 7.3, λ_{ex} = 276 nm).

The titrations revealed the restoration of the spectral form of the free complex **[EuL^7]** at high concentrations of the competing ligand, demonstrating that the binding of Zn^{2+} is reversible. The stability of complexes of Zn^{2+} with EDTA and DTPA are known to be $\log K_{ML}$ = 16.5 and 18.7 respectively, and the competitive titrations indeed showed that binding to these ligands is stronger than **[LnL^7]**. Binding curves were plotted using the ratio of the intensity integrals for the ΔJ = 2 and ΔJ = 1 bands. The binding curve constructed for DTPA showed that at a 1:1:1 ratio of Zn^{2+}:**[EuL^7]**:DTPA, almost full restoration of the free complex (~87%) could be seen (Figure 4.21). Addition of EDTA was found to be slightly less competitive (~85%), as expected from its lower stability constant with Zn^{2+}.

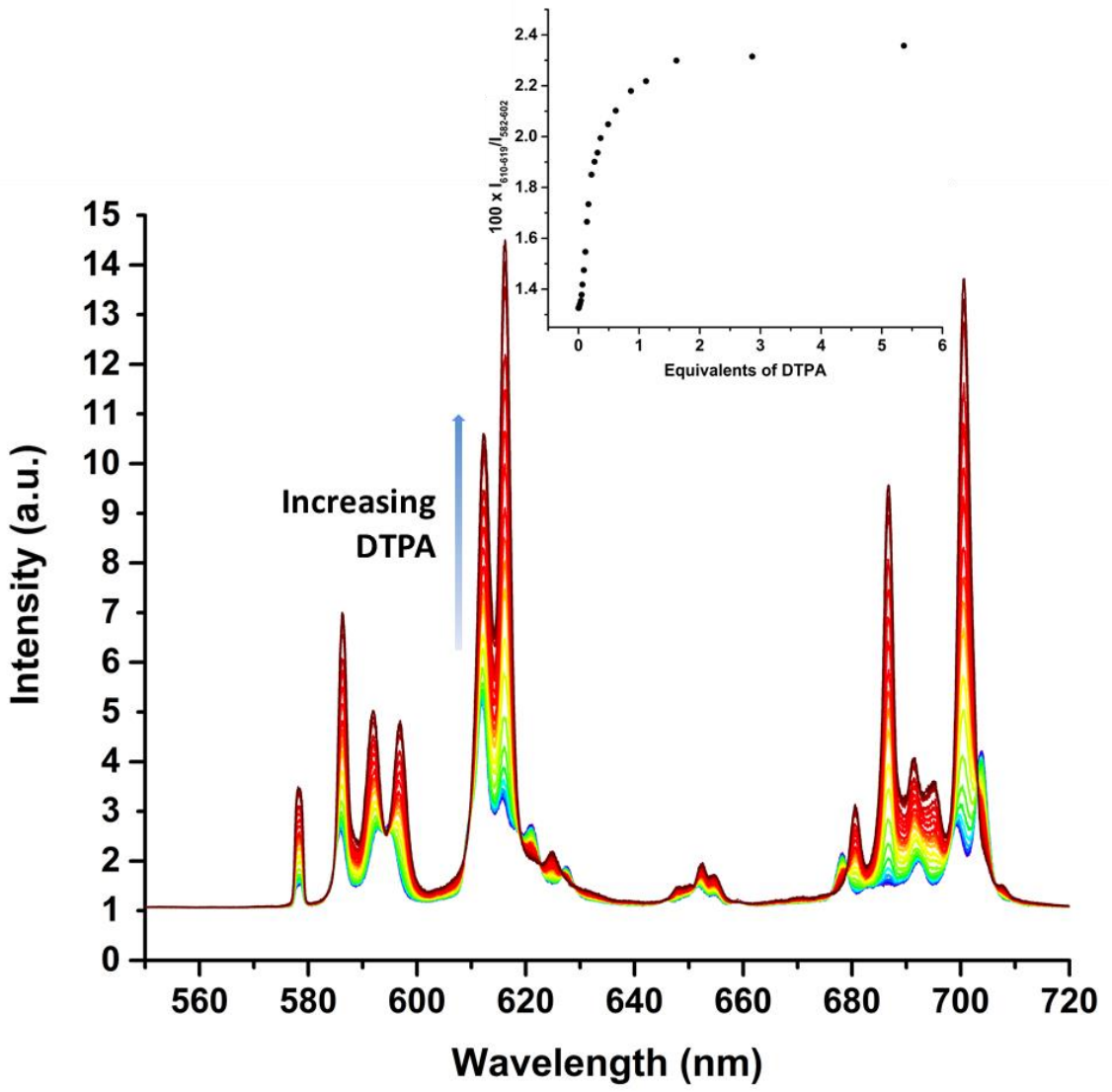

Figure 4.21 Variation of emission spectra of a 1:1 solution of $ZnCl_2$ (20 µM) and **[EuL^7]** (20 µM)as a function of DTPA concentration. (Inset) Ratio of ΔJ = 2 ($I_{610\text{-}619\ nm}$) / ΔJ = 1 ($I_{582\text{-}610\ nm}$) as a function of equivalents of Zn^{2+} (295 K, H_2O, 0.1 M TRIS, pH/pD = 7.3, λ_{ex} = 276 nm).

4.4.2 Mass spectrometric analysis of [TbL^7]: Zn^{2+} response

Mass spectrometry was employed to probe the stoichiometry of the Zn^{2+} interaction with **[LnL^7]**. Electrospray mass spectrometry experiments were conducted using a 1:2 mixture of **[TbL^7]** and $ZnCl_2$ in H_2O (Figure 4.22). A 1:2 ratio of Zn^{2+}:**[TbL^7]** was chosen first, to probe the possibility of the presence of the 1:2 ternary complex, as a related system has exhibited this stoichiometry.[28] The Tb complex was chosen in order to simplify the isotopic pattern, due to the presence of only one stable isotope of this lanthanide. The buffer TRIS is involatile and can inhibit electrospray mass spectral analysis, and so was not used. However, the pH of the solution was adjusted to 7.3 with aqueous NaOH in order to best recreate the titration conditions.

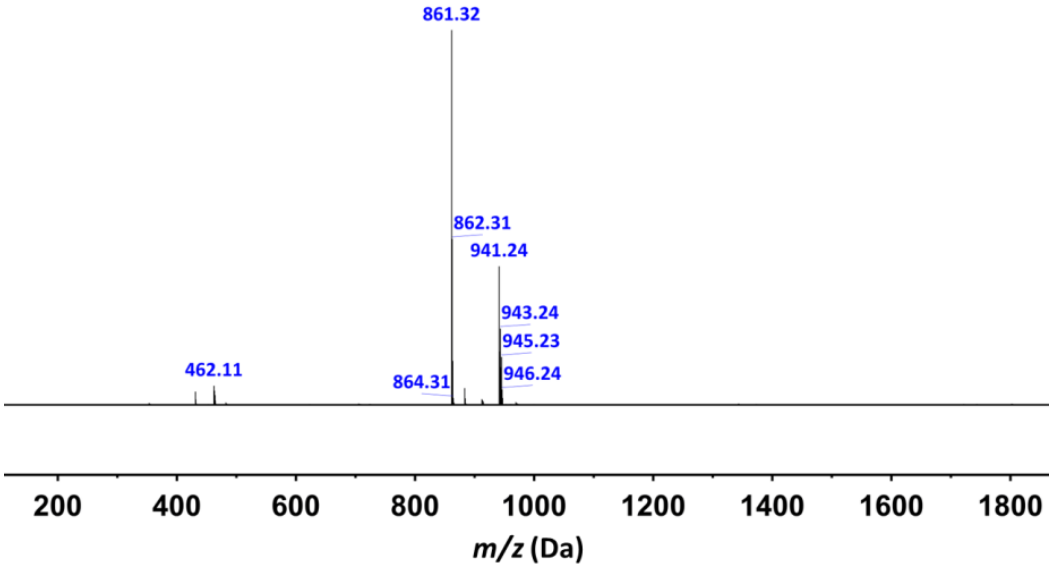

Figure 4.22 Observed ESI-HRMS (+) spectrum of a 1:2 solution of $ZnCl_2$ and **[TbL^7]** in H_2O (pH 7.3).

The spectrum shows the presence of protonated free complex (*m/z* = 861.3, {**[TbL^7]**+H}$^+$) as the major ion and two other main species. The ion at 462.1 exhibits the distinctive isotope pattern of Zn and is found to be the half mass of the doubly charged ion in a 1:1 stoichiometric complex {**[TbL^7]**+Zn+H_2O}$^{2+}$. The ion corresponding to a mass of 941.2 is the related singly charged deprotonated complex {**[TbL^7]**+Zn+OH}$^+$ (Figure 4.23). Typically, the inner sphere water molecules of lanthanide complexes are not seen by electrospray mass spectrometry. It is therefore reasonable to hypothesise that in solution two water molecules are bound to the complex, one residing on each metal centre and the water/hydroxide seen by mass spectrometry is bound to zinc. It is known that zinc aqua species possess relatively acidic coordinated water molecules, typically with a pK_a value between 7 and 9.

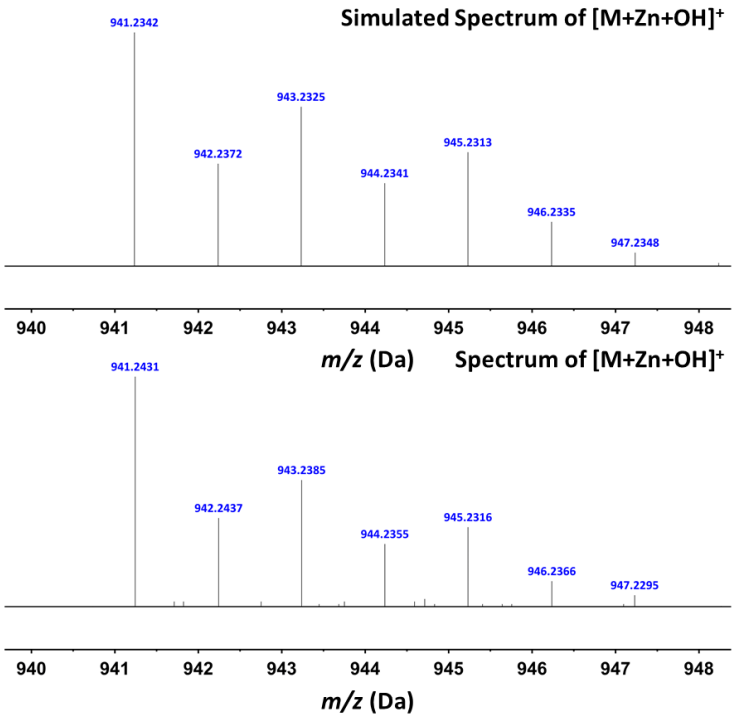

Figure 4.23 (*Top*) Simulated ESI-HRMS (+) spectrum of **{[TbL^7]+Zn+OH}$^+$**. (*Bottom*) Observed ESI-HRMS (+) spectrum of **{[TbL^7]+Zn+OH}$^+$**.

No species corresponding to any other binding stoichiometry was present in the mass spectrum. Mass spectrometry however, cannot conclusively preclude the existence of other binding modes in solution.

4.4.3 Diamagnetic NMR studies of [YL^7]: Zn^{2+} response

An initial NMR titration was conducted on the diamagnetic complex **[YL^7]**, maintaining the pD at 7.3 with 1 M TRIS buffer (Figure 4.24).

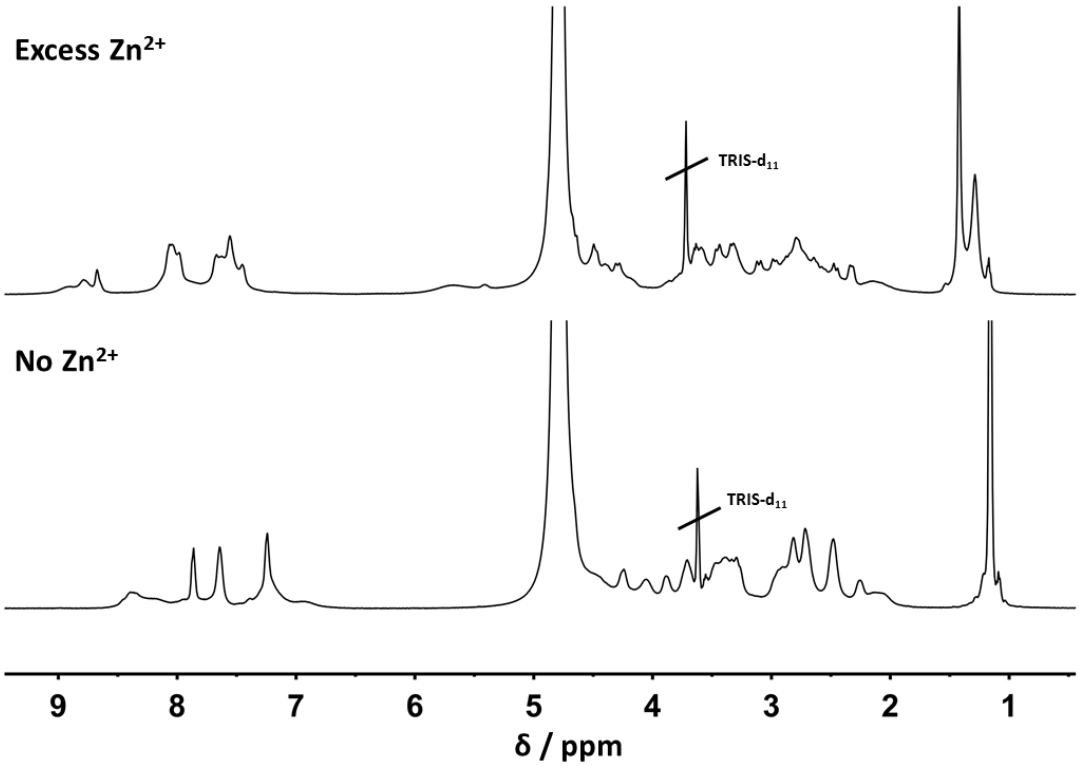

Figure 4.24 Stacked ^{1}H NMR spectra of **[YL^{7}]** at different concentrations of Zn^{2+}; (*top*) 3 equivalents and (*bottom*) no equivalents (D_2O, 1 M TRIS-d_{11}, pD 7.3, 11.7 T, 295 K).

Upon addition of $ZnCl_2$ new resonances appear in the aromatic and macrocyclic regions. Within the aromatic region, a general trend of the observed resonances shifting to higher frequency was observed, which is consistent with the association of a Zn^{2+} ion to the DPA moiety. The *tert*-butyl resonance of the free complex decreases and at least two new resonances appear (Figure 4.25). The major new *tert*-butyl resonance is now found at 1.4 ppm, compared to 1.2 ppm of free complex. The slight increase in chemical shift suggests that there has been a significant change to the chemical environment of the *tert*-butyl appended pyridine, as this *tert*-butyl resonance was found in ligand syntheses to be relatively insensitive to proximate functional group interconversion. The new resonances observed were broader than that of the free complex, which is indicative of a chemical exchange process occurring that is of the order of the NMR timescale.

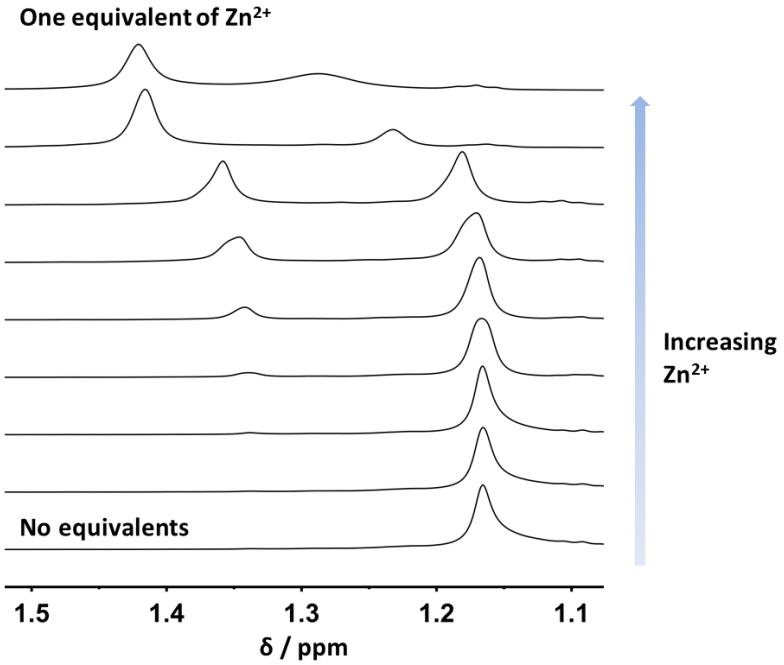

Figure 4.25 Stacked ^{1}H NMR spectra of the *tert*-butyl resonances of **[YL^{7}]** as a function of Zn^{2+} (D_2O, 1 M TRIS-d_{11}, pD 7.3, 11.7 T, 295 K).

During the NMR titration a precipitate was observed to form slowly at a Zn^{2+} equivalence greater than 1. Initially, it was thought that the precipitate was $Zn(OH)_2$. To assess this possibility, the NMR solution was centrifuged and a small amount of the relatively insoluble solid was re-dissolved in a 50:50 mixture of acetonitrile and H_2O. Electrospray mass spectral analysis of the dissolved solute revealed the presence of the free Y complex, {**[YL^{7}]**+H}$^{+}$ (791.4 and 396.4), but also {**L^{7}**+2Zn}$^{+}$ (833.3 and 417.3) and {**L^{7}**+Zn+2H}$^{+}$ (767.4), in which the Y^{3+} has been lost and replaced by Zn^{2+} (Figure 4.26 and 4.27). The species containing only one Zn^{2+} ion is assumed to be the 7-coordinate complex, in which Zn^{2+} has displaced Y^{3+} from the DO3A macrocycle.

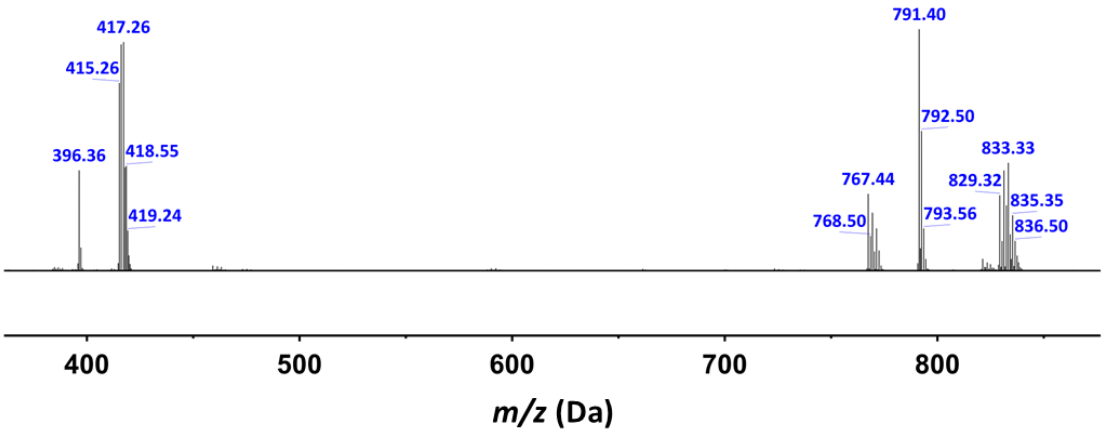

Figure 4.26 Observed ESI-LRMS (+) spectrum of the 1:2 solution of $ZnCl_2$ and **[YL^{7}]** in 1:1 H_2O:MeCN.

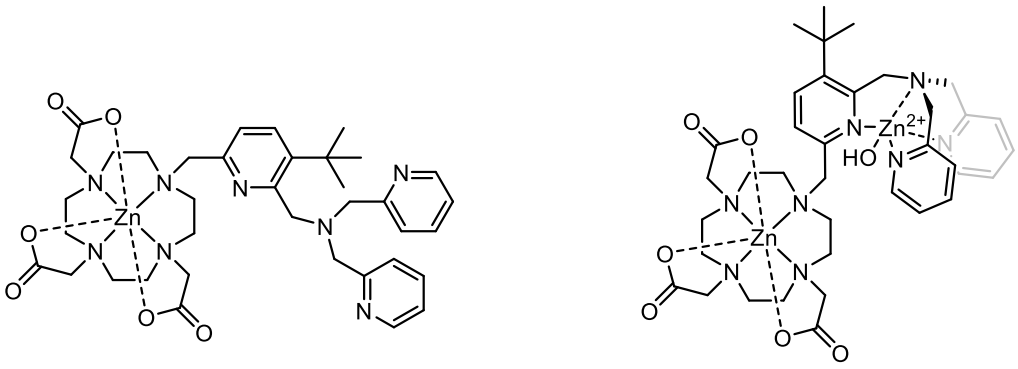

Figure 4.27 Proposed structures of **{L^7 + Zn}** (*left*) and **{L^7 + 2Zn}** (*right*).

As Zn^{2+} is a diamagnetic ion, distinguishing between the Zn^{2+} and Y^{3+} complexes using NMR is impracticable. However, as the Zn^{2+} substituted complexes were observed as a precipitate and were found to be insoluble in most solvents, the NMR spectra acquired during the original titration can be assumed to be species based on the 1:1 Y^{3+} complex, **[YL^7]**.

The time-dependent trans-metallation of DO3A-based lanthanide(III) complexes in the presence of metal cations, including Zn^{2+}, is a known process (Equation 4.1). It is generally thought that this is normally an acid-catalysed process only occurring at low pH.[29,30]

$$[LnL]^n + M^{2+} \rightleftharpoons Ln^{3+} + [ML]^{n-1} \qquad (4.1)$$

The stability of various gadolinium contrast agents to trans-metallation by Zn^{2+} has been studied previously when assessing their kinetic stability in solution.[29,30] The longitudinal relaxation rate of water was measured in a phosphate-buffered solution in the presence of Zn^{2+}. If trans-metallation occurs, the released Gd^{3+} will react to form insoluble $GdPO_4$ and can no longer enhance the relaxation rate of water. The decrease in proton relaxation rate is thus proportional to the extent of trans-metallation that has occurred. The studies were conducted on 9-coordinate macrocyclic Gd^{3+} contrast agents based on octadentate ligands (e.g. with DOTA and HPDO3A) at pH 7 and 310 K. It was found that after 3 days of stirring, more than 98% of relaxivity was retained; suggesting that trans-metallation with Zn^{2+} is extremely slow in these complexes.

It is known that trans-metallation of lanthanides occurs more quickly in 7-coordinate complexes. Similar experiments have been conducted on **[GdDO3A]** in the presence of between 10 to 40 equivalents of Cu^{2+}.[31] Although **[CuDO3A]** was shown to have a

significantly higher stability constant (25.8) than **[GdDO3A]** (21.6), the half-life of **[GdDO3A]** in the presence of copper was calculated to be ~24 years. The rate constant of trans-metallation, k_d, was assumed to be made up of two contributions, k_0 and k_1 (Equation 4.2):

$$k_d = k_0 + k_1[H^+] \qquad (4.2)$$

where k_0 describes the spontaneous dissociation of Gd^{3+} from **[GdDO3A]**, followed by the fast reaction of the free ligand with Cu^{2+}, and k_1 describes the proton-assisted dissociation of Gd^{3+} and replacement with Cu^{2+}. Values of k_0 were found to be extremely low (10^{-8} - 10^{-9} s^{-1}) and indicated that spontaneous dissociation does not contribute to trans-metallation.

Significant trans-metallation of Zn^{2+} has occurred in **[YL^7]** at room temperature in the presence of 3 equivalents of Zn^{2+} at pH 7.3. It is unlikely that trans-metallation occurs with the free complex **[YL^7]**, as this has been shown by luminescence lifetime and NMR analysis to be at least 8-coordinate. The ease of dissociation of Y^{3+} suggests that the initial complexation of Zn^{2+} to the DPA moiety induces a conformational change that increases the susceptibility of the complex to trans-metallation.

4.4.4 Solid state structure analysis

Crystals of **[DyL^7]** were grown by slow diffusion of diethyl ether into a methanol solution of the complex (Figure 4.28). The complex crystallised in the centrosymmetric space group $P2_1/c$, meaning that both enantiomers were present within the crystal lattice and are symmetry related. Hydrogen bonding was present, involving two of the carbonyl groups serving as H-bond acceptors to two donor solvent methanol molecules.

The coordination number of Dy^{3+} in **[DyL^7]** is 9, in an environment of N_6O_3. The Dy^{3+} ion is coordinated by the four ring nitrogen atoms (N_4) and the *tert*-butyl pyridine nitrogen atom and three anionic oxygen atoms (O_3N) in a SAP geometry (Δ-(λλλλ)). The coordination sphere is completed by the DPA amine nitrogen atom, which is coordinated axially to the lanthanide ion.

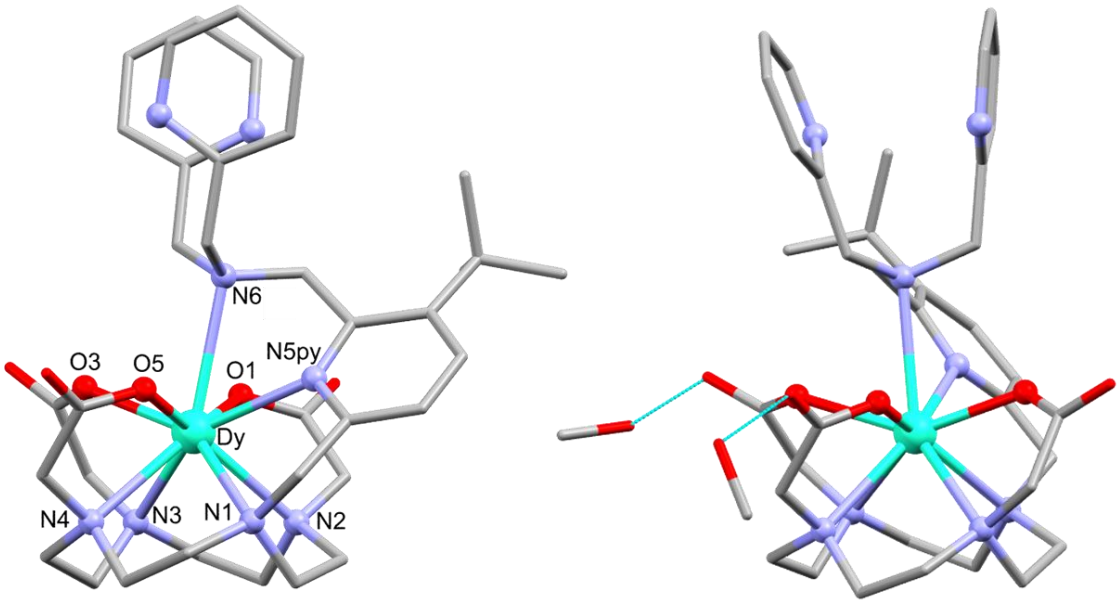

Figure 4.28 (*Right*) Molecular structure of Δ-(λλλλ)-**[DyL^7]**. (*Left*) Molecular structure of Δ-(λλλλ)-**[DyL^7]** showing the hydrogen bonding to solvent methanol. H atoms are omitted for clarity.

Bond distances between Dy^{3+} ion and the donors varied (Table 4.5). The bonds to the neutral nitrogen donors are much longer than those to the anionic carboxylate oxygens. A long, axial bond of 2.83 Å between the lanthanide and the DPA amine nitrogen was found, as predicted from the NMR studies.

Table 4.5 Bond distances in the N_6O_3 coordination sphere for **[DyL^7]**.

bond	bond length (Å)
Dy-N1	2.605(3)
Dy-N2	2.655(3)
Dy-N3	2.654(3)
Dy-N4	2.632(4)
Dy-N5py	2.559(3)
Dy-O1	2.321(3)
Dy-O3	2.266(2)
Dy-O5	2.267(2)
Dy-N6	2.833(3)

The average distance of the *tert*-butyl protons to the Dy^{3+} ion was 6.78 Å, similar to that found with **[YbL^{H}]** (6.70 Å), and in accordance with the ionic radius variation of the lanthanide contraction.

The additional axial interaction with the DPA amine nitrogen (N6) results in the metal ion being shifted towards the O_3N_1 antiprism base. In the related carboxylate complex **[YbL^{H}]**, the Yb^{3+} ion is found 1.07 and 1.44 Å from the O_3N and N_4 bases respectively. In **[DyL^{7}]**, the distances of the Dy^{3+} ion to the O_3N and N_4 bases are now 0.78 and 1.61 Å.

In order to explore the nature of the Zn^{2+} binding to both the DPA moiety and the DO3A-macrocycle, crystals of the complex **[YL^{7}]** in the presence of $ZnCl_2$ were grown. A methanol solution of **[YL^{7}]** with 1 equivalent of $ZnCl_2$ and 1 equivalent of NH_4PF_6 to act as a bulky counter anion was prepared. Diffusion of diethyl ether into this mixture resulted in the growth of crystals. It was hoped that a 1:1 ratio of **[YL^{7}]**:ZnCl would yield crystals of **[YZnL^{7}],** however, analysis of the crystals grown proved them to be the trans-metallation product, **[Zn$_2$L^{7}]$^{+}$** (Figure 4.29). The cationic di-zinc complex crystallised as the chloride salt and hydrogen bonding to solvent methanol was observed for two of the carbonyl atoms.

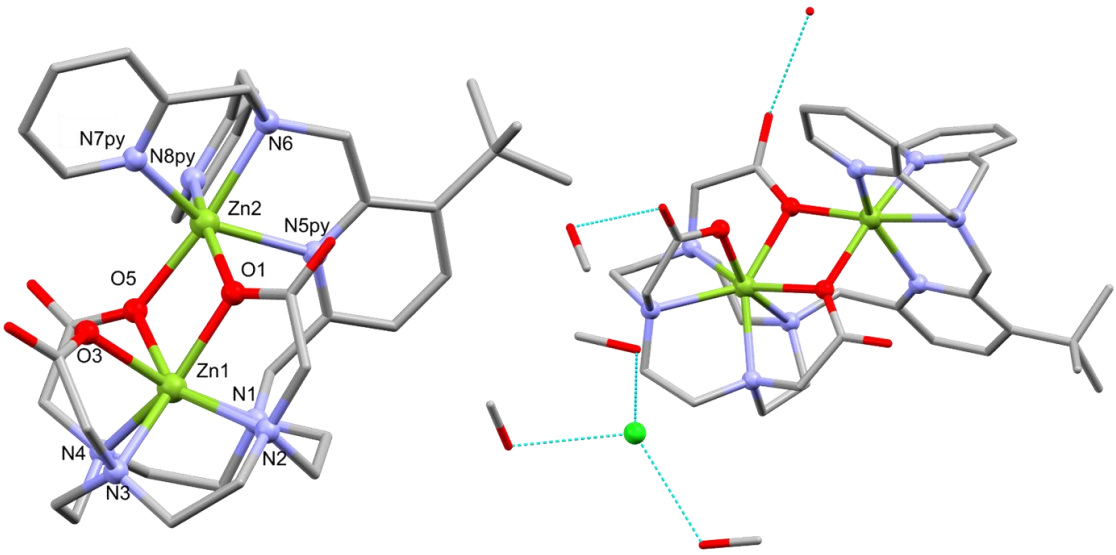

Figure 4.29 (*Right*) Molecular structure of **[Zn$_2$L^{7}]**. (*Left*) Molecular structure of **[Zn$_2$L^{7}]** showing the chloride counter ion and hydrogen bonding to solvent methanol. H atoms are omitted for clarity.

The two Zn^{2+} ions of **[Zn$_2$L^{7}]** were 6- and 7- coordinate, with two of the carboxylate donors acting as bridging donors. The 7-coordinate metal (Zn1) was encapsulated within the DO3A-based macrocycle giving a N_4O_3 coordination environment. Zinc

species with such a high coordination number are relatively rare. Complexes containing a 7-coordinate Zn^{2+} ion in which the 7 donor atoms are provided by a single polydentate ligand are even more uncommon, although there are a few literature examples.[32–37] The cyclen-based Zn^{2+} complex **[ZnL^{G1}]**, for example, has been synthesised and studied as a monomer for heterometallic coordination polymers (Figure 4.30).[37] The coordination geometry is similar to that of Zn1, however one of the O donors arises from a neutral amide.

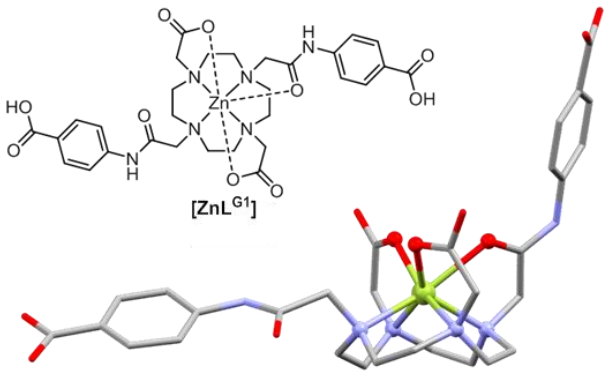

Figure 4.30 Molecular structure of **[ZnL^{G1}]**. H atoms are omitted for clarity.[37] CCDC identifier: 1443839 / MABVET.

The 6-coordinate Zn^{2+} ion (Zn2) was ligated by the four nitrogen donors of the tripicolyl moiety and the two bridging carboxylates in a distorted octahedral (N_4O_2) geometry. The geometry of Zn2 is similar to that of the Zn-TPA complex **[Zn$_2$(TPA)$_2$(OH)$_2$]$^{2+}$** (Figure 4.31),[38] in which both Zn^{2+} ions are ligated in a distorted octahedral geometry by the 4 neutral nitrogen donors of the TPA ligand and two bridging O donors. In this case the bridging O donors are hydroxide groups, however, carboxylate bridges (μ-$O_{carboxylate}$) in di-zinc species are also known.[39–41] The Zn-Zn distance of **[Zn$_2$L^7]** was found to be 3.36 Å which is comparable to those reported in similar zinc complexes with (μ-$O_{carboxylate}$)$_2$ bridges (3.11 – 3.50 Å).[38]

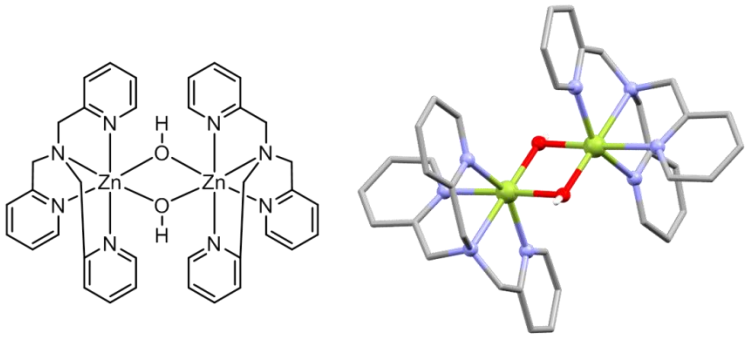

Figure 4.31 Molecular structure of **[Zn$_2$(TPA)$_2$(OH)$_2$]$^{2+}$**. H atoms of the TPA ligand are omitted for clarity. CCDC identifier: 1230684 / PEMBIS.

As the ionic radius of Zn^{2+} is much smaller than that of Dy^{3+}, the metal-donor bond distances to the transition metal are decreased from those seen in **[DyL^7]** (Table 4.6).

Table 4.6 Bond distances in the coordination sphere of Zn1 (*left*) and Zn2 (*right*) in **[Zn$_2$L^7]$^+$**.

bond	bond distance (Å)
Zn1-N1	2.418(5)
Zn1-N2	2.237(4)
Zn1-N3	2.342(5)
Zn1-N4	2.212(5)
Zn1-O1	2.080(3)
Zn1-O3	2.123(4)
Zn1-O5	2.244(3)

bond	bond distance (Å)
Zn2-N5py	2.236(4)
Zn2-N6	2.183(4)
Zn2-N7py	2.120(4)
Zn2-N8py	2.179(5)
Zn2-O1	2.125(3)
Zn2-O5	2.060(3)

4.4.5 Paramagnetic NMR studies of [LnL^7]: Zn^{2+} response

The paramagnetic spectra of the Dy, Tb and Tm complexes of **[LnL^7]** were measured in the absence and presence of varying Zn^{2+} concentrations. In each case, the intensity of the resonance corresponding to the *tert*-butyl of the free complex decreased upon addition of $ZnCl_2$. As the concentration of Zn^{2+} increased, multiple new resonances appeared making the identification of the *tert*-butyl peaks challenging. After addition of one equivalent of Zn^{2+}, all resonances were integrated and *tert*-butyl peaks were found by identifying a 9:1 ratio with other proton resonances. Trans-metallation of the lanthanide ion was not observable by NMR at this concentration, as no ligand resonances were observed in the diamagnetic region. However, above this concentration of added $ZnCl_2$, a precipitate was observed and the integrals of the complex resonances decreased slightly.

Upon addition of $ZnCl_2$ to **[DyL^7]** three new *tert*-butyl resonances appeared, as identified by integration (Figure 4.32, Table 4.7).

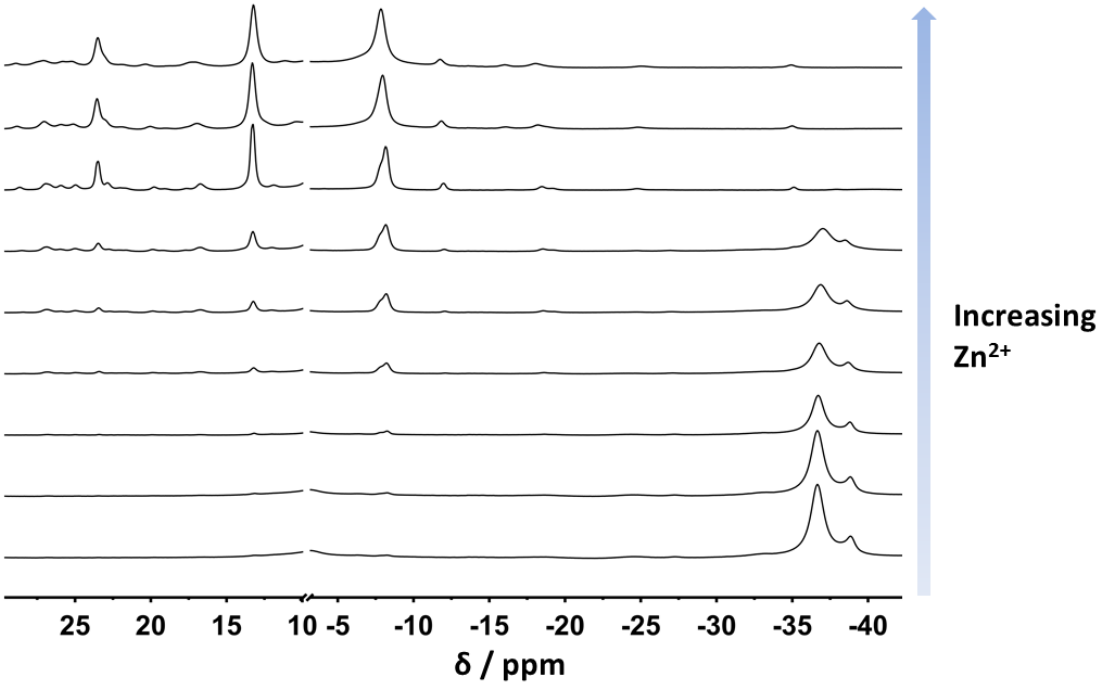

Figure 4.32 Stacked ^{1}H NMR spectra of the *tert*-butyl resonances of **[DyL^{7}]** as a function of Zn^{2+} (D_2O, 1 M TRIS-d_{11}, pD 7.3, 11.7 T, 295 K).

A binding curve was produced by plotting the ratio of the integral of the free complex *tert*-butyl resonance and the sum of the newly formed *tert*-butyl integrals against the number of equivalents of added Zn^{2+} (Figure 4.33). The curve is similar in form to that found from luminescence titrations of **[EuL^{7}]**, and similarly the binding was too strong to be effectively fitted.

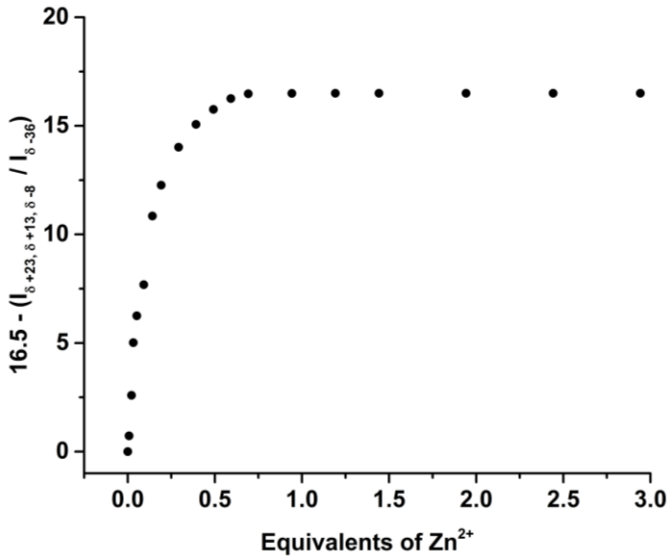

Figure 4.33 Ratio of the integrals of *tert*-butyl resonances at +23, +13 and -8 ppm ($I_{\delta +23, +13, -8}$) and the integral of *tert*-butyl resonance at -36 ppm ($I_{\delta -23}$) of **[DyL^{7}]** as a function of the number of equivalents of Zn^{2+} (D_2O, 1 M TRIS-d_{11}, pD 7.3, 11.7 T, 295 K).

Titrations with **[TbL^7]** and **[TmL^7]** yielded similar results; the NMR spectra of the initial and end points of the titration and the plotted binding curves are shown in Figure 4.34. As with **[DyL^7]**, addition of Zn^{2+} led to the appearance of additional *tert*-butyl peaks, some of which are also shifted in the opposite direction to the shift of the *tert*-butyl resonance in the free complex. Similarly to the Dy^{3+} complex, the binding was too strong (K_d < 1 µM) to be effectively fitted.

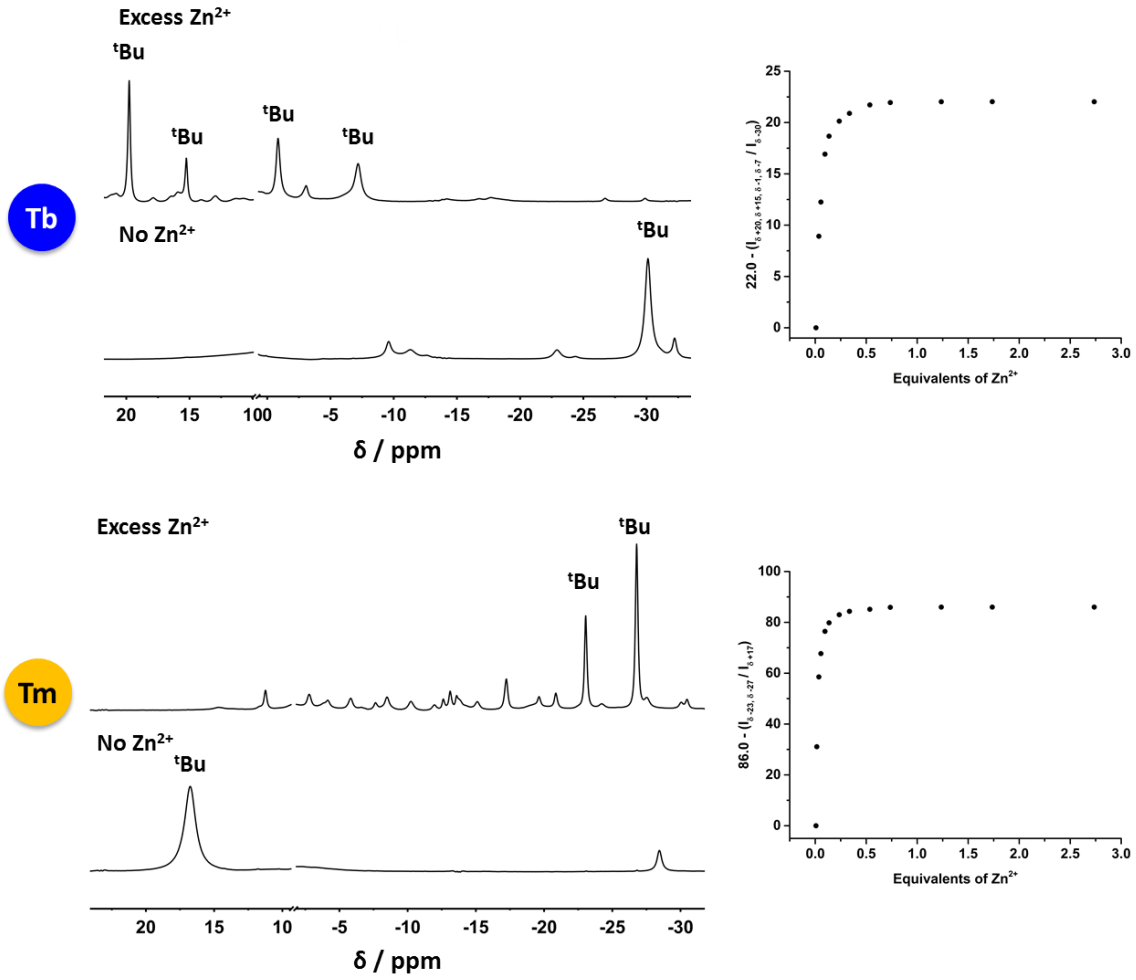

Figure 4.34 (*Left*) Stacked ^{1}H NMR spectra of the *tert*-butyl resonances of **[TbL^7]** (*top*) and **[TmL^7]** (*bottom*) before and after addition of excess Zn^{2+}. (*Right*) Ratio of the integrals of *tert*-butyl resonances of **[TbL^7]** (*top*) and **[TmL^7]** (*bottom*) as a function of the number of equivalents of added Zn^{2+} (D_2O, 1 M TRIS-d_{11}, pD 7.3, 11.7 T, 295 K).

The shift and relaxation rate data of the identified *tert*-butyl resonances for **[LnL^7]** before and after addition of Zn^{2+} are listed in Table 4.7.

Table 4.7 Comparison of NMR properties of the *tert*-butyl resonances in **[DyL^7]** (*top*), **[TbL^7]** (*centre*) and **[TmL^7]** (*bottom*), with and without addition of Zn^{2+} (D_2O, 1 M TRIS-d_{11}, pD 7.3, 11.7 T, 295 K).

	Shift (ppm)	Linewidth (Hz)	R_1 (Hz)	Integral
No Zinc	-36	584	182	1
Zinc	+23	244	53	0.16
	+13	255	55	0.31
	-8	320	21	0.52

	Shift (ppm)	Linewidth (Hz)	R_1 (Hz)	Integral
No Zinc	-30	280	112	1
Zinc	+20	109	44	0.33
	+15	108	34	0.12
	-1	185	16	0.27
	-7	313	26	0.27

	Shift (ppm)	Linewidth (Hz)	R_1 (Hz)	Integral
No Zinc	+17	488	63	1
Zinc	-23	105	17	0.36
	-27	110	26	0.64

All the longitudinal and transverse relaxation rates of the Zn^{2+}-bound complex were significantly decreased compared to those measured in the free complex. A decrease in relaxation rates most likely arises from an increase in the internuclear distance, r. Additionally, the presence of new *tert*-butyl resonances that are shifted in the opposite direction to free **[LnL^7]** indicates a dramatic change in the structure of the complex upon binding to Zn^{2+}. The paramagnetic NMR titrations results are consistent with a process in which the *tert*-butyl appended pyridine moiety dissociates from the lanthanide ion upon addition of Zn^{2+} ions.

Addition of excess Mg^{2+} and Ca^{2+} induced negligible changes in chemical shift behaviour of **[DyL^7]** (Figures 4.35 and 4.36), consistent with the expected high selectivity for Zn^{2+}.

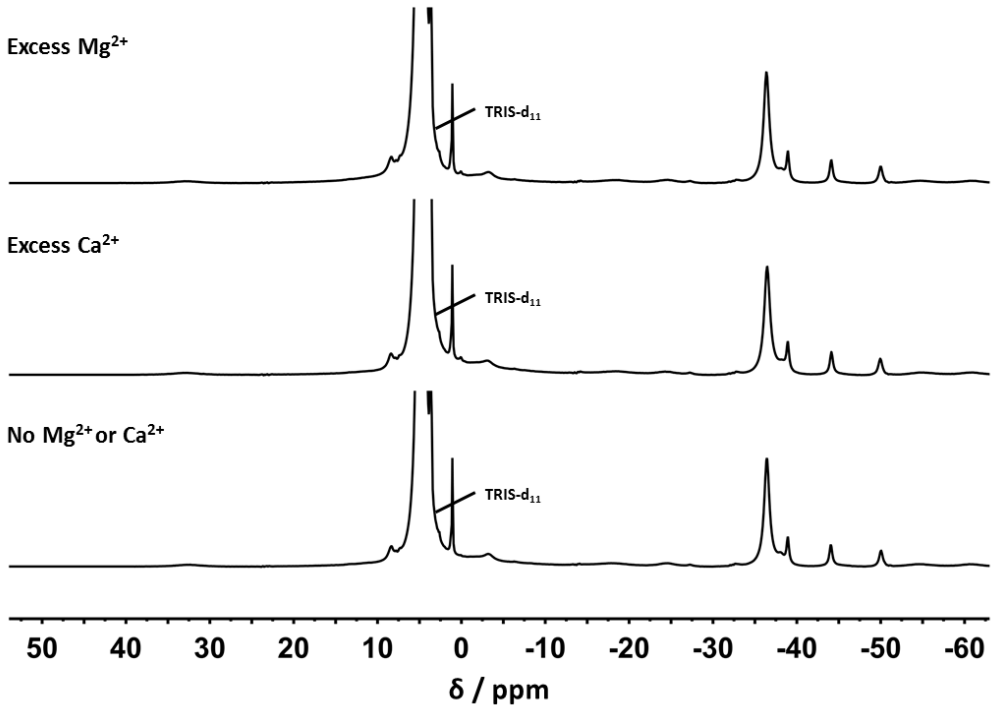

Figure 4.35 Stacked ^{1}H NMR spectra of **[DyL^{7}]** (*bottom*) and after addition of excess Ca^{2+} (*centre*) or Mg^{2+} (*top*). (D_2O, 1 M TRIS-d_{11}, pD 7.3, 11.7 T, 295 K).

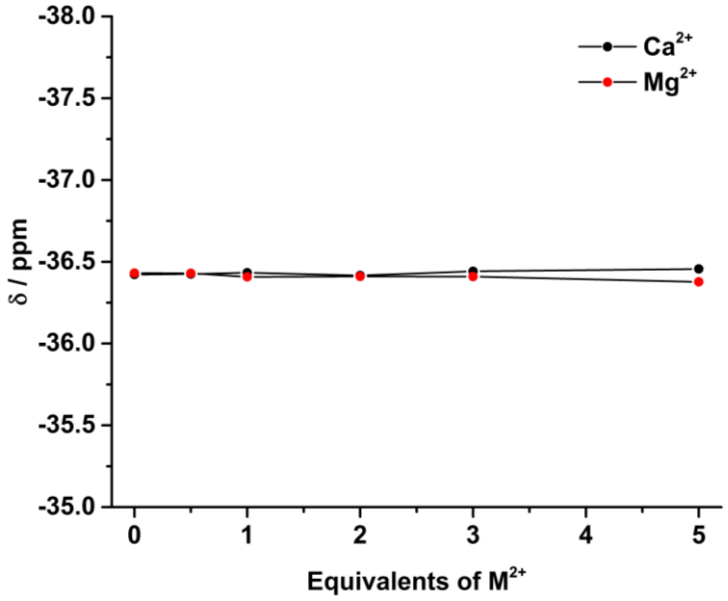

Figure 4.36 Chemical shift of the *tert*-butyl resonance of **[DyL^{7}]** as a function of the number of equivalents of Ca^{2+} (*black*) and Mg^{2+} (*red*). (D_2O, 1 M TRIS-d_{11}, pD 7.3, 11.7 T, 295 K).

4.5 Conclusions and Future Work

A novel NMR Zn^{2+} sensor, **[LnL^{7}]**, based on a DO3A macrocycle bearing a pendant pyridine arm containing both a *tert*-butyl reporter group and a DPA moiety has been synthesised and characterised.

The tripicolyl amine Zn^{2+} sensing arm was synthesised in moderate yield using a 10 step linear synthesis, including a 100% regioselective reduction step, with the aid of simple protecting chemistry. Alkylation of the pendant arm onto both a trimethylphosphinate and carboxylate appended macrocycle proceeded successfully. However, complexation could only be achieved with the less sterically bulky carboxylate-based macrocycle, DO3A.

Solid state structure analysis showed that the complex was 9-coordinate, with the amine nitrogen atom of the DPA moiety completing the coordination with a long, axial bond to the lanthanide. At high temperature or low pH this bond was weakened or lost, as observed from lifetime measurements of the Eu^{3+} and Tb^{3+} complexes and the diamagnetic and paramagnetic NMR spectra of the Y^{3+} and Dy^{3+} complexes. The pK_a value of the complex was measured to be 5.7 by luminescence. This value is low enough that changes in pH within a biological range of 6.5-7.5 will have minimal impact on the behaviour of the complex.

The *tert*-butyl resonance of the Dy, Tb and Tm complexes shift beyond the diamagnetic region, in principle allowing them to be imaged against zero background. The PARASHIFT properties of these resonances have been investigated at different temperatures and magnetic fields. High longitudinal relaxation rates at low fields allow for fast acquisition, and linear temperature sensitivities will allow for non-invasive temperature measurement.

The binding to Zn^{2+} has been probed using both luminescence and NMR studies revealing an extremely strong affinity. Large changes are observed in emission and NMR properties of the complexes, indicating a 1:1 binding mode and suggesting a decrease in the coordination number of the lanthanide ion. Mass spectrometry studies provided further proof of the 1:1 binding mode. Selectivity was demonstrated for Zn^{2+} over Ca^{2+} and Mg^{2+} and binding reversibility was shown through competitive titrations with EDTA and DTPA. The affinity of the complex to Zn^{2+} could be adapted by modification of the chelating group. Removal of one of the pyridines of the DPA moiety could reduce the Zn^{2+} binding strength but the replacement chelator must be chosen carefully to avoid the loss of selectivity.

At higher concentrations of Zn^{2+}, trans-metallation was observed in which the lanthanide is replaced to form a novel di-zinc species. Trans-metallation of DO3A-based lanthanide complexes is unprecedented at this pH. X-ray crystallography elucidated the solid state structure of the trans-metallated di-zinc species. One Zn^{2+} ion was found to be 7-coordinate, an unusually high, although not unique, coordination number. Two carboxylate groups of the DO3A macrocycle were found to be bridging both Zn^{2+} ions.

The kinetic stability of the complex with respect to trans-metallation within biological media must be explored. Further *in vitro* work to investigate any potential interactions with proteins is also required to ensure that binding to Zn^{2+} would be unperturbed *in vivo*. Additional titrations would allow for the creation of calibration curves and phantom imaging studies using a preclinical MRI scanner could then be used to demonstrate the feasibility of an *in vivo* measurement of Zn^{2+}.

4.6 References

1 C. J. Frederickson, J. Y. Koh and A. I. Bush, *Nat. Rev. Neurosci.*, 2005, **6**, 449–462.
2 P. Jiang and Z. Guo, *Coord. Chem. Rev.*, 2004, **248**, 205–229.
3 K. P. Carter, A. M. Young and A. E. Palmer, *Chem. Rev.*, 2014, **114**, 4564–4601.
4 G. K. Walkup, S. C. Burdette, S. J. Lippard and R. Y. Tsien, *J. Am. Chem. Soc.*, 2000, **122**, 5644–5645.
5 D. W. Gruenwedel, *Inorg. Chem.*, 1968, **7**, 495–501.
6 G. Anderegg and E. Hubmann, *Helv. Chim. Acta*, 1977, **60**, 123–140.
7 C. S. Bonnet and É. Tóth, *Future Med. Chem.*, 2010, **2**, 367–384.
8 E. L. Que and C. J. Chang, *Chem. Soc. Rev.*, 2010, **39**, 51–60.
9 K. Hanaoka, K. Kikuchi, Y. Urano and T. Nagano, *J. Chem. Soc. Perkin Trans. 2*, 2001, **25**, 1840–1843.
10 K. Hanaoka, K. Kikuchi, Y. Urano, M. Narazaki, T. Yokawa, S. Sakamoto, K. Yamaguchi and T. Nagano, *Chem. Biol.*, 2002, **9**, 1027–1032.
11 R. Trokowski, J. Ren, F. K. Kálmán and A. D. Sherry, *Angew. Chem. Int. Ed.*, 2005, **44**, 6920–6923.
12 A. C. Esqueda, J. A. López, G. Andreu-de-Riquer, J. C. Alvarado-Monzón, J. Ratnakar, A. J. M. Lubag, A. D. Sherry and L. M. De León-Rodríguez, *J. Am. Chem. Soc.*, 2009, **131**, 11387–11391.
13 A. J. M. Lubag, L. M. De Leon-Rodriguez, S. C. Burgess and A. D. Sherry, *Proc. Natl. Acad. Sci.*, 2011, **108**, 18400–18405.
14 M. V. Clavijo Jordan, S.-T. Lo, S. Chen, C. Preihs, S. Chirayil, S. Zhang, P. Kapur, W.-H. Li, L. M. De Leon-Rodriguez, A. J. M. Lubag, N. M. Rofsky and A. D. Sherry, *Proc. Natl. Acad. Sci.*, 2016, **113**, 5464–5471.
15 J. L. Major, G. Parigi, C. Luchinat and T. J. Meade, *Proc. Natl. Acad. Sci.*, 2007, **104**, 13881–13886.
16 J. L. Major, R. M. Boiteau and T. J. Meade, *Inorg. Chem.*, 2008, **47**, 10788–10795.
17 X.-A. Zhang, K. S. Lovejoy, A. Jasanoff and S. J. Lippard, *Proc. Natl. Acad. Sci.*, 2007, **104**,

10780–5.
18 T. Lee, X. Zhang, S. Dhar, H. Faas, S. J. Lippard and A. Jasanoff, *Chem. Biol.*, 2010, **17**, 665–673.
19 S. J. A. Pope and R. H. Laye, *Dalton Trans.*, 2006, **44**, 3108.
20 Y. Morimoto, H. Kurihara, C. Yokoe and T. Kinoshita, *Chem. Lett.*, 1998, **27**, 829–830.
21 Y. Morimoto, H. Kurihara, T. Shoji and T. Kinoshita, *Heterocycles*, 2000, **53**, 1471.
22 I. Mamedov, A. Mishra, G. Angelovski, H. A. Mayer, L. O. Pålsson, D. Parker and N. K. Logothetis, *Dalton Trans.*, 2007, **9226**, 5260–5267.
23 P. Harvey, A. M. Blamire, J. I. Wilson, K.-L. N. A. Finney, A. M. Funk, P. K. Senanayake and D. Parker, *Chem. Sci.*, 2013, **4**, 4251.
24 A. Beeby, I. M. Clarkson, R. S. Dickins, S. Faulkner, D. Parker, L. Royle, A. S. de Sousa, J. A. G. Williams and M. Woods, *J. Chem. Soc. Perkin Trans. 2*, 1999, **2**, 493–504.
25 G. Anderegg and F. Wenk, *Helv. Chim. Acta*, 1967, **50**, 2330–2332.
26 R. S. Dickins, D. Parker, J. I. Bruce and D. J. Tozer, *Dalton Trans.*, 2003, 1264–1271.
27 O. A. Blackburn, N. F. Chilton, K. Keller, C. E. Tait, W. K. Myers, E. J. L. McInnes, A. M. Kenwright, P. D. Beer, C. R. Timmel and S. Faulkner, *Angew. Chem. Int. Ed.*, 2015, **54**, 10783–10786.
28 S. Shuvaev, M. A. Fox and D. Parker, *Angew. Chem. Int. Ed.*, 2018, **57**, 7488–7492.
29 S. Laurent, L. Vander Elst, F. Copoix and R. N. Muller, *Invest. Radiol.*, 2001, **36**, 115–122.
30 S. Laurent, L. Vander Elst and R. N. Muller, *Contrast Media Mol. Imaging*, 2006, **1**, 128–137.
31 A. Takács, R. Napolitano, M. Purgel, A. C. Bényei, L. Zékány, E. Brücher, I. Tóth, Z. Baranyai and S. Aime, *Inorg. Chem.*, 2014, **53**, 2858–2872.
32 G. de Martino Norante, M. Di Vaira, F. Mani, S. Mazzi and P. Stoppioni, *Inorg. Chem.*, 1990, **29**, 2822–2829.
33 S. Aoki, H. Kawatani, T. Goto, E. Kimura and M. Shiro, *J. Am. Chem. Soc.*, 2001, **123**, 1123–1132.
34 H. Keypour, H. Khanmohammadi, K. P. Wainwright and M. R. Taylor, *Inorg. Chim. Acta*, 2003, **355**, 286–291.
35 L. Vaiana, C. Platas-Iglesias, D. Esteban-Gómez, F. Avecilla, A. De Blas and T. Rodríguez-Blas, *Eur. J. Inorg. Chem.*, 2007, 1874–1883.
36 L. Vaiana, M. Regueiro-Figueroa, M. Mato-Iglesias, C. Platas-Iglesias, D. Esteban-Gómez, A. De Blas and T. Rodríguez-Bias, *Inorg. Chem.*, 2007, **46**, 8271–8282.
37 J. Aríñez-Soriano, J. Albalad, J. Pérez-Carvajal, I. Imaz, F. Busqué, J. Juanhuix and D. Maspoch, *CrystEngComm*, 2016, **18**, 4196–4204.
38 N. N. Murthy and K. D. Karlin, *J. Chem. Soc. Chem. Commun.*, 1993, 1236.
39 J. M. González Pérez, J. Niclós Gutiérrez, D. Nguyen-Huy, B. Viossat, A. Busnot and M. Wintenberger, *Inorg. Chim. Acta*, 1991, **184**, 243–249.
40 A. Grirrane, A. Pastor, E. Álvarez, C. Mealli, A. Ienco and A. Galindo, *Inorg. Chem. Commun.*, 2006, **9**, 160–163.
41 S. Shit, A. Sasmal, P. Dhal, C. Rizzoli and S. Mitra, *J. Mol. Struct.*, 2016, **1108**, 475–481.

5. Summary and outlook

The aim of this project was to investigate novel paramagnetic lanthanide complexes for use as responsive ^{1}H PARASHIFT probes for magnetic resonance spectroscopy by incorporating varying responsive functional groups into previously reported complexes.

The incorporation of a pH responsive, phosphonate group in close proximity to the reporter *tert*-butyl group revealed the pH dependence of the pseudocontact chemical shift. The observed pK_a was around 7.2 enabling pH and temperature measurements of selected organs within a mouse model. Structural modification of the ligand backbone was sought in order to change the biodistribution profile. The change from trimethylphosphinate to tribenzylphosphinate caused neither minimal changes to paramagnetic properties nor the rate of clearance *in vivo*. However, investigation of the dibenzylphosphinate analogue showed large and unexpected variations in the shift and relaxation properties of the trans-disubstituted complex.

In order to further probe how this structural modification affects the paramagnetic NMR properties of such probes an in-depth NMR investigation was undertaken on the analogous benzylphosphinate complexes with no pH responsive behaviour. This study revealed that the change of symmetry of the complex drastically affects the magnetic susceptibility tensor, with both a change in the nature, sign and orientation of the principal component observed.

Finally, a Zn^{2+} responsive probe was investigated through the incorporation of a specific Zn^{2+} chelating group (dipicolylamine). The complex was found to bind Zn^{2+} extremely strongly through a number of techniques. In particular, the paramagnetic NMR of the complexes was found to drastically vary, both in chemical shift and relaxation, upon addition of Zn^{2+}.

The work undertaken in this thesis demonstrates that responsive behaviour can be incorporated into existing probes through the addition of specific functional groups. Whilst only two responsive functionalities have been investigated (pH and Zn^{2+}), the concept could be extended to other biologically relevant markers (e.g. Ca^{2+}, Mg^{2+}).

Further modification to these probes to include targeting vectors, would improve the potential application of PARASHIFT probes.

However, ligand modification must be performed judiciously, as it has been demonstrated in this work that variations in the symmetry of complexes results in dramatic changes to the magnetic susceptibility tensor. The changes to the paramagnetic NMR properties of such complexes may not be immediately obvious from chemical shift or relaxation data alone.

6. Experimental Methods

6.1 General procedures

Commercially available reagents were used as received. Solvents were laboratory grade and were dried over appropriate drying agents when required. Diethylbenzylphosphite was prepared by Dr. P. Kanthi Senanayake. Reactions requiring anhydrous conditions were carried out under an atmosphere of argon using Schlenk-line techniques. Where appropriate, solvents were degassed using three freeze-pump-thaw cycles.

Thin layer chromatography (TLC) was carried out on aluminium-backed silica gel plates with 0.2 mm thick silica gel 60 F_{254} (Merck) or 0.2 mm thick neutral alumina gel 60 F_{254} (Merck). Compounds were visualised by UV irradiation at 254 nm, or by staining with either iodine or Dragendorff's reagent (solution of bismuth nitrate and potassium iodide in AcOH and H_2O). Preparative flash column chromatography was performed using flash silica gel 60 (230-400 mesh) from Merck or Fluorochem or neutral alumina (Merck Aluminium Oxide 90, activity II-III, 70-230 mesh), with the latter pre-soaked in ethyl acetate overnight before use.

Electrospray mass spectra were obtained on a TQD mass spectrometer equipped with an Acquity UPLC system, an electrospray ion source and an Acquity photodiode array detector (Waters Ltd., UK). Accurate masses were recorded on an LCT Premier XE mass spectrometer or a QToF Premier Mass spectrometer, both equipped with an Acquity UPLC, a lock-mass electrospray ion source and an Acquity photodiode array detector (Waters Ltd., UK). Methanol or acetonitrile were used as the carrier solvents.

pH measurements were carried out at 295 K using a Jenway 3320 pH meter with a Sigma Aldrich micro-pH combination electrode. Calibration was performed using commercially available buffer solutions at pH 4.00±0.02, pH 7.00±0.02, and pH 10.00±0.02 (Sigma Aldrich). Diluted aqueous solutions of NaOD and DCl (in D_2O) were used for pD adjustments; NaOH and HCl (in H_2O) for pH adjustments. For measurements in D_2O, the pD is calculated as pD = pH + 0.41, where pH is the meter reading.

6.2 NMR Spectroscopy

^{1}H, ^{13}C and ^{31}P NMR spectra were recorded in commercially available deuterated solvents on a Varian Mercury-200 (^{1}H at 199.975, ^{13}C at 50.289, ^{31}P at 80.985 MHz), Varian Mercury-400 (^{1}H at 399.960, ^{13}C at 100.572, ^{31}P at 161.943 MHz), Bruker Avance-400 (^{1}H at 400.052, ^{13}C at 100.603, ^{31}P at 161.980 MHz), Varian Inova-500 (^{1}H at 499.722, ^{13}C at 125.671, ^{31}P at 202.375 MHz), Appleby VNMRS-600 (^{1}H at 599.832, ^{13}C at 150.828, ^{31}P at 242.862 MHz), or Varian VNMRA-700 (^{1}H at 699.731, ^{13}C at 175.948, ^{31}P at 283.256 MHz) spectrometer. All chemical shifts are given in ppm and all coupling constants are reported in Hz, to the nearest 0.5. Where required, the operating temperature of the spectrometer was measured with the aid of an internal calibration solution of ethylene glycol. Measurements at 1.0 T (^{1}H at 42.5 MHz) were made on a Magritek Spinsolve spectrometer. The recorded free induction decays were processed using backward linear prediction, optimal exponential weighting, zero-filling, Fourier transform, phasing and baseline correction. The signals were integrated by Lorentzian line fitting.

Concentrations of the lanthanide(III) complexes were calculated using the bulk magnetic susceptibility (BMS) method, using 10% ^{t}BuOH/ H_2O solutions of the complexes, with a coaxial insert containing the same solution without the complex added.

^{1}H longitudinal relaxation times were measured in dilute D_2O solutions at 295 K using the inversion-recovery technique, on spectrometers operating at fields of 1.0, 4.7, 9.4, 11.7, 14.1 and 16.4 T. Each relaxation time measurement was repeated at least three times to reduce experimental error. The number of transients used in the measurements was determined by the signal-to-noise ratio of the sample. The signal was fully recovered during the inversion-recovery sequence to minimise the experimental error. Fitting errors were determined by calculating the standard deviation of a set of relaxation times. The line width data were obtained by Lorentzian line fitting.

Relaxation rate data was fitted using a modified algorithm originally provided by Dr. Ilya Kuprov at the University of Southampton. The algorithm uses the SBM equations

to fit the measured relaxation rate data using the Matlab R2014a internal Levenberg-Marquardt minimisation of the non-linear squares error function and the results were analysed iteratively. Some parameters were used globally in the series, and others used for each lanthanide individually. Magnetic moments for each lanthanide(III) were taken from the literature.

Variable temperature NMR spectroscopy was carried out using the Varian Inova-500 spectrometer with the assistance using the ethylene glycol method described above to confirm the operating temperature of the spectrometer at each temperature measured.

Protonation constants were measured at 295 K and 500 MHz in D_2O, unless otherwise stated. The resulting curves reporting the ^1H NMR chemical shift vs. pD were fitted by non-linear least squares iterative analysis by Boltzmann using OriginPro 2016 software, producing estimates of the pKa values.

6.3 Optical techniques

All solution state optical analyses were carried out in quartz cuvettes with a path length of 1 cm. UV/Vis absorbance spectra were measured on an ATI Unicam UV/Vis spectrometer (Model UV2) using Vision software (version 3.33). Emission spectra were recorded using either an ISA Jobin-Yvon Spex Fluorolog-3 luminescence spectrometer using DataMax software (version 2.2.10) or a HORIBA Jobin-Yvon Fluorolog-3 luminescence spectrometer equipped with an iHR320 module, which selects either a HORIBA FL-1073 (Hammatsu R928P) photomultiplier tube or a HORIBA Synapse BIDD CCD for detection of emitted light, using FluorEssence software (based on Origin® software).

Lifetime measurements were carried out using a Perkin Elmer LS55 spectrometer using FL Winlab software. The obtained decay curves were fitted using OriginPro 2016 software.

6.4 HPLC analysis

Reverse phase HPLC was performed at 295 K using a Shimadzu system comprising a Degassing Unit (DGU-20A5R), a Prominence Preparative Liquid Chromatography pump (LC-20AP), a Prominence UV-Vis Detector (SPD-20A) and Communications Bus Module (CBM-20A). For preparative HPLC an XBridge C18 OBD column was used (19 x 100 mm, 5 µm) with a flow rate of 17 mL/min. Fraction collection was performed manually. A solvent system of H_2O / CH_3CN was used with gradient elution as follows:

Time (min)	% H_2O	% CH_3CN
0	90	10
3	90	10
13	0	100
16	0	100
17	90	10

6.5 X-Ray studies

X-ray diffraction structures were carried out by Dr. Andrei S. Batsanov or Dr. Dmitry S. Yufit. Single crystal X-ray data was collected at 120 K on D8V_Mo diffractometer. The crystal was kept at 120 K during data collection. Using Olex2,[1] the structure was solved with the ShelXT[2] structure solution program using Intrinsic Phasing and refined with the ShelXL[3] refinement package using Least Squares minimisation. X-ray crystal structure images were produced using Mercury CSD 3.10 software.

6.6 DFT studies

The model geometries of **$[YL^4]$**, as a neutral species, and **$[YL^5]^+$**, as a cation, were fully optimised without symmetry constraints using the hybrid-DFT B3LYP functional[4,5] and 3-21G* basis set[3–7] for all atoms with the Gaussian 09 package.[11] B3LYP/3-21G* is shown elsewhere[12] to be an appropriate functional/basis set for Y^{3+} complexes and therefore suitable models for Yb^{3+} complexes. The paramagnetic Yb^{3+} complexes are very difficult to model computationally. The Gaussian09 default polarisation continuum solvent model (IEFPCM)[13] was applied to all calculations using water as solvent. Many other optimised geometries of **$[YL^4]$** and **$[YL^5]^+$** were located with higher

total energies. These higher energy geometries differed in the orientations of the CH_2Ph groups. Frequency calculations confirmed all the geometries to be true minima. The relative energies reported here were obtained as single point calculations at M062X/SDD:3-21G* from the most stable geometries at B3LYP/3-21G*. The M062X functional[14] with a mixed pseudopotential[15]: basis set was shown previously to be appropriate for relative energy calculations of closely related Y and Yb isomer complexes.[16] Figures of the lowest energy optimised geometries were generated using GaussView software.[17]

6.7 Assignment and fitting

Processing and deconvolution of ^1H spectra were done using the MestReNova v11.0.3 software in order to obtain positions, linewidths and integrals for all signals. The signals with small integrals were assigned to minor conformer and were excluded from the further analysis. Molecular frames of the optimized geometries were unified so that the origin is located at the lanthanide position, the z-axis is pointing in the middle of four nitrogen atoms of the cyclen group and the x-axis is pointing at the first nitrogen atom of the cyclen group located under pyridine. It was assumed that hyperfine shift (difference between observed paramagnetic shift and the shift of diamagnetic reference) is dominated by the pseudocontact contribution (PCS) and can be described by Equation 5.3, using the molecular frame coordinate system:

$$\delta_{para} - \delta_{dia} = \frac{10^6}{4\pi r^5}\left[\chi_{xx}(x^2 - z^2) + \chi_{xy}(2xy) + \chi_{xz}(2xz) + \chi_{yy}(y^2 - z^2) + \chi_{yz}(2yz)\right] \quad (5.3)$$

where shift is in the units of ppm, coordinates are defined relative to the lanthanide in Å, components of the traceless part of the susceptibility tensor are in the units of $Å^3$ in SI system. Atomic coordinates were taken from DFT optimized geometries, and for the tert-butyl group the structural functions were averaged assuming their fast rotation. Since PCS depends linearly on five components of the susceptibility tensor the robust linear regression with 'bisquare' weight function as implemented in MATLAB R2017a was used to fit their values. The permutation with the largest adjusted Pearson coefficient was taken as the best fit. Using the best fit tensor the PCS

for all other protons have been predicted. The line widths were fitted using a simple isotropic model (Equation 5.4):

$$\Delta v = \frac{C_1}{r^6} + C^2 \quad (5.4)$$

where the constants C_1 and C_2 were fitted for the assigned signals and used to predict the linewidth for all other protons. The total shift vs width plots of predicted and experimentally observed signals were used for further assignment. Well isolated groups of experimental signals were assigned to closely located groups of predicted signals and all possible permutations within the groups were checked, the assignment that gave the largest adjusted Pearson coefficient was chosen as the best fit.

The contact contribution to paramagnetic shift was neglected as it was assumed that for protons it is smaller than the standard deviation of PCS of the model, which is mostly due to errors in the structural function defined by DFT.

The best fit susceptibility tensors are presented in the main text as axiality, rhombicity and three Euler angles. The following convention is used for defining axiality, rhombicity and Euler angles of a traceless susceptibility tensor. Diagonalization of a traceless susceptibility tensor gives eigenvalues and eigenvectors which are labelled to satisfy the relation $|\chi_x|<|\chi_y|<|\chi_z|$ Then, the axiality is defined as 3/2 χ_z and rhombicity as (χ_x - χ_y)/2. In such a definition, axiality and rhombicity have the same sign and the limiting value of the ratio of rhombicity to axiality is 1/3 ($0 < \chi_{rh}/\chi_{ax} < 1/3$).

Euler angles specify the orientation of the labelled eigenvectors of the susceptibility tensor with respect to the chosen molecular frame. In the axial case only two angles are defined: the angle β between the z-axis of the frame and eigenvector of χ_z ($0 \leq \beta \leq \pi$) and the angle α between the x-axis and the projection of χ_z onto the xy plane ($0 \leq \alpha \leq 2\pi$), in the direction from the x-axis to the y-axis). If rhombicity is non-zero then the χ_x vector defines the direction of a dip in the PCS. The angle between the projection of χ_z and the projection of χ_x onto the xy-plane is the angle γ ($0 \leq \gamma < 2\pi$, counting in the same direction from x to y).

6.8 Imaging studies

Imaging studies were carried out by Prof. Andrew Blamire, Ian Wilson and Dr. Dara O'Hogain at the Newcastle Magnetic Resonance Centre. *In vitro* and *in vivo* imaging experiments were performed by using a 7 T preclinical MRI system (20 cm bore, Varian Direct Drive scanner, Agilent, Palo Alta, CA) equipped with a 30mm i.d. quadrature birdcage RF coil (Rapid Biomedical GmbH, Germany) for excitation and detection of the water and PARASHIFT agent signals.

Two types of scan acquisition were used 3-dimensional gradient echo (3DGE) imaging and 2-dimensional spectroscopic imaging (2DSI), which were applied either for imaging single resonances or for triple frequency imaging. In every case, the excitation RF pulse was a 500 ms duration Gaussian modulated pulse which has a FWHM bandwidth of 2100 Hz, falling to a fractional excitation of $<10^{-3}$ at 20 kHz. This pulse specification allows separate excitation of water only or the tert-butyl group of the PARASHIFT probes by varying the transmit frequency.

6.9 Synthetic procedures

1,4,7-Tri-benzyl-1,4,7,10-tetraazacyclododecane-1,4,7-tricarboxylate, 1

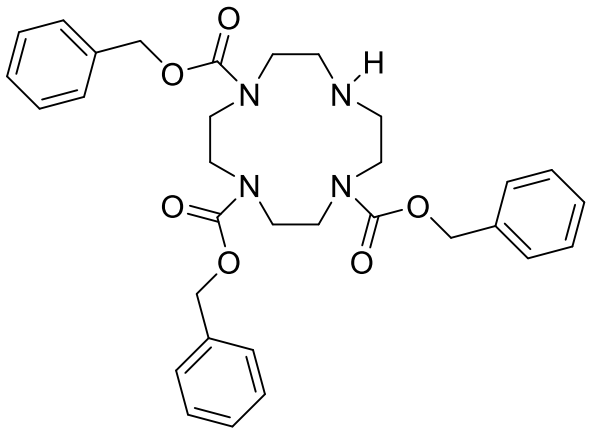

1,4,7,10-Tetraazacyclododecane (2.50 g, 14.5 mmol) was dissolved in anhydrous CH_2Cl_2 (80 mL) and to this triethylamine (6.3 mL, 45 mL) was added. The resulting solution was stirred under argon at 5^{o}C and a solution of benzyl chloroformate (6.4 mL, 45 mmol) in CH_2Cl_2 (20 mL) was added dropwise. The reaction was stirred at room temperature for a further 18 h before the solvent was removed under reduced

pressure. The resulting yellow oil was purified by silica gel column chromatography (100% CH_2Cl_2 to 2% MeOH/ CH_2Cl_2) to yield a colourless oil (4.78 g, 57%). R_f (10% MeOH/ CH_2Cl_2) = 0.54. ^{1}H NMR (400 MHz,$CDCl_3$) δ 7.48-7.11 (m, 15H, ArH), 5.19-5.00 (m, 6H, CH_2O) 3.89-2.21 (m, 16H, cyclen CH_2); ^{13}C NMR (101 MHz, $CDCl_3$) δ 156.1 (CO), 136.4 (Ar), 136.3 (Ar), 128.4 (Ar), 128.3 (Ar), 127.7 (Ar), 127.6 (Ar), 127.4 (Ar), 67.2 (CH_2O), 66.8 (CH_2O), 53.5 (cyclen CH_2), 50.6 (cyclen CH_2), 50.3 (cyclen CH_2), 50.2 (cyclen CH_2), 50.1 (cyclen CH_2), 45.6 (cyclen CH_2); ESI-LCMS (+) *m/z* 575.1 $[M+H]^+$. ESI-HRMS (+) calcd for $[C_{32}H_{39}N_4O_6]^+$ 575.2870, found 575.2864.

1,4,7-Tri-benzyl 10-*tert*-butyl 1,4,7,10-tetraazacyclododecane 1,4,7-tricarboxylate, 2

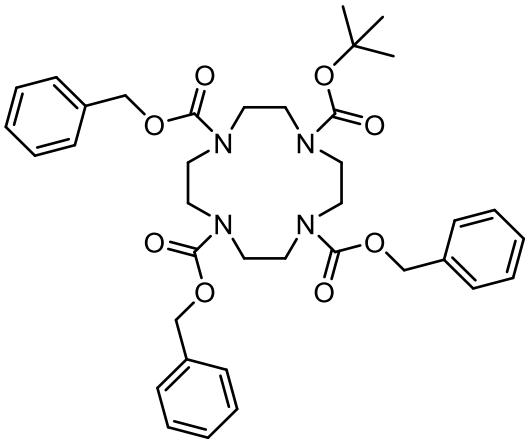

1,4,7-Tri-benzyl-1,4,7,10-tetraazacyclododecane-1,4,7-tricarboxylate (4.68 g, 8.3 mmol) was dissolved in anhydrous CH_2Cl_2 (60 mL) and to this triethylamine (1.6 mL, 10.8 mmol) was added. The resulting solution was stirred under argon before the addition of di-tert-butyl dicarbonate (2.36 g, 10.8 mmol). After addition, the solution was stirred at room temperature for a further 18 h. The solvent was removed under reduced pressure and the resulting yellow oil was purified by silica gel column chromatography (100% CH_2Cl_2 to 2% MeOH/ CH_2Cl_2) to yield a white solid (5.2 g, 93%). R_f (10% MeOH/ CH_2Cl_2) = 0.69. ^{1}H NMR (400 MHz,$CDCl_3$) δ 7.58-6.90 (m, 15H, ArH), 5.09-4.76 (m, 6H, CH_2O) 3.87-2.70 (m, 16H, cyclen CH_2) 1.31 (s, 9H, $C(CH_3)_3$); ^{13}C NMR (101 MHz, $CDCl_3$) δ 156.8 (CO), 136.4 (Ar), 128.6 (Ar), 128.4 (Ar), 128.3 (Ar), 128.2 (Ar), 82.8 ($\underline{C}(CH_3)_3$), 67.3 (CH_2O), 50.7-49.9 (br, cyclen CH_2), 28.4 ($C(\underline{C}H_3)_3$), ESI-LCMS (+) *m/z* 675.5 $[M+H]^+$. ESI-HRMS (+) calcd for $[C_{37}H_{47}N_4O_8]^+$ 675.3394, found 675.3406.

tert-Butyl-1,4,7,10-tetraazacyclododecane-1,4,7-tricarboxylate, 3

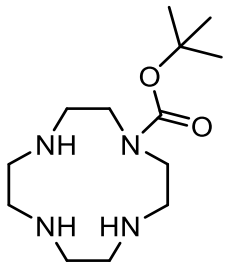

1,4,7-Tri-benzyl-10-_tert_-Butyl-1,4,7,10-tetraazacyclododecane-1,4,7-tricarboxylate (3.5 g, 5.2 mmol) was dissolved in MeOH (30 mL) and to this was added $Pd(OH)_2/C$ (~100 mg). The reaction vessel was loaded onto a Parr hydrogenator, where it was subjected to agitation for 18 h, under a 30 psi pressure of H_2. The resulting solution was filtered through celite to ensure removal of catalyst and the solvent removed under reduced pressure to yield a pale yellow oil (1.23 g, 87%). ^{1}H NMR (400 MHz,$CDCl_3$) δ 5.31 (br s, NH), 3.75-2.83 (m, 16H, cyclen CH_2) 1.48 (s, 9H, $C(CH_3)_3$); ^{13}C NMR (101 MHz, $CDCl_3$) δ 157.5 (CO) , 82.3 ($\underline{C}(CH_3)_3$), 48.2 (cyclen CH_2), 46.9 (cyclen CH_2), 45.6 (cyclen CH_2), 44.5 (cyclen CH_2), 28.7 ($C(\underline{C}H_3)_3$), ESI-LCMS (+) *m/z* 273.8 $[M+H]^+$. ESI-HRMS (+) calcd for $[C_{13}H_{29}N_4O_2]^+$ 273.2291, found 273.2292.

tert-Butyl-4,7,10-tri{[ethyoxy(methyl)phosphoryl]methyl}-1,4,7,10-tetraazacyclododecane-1-carboxylate, 4

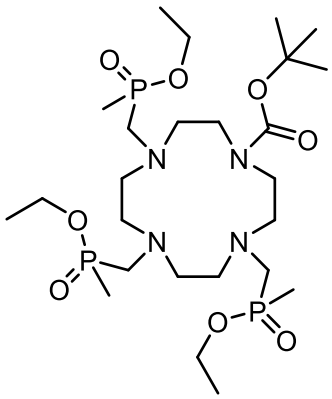

tert-Butyl-1,4,7,10-tetraazacyclododecane-1,4,7-tricarboxylate (0.60 g, 2.21 mmol) and paraformaldehyde (1.45 g, 46.3 mmol) were dissolved in anhydrous THF (30 mL) and the resulting suspension was stirred under argon at 80°C for 30 min. Diethyl methylphosphonite (1.94 g, 13.27 mmol) was added and the reaction was stirred at 80°C for a further 18 h. The solution was filtered and the solvent was removed under

reduced pressure. The resulting orange oil was purified by alumina gel column chromatography (100% CH_2Cl_2 to 2% MeOH/ CH_2Cl_2) to yield a yellow oil (435 mg, 38%). R_f (10% MeOH/ CH_2Cl_2) = 0.76. ^{1}H NMR (400 MHz,$CDCl_3$) δ 4.07-3.86 (m, 6H, $POCH_2CH_3$), 3.62-3.12 (br m, 6H, PCH_2NH), 3.04-2.44 (br m, 16H, cyclen CH_2), 1.53-1.37 (m, 9H, PCH_3), 1.35 (s, 9H, $C(CH_3)_3$), 1.21 (t, ^3J = 7, 9H, $POCH_2CH_3$); ^{31}P NMR (162 MHz, $CDCl_3$) δ 53.1-52.0; ^{13}C NMR (101 MHz, $CDCl_3$) δ 155.5 (CO) , 79.5 ($C(CH_3)_3$), 60.1-59.9 (m, $POCH_2$) 55.1-52.7 (m, cyclen CH_2), 45.9 (PCH_2N), 45.6 (PCH_2N), 45.5 (PCH_2N), 28.4 ($C(CH_3)_3$), 16.6 ($POCH_2CH_3$), 13.9-13.5 (m, PCH_3); ESI-LCMS (+) *m/z* 633.1 $[M+H]^+$. ESI-HRMS (+) calcd for $[C_{25}H_{56}N_4O_8P_3]^+$ 633.3311, found 633.3308.

Ethyl[(4,7,10-di{[ethoxy(methyl)phosphoryl]methyl}-1,4,7,10-tetraazadodecane-1-yl](methyl)phosphinate, 5

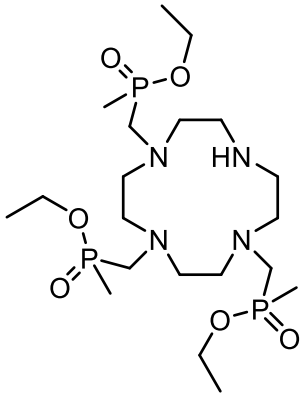

tert-Butyl-4,7,10-tri{[ethyoxy(methyl)phosphoryl]methyl}-1,4,7,10-tetraazacyclododecane-1-carboxylate (435 mg, 0.69 mmol) was dissolved in anhydrous CH_2Cl_2 (3 mL) and to this was added TFA (3 mL). The solution was stirred at room temperature for 18 h, before the solvent was removed under reduced pressure. The resulting yellow oil was dissolved in H_2O (1 mL) and the pH of this solution was adjusted to 12 with solid NaOH pellets before the aqueous solution was extracted with CH_2Cl_2 (4 x 10 mL). The organic layers were combined, dried over $MgSO_4$, and the solvent removed under reduced pressure to yield a yellow oil (266 mg, 75%). ^{1}H NMR (400 MHz,$CDCl_3$) δ 4.08-3.90 (m, 6H, $POCH_2$), 3.32-2.60 (br m, 22H, cyclen CH_2, PCH_2N), 1.46 (s, 9H, PCH_3), 1.25 (t, $^3J_{PH}$= 7, 9H, $POCH_2CH_3$); ^{31}P NMR (162 MHz, $CDCl_3$) δ 54.2-50.4; ^{13}C NMR (101 MHz, $CDCl_3$) δ 60.6-60.1 (m, $POCH_2$), 56.6-56.2 (m, cyclen CH_2), 55.5-55.1 (m, cyclen CH_2), 53.2-52.5 (m, cyclen CH_2), 47.3-46.8 (PCH_2N), 16.7

($POCH_2\underline{C}H_3$); ESI-LCMS (+) *m/z* 533.3 $[M+H]^+$. ESI-HRMS (+) calcd for $[C_{20}H_{48}N_4O_6P_3]^+$ 533.2787, found 533.2811.

5-*tert*-Butyl-2-methylpyridine, 6

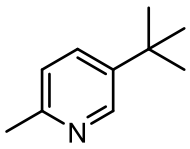

Copper(I) cyanide (20 mg) was added to a solution of anhydrous THF (15 mL) and anhydrous Et_2O (100 mL) under argon. The resulting suspension was cooled to -78°C before *tert*-butylmagnesium chloride (58 mL, 2.0 M in Et_2O, 116.2 mmol) was added. 5-Bromo-2-methylpyridine (10.0 g, 58.1 mmol) was added and the resulting yellow solution was allowed to warm to room temperature and stirred for a further 18 h. The reaction was quenched by the dropwise addition of NH_4OH (sat. aq. solution, 50 mL) and the aqueous layer was extracted with Et_2O (3 x 200 mL). The organic layers were combined and dried with $MgSO_4$. The solvent was removed under reduced pressure to yield a pale yellow liquid that was used without further purification. ^{1}H NMR (400 MHz,$CDCl_3$) δ 8.43 (s, 1H, H^6), 7.44 (dd, ^3J = 8, ^4J = 2, 1H, H^4), 6.95 (d, ^3J = 8, 1H, H^3), 2.38 (s, 3H, CH_3), 1.20 (s, 9H, $C(C\underline{H}_3)_3$); ^{13}C NMR (101 MHz, $CDCl_3$) δ 154.8 (C^2), 146.1 (C^6), 142.3 (C^5), 132.8 (C^4), 122.1 (C^3), 32.8 ($\underline{C}(CH_3)_3$), 30.6 ($C(\underline{C}H_3)$), 20.4 (CH_3); ESI-LCMS (+) *m/z* 150.1 $[M+H]^+$. ESI-HRMS (+) calcd for $[C_{10}H_{16}N]^+$ 150.1283, found 150.1275.

5-*tert*-Butyl-2-methylpyridin-1-oxide, 7

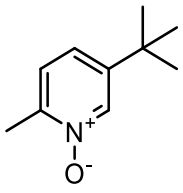

5-*tert*-Butyl-2-methylpyridine (8.53 g, 57.25 mmol) was dissolved in $CHCl_3$ (200 mL) and to this was added *m*CPBA (17.0 g, 98.5 mmol). The resulting solution was stirred for 18 h at room temperature under argon, before the reaction was quenched by Na_2SO_4 (sat. aq. solution, 50 mL). The organic layer was extracted and washed with aqueous NaOH solution (0.5 M, 5 x 100 mL). The aqueous layer was extracted with

CH_2Cl_2 (3 x 200 mL). The organic layers were combined and dried over $MgSO_4$ and the solvent removed under reduced pressure to yield a yellow oil (5.25 g, 54% over two steps). R_f (10% MeOH/ CH_2Cl_2) = 0.46. ^{1}H NMR (400 MHz,$CDCl_3$) δ 8.22 (s, 1H, H^6), 7.19-7.14 (m, 2H, H^3, H^4), 2.41 (s, 3H, CH_3), 1.22 (s, 9H, C($C\underline{H}_3$)$_3$); ^{13}C NMR (101 MHz, $CDCl_3$) δ 146.5 (C^2), 144.8 (C^6), 136.4 (C^5), 124.8 (C^4), 123.0 (C^3), 32.6 ($\underline{C}(CH_3)_3$), 32.6 (C($\underline{C}H_3$)), 16.4 (CH_3); ESI-LCMS (+) *m/z* 166.1 $[M+H]^+$. ESI-HRMS (+) calcd for $[C_{10}H_{16}NO]^+$ 166.1232, found 166.1232.

5-*tert*-Butyl-4-nitro-2-methylpyridin-1-oxide, 8

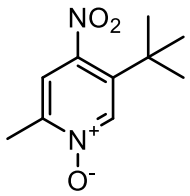

5-*tert*-Butyl-2-methylpyridin-1-oxide (5.25 g, 31.8 mmol) was dissolved in conc. H_2SO_4 (98%, 18 mL, 342.8 mmol) at 5^{o}C. Conc. HNO_3 (70%, 11.5 mL, 264.5 mmol) was added dropwise and the resulting solution was stirred at 100^{o}C for a further 18 h. The solution was then poured over ice and stirred for 1 h. This aqueous solution was extracted with CH_2Cl_2 (3 x 200 mL). The organic layers were combined, dried over $MgSO_4$ and the solvent was then removed under reduced pressure. The resulting pale green oil was purified by silica gel column chromatography (100% CH_2Cl_2 to 2% MeOH/ CH_2Cl_2) to yield a yellow oil (4.00 g, 60%). R_f (10% MeOH/ CH_2Cl_2) = 0.47. ^{1}H NMR (400 MHz,$CDCl_3$) δ 8.50 (s, 1H, H^6), 7.48 (s, 1H, H^3), 2.53 (s, 3H, CH_3), 1.38 (s, 9H, C($C\underline{H}_3$)$_3$); ^{13}C NMR (101 MHz, $CDCl_3$) δ 152.5 (C^2), 151.1 (C^5), 142.3 (C^6), 139.3 (C^4), 122.6 (C^3), 35.7 ($\underline{C}(CH_3)_3$), 29.9 (C($\underline{C}H_3$)), 17.5 (CH_3); ESI-LCMS (+) *m/z* 211.1 $[M+H]^+$. ESI-HRMS (+) calcd for $[C_{10}H_{15}N_2O_3]^+$ 211.1083, found 211.1088.

5-*tert*-Butyl-4-amino-2-methylpyridin-1-oxide, 9

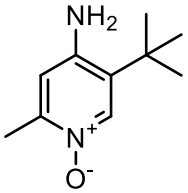

5-*tert*-Butyl-4-nitro-2-methylpyridin-1-oxide (2.00 g, 9.5 mmol) was dissolved in MeOH (30 mL) and to this was added Pd/C (~300 mg). The reaction vessel was loaded onto a Parr hydrogenator, where it was subjected to agitation for 18 h, under a 30 psi pressure of H_2. The resulting solution was filtered through celite to ensure removal of catalyst and the solvent was removed under reduced pressure to yield a yellow oil (1.54 g, 90%). R_f (10% MeOH/ CH_2Cl_2) = 0.28. ^{1}H NMR (400 MHz,CD_3OD) δ 7.84 (s, 1H, H^6), 6.61 (s, 1H, H^3), 2.34 (s, 3H, CH_3), 1.33 (s, 9H, C($C\underline{H}_3$)$_3$); ^{13}C NMR (101 MHz, CD_3OD) δ 157.2 (C^2), 148.0 (C^5), 138.1 (C^3), 129.4 (C^6), 112.2 (C^4), 34.1 ($\underline{C}(CH_3)_3$), 28.6 ($C(\underline{C}H_3)$), 16.9 (CH_3); ESI-LCMS (+) *m/z* 181.1 $[M+H]^+$. ESI-HRMS (+) calcd for $[C_{10}H_{17}N_2O]^+$ 180.1263, found 180.1260.

5-*tert*-Butyl-4-iodo-2-methylpyridine-1-oxide, 10

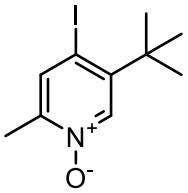

5-*tert*-Butyl-4-amino-2-methylpyridin-1-oxide (1.5 g, 8.33 mmol) was dissolved in cold H_2O (40 mL) and to this was added HBF_4 (2.2 mL, 16.7 mmol). A solution of $NaNO_2$ (1.15g, 16.7 mmol) in H_2O (5 mL) was added dropwise. Potassium iodide (1.94 g, 11.7 mmol) was added in portions over 30 min and the resulting brown solution was stirred for 5 min. The mixture was then heated to 60^{o}C and stirred for a further 30 min and then allowed to cool to room temperature. The pH of the solution was adjusted to 10 with 2.5 M aqueous KOH solution, and the solution washed with CH_2Cl_2 (3 x 150 mL). The organic layers were combined and dried over $MgSO_4$ and the solvent removed under reduced pressure. The resulting brown oil was purified using silica gel column chromatography (100% CH_2Cl_2 to 2% MeOH/ CH_2Cl_2) to yield an orange oil

(1.25 g, 52%). R_f (10% MeOH/ CH_2Cl_2) = 0.37. ^{1}H NMR (400 MHz,$CDCl_3$) δ 8.20 (s, 1H, H^6), 7.77 (s, 1H, H^3), 2.37 (s, 3H, CH_3), 1.45 (s, 9H, $C(\underline{C}H_3)_3$); ^{13}C NMR (101 MHz, $CDCl_3$) δ 146.5 (C^5), 146.4 (C^2), 139.7 (C^3), 138.3 (C^6), 89.8 (C^4), 35.8 ($\underline{C}(CH_3)_3$), 29.1 ($C(\underline{C}H_3)$), 16.6 (CH_3); ESI-LCMS (+) *m/z* 292.0 $[M+H]^+$. ESI-HRMS (+) calcd for $[C_{10}H_{15}{}^{127}INO]^+$ 292.0198, found 292.0200.

(5-*tert*-Butyl-4-iodopyridin-2-yl)methyl acetate, 11

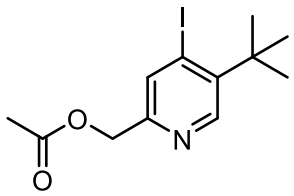

5-*tert*-Butyl-4-iodo-2-methylpyridin-1-oxide (1.25 g, 4.3 mmol) was dissolved in acetic anhydride (16 mL) and this was stirred for 3 h at 75°C. The solvent was removed under reduced pressure and the resulting orange oil was purified using silica gel column chromatography (100% CH_2Cl_2 to 2% MeOH/ CH_2Cl_2) to yield an orange oil (1.09 g, 52%). R_f (10% MeOH/ CH_2Cl_2) = 0.62. ^{1}H NMR (400 MHz,$CDCl_3$) δ 8.50 (s, 1H, H^6), 7.91 (s, 1H, H^3), 5.09 (s, 2H, CH_2), 2.14 (s, 3H, CH_3), 1.52 (s, 9H, $C(\underline{C}H_3)_3$); ^{13}C NMR (101 MHz, $CDCl_3$) δ 170.8 (CO), 153.6 (C^2), 147.7 (C^5), 145.0 (C^3), 136.3 (C^6), 107.0 (C^4), 65.6 (CH_2), 36.0 ($\underline{C}(CH_3)_3$), 29.6 ($C(\underline{C}H_3)$), 21.1 (CH_3); ESI-LCMS (+) *m/z* 334.0 $[M+H]^+$. ESI-HRMS (+) calcd for $[C_{12}H_{17}{}^{127}INO_2]^+$ 334.0304, found 334.0310.

[5-*tert*-Butyl-4-(diethoxyphosphoryl)pyridin-2-yl]methyl acetate, 12

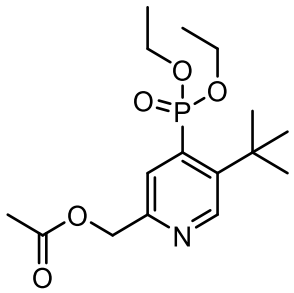

(5-*tert*-Butyl-4-iodopyridin-2-yl)methyl acetate (750 mg, 2.25 mmol) was dissolved in triethylphosphite (10 mL, 58.4 mmol). $Pd_2(dba)_3$ (211 mg, 0.23 mmol) was added and the solution was degassed (freeze-pump-thaw cycle x 3). The resulting solution was stirred under argon at 120°C for 18 h. The solvent was removed by vacuum distillation

and the resulting brown oil was purified using silica gel column chromatography (100% CH_2Cl_2 to 2% MeOH/ CH_2Cl_2) to yield a yellow oil (580 mg , 75%). R_f (10% MeOH/ CH_2Cl_2) = 0.56. ^{1}H NMR (400 MHz,$CDCl_3$) δ 8.61 (d, $^4J_{HP}$ = 8, 1H, H^6), 7.59 (d, $^3J_{HP}$ = 16, 1H, H^3), 4.99 (s, 2H, CH_2), 3.99-3.90 (m, 4H, $POCH_2$), 1.92 (s, 3H, $COCH_3$), 1.35 (s, 9H, $C(C\underline{H}_3)_3$), 1.17-1.05 (m, 6H, $POCH_2C\underline{H}_3$) ; ^{31}P NMR (162 MHz, $CDCl_3$) δ 16.1; ^{13}C NMR (101 MHz, $CDCl_3$) δ 170.0 (CO), 152.8 (d, $^3J_{CP}$ = 12, C^6), 148.7 (d, $^3J_{CP}$ = 13, C^2), 145.0 (d, $^2J_{CP}$ = 11, C^5), 136.5 (d, $^1J_{CP}$ = 178, C^4), 107.0 (C^3), 65.9 (CH_2O), 62.2 (d, $^2J_{CP}$ = 6, $POCH_2$) 35.4 ($\underline{C}(CH_3)_3$), 31.1 ($C(\underline{C}H_3)$), 20.4 (CH_3), 15.8 (d, $^3J_{CP}$ = 6, $POCH_2C\underline{H}_3$) ; ESI-LCMS (+) *m/z* 344.1 $[M+H]^+$. ESI-HRMS (+) calcd for $[C_{16}H_{27}NO_4P]^+$ 344.1627, found 344.1628.

5-*tert*-Butyl-4-(diethoxyphosphoryl)-2-hydroxymethyl-pyridine, 13

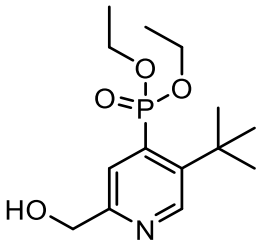

[5-tert-Butyl-4-(diethoxyphosphoryl)pyridin-2-yl]methyl acetate (300 mg, 0.87 mmol) was dissolved in anhydrous EtOH (7 mL) and the solution was purged with argon for 10 min before the addition of sodium metal (~15 mg). The reaction was stirred at room temperature and monitored by TLC. After 1 h, ionic cation exchange resin was added and the solution was stirred for a further 10 min. The reaction was filtered and the solvent was removed under reduced pressure and the resulting brown oil was dissolved in CH_2Cl_2 (7 mL) and washed with H_2O (10 mL). The aqueous layer was extracted with CH_2Cl_2 (3 x 7 mL), and the organic layers were combined, dried over $MgSO_4$ and the solvent removed under reduced pressure. The resulting brown oil was purified using silica gel column chromatography (100% CH_2Cl_2 to 2% MeOH/ CH_2Cl_2) to yield a yellow oil (213 mg, 82%). R_f (10% MeOH/ CH_2Cl_2) = 0.48. ^{1}H NMR (400 MHz,$CDCl_3$) δ 8.69 (d, $^4J_{HP}$ = 8, 1H, H^6), 7.78 (d, $^3J_{HP}$ = 16, 1H, H^3), 4.72 (s, 2H, CH_2), 4.16-3.97 (m, 4H, $POCH_2$), 1.50 (s, 9H, $C(C\underline{H}_3)_3$), 1.31-1.23 (m, 6H, $POCH_2C\underline{H}_3$) ; ^{31}P NMR (162 MHz, $CDCl_3$) δ 15.6; ^{13}C NMR (101 MHz, $CDCl_3$) δ 157.3 (d, $^3J_{CP}$ = 11, C^6), 148.1 (d, $^3J_{CP}$ = 13, C^2), 146.7 (d, $^2J_{CP}$ = 11, C^5), 136.5 (d, $^1J_{CP}$ = 178, C^4), 123.5 (C^3), 64.2 (CH_2O), 62.7 (d, $^2J_{CP}$ = 6, $POCH_2$) 35.8 ($\underline{C}(CH_3)_3$), 31.6 ($C(\underline{C}H_3)$), 16.3 (d, $^3J_{CP}$ = 6, $POCH_2C\underline{H}_3$) ; ESI-

LCMS (+) *m/z* 302.1 $[M+H]^+$. ESI-HRMS (+) calcd for $[C_{16}H_{27}NO_4P]^+$ 302.1521, found 302.1525.

[5-*tert*-Butyl-4-(diethoxyphosphoryl)pyridine-4-yl]methyl methane sulfonate, 14

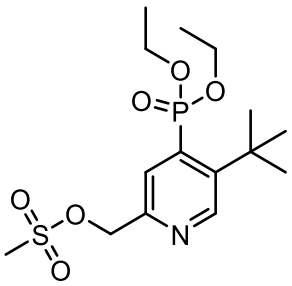

5-tert-Butyl-4-(diethoxyphosphoryl)-2-hydroxymethyl-pyridine (213 mg, 0.71 mmol) was dissolved in anhydrous THF (5 mL) and stirred at 5°C for 10 min, before the addition of NEt_3 (199 µL, 1.42 mmol). Mesyl chloride (83 µL, 1.07 mmol) was added dropwise and the resulting solution was allowed to stir at room temperature for 30 min. The solvent was removed under reduced pressure and the residue was dissolved in H_2O (5 mL) and extracted with CH_2Cl_2 (3 x 10 mL). The organic layers were combined, dried over $MgSO_4$ and the solvent removed under reduced pressure. The resulting orange oil was used without further purification (248 mg, 92%). ^{1}H NMR (400 MHz, $CDCl_3$) δ 8.78 (d, $^4J_{HP}$ = 8, 1H, H^6), 7.84 (d, $^3J_{HP}$ = 15, 1H, H^3), 5.26 (s, 2H, CH_2), 4.06-4.16 (m, 4H, $POCH_2$), 3.05 (s, 3H, CH_3), 1.52 (s, 9H, $C(CH_3)_3$), 1.29 (m, 6H, $POCH_2C\underline{H}_3$); ^{31}P NMR (162 MHz, $CDCl_3$) δ 15.6; ESI-LCMS (+) *m/z* 380.0 $[M+H]^+$.

Diethyl {5-tert-butyl-2-[(4,7,10-tri{[ethoxy(methyl)phosphoryl]methyl}-1,4,7,10-tetraazacyclododecan-1-yl)methyl]pyridine-4-yl}phosphonate, L^1

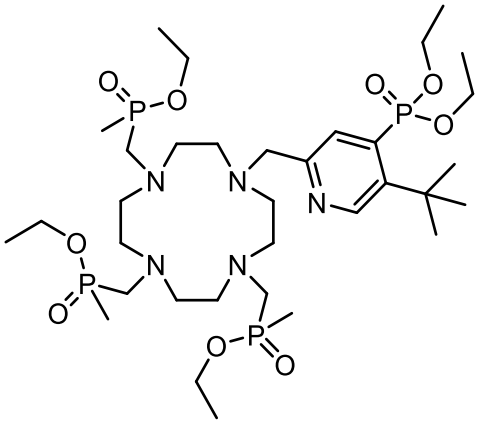

Ethyl[(4,7-di{[ethoxy(methyl)phosphoryl]methyl}-1,4,7,10-tetraazacyclododecane-1-yl)methyl](methyl)phosphinate (216 mg, 0.49 mmol) was dissolved in anhydrous MeCN (3 mL) and K_2CO_3 (69 mg, 0.49 mmol) was added. [5-tert-Butyl-4-(diethoxyphosphoryl)pyridin-2-yl]methyl methane sulfonate (190 mg, 0.5 mmol) was then added dropwise as a solution in anhydrous MeCN (5 mL). The resulting solution was heated to 70°C and stirred for 18 h after which the reaction was filtered to remove inorganic salts. The solvent was removed under reduced pressure and the resulting red oil was purified by alumina gel column chromatography (100% CH_2Cl_2 to 2% MeOH/ CH_2Cl_2) to yield a yellow oil (90 mg, 22%). R_f (10% MeOH/ CH_2Cl_2) = 0.65; ^{1}H NMR (400 MHz, $CDCl_3$) δ 8.73 (d, $^4J_{HP}$ = 8, 1H, H^6), 7.88 (d, $^3J_{HP}$ = 16, 1H, H^3), 4.09-4.16 (m, 4H, $POCH_2$), 3.93-4.05 (m, 6H, $POCH_2$), 3.50-3.74 (m, 8H, NCH_2), 2.53-3.49 (br m, 16H, cyclen CH_2), 1.39-1.54 (m, 18H, $C(CH_3)_3$, PCH_3), 1.20-1.32 (m, 15H, $POCH_2C\underline{H}_3$); ^{31}P NMR (162 MHz, $CDCl_3$) δ 53.5-51.5 (NCH_2P), 16.6-14.4 (pyP); ^{13}C NMR (101 MHz, $CDCl_3$) δ 149.0 (C^2), 136.2 (C^5), 129.5 (C^6), 127.3 (C^4), 111.7 (C^3), 62.5-62.8 (m, $POCH_2$), 59.7-60.3 (m, $POCH_2$), 53.0-55.0 (m, PCH_2N, $pyCH_2$, cyclen CH_2), 36.3 ($\underline{C}(CH_3)_3$), 31.3 ($C(\underline{C}H_3)_3$), 16.6 (d, $^3J_{CP}$ = 6, $POCH_2\underline{C}H_3$), 16.2 (d, $^3J_{CP}$ = 6, $POCH_2\underline{C}H_3$), 13.0-14.9 (m, $P\underline{C}H_3$); ESI-LCMS (+) *m/z* 816.7 $[M+H]^+$. ESI-HRMS (+) calcd for $[C_{34}H_{70}N_5O_9P_4]^+$ 816.4129, found 816.4129.

Terbium(III) complex of {5-tert-butyl-2-[(4,7,10-tri{[hydroxy(methyl)phosphoryl]methyl}-1,4,7,10-tetraazacyclododecan-1-yl)methyl]pyridine-4-yl}phosphonic acid, [TbL^1]

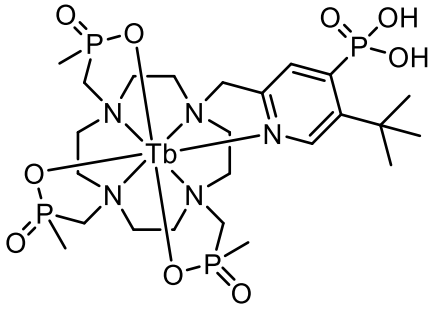

Diethyl {5-tert-butyl-2-[(4,7,10-tri{[ethoxy(methyl)phosphoryl]methyl}-1,4,7,10-tetraazacyclododecan-1-yl)methyl]pyridine-4-yl}phosphonate (22 mg, 0.027 mmol) was dissolved in aqueous HCl (1 mL, 6 M) and stirred at 70^{o}C for 18 h. Complete ester cleavage was confirmed by ESI-MS (+) (LR: *m/z* 676.6 $[M+H]^+$). The solvent was removed under reduced pressure to yield a yellow oil which was dissolved in H_2O (2 mL), the pH of the resulting solution was adjusted to 5.5 using aqueous NaOH solution (2.5 M), before $TbCl_3 \cdot 6H_2O$ (14 mg, 0.037 mmol) was added. The solution was stirred at 70^{o}C for 18 h before the solvent was removed under reduced pressure. The resulting yellow solid was purified by reverse-phase HPLC (10-100% MeOH in H_2O over 10 min; t_R = 2.3 min) to yield a white solid (4 mg, 19%). ESI-LCMS (-) *m/z* 829.7 $[M-H]^-$. ESI-HRMS (+) calcd for $[C_{24}H_{47}N_5O_9P_4{}^{159}Tb]^+$ 832.1578, found 832.1578.

[HoL^1]

An analogous procedure to that described for the synthesis of [TbL^1] was followed using diethyl {5-tert-butyl-2-[(4,7,10-tri{[ethoxy(methyl)phosphoryl]methyl}-1,4,7,10-tetraazacyclododecan-1-yl)methyl]pyridine-4-yl}phosphonate (15 mg, 0.02 mmol) and $DyCl_3 \cdot 6H_2O$ (15 mg, 0.04 mmol), to yield a white solid (4 mg, 24%). ESI-LCMS (-) *m/z* 837.2 $[M-H]^-$; ESI-HRMS (-) calcd for $[C_{24}H_{45}N_5O_9P_4{}^{165}Ho]^-$ 836.1471, found 836.1473.

[DyL^1]

An analogous procedure to that described for the synthesis of [Tb.L^1] was followed using diethyl {5-tert-butyl-2-[(4,7,10-tri{[ethoxy(methyl)phosphoryl]methyl}-1,4,7,10-tetraazacyclododecan-1-yl)methyl]pyridine-4-yl}phosphonate (38 mg, 0.046 mmol) and

$DyCl_3 \cdot 6H_2O$ (23 mg, 0.06 mmol), to yield a white solid (18 mg, 47%). ESI-LCMS (-) *m/z* 835.8 $[M-H]^-$. ESI-HRMS (+) calcd for $[C_{24}H_{47}N_5O_9P_4{}^{160}Dy]^+$ 833.1576, found 833.1573.

[TmL^1]

An analogous procedure to that described for the synthesis of [TbL^1] was followed using diethyl {5-tert-butyl-2-[(4,7,10-tri{[ethoxy(methyl)phosphoryl]methyl}-1,4,7,10-tetraazacyclododecan-1-yl)methyl]pyridine-4-yl}phosphonate (15 mg, 0.02 mmol) and $TmCl_3 \cdot 6H_2O$ (11 mg, 0.03 mmol), to yield a white solid (8 mg, 48%). ESI-LCMS (+) *m/z* 832.2 $[M-H]^-$. ESI-HRMS (+) calcd for $[C_{24}H_{47}N_5O_9P_4{}^{169}Tm]^+$ 842.1667, found 842.1647.

10-*tert*-Butyl-1,4,7-Tri{[ethoxy(benzyl)phosphoryl]methyl}-1,4,7,10-tetraazacyclododecane-10-carboxylate, 15

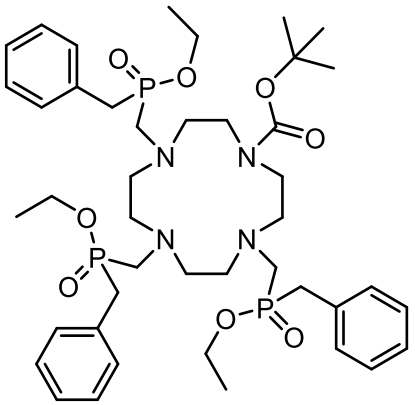

10-*tert*-Butyl-1,4,7,10-tetraazacyclododecane-10-carboxylate (320 mg, 1.2 mmol) and paraformaldehyde (800 mg, 24.7 mmol) were dissolved in anhydrous THF (30 mL) and the resulting suspension was stirred under argon at 80°C for 30 min. Diethyl benzylphosphonite (1.5 mL, 7.1 mmol) was added and the reaction was stirred at 80°C for a further 18 h. The solution was filtered and the solvent was removed under reduced pressure. The resulting orange oil was purified by alumina gel column chromatography (100% CH_2Cl_2 to 1% MeOH/ CH_2Cl_2) to yield a yellow oil (380 mg, 44%). R_f (5% MeOH/ CH_2Cl_2) = 0.48. ^{1}H NMR (600 MHz,$CDCl_3$) δ 7.32-7.07 (m, Ar), 4.09-3.64 (m, 6H, $POCH_2$), 3.59-2.40 (m, 28H, PCH_2N, PCH_2Ar, cyclen CH_2), 1.30 (s, 9H, $C(CH_3)_3$), 1.21-1.03 (m, 9H, $POCH_2C\underline{H}_3$); ^{31}P NMR (243 MHz, $CDCl_3$) δ 51.5-47.5; ^{13}C NMR (151 MHz, $CDCl_3$) δ 155.7 (CO), 131.3-127.7 (Ar), 79.9 ($\underline{C}(CH_3)_3$), 64.4 (PCH_2N), 60.7 ($POCH_2$) 55.1-51.5 (m, cyclen CH_2), 37.3-35.0 (m, $\underline{C}H_2Ar$), 28.5 ($C(\underline{C}H_3)_3$), 16.5

($POCH_2\underline{C}H_3$); ESI-LCMS (+) *m/z* 861.4 $[M+H]^+$. ESI-HRMS (+) calcd for $[C_{43}H_{68}N_4O_8P_3]^+$ 861.4250, found 861.4265.

1,4,7-Tri{[ethoxy(benzyl)phosphoryl]methyl}-1,4,7,10-tetraazacyclododecane, 16

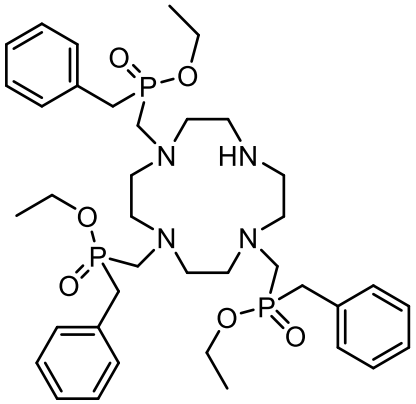

10-tert-Butyl-4,7,10-tri{[ethyoxy(benzyl)phosphoryl]methyl}-1,4,7,10-tetraazacyclododecane-10-carboxylate (350 mg, 0.41 mmol) was dissolved in anhydrous CH_2Cl_2 (2 mL) and to this was added TFA (2 mL). The solution was stirred at room temperature for 18 h, before the solvent was removed under reduced pressure. The resulting yellow oil was dissolved in H_2O (1 mL) and the pH of this solution was adjusted to 12 using aqueous NaOH solution (2.5 M) before the aqueous solution was extracted with CH_2Cl_2 (4 x 10 mL). The organic layers were combined, dried over $MgSO_4$, and the solvent removed under reduced pressure to yield a yellow oil (285 mg, 75%). ^{1}H NMR (400 MHz,$CDCl_3$) δ 7.35-7.14 (m, 15H, Ar), 4.20-3.58 (m, 6H, $POCH_2$), 3.37-2.44 (m, 28H, PCH_2N, PCH_2Ar, cyclen CH_2), 1.23-1.10 (m, 9H, $POCH_2C\underline{H}_3$); ^{31}P NMR (162 MHz, $CDCl_3$) δ 50.5-47.0; ESI-LCMS (+) *m/z* 761.2 $[M+H]^+$. ESI-HRMS (+) calcd for $[C_{38}H_{60}N_4O_6P_3]^+$ 761.3726, found 761.3734.

1,4,7-Tri{[ethoxy(benzyl)phosphoryl]methyl}-10-(5-*tert*-butyl-4-(diethoxyphosphoryl)pyridine-2-yl)methyl- 1,4,7,10-tetraazacyclododecane, L^2

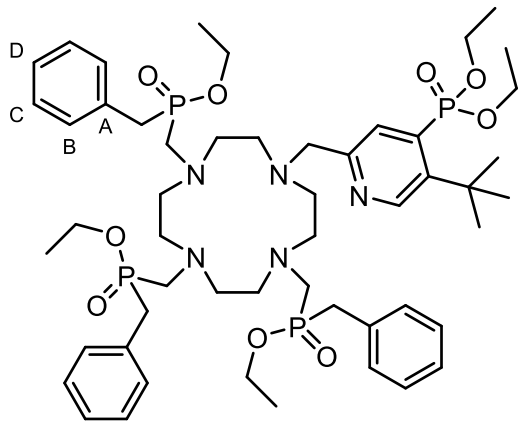

1,4,7-Tri{[ethoxy(benzyl)phosphoryl]methyl}-1,4,7,10-tetraazacyclododecane (190 mg, 0.25 mmol) was dissolved in anhydrous MeCN (2 mL) and to this was added Cs_2CO_3 (130 mg, 0.4 mmol). [5-tert-Butyl-4-(diethoxyphosphoryl)pyridine-4-yl]methyl methane sulfonate (150 mg, 0.4 mmol) was then added dropwise as a solution in anhydrous MeCN (4 mL). The resulting solution was heated to 70°C and stirred for 18 h after which the reaction was filtered to remove inorganic salts. The solvent was removed under reduced pressure and the resulting red oil was purified by alumina gel column chromatography (100% CH_2Cl_2 to 2% MeOH/ CH_2Cl_2) to yield a yellow oil (135 mg, 52%). R_f (5% MeOH/ CH_2Cl_2) = 0.58; ^{1}H NMR (700 MHz, $CDCl_3$) δ 8.69 (s, 1H, H^6), 7.93 (s, 1H, H^3), 7.31 - 7.05 (m, 15H, Ar), 4.23 – 4.05 (m, 4H, $POCH_2$), 3.99 – 3.70 (m, 8H, $POCH_2$, NCH_2py), 3.30 – 2.52 (m, 30H, , PCH_2N, PCH_2Ar, cyclen CH_2), 1.49 (s, 9H, $C(CH_3)_3$), 1.3 (t, ^3J = 7, 6H, $POCH_2C\underline{H}_3$), 1.14-1.06 (m, 9H, $POCH_2C\underline{H}_3$); ^{31}P NMR (162 MHz, $CDCl_3$) δ 49.2 (NCH_2P), 47.8 (NCH_2P), 15.5 (pyP) ^{13}C NMR (175 MHz, $CDCl_3$) δ 131.5-131 (C^A), 130.0-129.6 (C^B), 128.7-128.4 (C^C), 127.0-126.6 (C^D), 62.8 ($POCH_2$), 61.0-60.7 ($POCH_2$, NCH_2py), 54.6-50.2 (cyclen CH_2, NCH_2P), 37.1-35.9 (m, $\underline{C}H_2Ar$), 35.9 ($\underline{C}(CH_3)_3$), 31.4 ($C(\underline{C}H_3)_3$), 16.8-16.1 ($POCH_2\underline{C}H_3$); ESI-LCMS (+) *m/z* 1044.5 $[M+H]^+$; ESI-HRMS (+) calcd for $[C_{52}H_{82}N_5O_9P_4]^+$ 1044.5063, found 1044.5082.

Thulium (III) complex of 1,4,7-Tri{[ethoxy(benzyl)phosphoryl]methyl}-10-(5-*tert*-butyl-4-(diethoxyphosphoryl)pyridine-2-yl)methyl- 1,4,7,10-tetraazacyclododecane, [TmL^2]

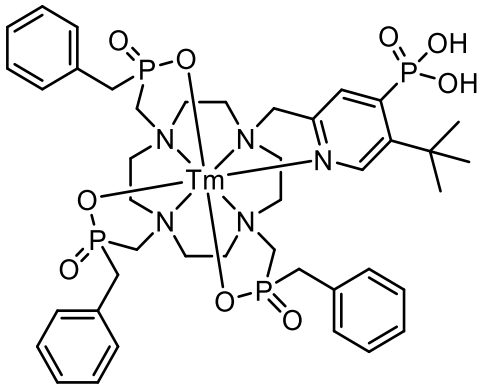

1,4,7-Tri{[ethoxy(benzyl)phosphoryl]methyl}-10-(5-*tert*-butyl-4-(diethoxyphosphoryl)pyridine-2-yl)methyl- 1,4,7,10-tetraazacyclododecane (16 mg, 0.015 mmol) was dissolved in aqueous HCl (1 mL, 6 M) and stirred at 70^{o}C for 18 h. Complete ester cleavage was confirmed by ESI-MS (-) (LR: *m/z* 902.4 $[M-H]^-$). The solvent was removed under reduced pressure to yield a yellow oil which was dissolved in H_2O (2 mL). The pH of the resulting solution was adjusted to 5.5 using aqueous NaOH solution (2.5 M) and $TmCl_3{\cdot}6H_2O$ (9 mg, 0.023 mmol) was added. The solution was stirred at 70^{o}C for 18 h before the solvent was removed under reduced pressure. The resulting yellow solid was purified by reverse-phase HPLC (10-100% MeCN in H_2O over 10 min; t_R = 8.3 min) to yield a glassy white solid (5 mg, 31%). ESI-LCMS (+) *m/z* 1070.2 $[M+H]^+$; ESI-HRMS (+) calcd for $[C_{42}H_{58}N_5O_9P_4{}^{169}Tm]^+$ 1070.2605, found 1070.2650.

[GdL^2]

An analogous procedure to that described for the synthesis of [TmL^2] was followed using 1,4,7-tri{[ethoxy(benzyl)phosphoryl]methyl}-10-(5-*tert*-butyl-4-(diethoxyphosphoryl)pyridine-2-yl)methyl- 1,4,7,10-tetraazacyclododecane (22 mg, 0.020 mmol) and $GdCl_3{\cdot}6H_2O$ (15 mg, 0.04 mmol), to yield a white solid (7 mg, 33 %) . ESI-LCMS (+) *m/z* 1058.9 $[M+H]^+$; ESI-HRMS (+) calcd for $[C_{42}H_{58}N_5O_9P_4{}^{158}Gd]^+$ 1059.2515, found 1059.2563.

(5-*tert*-Butylpyridin-2-yl)methanol, 17

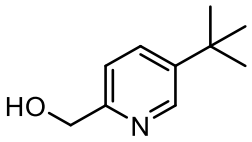

5-*tert*-Butyl-2-methylpyridin-1-oxide (5.0 g, 30.3 mmol) was dissolved in anhydrous CH_2Cl_2 (40 mL) and TFA (22 mL, 156.8 mmol) was added. The resulting solution was stirred for 18 h at 60°C under argon. The reaction was monitored by ^1H NMR spectroscopy, and upon completion the solvent was removed under reduced pressure. The resulting yellow oil was stirred in a mixture of H_2O (25 mL) and EtOH (25 mL) at room temperature for 2h. The solution was concentrated (*ca.* 15 mL) and extracted with CH_2Cl_2 (3 x 100 mL). The organic layers were combined, dried over $MgSO_4$ and the solvent removed under reduced pressure. The resulting orange oil was purified by silica gel column chromatography (100% CH_2Cl_2 to 5% MeOH/ CH_2Cl_2) to yield a yellow oil (4.3 g, 86%). R_f (10% MeOH/ CH_2Cl_2) = 0.46. ^1H NMR (400 MHz, $CDCl_3$) δ 8.57 (s, 1H, H^6), 8.26 (d, *J* = 8 Hz, 1H, H^4), 7.75 (d, *J* = 8 Hz, 1H, H^3), 4.88 (s, 2H, CH_2OH), 1.26 (s, 9H, $C(CH_3)_3$). ^{13}C NMR (101 MHz, $CDCl_3$) δ 154.4 (C^2), 149.1 (C^6), 142.9 (C^5), 137.9 (C^3), 124.3 (C^4), 60.0 ($\underline{C}H_2OH$), 34.1 ($\underline{C}(CH_3)_3$), 30.2 ($C(\underline{C}H_3)_3$). ESI-LCMS (+) m/z 166.3 $[M+H]^+$. ESI-HRMS (+) calcd for $[C_{10}H_{16}NO]^+$ 166.1232, found 166.1231.

(5-*tert*-Butylpyridin-2-yl)methyl methanesulfonate, 18

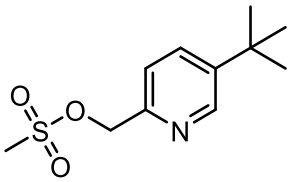

(5-*tert*-Butylpyridin-2-yl)methanol (200 mg, 1.2 mmol) was dissolved in anhydrous THF (5 mL) and stirred at 5°C for 10 min, before the addition of NEt_3 (340 µL, 2.4 mmol). Mesyl chloride (140 µL, 1.8 mmol) was added dropwise and the resulting solution was allowed to stir at room temperature for 30 min. The solvent was removed under reduced pressure and the residue was dissolved in H_2O (5 mL) and extracted with CH_2Cl_2 (3 x 10 mL). The organic layers were combined, dried over $MgSO_4$ and the solvent removed under reduced pressure. The resulting orange oil was used without further purification (247 mg, 84 %). R_f (10% MeOH/ CH_2Cl_2) = 0.76; ^1H NMR (400 MHz,

$CDCl_3$) δ 8.57 (s, 1H, H^6), 8.15 (d, *J* = 8 Hz, 1H, H^4), 7.75 (d, *J* = 8 Hz, 1H, H^3), 5.44 (s, 2H, CH_2OMs), 3.07 (s, 3H, SCH_3) 1.25 (s, 9H, $C(CH_3)_3$). ESI-LCMS (+) m/z 244.3 $[M+H]^+$.

1,4,7-Tri{[ethoxy(benzyl)phosphoryl]methyl}-10-(5-tert-butylpyridin-2-yl)methyl-1,4,7,10-tetraazacyclododecane, L^4

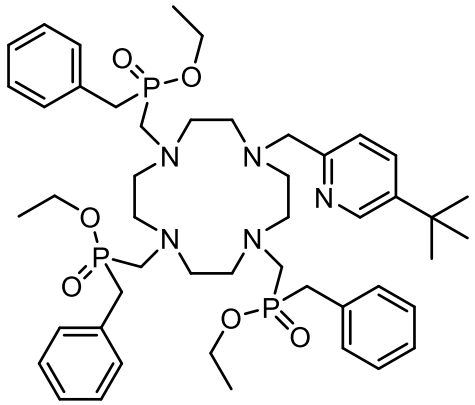

1,4,7-Tri{[ethoxy(benzyl)phosphoryl]methyl}-1,4,7,10-tetraazacyclododecane (285 mg, 0.38 mmol) was dissolved in anhydrous MeCN (2 mL) and to this was added Cs_2CO_3 (210 mg, 0.64 mmol). (5-*tert*-Butylpyridin-2-yl)methyl methanesulfonate (130 mg, 0.525 mmol) was then added dropwise as a solution in anhydrous MeCN (4 mL). The resulting solution was heated to 70°C and stirred for 18 h before being cooled to room temperature and filtered to remove inorganic salts. The solvent was removed under reduced pressure and the resulting red oil was purified by alumina gel column chromatography (100% CH_2Cl_2 to 2% MeOH/ CH_2Cl_2) to yield an orange oil (90 mg, 22%). R_f (5% MeOH/ CH_2Cl_2) = 0.45; ^{1}H NMR (400 MHz, $CDCl_3$) δ 8.62 (s, 1H, H^6), 7.78 - 7.68 (m, 2H, H^3, H^4), 7.30-7.14 (m, 15H, Ar), 4.68 (s, 2H, NCH_2Py), 4.24-2.44 (m, 34H, $POCH_2$, PCH_2N, PCH_2Ar, cyclen CH_2), 1.52-1.37 (m, 9H, $POCH_2C\underline{H}_3$), 1.29 (s, 9H, $C(CH_3)_3$); ^{31}P NMR (162 MHz, $CDCl_3$) δ 52.5 – 48.3 (mixture of isomers); ESI-LCMS (+) *m/z* 908.3 $[M+H]^+$; ESI-HRMS (+) calcd for $[C_{48}H_{73}N_5O_6P_3]^+$ 908.4774, found 908.4774.

Dysprosium(III) complex of 1,4,7-tri{[(benzyl)phosphoryl]methyl}-10-(5-tert-butylpyridin-2-yl)methyl-1,4,7,10-tetraazacyclododecane, [LnL^4]

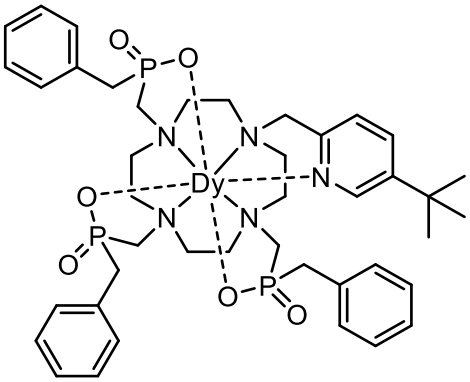

1,4,7-Tri{[ethoxy(benzyl)phosphoryl]methyl}-10-(5-tert-butylpyridin-2-yl)methyl-1,4,7,10-tetraazacyclododecane (11 mg, 0.011 mmol) was dissolved in aqueous HCl (1 mL, 6 M) and stirred at 100^{o}C for 18 h. Complete ester cleavage was confirmed by ESI-MS (+) (LR: *m/z* 824.4 $[M+H]^+$). The solvent was removed under reduced pressure to yield a yellow oil which was dissolved in H_2O (2 mL). The pH of the solution was adjusted to 5.5 using aqueous NaOH solution (2.5 M) and $DyCl_3{\cdot}6H_2O$ (20 mg, 0.053 mmol) was added. The solution was stirred at 70^{o}C for 18 h before the solvent was removed under reduced pressure. The resulting yellow solid was purified by reverse-phase HPLC (10-100% MeCN in H_2O over 10 min; t_R = 10.0 min) to yield a glassy white solid (6 mg, 52%). ESI-LCMS (+) *m/z* 985.3 $[M+H]^+$. ESI-HRMS (+) calcd for $[C_{42}H_{58}N_5O_6P_3{}^{160}Dy]^+$ 981.2852, found 981.2886.

[TbL^4]

An analogous procedure to that described for the synthesis of [DyL^4] was followed using 1,4,7-tri{[ethoxy(benzyl)phosphoryl]methyl}-10-(5-tert-butylpyridin-2-yl)methyl-1,4,7,10-tetraazacyclododecane (35 mg, 0.039 mmol) and $TbCl_3{\cdot}6H_2O$ (17 mg, 0.045 mmol), to yield a white solid (27 mg, 71%). ESI-LCMS (+) *m/z* 980.1 $[M+H]^+$. ESI-HRMS (+) calcd for $[C_{42}H_{58}N_5O_6P_3{}^{159}Tb]^+$ 980.2840, found 980.2884

[HoL^4]

An analogous procedure to that described for the synthesis of [DyL^4] was followed using 1,4,7-tri{[ethoxy(benzyl)phosphoryl]methyl}-10-(5-tert-butylpyridin-2-yl)methyl-

1,4,7,10-tetraazacyclododecane (76 mg, 0.083 mmol) and $HoCl_3 \cdot 6H_2O$ (38 mg, 0.016 mmol), to yield a white solid (4 mg, 47%). ESI-LCMS (+) *m/z* 987.8 $[M+H]^+$. ESI-HRMS (+) calcd for $[C_{42}H_{58}N_5O_6P_3{}^{165}Ho]^+$ 986.2903, found 986.2906.

[ErL^4]

An analogous procedure to that described for the synthesis of [DyL^4] was followed using 1,4,7-tri{[ethoxy(benzyl)phosphoryl]methyl}-10-(5-tert-butylpyridin-2-yl)methyl-1,4,7,10-tetraazacyclododecane (17 mg, 0.019 mmol) and $ErCl_3 \cdot 6H_2O$ (10 mg, 0.03 mmol), to yield a white solid (12 mg, 64%). ESI-LCMS (+) *m/z* 987.4 $[M+H]^+$. ESI-HRMS (+) calcd for $[C_{42}H_{58}N_5O_6P_3{}^{164}Er]^+$ 985.2892, found 985.2911.

[TmL^4]

An analogous procedure to that described for the synthesis of [DyL^4] was followed using 1,4,7-Tri{[ethoxy(benzyl)phosphoryl]methyl}-10-(5-tert-butylpyridin-2-yl)methyl-1,4,7,10-tetraazacyclododecane (35 mg, 0.039 mmol) and $TmCl_3 \cdot 6H_2O$ (17 mg, 0.045 mmol), to yield a white solid (25 mg, 65%). ESI-LCMS (+) *m/z* 990.8 $[M+H]^+$. ESI-HRMS (+) calcd for $[C_{42}H_{58}N_5O_6P_3{}^{169}Tm]^+$ 990.2942, found 990.2952.

[YbL^4]

An analogous procedure to that described for the synthesis of [DyL^4] was followed using 1,4,7-tri{[ethoxy(benzyl)phosphoryl]methyl}-10-(5-tert-butylpyridin-2-yl)methyl-1,4,7,10-tetraazacyclododecane (44 mg, 0.049 mmol) and $YbCl_3 \cdot 6H_2O$ (21 mg, 0.055 mmol), to yield a white solid (33 mg, 68%). ESI-LCMS (+) *m/z* 995.4 $[M+H]^+$. ESI-HRMS (+) calcd for $[C_{42}H_{58}N_5O_6P_3{}^{170}Yb]^+$ 991.2948, found 991.2958.

Crystals of the ytterbium complex were grown by slow diffusion of diethyl ether into a solution of methanol and examined by X-ray crystallography: $C_{42}H_{57}N_5O_6P_3Yb$ x $\frac{3}{2}$ CH_3OH x H_2O, M_r = 1106.02 g/mol, monoclinic, space group $P2_1/c$ (no. 14), a = 30.3971(15) Å, b = 17.3173(8) Å, c = 19.4270(10) Å, β = 100.7201(16) , V = 10047.8(9) Å^3, Z = 2, T = 120 K, μ(MoKα) = 2.015 mm^{-1}, D_{calc} = 1.462 g/cm^3, 192170 reflections measured (3.92°≤ 2Θ ≤ 60°), 29289 unique (R_{int} = 0.0425, R_{sigma} = 0.0318) which were used in all calculations. The final R_1 was 0.0381 (I > 2σ(I)) and wR_2 was 0.0942 (all data).

[EuL^4]

An analogous procedure to that described for the synthesis of [DyL^4] was followed using 1,4,7-tri{[ethoxy(benzyl)phosphoryl]methyl}-10-(5-tert-butylpyridin-2-yl)methyl-1,4,7,10-tetraazacyclododecane (38 mg, 0.042 mmol) and $EuCl_3 \cdot 6H_2O$ (18 mg, 0.05 mmol), to yield a white solid (25 mg, 61%). ESI-LCMS (+) *m/z* 972.2 $[M+H]^+$. ESI-HRMS (+) calcd for $[C_{42}H_{58}N_5O_6P_3{}^{151}Eu]^+$ 972.2799, found 972.2820.

[YL^4]

An analogous procedure to that described for the synthesis of [DyL^4] was followed using 1,4,7-tri{[ethoxy(benzyl)phosphoryl]methyl}-10-(5-tert-butylpyridin-2-yl)methyl-1,4,7,10-tetraazacyclododecane (35 mg, 0.038 mmol) and $YCl_3 \cdot 6H_2O$ (18 mg, 0.05 mmol), to yield a white solid (22 mg, 64%). ^{31}P NMR (162 MHz, CD_3OD) δ 37.2 (d, $^2J_{YP}$ = 6 Hz, P^1), 36.4 (d, $^2J_{YP}$ = 6 Hz, P^2), 34.2 (d, $^2J_{YP}$ = 6 Hz, P^3); ^{1}H NMR (600 MHz, CD_3OD) and ^{13}C NMR (151 MHz, CD_3OD):

Carbon Label	Shift, ppm (CP coupling)	Proton Label	Shift, ppm
py2	156.1		
py3	124.9	py3	7.45
py4		py4	8.05
py5	147.7		
py6	146.0	py6	9.04
tbu	34.9		
tbu	31.3	tbu	1.39
c1	51.6	ax	3.69
		eq	2.50
c2	54.9	ax	3.81
		eq	2.59
c3	53.5 (15)	ax	3.56
		eq	2.43
c4	55.7	ax	3.85
		eq	2.50
c5	53.0 (13)	ax	3.60
		eq	2.33
c6	55.2	ax	4.27
		eq	2.45
c7	53.5 (15)	ax	3.56
		eq	2.36
c8	54.3	ax	3.21
		eq	2.51
ap	61.2	ax	4.72
		eq	3.72
a1	58.0 (94.9)	ax	3.67
		eq	2.52
a2	57.14 (95.2)	ax	4.04
		eq	2.54
a3	57.06 (97.9)	ax	2.95
		eq	2.44

r1	38.6 (90.8)	ax	3.24
		eq	2.92
r2	39.0 (91.7)	ax	3.65
		eq	3.35
r3	40.4 (91.6)	ax	3.21
		eq	2.97
ph1i	134.4		
ph1o	131.5	ph1o	7.12
ph1m	128.8	ph1m	7.12
ph1p	126.7	ph1p	7.06
ph2i	127.1		
ph2o	131.5	ph2o	7.61
ph2m	129.2	ph2m	7.27
ph2p	127.1	ph2p	7.15
ph3i	134.3		
ph3o	130.8	ph3o	7.29
ph3m	129.6	ph3m	7.21
ph3p	127.6	ph3p	7.17

1,7-Dibenzyl 1,4,7,10-tetraazacyclododecane 1,7-dicarboxylate, 19

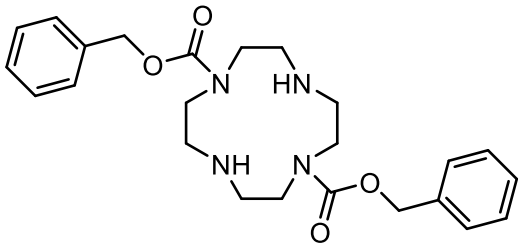

1,4,7,10-Tetraazacyclododecane (3.5 g, 20.3 mmol) was dissolved in a solution of distilled H_2O:1,4-dioxane (50:20 mL) and to this was added Na_2HPO_4 (9.8 g, 69.0 mmol). The pH of the solution was adjusted to 2.5 by addition of conc. HCl (aq). A solution of benzyl chloroformate (7.3 mL, 50.8 mmol) in 1,4-dioxane (10 mL) was added dropwise over a period of 30 min and the resulting solution was stirred at room temperature for 18 h. The solvent was removed under reduced pressure and the residue dissolved in H_2O (200 mL) and the pH adjusted to 7 by the addition of conc. KOH (aq). The resulting aqueous solution was then washed with Et_2O (3 x 100 mL) to remove side products, the aqueous phase was then extracted with CH_2Cl_2 (3 x 100 mL). The organic phases were combined, dried over $MgSO_4$ and the solvent removed under reduced pressure to yield a colourless oil. The oil was redissolved in CH_2Cl_2 (5 mL) followed by precipitation of the desired product via the addition of cold Et_2O (200 mL) to yield a white solid that was collected by filtration (6.12 g, 69%). ^{1}H NMR (700 MHz,$CDCl_3$) δ 7.14-6.81 (m, 10H, ArH), 4.81 (s, 4H, CH_2O), 3.49-3.14 (m, 8H, cyclen CH_2), 2.83-2.45 (m, 8H, cyclen CH_2); ^{13}C NMR (176 MHz, $CDCl_3$) δ 154.9 ($\underline{C}OCH_2Ar$),

135.1 (Ar), 127.7-126.9 (Ar), 66.5 (CO<u>C</u>H_2Ar), 49.4-48.1 (cyclen CH_2); ESI-LCMS (+) *m/z* 441.2 $[M+H]^+$. ESI-HRMS (+) calcd for $[C_{24}H_{33}N_4O_4]^+$ 441.2502, found 441.2492.

1,7-Di-benzyl-4,10-*tert*-butyl-1,4,7,10-tetraazacyclododecane-1,4,7,10-tetracarboxylate, 20

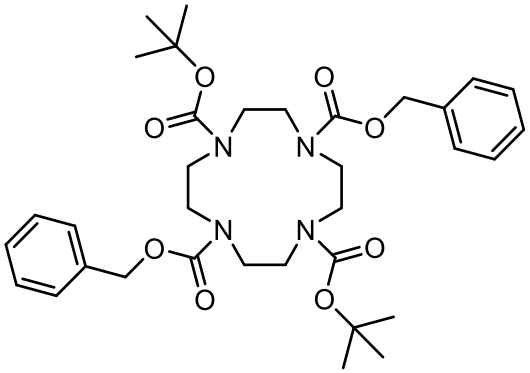

1,7-Di-benzyl-1,4,7,10-tetraazacyclododecane-1,7-dicarboxylate (1.1 g, 2.5 mmol) was dissolved in anhydrous CH_2Cl_2 (20 mL) and to this was added triethylamine (0.9 mL, 6.5 mmol) was added. The resulting solution was stirred under argon for 10 minutes before the addition of di-tert-butyl dicarbonate (1.4 g, 6.5 mmol). After addition, the solution was stirred at room temperature for a further 18 h. The solvent was removed under reduced pressure and the resulting yellow oil was purified by silica gel column chromatography (100% CH_2Cl_2 to 2% MeOH/ CH_2Cl_2) to yield a white solid (1.49 g, 95%). R_f (10% MeOH/ CH_2Cl_2) = 0.66. ^{1}H NMR (400 MHz,$CDCl_3$) δ 7.34-7.14 (m, 10H, Ar), 5.04 (s, 4H, OCH_2Ar) 3.29 (br, 16H, cyclen CH_2) 1.31 (s, 18H, $C(CH_3)_3$); ^{13}C NMR (101 MHz, $CDCl_3$) δ 156.9 (CO), 136.4 (Ar), 128.6 (Ar), 128.4 (Ar), 128.3 (Ar), 80.1 (<u>C</u>$(CH_3)_3$), 67.3 (CH_2O), 50.2 (br, cyclen CH_2), 28.4 ($C(\underline{C}H_3)_3$), ESI-LCMS (+) *m/z* 641.0 $[M+H]^+$.

tert-Butyl-1,4,7,10-tetraazacyclododecane-1,7-carboxylate, 21

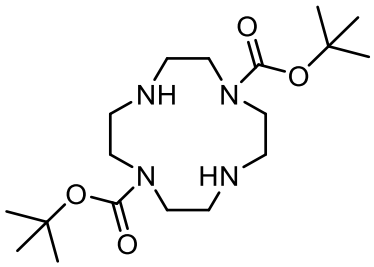

1,7-Di-benzyl-4,10-_tert_-butyl-1,4,7,10-tetraazacyclododecane-1,4,7,10-tetracarboxylate (1.4 g, 2.2 mmol) was dissolved in MeOH (20 mL) and to this was added $Pd(OH)_2/C$ (~300 mg). The reaction mixture was loaded onto a Parr hydrogenator, where it was subjected to agitation for 18 h, under an atmosphere of H_2 (30 psi). The resulting solution was filtered through celite to ensure removal of catalyst, the solvent was then removed under reduced pressure to yield a pale yellow oil (0.66 g, 80%). ^{1}H NMR (400 MHz,$CDCl_3$) δ 5.31 (br s, NH), 3.75-2.83 (m, 16H, cyclen CH_2) 1.48 (s, 9H, $C(CH_3)_3$); ^{13}C NMR (101 MHz, $CDCl_3$) δ 157.5 (CO) , 82.3 ($\underline{C}(CH_3)_3$), 48.2 (cyclen CH_2), 46.9 (cyclen CH_2), 45.6 (cyclen CH_2), 44.5 (cyclen CH_2), 28.7 ($C(\underline{C}H_3)_3$), ESI-LCMS (+) *m/z* 373.4 $[M+H]^+$.

1,7-_tert_-Butyl-4,10-tri{[ethyoxy(benzyl)phosphoryl]methyl}-1,4,7,10-tetraazacyclododecane-1,7-carboxylate, 22

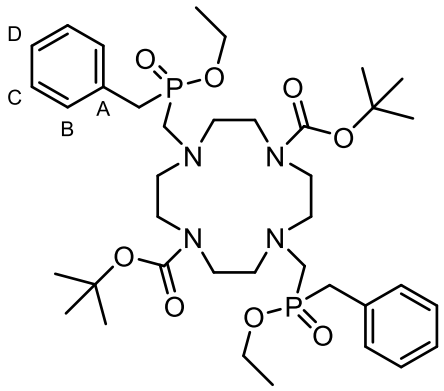

tert-Butyl-1,4,7,10-tetraazacyclododecane-1,7-dicarboxylate (1.08 g, 2.9 mmol) and paraformaldehyde (1.3 g, 40 mmol) were dissolved in anhydrous THF (60 mL) and the resulting suspension was stirred under argon at 80^{o}C for 10 minutes. Diethyl benzylphosphonite (2.5 mL, 11.6 mmol) was added and the reaction was stirred at 80^{o}C for a further 18 h. The solution was filtered and the solvent was removed under

reduced pressure. The resulting yellow oil was purified by alumina gel column chromatography (100% CH_2Cl_2 to 1% MeOH/ CH_2Cl_2) to yield a colourless oil (1.82 mg, 82%). R_f (10% MeOH/ CH_2Cl_2) = 0.76. ^{1}H NMR (700 MHz,$CDCl_3$) δ 7.32-7.16 (m, 10H, Ar), 3.99-3.75 (m, 4H, $POC\underline{H}_2CH_3$), 3.46-2.72 (m, 24H, PCH_2N, PCH_2Ar, cyclen CH_2), 1.39 (s, 9H, $C(CH_3)_3$), 1.14 (t, ^3J = 8, 6H, $POCH_2C\underline{H}_3$); ^{31}P NMR (283 MHz, $CDCl_3$) δ 48.9; ^{13}C NMR (176 MHz, $CDCl_3$) δ 155.9 (CO), 131.6 (d, $^2J_{CP}$ = 8, C^A), 129.9 (d, $^3J_{CP}$ = 5.5, C^B), 128.6 (d, $^4J_{CP}$ = 2.5, C^C), 126.8 (C^D), 79.6 ($\underline{C}(CH_3)_3$), 60.7 ($POCH_2$), 55.7 (br, cyclen CH_2), 52.3 (d, $^1J_{CP}$ = 104.5, NCH_2P), 46.4 (cyclen CH_2), 35.9 (d, $^1J_{CP}$ = 104.5, $P\underline{C}H_2Ar$), 28.2 ($C(\underline{C}H_3)_3$), 16.6 ($POCH_2\underline{C}H_3$); ESI-LCMS (+) *m/z* 764.9 $[M+H]^+$. ESI-HRMS (+) calcd for $[C_{38}H_{63}N_4O_8P_2]^+$ 765.4121, found 765.4155.

1,7-Tri{[ethyoxy(benzyl)phosphoryl]methyl}-1,4,7,10-tetraazacyclododecane, 23

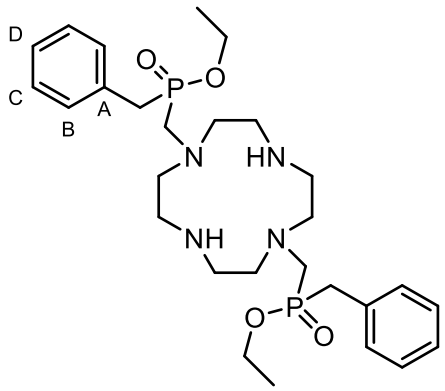

1,7-*tert*-Butyl-4,10-tri{[ethyoxy(benzyl)phosphoryl]methyl}-1,4,7,10-tetraazacyclododecane-1,7-carboxylate (250 mg, 0.33 mmol) was dissolved in anhydrous CH_2Cl_2 (2 mL) and to this was added TFA (2 mL). The solution was stirred at room temperature for 18 h after which the solvent was removed under reduced pressure. The resulting yellow oil was dissolved in H_2O (1 mL) and the pH of this solution was adjusted to 12 with aqueous NaOH solution (2.5 M) before being extracted with CH_2Cl_2 (4 x 10 mL). The organic layers were combined, dried over $MgSO_4$, and the solvent removed under reduced pressure to yield a yellow oil (148 mg, 79%). ^{1}H NMR (700 MHz,$CDCl_3$) δ 7.31-7.13 (m, 10H, Ar), 4.04-3.78 (m, 4H, $POC\underline{H}_2CH_3$), 3.26-2.75 (m, 24H, PCH_2N, PCH_2Ar, cyclen CH_2), 1.18 (t, ^3J = 6, 6H, $POCH_2C\underline{H}_3$); ^{31}P NMR (283 MHz, $CDCl_3$) δ 49.6; ^{13}C NMR (176 MHz, $CDCl_3$) δ 130.8 (d, $^2J_{CP}$ = 7.5, C^A), 129.8 (d, $^3J_{CP}$ = 5.5, C^B), 128.9 (d, $^4J_{CP}$ = 2.5, C^C), 127.3 (C^D), 61.5 ($POCH_2$), 52.0 (br, NCH_2P), 44.5

(cyclen CH_2), 36.1 (d, $^1J_{CP}$ = 78.5, P<u>C</u>H_2Ar), 16.4 (POCH_2<u>C</u>H_3); ESI-LCMS (+) *m/z* 564.9 $[M+H]^+$. ESI-HRMS (+) calcd for $[C_{28}H_{47}N_4O_4P_2]^+$ 565.3073, found 565.3077.

1,7-(5-*tert*-Butylpyridin-2-yl)methyl-4,10-di{[ethoxy(benzyl)phosphoryl]methyl}-1,4,7,10-tetraazacyclododecane, L^5

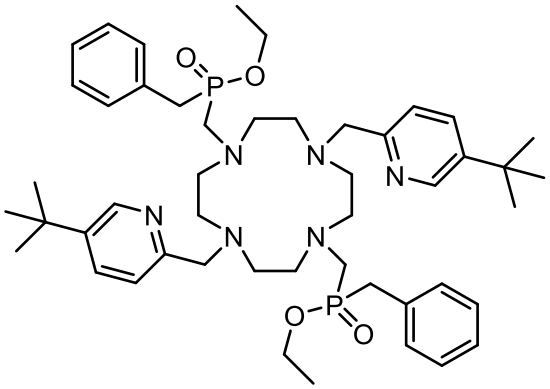

1,7-Tri{[ethyoxy(benzyl)phosphoryl]methyl}-1,4,7,10-tetraazacyclododecane (150 mg, 0.27 mmol) was dissolved in anhydrous MeCN (3 mL) and to this was added Cs_2CO_3 (350 mg, 1.07 mmol). (5-*tert*-Butylpyridin-2-yl)methyl methanesulfonate (183 mg, 0.74 mmol) was then added dropwise as a solution in anhydrous MeCN (6 mL). The resulting solution was heated to 70^{o}C and stirred for 18 h after which the reaction was filtered to remove inorganic salts. The solvent was removed under reduced pressure and the resulting red oil was purified by alumina gel column chromatography (100% CH_2Cl_2 to 2% MeOH/ CH_2Cl_2) to yield a yellow oil (220 mg, 27%). R_f (5% MeOH/ CH_2Cl_2) = 0.46. ^{1}H NMR (700 MHz,$CDCl_3$) δ 8.52 (d, ^4J = 2.5, 2H, H^6), 7.54 (dd, ^3J = 8, ^4J = 2.5, 2H, H^4), 7.44(d, ^3J = 8, 2H, H^3), 7.31-7.09 (m, 10H, Ar), 4.07-3.66 (m, 12H, $POCH_2$, PCH_2N, NCH_2py), 3.23-3.04 (m, 4H, PCH_2Ar), 3.00-2.90 (br m, 4H, cyclen CH_2), 2.86-2.76 (br m, 4H, cyclen CH_2), 2.74-2.62 (br m, 8H, cyclen CH_2), 1.24 (s, 18H, $C(CH_3)_3$), 1.06 (t, ^3J = 7, 6H, POCH_2C<u>H</u>$_3$); ^{31}P NMR (243 MHz, $CDCl_3$) δ 49.4, 48.9; ESI-LCMS (+) *m/z* 859.5 $[M+H]^+$; ESI-HRMS (+) calcd for $[C_{48}H_{73}N_6O_4P_2]^+$ 859.5169, found 859.5174.

Dysprosium (III) complex of 1,7-(5-*tert*-butylpyridin-2-yl)methyl-4,10-di{[benzylphosphoryl]methyl}-1,4,7,10-tetraazacyclododecane chloride [DyL^5]Cl

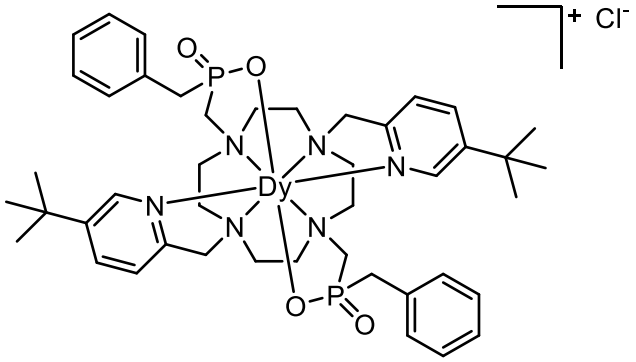

1,7-(5-tert-Butylpyridin-2-yl)methyl-1,4,7,10-tetraazacyclododecane (220 mg, 0.26 mmol) was dissolved in aqueous HCl (5 mL, 6 M) and stirred at 70^{o}C for 18 h. Complete ester cleavage was confirmed by ESI-MS (-) (LR: *m/z* 801.4 $[M-H]^-$). The solvent was removed under reduced pressure to yield a yellow oil which was dissolved in H_2O (2 mL). The pH of the solution was adjusted to 5.5 using aqueous NaOH solution (2.5 M) and $DyCl_3{\cdot}6H_2O$ (20 mg, 0.053 mmol) was added. The solution was stirred at 70^{o}C for 18 h before the solvent was removed under reduced pressure. The resulting yellow solid was purified by reverse-phase HPLC (10-100% MeCN in H_2O over 10 min; t_R = 9.3 min) to yield a glassy white solid (15 mg, 39%). ESI-LCMS (+) *m/z* 964.1 $[M]^+$. ESI-HRMS (+) calcd for $[C_{44}H_{62}N_6O_4P_2{}^{160}Dy]^+$ 960.3560, found 960.3569.

[TbL^5]Cl

An analogous procedure to that described for the synthesis of [DyL^5]Cl was followed using 1,7-(5-*tert*-butylpyridin-2-yl)methyl-4,10-di{[benzylphosphoryl]methyl}-1,4,7,10-tetraazacyclododecane (8 mg, 0.01 mmol) and $TbCl_3{\cdot}6H_2O$ (6 mg, 0.016 mmol), to yield a white solid (5 mg, 52%). ESI-LCMS (+) *m/z* 959.4 $[M]^+$. ESI-HRMS (+) calcd for $[C_{44}H_{62}N_6O_4P_2{}^{159}Tb]^+$ 959.3561, found 959.3588.

The complex **[TbL^5]Cl** (1 eq.) was dissolved in methanol and to this solution was added ammonium hexafluorophosphate (5 eq.). The solvent was removed under reduced pressure and the resulting white solid was suspended in water (1.5 mL). The suspension was centrifuged and the white solid was isolated and dried under vacuum. Crystals of the terbium complex were grown by slow diffusion of diethyl ether into a

solution of methanol and examined by X-ray crystallography: $C_{44}H_{62}N_6O_4P_2Tb$ x PF_6 x 3 CH_3OH, M_r = 1297.07 g/mol, triclinic, space group P-1 (no. 2), a = 13.0815(7) Å, b = 13.3828(7) Å, c = 33.0590(17) Å, α = 84.676(2), β = 85.9292(19), γ = 82.7638(19), V = 5706.4(5) Å^3, Z = 4, T = 120 K, μ(MoKα) = 1.403 mm^{-1}, D_{calc} = 1.510 g/cm^3, 111088 reflections measured (3.886° ≤ 2Θ ≤ 60.068°), 33377 unique (R_{int} = 0.0393, R_{sigma} = 0.0521) which were used in all calculations. The final R_1 was 0.0366 (I > 2σ(I)) and wR_2 was 0.0809 (all data).

[HoL^5]Cl

An analogous procedure to that described for the synthesis of [DyL^5]Cl was followed using 1,7-(5-*tert*-butylpyridin-2-yl)methyl-4,10-di{[benzylphosphoryl]methyl}-1,4,7,10-tetraazacyclododecane (4 mg, 0.005 mmol) and $TbCl_3{\cdot}6H_2O$ (3 mg, 0.008 mmol), to yield a white solid (2.2 mg, 44 %). ESI-LCMS (+) *m/z* 965.6 $[M]^+$. ESI-HRMS (+) calcd for $[C_{44}H_{62}N_6O_4P_2{}^{165}Ho]^+$ 965.3611, found 965.3643.

[ErL^5]Cl

An analogous procedure to that described for the synthesis of [DyL^5]Cl was followed using 1,7-(5-*tert*-butylpyridin-2-yl)methyl-4,10-di{[benzylphosphoryl]methyl}-1,4,7,10-tetraazacyclododecane (8 mg, 0.01 mmol) and $ErCl_3{\cdot}6H_2O$ (6 mg, 0.016 mmol), to yield a white solid (6.3 mg, 65%). ESI-LCMS (+) *m/z* 966.3 $[M]^+$. ESI-HRMS (+) calcd for $[C_{44}H_{62}N_6O_4P_2{}^{164}Er]^+$ 964.3600, found 964.3606.

[TmL^5]Cl

An analogous procedure to that described for the synthesis of [DyL^5]Cl was followed using 1,7-(5-*tert*-butylpyridin-2-yl)methyl-4,10-di{[benzylphosphoryl]methyl}-1,4,7,10-tetraazacyclododecane (8 mg, 0.01 mmol) and $TmCl_3{\cdot}6H_2O$ (6 mg, 0.016 mmol), to yield a white solid (5.5 mg, 57%). ESI-LCMS (+) *m/z* 969.4 $[M]^+$. ESI-HRMS (+) calcd for $[C_{44}H_{62}N_6O_4P_2{}^{169}Tm]^+$ 969.3650, found 969.3679.

[YbL^5]Cl

An analogous procedure to that described for the synthesis of [DyL^5]Cl was followed using 1,7-(5-*tert*-butylpyridin-2-yl)methyl-4,10-di{[benzylphosphoryl]methyl}-1,4,7,10-

tetraazacyclododecane (12 mg, 0.015 mmol) and $YbCl_3 \cdot 6H_2O$ (8 mg, 0.02 mmol), to yield a white solid. ESI-LCMS (+) *m/z* 974.2 $[M]^+$. ESI-HRMS (+) calcd for $[C_{44}H_{62}N_6O_4P_2{}^{170}Yb]^+$ 970.3656, found 970.3677.

The complex **[YbL^5]Cl** (1 eq.) was dissolved in methanol and to this solution was added ammonium hexafluorophosphate (5 eq.). The solvent was removed under reduced pressure and the resulting white solid was suspended in water (1.5 mL). The suspension was centrifuged and the white solid was isolated and dried under vacuum. Crystals of the ytterbium complex **[YbL^5]PF$_6$** were grown by slow diffusion of diethyl ether into a solution of methanol and examined by X-ray crystallography: $C_{44}H_{62}N_6O_4P_2Yb \times PF_6 \times 3\ CH_3OH$, M_r = 1215.07 g/mol, triclinic, space group P-1 (no. 2), a = 13.0386(7) Å, b = 13.3379(7) Å, c = 17.3611(9) Å, α = 92.8811(19), β = 108.9003(18), γ = 96.7856(19), V = 2823.8(3) Å^3, Z = 1, T = 120 K, μ(MoKα) = 1.811 mm^{-1}, D_{calc} = 1.429 g/cm^3, 62291 reflections measured (4.146° ≤ 2Θ ≤ 60.324°), 16643 unique (R_{int} = 0.0471, R_{sigma} = 0.0556) which were used in all calculations. The final R_1 was 0.0586 (I > 2σ(I)) and wR_2 was 0.1430 (all data).

[YL^5]Cl

An analogous procedure to that described for the synthesis of [DyL^5]Cl was followed 1,7-(5-*tert*-butylpyridin-2-yl)methyl-4,10-di{[benzylphosphoryl]methyl}-1,4,7,10-tetraazacyclododecane (12 mg, 0.015 mmol) and $YCl_3 \cdot 6H_2O$ (8 mg, 0.02 mmol), to yield a white solid. ESI-LCMS (+) *m/z* 889.3 $[M]^+$. ESI-HRMS (+) calcd for $[C_{44}H_{62}N_6O_4P_2Y]^+$ 889.3366, found 889.3381. ^{31}P NMR (243 MHz, CD_3OD) δ 34.9;,^{1}H NMR (600 MHz, CD_3OD) and ^{13}C NMR (151 MHz, CD_3OD):

Carbon Label	Shift, ppm (CP coupling)	Proton Label	Shift, ppm
py2	155.6		
py3	125.2	py3	7.60
py4	139.4	py4	8.22
py5	148.3		
py6	146.1	py6	8.94
tbu	34.9		
tbu	31.3	tbu	1.39
c1	51.6	ax	3.84
		eq	2.58
c2	54.9	ax	4.25
		eq	2.64
c3	54.1 (14.4)	ax	3.64
		eq	2.53
c4	54.6	ax	3.34
		eq	2.59

ap	60.0	ax	5.15
		eq	3.87
a1	57.4 (97.9)	ax	3.06
		eq	2.56
r1	39.0 (91.7)	ax	3.01
		eq	2.87
ph1i	133.8 (6.9)		
ph1o	130.6 (5.9)	ph1o	7.13
ph1m	129.6 (2)	ph1m	7.20
ph1p	127.7	ph1p	7.17

[EuL^5]Cl

An analogous procedure to that described for the synthesis of [DyL^5]Cl was followed using 1,7-(5-*tert*-butylpyridin-2-yl)methyl-4,10-di{[benzylphosphoryl]methyl}-1,4,7,10-tetraazacyclododecane (4 mg, 0.005 mmol) and $EuCl_3 \cdot 6H_2O$ (3 mg, 0.008 mmol), to yield a white solid (2.2 mg, 44%). ESI-LCMS (+) *m/z* 953.4 $[M]^+$. ESI-HRMS (+) calcd for $[C_{44}H_{62}N_6O_4P_2{}^{151}Eu]^+$ 951.3506, found 951.3516.

3-*tert*-Butyl-2,6-dimethylpyridine, 24

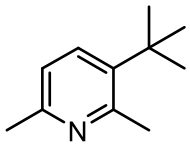

Copper(I) cyanide (20 mg) was suspended in THF (150 mL) under argon. The resulting suspension was cooled to -78°C before *tert*-butylmagnesium chloride (27 mL, 2.0 M in Et_2O, 54 mmol) was added. 3-Bromo-2,6-dimethylpyridine (5.0 g, 26.9 mmol) was added and the resulting yellow solution was allowed to warm to room temperature and then heated to 50°C stirred for a further 18 h. NH_4OH (sat. aq. solution, 20 mL) was added dropwise to the resulting red solution. The resulting suspension was filtered and the solid was washed with Et_2O (3 x 200 mL). The organic layers were combined and dried over $MgSO_4$. The solvent was removed under reduced pressure to yield an orange liquid that was purified by silica gel column chromatography (100% hexane to 5% EtOAc/ hexane) to yield a yellow liquid (2.68 g, 61%). R_f (20% EtOAc/ hexane) = 0.43. ^{1}H NMR (700 MHz,$CDCl_3$) δ 7.42 (d, ^3J = 8, 1H, H^4), 6.80 (d, ^3J = 8, 1H, H^5), 2.63 (s, 3H, C^{2}H$_3$), 2.38 (s, 3H, C^{6}H$_3$), 1.30 (s, 9H, C(C$\underline{H}_3$)$_3$); ^{13}C NMR (176 MHz, $CDCl_3$) δ 155.8 (C^2), 154.1 (C^6), 139.9 (C^3), 134.0 (C^4), 120.2 (C^5), 34.1 (C(CH$_3$)$_3$), 30.5 (C($\underline{C}$H$_3$)), 26.1 (C^{2}H$_3$), 23.6 (C^{6}H$_3$); ESI-LCMS (+) *m/z* 164.8 $[M+H]^+$; ESI-HRMS (+) calcd for $[C_{11}H_{18}N]^+$ 164.1439, found 164.1448.

3-*tert*-Butyl-2,6-dimethylpyridin-1-oxide, 25

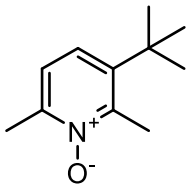

3-*tert*-Butyl-2,6-dimethylpyridine (1.08 g, 6.6 mmol) was dissolved in $CHCl_3$ (30 mL) and to this was added *m*CPBA (1.4 g, 8.1 mmol). The resulting solution was stirred for 18 h at room temperature under argon, before being quenched by Na_2SO_4 (sat. aq. solution, 20 mL). The organic layer was extracted and washed with aqueous NaOH solution (2 x 20 mL, 0.5 M), dried over $MgSO_4$ and the solvent removed under reduced pressure to yield a pale yellow liquid (1.1 g, 96%). R_f (10% MeOH/ CH_2Cl_2) = 0.49. ^{1}H NMR (600 MHz,$CDCl_3$) δ 7.02 (d, ^3J = 8.5, 1H, H^4), 6.91 (d, ^3J = 8.5, 1H, H^5), 2.56 (s, 3H, C^2H_3), 2.34 (s, 3H, C^6H_3), 1.24 (s, 9H, $C(C\underline{H}_3)_3$); ^{13}C NMR (101 MHz, $CDCl_3$) δ 149.0 (C^2), 145.7 (C^6), 143.9 (C^3), 122.4 (C^4), 121.9 (C^5), 34.6 ($\underline{C}(CH_3)_3$), 30.4 ($C(\underline{C}H_3)$), 18.1 (C^6H_3), 17.5 (C^2H_3); ESI-LCMS (+) *m/z* 179.9 $[M+H]^+$; ESI-HRMS (+) calcd for $[C_{11}H_{18}NO]^+$ 180.1388, found 180.1378.

(6-Methyl-3-*tert*-butyl-pyridin-2-yl)methanol, 26

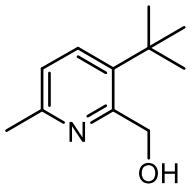

3-*tert*-Butyl-2,6-dimethylpyridin-1-oxide (1.67 g, 9.34 mmol) was dissolved in anhydrous DCM (10 mL) and trifluoroacetic anhydride (7 mL, 49.9 mmol) was added. The resulting solution was stirred for 18 h at 60°C under an atmosphere of argon. The reaction was monitored by ^{1}H NMR spectroscopy, and upon completion the solvent was removed under reduced pressure. The resulting yellow oil was stirred in a mixture of H_2O (10 mL) and EtOH (10 mL) at room temperature for 2 h. The solution was concentrated under reduced pressure (*ca.* 5 mL) and extracted with DCM (3 x 50 mL). The organic layers were combined, dried over $MgSO_4$, and the solvent removed under reduced pressure. The resulting orange oil was purified by silica gel column chromatography (100% CH_2Cl_2 to 1% MeOH/ CH_2Cl_2) to yield a yellow oil (1.1 g, 64%).

R_f (10% MeOH/ CH_2Cl_2) = 0.74. ^{1}H NMR (700 MHz, $CDCl_3$) δ 7.54 (d, ^3J = 8, 1H, H^4), 6.97 (d, ^3J = 8, 1H, H^5), 4.80 (s, 2H, CH_2OH), 2.46(s, 3H, CH_3) 1.30 (s, 9H, $C(CH_3)_3$). ^{13}C NMR (176 MHz, $CDCl_3$) δ 155.1 (C^2), 153.0 (C^6), 139.0 (C^3), 133.9 (C^4), 121.5 (C^5), 62.7 ($\underline{C}H_2OH$), 34.3 ($\underline{C}(CH_3)_3$), 30.6 ($C(\underline{C}H_3)_3$), 23.3 (CH_3). ESI-LCMS (+) m/z 180.3 $[M+H]^+$; ESI-HRMS (+) calcd for $[C_{11}H_{18}NO]^+$ 180.1388, found 180.1391.

(6-Methyl-3-*tert*-butyl-pyridin-2-yl)methyl methanesulfonate, 27

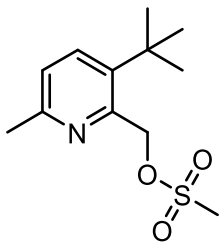

(6-Methyl-3-*tert*-butyl-pyridin-2-yl)methanol (98 mg, 0.55 mmol) was dissolved in anhydrous THF (2 mL) and stirred at 5°C for 10 min, before the addition of NEt_3 (125 µL, 0.9 mmol). Mesyl chloride (47 µL, 0.6 mmol) was added dropwise and the resulting solution was allowed to stir at room temperature for 30 min. The solvent was removed under reduced pressure and the residue was dissolved in H_2O (5 mL) and extracted with DCM (3 x 10 mL). The organic layers were combined and dried over $MgSO_4$ and the solvent removed under reduced pressure. The resulting orange oil was used immediately (133 mg, 94 %). R_f (10% MeOH/ CH_2Cl_2) = 0.81; ^{1}H NMR (400 MHz, $CDCl_3$) δ 7.59 (d, ^3J = 8, 1H, H^4), 7.00 (d, ^3J = 8, 1H, H^5), 4.83 (s, 2H, CH_2OMs), 3.07 (s, 3H, SCH_3), 2.46 (s, 3H, $pyCH_3$) 1.25 (s, 9H, $C(CH_3)_3$). ESI-LCMS (+) m/z 258.9 $[M+H]^+$. ESI-HRMS (+) calcd for $[C_{12}H_{20}NO_3S]^+$ 258.1164, found 258.1139.

2-(Dipicolylaminomethyl)-3-*tert*-butyl-6-methylpyridine, 28

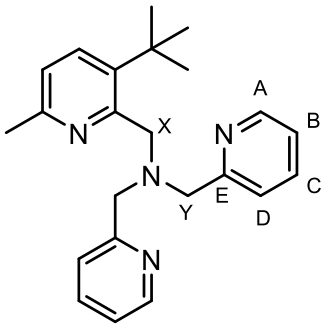

K_2CO_3 (345 mg, 2.5 mmol) was suspended in anhydrous MeCN (2 mL) and to this suspension was added dipicolylamine (430 µL, 2.4 mmol). (6-methyl-3-*tert*-butyl-pyridin-2-yl)methyl methanesulfonate (396 mg, 1.54 mmol) was then added dropwise as a solution in anhydrous MeCN (3 mL). The resulting solution was heated to 70°C and stirred for 18 h before being cooled to room temperature and filtered to remove inorganic salts. The resulting orange oil was purified by reverse-phase HPLC (10-100% MeCN in H_2O over 10 min; t_R = 11.1 min) to yield a yellow oil (233 mg, 42%). ^{1}H NMR (700 MHz, $CDCl_3$) δ 8.45 (m, 2H, H^A), 7.65 (d, ^3J = 7.5, 2H, H^D), 7.56 (m, 2H, H^B), 7.47 (d, ^3J = 8, 1H, H^4), 7.04 (m, 2H, H^C), 6.86 (d, ^3J = 8, 2H, H^5), 4.14 (s, 2H, C^XH_2), 3.98 (s, 4H, C^YH_2), 2.46 (s, 3H, CH_3), 1.26 (s, 9H, $C(CH_3)_3$). ^{13}C NMR (176 MHz, $CDCl_3$) δ 160.3 (C^E), 156.2 (C^2), 154.3 (C^6), 148.7 (C^A), 141.1 (C^3), 136.2 (C^B), 134.5 (C^4), 123.5 (C^D), 121.7 (C^C), 121.0 (C^5), 60.3 (C^YH_2), 58.8 (C^XH_2), 34.4 ($\underline{C}(CH_3)_3$), 31.4 ($C(\underline{C}H_3)_3$), 23.8 (CH_3). ESI-LCMS (+) m/z 360.8 $[M+H]^+$. ESI-HRMS (+) calcd for $[C_{23}H_{29}N_4]^+$ 361.2392, found 361.2401.

2-(Hydroxymethyl)-6-methyl-3-*tert*-butyl-pyridin-1-oxide, 29

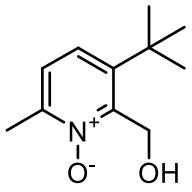

(6-Methyl-3-*tert*-butyl-pyridin-2-yl)methanol (540 mg, 3 mmol) was dissolved in $CHCl_3$ (30 mL) and to this was added *m*CPBA (650 mg, 3.6 mmol). The resulting solution was stirred for 18 h at room temperature under argon, before being quenched by Na_2SO_4 (sat. aq. solution, 15 mL). The organic layer was extracted and washed with aqueous

NaOH solution (2 x 20 mL, 0.5 M), dried over $MgSO_4$ and the solvent removed under reduced pressure to yield a pale yellow liquid (550 mg, 93%). R_f (10% MeOH/ CH_2Cl_2) = 0.66. ^{1}H NMR (600 MHz,$CDCl_3$) δ 7.22 (d, ^3J = 8.5, 1H, H^4), 7.10 (d, ^3J = 8.5, 1H, H^5), 4.98 (s, 2H, CH_2OH), 2.42 (s, 3H, CH_3), 1.34 (s, 9H, $C(C\underline{H}_3)_3$); ^{13}C NMR (101 MHz, $CDCl_3$) δ 149.8 (C^2), 146.5 (C^6), 144.4 (C^3), 124.4 (C^4), 124.0 (C^5), 59.5 (CH_2OH), 34.7 ($\underline{C}(CH_3)_3$), 31.4 ($C(\underline{C}H_3)$), 17.6 (CH_3); ESI-LCMS (+) *m/z* 196.2 $[M+H]^+$; ESI-HRMS (+) calcd for $[C_{11}H_{18}NO_2]^+$ 196.1338, found 196.1337.

2-([Methanesulfonyloxy]methyl)- 6-methyl-3-*tert*-butyl-pyridin-1-oxide, 30

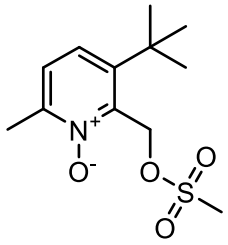

2-(Hydroxymethyl)-6-methyl-3-*tert*-butyl-pyridin-1-oxide (200 mg, 1 mmol) was dissolved in anhydrous THF (2 mL) and stirred at 5°C for 10 min, before the addition of N,N-diisopropylethylamine (350 µL, 1.5 mmol). Methanesulfonic anhydride (260 mg, 2 mmol) was added and the resulting solution was allowed to stir at room temperature for 30 min. The solvent was removed under reduced pressure and the residue was dissolved in H_2O (5 mL) and extracted with DCM (3 x 10 mL). The organic layers were combined and dried over $MgSO_4$ and the solvent removed under reduced pressure. The resulting orange oil was used immediately (133 mg, 94 %). R_f (10% MeOH/ CH_2Cl_2) = 0.81; ^{1}H NMR (400 MHz, $CDCl_3$) δ 7.26 (s, 1H, H^4), 7.21 (s, 1H, H^5), 5.67 (s, 2H, CH_2OMs), 3.31 (s, 3H, SCH_3), 2.46 (s, 3H, $pyCH_3$) 1.42 (s, 9H, $C(CH_3)_3$). ESI-LCMS (+) *m/z* 274.4 $[M+H]^+$; ESI-HRMS (+) calcd for $[C_{12}H_{20}NO_4S]^+$ 274.1113, found 274.1117.

2-(Dipicolylaminomethyl)-3-*tert*-butyl-6-methylpyridin-1-oxide, 31

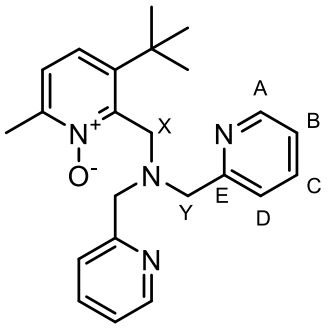

K_2CO_3 (305 mg, 2.2 mmol) was suspended in anhydrous MeCN (1 mL) and to this suspension was added dipicolylamine (360 µL, 2 mmol). 2-([Methanesulfonyloxy]methyl)- 2-([methanesulfonyloxy]methyl)- 6-methyl-3-*tert*-butyl-pyridin-1-oxide(438 mg, 1.6 mmol) was then added dropwise as a solution in anhydrous MeCN (2 mL). The resulting solution was heated to 70°C and stirred for 18 h before being cooled to room temperature and filtered to remove inorganic salts. The solvent was removed under reduced pressure and the resulting orange oil was purified by reverse-phase HPLC (10-100% MeCN in H_2O over 10 min; t_R = 10.0 min) to yield a yellow oil (245 mg, 41%). ^{1}H NMR (700 MHz, $CDCl_3$) δ 8.38 (d, ^3J = 5, 2H, H^A), 7.56 – 7.47 (m, 4H, H^D, H^B), 7.04 (d, ^3J = 8.5, 1H, H^4), 6.98 (ddd, ^3J = 7, ^3J = 5, ^4J = 1.5, 2H, H^C), 6.95 (d, ^3J = 8.5, 2H, H^5), 4.40 (s, 2H, C^XH_2), 3.88 (s, 4H, C^YH_2), 2.36 (s, 3H, CH_3), 1.29 (s, 9H, $C(CH_3)_3$). ^{13}C NMR (176 MHz, $CDCl_3$) δ 160.1 (C^E), 148.7 (C^A), 148.6 (C^2), 146.7 (C^3), 146.3 (C^6), 136.1 (C^B), 123.8 (C^5), 123.1 (C^D), 122.6 (C^4), 121.6 (C^C), 60.1 (C^YH_2), 50.7 (C^XH_2), 35.5 ($\underline{C}(CH_3)_3$), 31.7 ($C(\underline{C}H_3)_3$), 18.5 (CH_3). ESI-LCMS (+) *m/z* 377.3 $[M+H]^+$; ESI-HRMS (+) calcd for $[C_{23}H_{29}N_4O]^+$ 377.2341, found 377.2333.

6-(Methoxycarbonyl)-3-*tert*-butylpyridine-2-carboxylic acid, 32

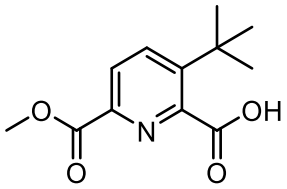

3-*tert*-Butyl-2,6-dimethylpyridine (3 g, 18.4 mmol) was added to H_2O (150 mL) and the two immiscible layers were stirred at 95°C for 10 min. $KMnO_4$ (14.5 g, 92 mmol) was added and the reaction was stirred at 95°C for 18 h. The resulting suspension was

allowed to cool to room temperature and filtered over celite. The solvent was removed under reduced pressure to yield an off white solid that was used without further purification (LCMS (+) *m/z* 223.9 $[M+H]^-$; ESI-HRMS (+) calcd for $[C_{11}H_{14}NO_4]^+$ 224.0923, found 224.0928). The salt was suspended in anhydrous MeOH (40 mL) and the suspension was cooled to 0°C. Thionyl chloride (13 mL, 180 mmol) was added dropwise and the reaction was heated at 65°C for 18 h, after which the solvent was removed under reduced pressure. The resulting yellow oil was purified by silica gel column chromatography (100% CH_2Cl_2 to 5% MeOH/ CH_2Cl_2) to yield a yellow viscous oil (1.53 g, 35%). R_f (5% MeOH/ CH_2Cl_2) = 0.16; ^{1}H NMR (700 MHz, $CDCl_3$) δ 8.04 (d, ^3J = 8.5, 1H, H^5), 7.97 (d, ^3J = 8.5, 1H, H^4), 3.93 (s, 3 H, CO_2CH_3), 1.41 (s, 9H, $C(C\underline{H}_3)_3$); ^{13}C NMR (176 MHz, $CDCl_3$) δ 169.1 (CO_2H), 164.9 ($\underline{C}O_2CH_3$), 150.1 (C^2), 148.2 (C^3), 143.4 (C^6), 137.2 (C^4), 125.8 (C^5), 53.0 (OCH_3), 35.2 ($\underline{C}(CH_3)_3$), 30.6 ($C(\underline{C}H_3)$); ESI-LCMS (+) *m/z* 238.4 $[M+H]^+$; ESI-HRMS (+) calcd for $[C_{12}H_{16}NO_4]^+$ 238.1079, found 238.1070.

Dimethyl 3-*tert*-butyl-2,6-pyridinecarboxylate was also isolated from the column as a yellow oil (1.07 g, 23%). R_f (5% MeOH/ CH_2Cl_2) = 0.89; ESI-LCMS (+) *m/z* 252.0 $[M+H]^+$.

Dimethyl 3-*tert*-butyl-2,6-pyridinecarboxylate, 33

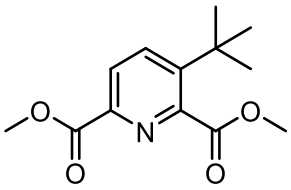

6-(Methoxycarbonyl)-3-tert-butylpyridine-2-carboxylic acid (2.7 g, 11.4 mmol) was dissolved in a solution of anhydrous DCM (20 mL) and anhydrous MeOH (1 mL) and stirred at 0°C under argon. DCC (3.76 g, 19.38 mmol) and DMAP (280 mg, 2.28 mmol) were added and the reaction mixture was allowed to warm to room temperature. The solution was stirred for 18h. The solvent was removed under reduced pressure and the resulting yellow oil was dissolved in CH_2Cl_2 (20 mL) and washed with H_2O (3 x 10 mL). The aqueous layer was extracted with CH_2Cl_2 (2 x 20 mL). The organic layers were combined, dried over $MgSO_4$ and the solvent removed under reduced pressure. The resulting yellow oil was purified by silica gel column chromatography (100% CH_2Cl_2 to 1% MeOH/ CH_2Cl_2) to yield a pale yellow oil (1.78 g, 62%). R_f (5% MeOH/ CH_2Cl_2) = 0.87; ^{1}H NMR (700 MHz, $CDCl_3$) δ 8.10 (d, ^3J = 8.5, 1H, H^5), 7.96 (d, ^3J = 8.5, 1H, H^4), 3.97

(s, 6H, OCH_3), 1.41 (s, 9H, $C(C\underline{H}_3)_3$); ^{13}C NMR (176 MHz, $CDCl_3$) δ 168.8 ($\underline{C}^2O_2CH_3$), 165.3 ($\underline{C}^6O_2CH_3$), 150.7 (C^2), 146.9 (C^3), 144.8 (C^6), 136.6 (C^4), 125.8 (C^5), 53.1 (OCH_3), 53.0 (OCH_3), 35.1 ($\underline{C}(CH_3)_3$), 30.9 ($C(\underline{C}H_3)$); ESI-LCMS (+) *m/z* 252.0 $[M+H]^+$; ESI-HRMS (+) calcd for $[C_{13}H_{18}NO_4]^+$ 252.1236, found 252.1227.

Methyl 6-hydroxymethyl-3-*tert*-butyl-2-pyridinecarboxylate, 34

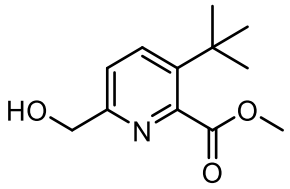

Dimethyl 3-*tert*-butyl-2,6-pyridinecarboxylate (500 mg, 1.98 mmol) was dissolved in a solution of anhydrous DCM (2 mL) and anhydrous MeOH (2 mL) and stirred at 0°C. $NaBH_4$ (166 mg, 4.4 mmol) was added and the reaction was stirred at 0°C for 30 min after which it was allowed to warm to room temperature and stirred for a further 1 h. The solution was cooled to 0°C before the addition of DCM (2 mL) and dilute HCl (2 mL, 1 M) to quench the reaction. The mixture was washed with water (5 mL) and the organic layer was dried with $MgSO_4$ before the solvent was removed under reduced pressure. The resulting yellow oil was purified by silica gel column chromatography (100% CH_2Cl_2 to 2% MeOH/ CH_2Cl_2) to yield a pale yellow oil (424 mg, 96%). R_f (5% MeOH/ CH_2Cl_2) = 0.47; ^1H NMR (700 MHz, $CDCl_3$) δ 7.78 (d, ^3J = 8.5, 1H, H^4), 7.29 (d, ^3J = 8.5, 1H, H^5), 4.69 (s, 2H, CH_2OH), 3.91 (s, 3 H, CO_2CH_3), 1.34 (s, 9H, $C(C\underline{H}_3)_3$); ^{13}C NMR (176 MHz, $CDCl_3$) δ 169.7 ($\underline{C}O_2CH_3$), 156.3 (C^6), 149.0 (C^2), 141.2 (C^3), 136.3 (C^4), 121.3 (C^5), 64.0 (CH_2OH), 52.7 (OCH_3), 34.3 ($\underline{C}(CH_3)_3$), 31.0 ($C(\underline{C}H_3)$); ESI-LCMS (+) *m/z* 223.8 $[M+H]^+$; ESI-HRMS (+) calcd for $[C_{12}H_{18}NO_3]^+$ 224.1287, found 224.1266.

Methyl 3-*tert*-butyl-6-(tetrahydropyran-2-yloxymethyl)-2-pyridinecarboxylate, 35

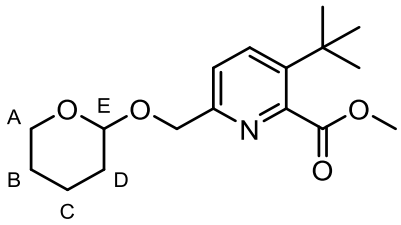

Methyl 6-hydroxymethyl-3-*tert*-butyl-2-pyridinecarboxylate (840 mg, 3.8 mmol) was dissolved in anhydrous DCM (6 mL) and stirred at 0°C. 3,4-dihydro-2*H*-pyran (700 µL,

7.6 mmol) and a catalytic amount of *p*-TsOH (10 mg, 0.04 mmol) was then added. The reaction was allowed to warm to room temperature and stirred for 72 h and then washed with $NaHCO_3$ (sat. aq. solution, 2 x 10 mL). The organic layer was dried over $MgSO_4$. The solvent removed was under reduced pressure and the resulting yellow oil was purified by silica gel column chromatography (100% CH_2Cl_2 to 1% MeOH/ CH_2Cl_2) to yield a yellow oil (1.09 g, 93 %). R_f (5% MeOH/ CH_2Cl_2) = 0.61; ^{1}H NMR (700 MHz, $CDCl_3$) δ 7.76 (d, ^3J = 8.5, 1H, H^4), 7.45 (d, ^3J = 8.5, 1H, H^5), 4.79 (m, 1H, CH_2OTHP), 4.67 (m, 1H, H^E), 4.55 (m, 1H, CH_2OTHP), 3.88 (s, 3H, CO_2CH_3), 3.80 (m, 1H, H^A), 3.46 (m, 1H, H^A), 1.88 – 1.40 (m, 6H, H^B, H^C, H^D), 1.31 (s, 9H, $C(C\underline{H}_3)_3$); ^{13}C NMR (176 MHz, $CDCl_3$) δ 169.6 ($\underline{C}O_2CH_3$), 155.5 (C^6), 149.3 (C^2), 140.9 (C^3), 135.9 (C^4), 121.9 (C^5), 98.3 (C^E), 69.1 (CH_2OTHP), 62.1 (C^A), 52.6 (OCH_3), 34.2 ($\underline{C}(CH_3)_3$), 30.9 ($C(\underline{C}H_3)$), 30.5 (C^D), 25.4 (C^b), 19.3 (C^C); ESI-LCMS (+) *m/z* 307.9 $[M+H]^+$; ESI-HRMS (+) calcd for $[C_{17}H_{26}NO_4]^+$ 308.1862, found 308.1865.

(3-*tert*-Butyl-6-(tetrahydropyran-2-yloxymethyl)-pyridin-2-yl) methanol, 36

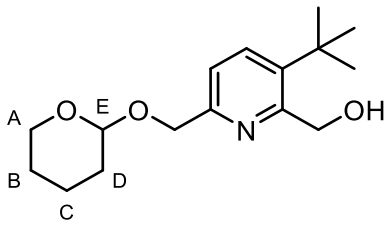

Methyl 3-*tert*-butyl-6-(tetrahydropyran-2-yloxymethyl)-2-pyridinecarboxylate (890 mg, 2.9 mmol) was dissolved in anhydrous THF (5 mL). The solution was cooled to 0°C and $LiAlH_4$ (2M in THF) (3 mL, 6 mmol) added dropwise. The reaction was stirred at 0°C for 3 h and then diluted with EtOAc (10 mL) and quenched by the addition of water (0.5 mL) and aqueous NaOH solution (0.5 mL, 2.5 M). The mixture was then filtered and extracted with EtOAc (2 x 50 mL), the organic layers were combined and dried over $MgSO_4$. The solvent removed was removed under reduced pressure and the resulting yellow oil was purified by silica gel column chromatography (100% CH_2Cl_2 to 2% MeOH/ CH_2Cl_2) to yield a yellow liquid (780 mg, 96 %). R_f (5% MeOH/ CH_2Cl_2) = 0.44; ^{1}H NMR (600 MHz, $CDCl_3$) δ 7.64 (d, ^3J = 8, 1H, H^4), 7.26 (d, ^3J = 8, 1H, H^5), 4.79 (d, ^2J = 13.5, 1H, CH_2OTHP), 4.79 (s, 2H, CH_2OH), 4.70 (t, ^3J = 3.5, 1H, H^E), 4.55 (d, ^2J = 13.5, 1H, CH_2OTHP), 3.84 (m, 1H, H^A), 3.48 (m, 1H, H^A), 1.83 – 1.78 (m, 1H, H^C), 1.71 – 1.60 (m, 2H, H^D), 1.54 – 1.43 (m, 3H, H^B, H^C), 1.29 (s, 9H, $C(C\underline{H}_3)_3$); ^{13}C NMR (151 MHz, $CDCl_3$)

δ 155.3 (C^2), 153.3 (C^6), 140.7 (C^3), 135.1 (C^4), 119.8 (C^5), 98.3 (C^E), 69.1 (CH_2OTHP), 62.7 (CH_2OH), 62.1 (C^A), 34.4 ($\underline{C}(CH_3)_3$), 30.5 (C^D), 30.4 ($C(\underline{C}H_3)$), 25.4 (C^b), 19.3 (C^C); ESI-LCMS (+) *m/z* 279.8 $[M+H]^+$; ESI-HRMS (+) calcd for $[C_{16}H_{26}NO_3]^+$ 280.1913, found 280.1920.

(3-*tert*-Butyl-6-(tetrahydropyran-2-yloxymethyl)-pyridin-2-yl)methyl methanesulfonate, 37

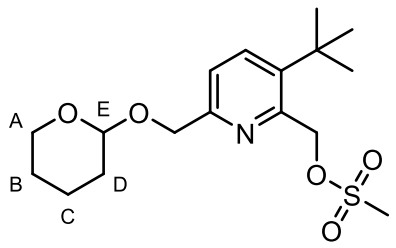

(3-*tert*-Butyl-6-(tetrahydropyran-2-yloxymethyl)-pyridin-2yl) methanol (150 mg, 0.53 mmol) was dissolved in anhydrous THF (2 mL) and stirred at 5°C for 10 min, before the addition of NEt_3 (125 µL, 0.9 mmol). Mesyl chloride (47 µL, 0.6 mmol) was added dropwise and the resulting solution was allowed to stir at room temperature for 30 min. The solvent was removed under reduced pressure and the residue was dissolved in H_2O (5 mL) and extracted with DCM (3 x 10 mL). The organic layers were combined and dried over $MgSO_4$ and the solvent removed under reduced pressure. The resulting yellow oil was used immediately (180 mg, 95 %). ^1H NMR (400 MHz, $CDCl_3$) δ 7.73 (d, ^3J = 8.5, 1H, H^4), 7.35 (d, ^3J = 8.5, 1H, H^5), 5.50 (s, 2H, CH_2OMs), 4.79 (d, ^2J = 13.5, 1H, CH_2OTHP), 4.70 (t, ^3J = 3.5, 1H, H^E), 4.54 (d, ^2J = 13.5, 1H, CH_2OTHP), 3.84 (m, 1H, H^A), 3.50 (m, 1H, H^A), 3.14 (s, 3H, CH_3) 1.88 –1.46 (m, 3H, H^B, H^C, H^D), 1.38 (s, 9H, $C(C\underline{H}_3)_3$); ESI-LCMS (+) *m/z* 358.3 $[M+H]^+$; ESI-HRMS (+) calcd for $[C_{17}H_{28}NO_5S]^+$ 358.1702, found 358.1699.

2-(Dipicolylaminomethyl)-3-*tert*-butyl-6-(tetrahydropyran-2-yloxymethyl)pyridine, 38

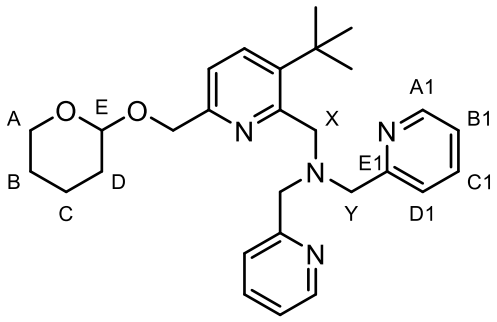

K_2CO_3 (207 mg, 1.5 mmol) was suspended in anhydrous MeCN (1 mL) and to this suspension was added dipicolylamine (270 µL, 1.5 mmol). 2-([Methanesulfonyloxy]methyl)- 2-([methanesulfonyloxy]methyl)- 6-methyl-3-*tert*-butyl-pyridin-1-oxide(445 mg, 1.25 mmol) was then added dropwise as a solution in anhydrous MeCN (2 mL). The resulting solution was heated to 70°C and stirred for 18 h before being cooled to room temperature and filtered to remove inorganic salts. The solvent was removed under reduced pressure and the resulting orange oil was purified by alumina gel column chromatography (100% CH_2Cl_2 to 1% MeOH/ CH_2Cl_2) to yield a pale orange oil (437 mg, 76%). R_f (2% MeOH/ CH_2Cl_2) = 0.48; ^{1}H NMR (700 MHz, $CDCl_3$) δ 8.43 (d, ^3J = 6.5, 2H, H^{A1}), 7.67 (d, ^3J = 8, 2H, H^{D1}), 7.59 (d, ^3J = 8, 1H, H^4), 7.55 (m, 2H, H^{B1}), 7.19 (d, ^3J = 8, 1H, H^5), 7.07 (m, 2H, H^{C1}), 4.85 (d, ^2J = 13.5, 1H, CH_2OTHP), 4.74 (t, ^3J = 3.5, 1H, H^E), 4.60 (d, ^2J = 13.5, 1H, CH_2OTHP), 4.13 (s, 2H, C^XH_2), 3.98 (s, 4H, C^YH_2), 3.88 (m, 1H, H^A), 3.50 (m, 1H, H^A), 1.83 (m, 1H, H^C), 1.71 (m, 1H, H^D), 1.64 (m, 1H, H^D), 1.55 (m, 1H, H^B), 1.52 – 1.49 (m, 2H, H^B, H^C), 1.25 (s, 9H, $C(CH_3)_3$). ^{13}C NMR (176 MHz, $CDCl_3$) δ 160.4 (C^{E1}), 156.5 (C^2), 154.7 (C^6), 148.7 (C^{A1}), 142.6 (C^3), 136.2 (C^{B1}), 134.6 (C^4), 123.4 (C^{D1}), 121.7 (C^{C1}), 119.0 (C^5), 98.4 (C^E), 69.9 (CH_2OTHP), 62.1 (C^A), 60.3 (C^YH_2), 58.5 (C^XH_2), 34.5 ($\underline{C}(CH_3)_3$), 31.2 ($C(\underline{C}H_3)_3$), 30.6 (C^D), 25.5 (C^B), 19.4 (C^C); ESI-LCMS (+) *m/z* 461.4 $[M+H]^+$; ESI-HRMS (+) calcd for $[C_{28}H_{37}N_4O_2]^+$ 461.2917, found 461.2928.

(2-(Dipicolylaminomethyl)-3-*tert*-butyl-pyridin-6-yl) methanol, 39

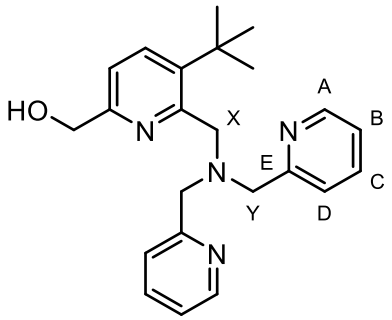

2-(Dipicolylaminomethyl)-3-*tert*-butyl-6-(tetrahydropyran-2-yloxymethyl)pyridine (106 mg, 0.23 mmol) was dissolved in MeOH (3 mL) and to this was added *p*-toluenesulfonic acid monohydrate (66 mg, 0.35 mmol). The resulting solution was stirred at 50°C for 18 h. The reaction was quenched with saturated aqueous $NaHCO_3$ (5 mL) and the solution concentrated under reduced pressure (ca. 4 mL). The resulting mixture was extracted with EtOAc (2 x 10 mL). The organic layers were combined, dried over $MgSO_4$ and the solvent removed under reduced pressure to yield a yellow oil (79 mg, 91%). ^{1}H NMR (600 MHz, $CDCl_3$) δ 8.45 (d, ^3J = 5, 2H, H^A), 7.62 – 7.56 (m, 5H, H^D, H^4, H^B), 7.07 (ddd, ^3J = 7, ^3J = 5, ^4J = 2, 2H, H^C), 6.97 (d, ^3J = 8, 2H, H^5), 4.65 (s, 2H, CH_2OH), 4.15 (s, 2H, C^XH_2), 3.95 (s, 4H, C^YH_2), 1.30 (s, 9H, $C(CH_3)_3$). ^{13}C NMR (151 MHz, $CDCl_3$) δ 159.9 (C^E), 155.8 (C^2), 155.1 (C^6), 148.9 (C^A), 142.8 (C^3), 136.5 (C^B), 135.0 (C^4), 123.2 (C^D), 123.0 (C^C), 118.2 (C^5), 63.6 (CH_2OH), 60.5 (C^YH_2), 58.6 (C^XH_2), 34.6 ($\underline{C}(CH_3)_3$), 31.3 ($C(\underline{C}H_3)_3$); ESI-LCMS (+) *m/z* 376.9 $[M+H]^+$; ESI-HRMS (+) calcd for $[C_{23}H_{29}N_4O]^+$ 377.2341, found 377.2353.

(2-(Dipicolylaminomethyl)-3-*tert*-butyl-pyridin-6-yl) methyl methanesulfonate, 40

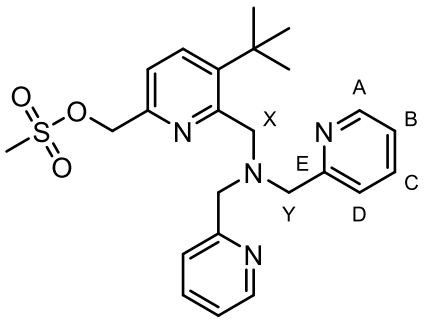

(2-(Dipicolylaminomethyl)-3-*tert*-butyl-pyridin-6-yl) methanol (79 mg, 0.21 mmol) was dissolved in anhydrous THF (3 mL) and stirred at 5°C for 10 min, before the addition of

NEt_3 (56 µL, 0.4 mmol). Mesyl chloride (19 µL, 0.24 mmol) was added dropwise and the resulting solution was allowed to stir at room temperature for 30 min. The solvent was removed under reduced pressure and the residue was dissolved in H_2O (5 mL) and extracted with DCM (3 x 10 mL). The organic layers were combined and dried over $MgSO_4$ and the solvent removed under reduced pressure. The resulting yellow oil was used immediately (88 mg, 92 %). ^{1}H NMR (400 MHz, $CDCl_3$) δ 8.46 (d, ^3J = 5, 2H, H^A), 7.69 – 7.64 (m, 3H, H^4, H^D), 7.61 (td, ^3J = 7.5, ^4J = 2, 2H, H^B), 7.21 (d, ^3J = 8, 2H, H^5), 7.07 (m, 2H, H^C), 5.35 (s, 2H, CH_2OMs), 4.18 (s, 2H, C^XH_2), 3.99 (s, 4H, C^YH_2), 3.01 (s, 3H, CH_3), 1.29 (s, 9H, $C(CH_3)_3$); ESI-LCMS (+) *m/z* 455.3 $[M+H]^+$; ESI-HRMS (+) calcd for $[C_{24}H_{31}N_4O_3S]^+$ 455.2117, found 455.2116.

1,4,7-Tri{[ethoxy(methyl)phosphoryl]methyl}-10-(2-(dipicolylaminomethyl)-3-*tert*-butyl-pyridin-6-yl) methyl-1,4,7,10-tetraazacyclododecane, L^6

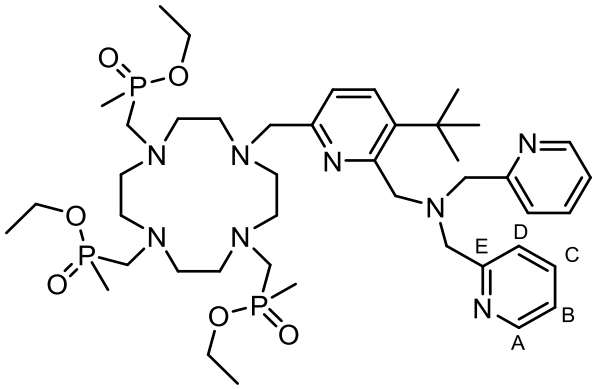

1,4,7-Tri{[ethoxy(methyl)phosphoryl]methyl}-1,4,7,10-tetraazacyclododecane (113 mg, 0.21 mmol) was dissolved in anhydrous MeCN (1 mL) and to this was added Cs_2CO_3 (82 mg, 0.25 mmol). (2-(Dipicolylaminomethyl)-3-*tert*-butyl-pyridin-6-yl) methyl methanesulfonate (88 mg, 0.19 mmol) was then added dropwise as a solution in anhydrous MeCN (2 mL). The resulting solution was heated to 70°C and stirred for 18 h before being cooled to room temperature and filtered to remove inorganic salts. The solvent was removed under reduced pressure and the resulting oil was purified by alumina gel column chromatography, (100% CH_2Cl_2 to 2% MeOH/ CH_2Cl_2) to yield an orange oil (64 mg, 38%). R_f (5% MeOH/ CH_2Cl_2) = 0.40 ^{1}H NMR (400 MHz, $CDCl_3$) δ 8.50 (d, ^3J = 5, 2H, H^A), 7.70 (d, ^3J = 8, 1H, H^4), 7.66 – 7.62 (d, ^3J = 7.5, 2H, H^B), 7.47 (d, ^3J = 8, 2H, H^D), 7.19 – 7.13 (m, 2H, H^C), 7.07 (d, ^3J = 8, 1H, H^5), 4.68 – 4.17 (m, 8H, NCH_2py), 4.13 – 3.94 (m, 6H, $OC\underline{H}_2CH_3$), 3.68 – 2.62 (m, 22H, cyclen CH_2, NCH_2P), 1.57 – 1.41 (m,

9H, PCH_3), 1.30 (s, 9H, $C(CH_3)_3$), 1.28 – 1.18 (m, 9H, $OCH_2C\underline{H}_3$); ^{31}P NMR δ (162 MHz) δ 52.6 – 50.0 (br m); ESI-LCMS (+) *m/z* 891.6 $[M+H]^+$; ESI-HRMS (+) calcd for $[C_{43}H_{74}N_8O_6P_3]^+$ 891.4944, found 891.4968.

1,4,7-Tris(*tert*-butoxycarbonylmethyl)-1,4,7,10-tetraazacyclododecane, 41

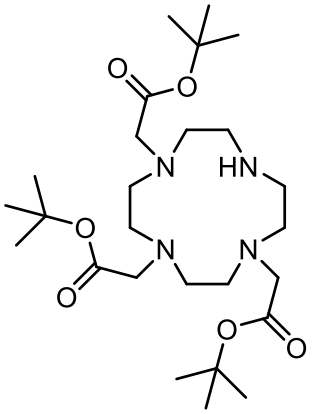

Tert-butyl bromoacetate (2.3 mL, 15.7 mL) was added to a stirred solution of 1,4,7,10-tetraazacyclododecane (1.00 g, 5.8 mmol) and $NaHCO_3$ (1.30 g, 14.5 mmol) in anhydrous MeCN (40 mL). The resulting mixture was stirred at room temperature for 18 h under argon before the inorganic salts were removed by filtration and the solvent was removed under reduced pressure. The resulting white residue was dissolved in the minimal amount of DCM and upon addition of Et_2O a white solid precipitated out of solution (1.46 g, 49%). ^1H NMR (600 MHz, $CDCl_3$) δ 3.36 (s, 4H, CH_2), 3.28 (s, 2H, CH_2), 3.08 (s, 4H, cyclen CH_2), 3.68 – 2.62 (m, 12H, cyclen CH_2), 1.44 (s, 18H, $C(CH_3)_3$), 1.44 (s, 9H, $C(CH_3)_3$); ESI-LCMS (+) *m/z* 515.9 $[M+H]^+$;). ^{13}C NMR (151 MHz, $CDCl_3$) δ 170.6 (CO), 169.7 (CO), 82.0 ($\underline{C}(CH_3)_3$), 81.8 ($\underline{C}(CH_3)_3$), 51.5 (cyclen CH_2), 49.4 (cyclen CH_2), 47.6 (cyclen CH_2), 28.4 ($C(\underline{C}H_3)_3$), 28.3 ($C(\underline{C}H_3)_3$); ESI-HRMS (+) calcd for $[C_{26}H_{51}N_5O_6]^+$ 515.3809, found 515.3809.

1,4,7-Tris(*tert*-butoxycarbonylmethyl)-10-(2-(dipicolylaminomethyl)-3-*tert*-butyl-pyridin-6-yl) methyl-1,4,7,10-tetraazacyclododecane, L^7

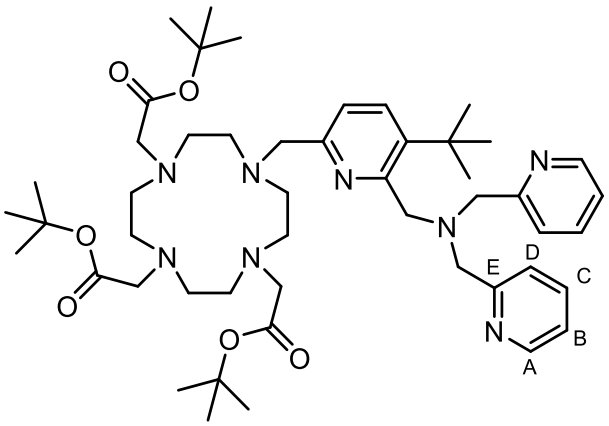

1,4,7-Tris(*tert*-butoxycarbonylmethyl)-1,4,7,10-tetraazacyclododecane (463 mg, 0.9 mmol) was dissolved in anhydrous MeCN (1 mL) and to this was added Cs_2CO_3 (359 mg, 1.1 mmol). (2-(Dipicolylaminomethyl)-3-*tert*-butyl-pyridin-6-yl) methyl methanesulfonate (346 mg, 0.83 mmol) was then added dropwise as a solution in anhydrous MeCN (2 mL). The resulting solution was heated to 70^{o}C and stirred for 18 h before being cooled to room temperature and filtered to remove inorganic salts. The solvent was removed under reduced pressure and the resulting oil was purified by alumina gel column chromatography (100% CH_2Cl_2 to 2% MeOH/ CH_2Cl_2) to yield an orange oil (450 mg, 62%). R_f (10% MeOH/ CH_2Cl_2) = 0.56; ^{1}H NMR (700 MHz, $CDCl_3$) δ 8.54 (d, ^3J = 5, 2H, H^A), 7.95 (d, ^3J = 8.5, 1H, H^4), 7.89 (m, ^3J = 8, ^4J = 2, 2H, H^B), 7.70 (d, ^3J = 8.5, 1H, H^5), 7.53 (d, ^3J = 8, 2H, H^D), 7.46 – 7.42 (m, 2H, H^C), 4.86 (s, 2H, NCH_2py), 4.65 (s, 4H, NCH_2py), 3.98 (s, 2H, NCH_2py), 3.56 – 2.79 (m, 22H, cyclen CH_2, NCH_2CO_2H), 1.32 (s, 9H, $C(CH_3)_3$); ESI-LCMS (+) *m/z* 873.0 $[M+H]^+$; ESI-HRMS (+) calcd for $[C_{54}H_{77}N_6O_4]^+$ 873.6006, found 873.5986.

Dysprosium (III) complex of 1,4,7-tris(acetic acid)-10-(2-(dipicolylaminomethyl)-3-*tert*-butyl-pyridin-6-yl) methyl-1,4,7,10-tetraazacyclododecane, [DyL^7]

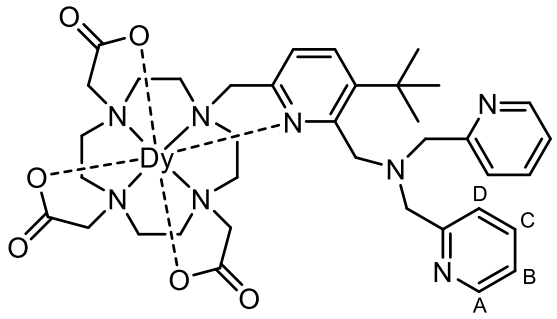

1,4,7-Tris(*tert*-butoxycarbonylmethyl)-10-(2-(dipicolylaminomethyl)-3-*tert*-butyl-pyridin-6-yl) methyl-1,4,7,10-tetraazacyclododecane (54 mg, 0.06 mmol) was dissolved in DCM (1 mL) and to this was added TFA (1 mL). The resulting solution was stirred at room temperature for 18 h. Complete ester cleavage was confirmed by ESI-MS (+) (LR: *m/z* 705.5 $[M+H]^+$). The solvent was removed under reduced pressure and the resulting residue was dissolved in H_2O (2 mL) and $DyCl_3{\cdot}6H_2O$ (34 mg, 0.09 mmol) was added. The pH of the resulting solution was adjusted to 5.5 using aqueous NaOH solution (2.5 M) and the reaction was stirred at 70^{o}C for 18 h before the solvent was removed under reduced pressure. The resulting yellow solid was purified by reverse-phase HPLC (10-100% MeCN in H_2O over 10 min; t_R = 8.0 min) to yield a glassy white solid (29 mg, 56%). ESI-LCMS (+) *m/z* 865.5 $[M+H]^+$; ESI-HRMS (+) calcd for $[C_{37}H_{50}N_8O_6{}^{160}Dy]^+$ 862.3105, found 862.3134.

Crystals of the dysprosium complex were grown by slow diffusion of diethyl ether into a solution of methanol and examined by X-ray crystallography: $C_{37}H_{49}DyN_8O_6$ x 2 CH_3OH, M_r = 928.42 g/mol, monoclinic, space group $P2_1/n$ (no. 2), a = 8.8025(5) Å, b = 14.0452(8) Å, c = 32.4607(18) Å, α = 90, β = 96.282(2), γ = 90, V = 3989.1(4) Å^3, Z = 4, T = 120 K, μ(MoKα) = 1.935 mm^{-1}, D_{calc} = 1.546 g/cm^3, 56391 reflections measured (4.688° ≤ 2Θ ≤ 58.998°), 11107 unique (R_{int} = 0.0607, R_{sigma} = 0.0577) which were used in all calculations. The final R_1 was 0.0674 (I > 2σ(I)) and wR_2 was 0.0855 (all data).

[TmL^7]

An analogous procedure to that described for the synthesis of [DyL^7] was followed using 1,4,7-tris(acetic acid)-10-(2-(dipicolylaminomethyl)-3-*tert*-butyl-pyridin-6-yl)

methyl-1,4,7,10-tetraazacyclododecane (6 mg, 0.009 mmol) and $TmCl_3 \cdot 6H_2O$ (6 mg, 0.016 mmol), to yield a white solid (5 mg, 68%). ESI-LCMS (+) *m/z* 871.3 $[M+H]^+$; ESI-HRMS (+) calcd for $[C_{37}H_{50}N_8O_6{}^{169}Tm]^+$ 871.3196, found 871.3220.

[TbL^7]

An analogous procedure to that described for the synthesis of [DyL^7] was followed using 1,4,7-tris(acetic acid)-10-(2-(dipicolylaminomethyl)-3-*tert*-butyl-pyridin-6-yl) methyl-1,4,7,10-tetraazacyclododecane (54 mg, 0.06 mmol) and $TbCl_3 \cdot 6H_2O$ (34 mg, 0.09 mmol), to yield a white solid (28 mg, 54%). ESI-LCMS (+) *m/z* 861.3 $[M+H]^+$; ESI-HRMS (+) calcd for $[C_{37}H_{50}N_8O_6{}^{159}Tb]^+$ 861.3107, found 861.3130.

[EuL^7]

An analogous procedure to that described for the synthesis of [DyL^7] was followed using 1,4,7-Tris(acetic acid)-10-(2-(dipicolylaminomethyl)-3-*tert*-butyl-pyridin-6-yl) methyl-1,4,7,10-tetraazacyclododecane (18 mg, 0.02 mmol) and $EuCl_3 \cdot 6H_2O$ (18 mg, 0.05 mmol), to yield a white solid (10 mg, 59%). ESI-LCMS (+) *m/z* 855.4 $[M+H]^+$; ESI-HRMS (+) calcd for $[C_{37}H_{50}N_8O_6{}^{151}Eu]^+$ 853.3052, found 853.3092.

[YbL^7]

An analogous procedure to that described for the synthesis of [DyL^7] was followed using 1,4,7-tris(acetic acid)-10-(2-(dipicolylaminomethyl)-3-*tert*-butyl-pyridin-6-yl) methyl-1,4,7,10-tetraazacyclododecane (54 mg, 0.06 mmol) and $YbCl_3 \cdot 6H_2O$ (27 mg, 0.09 mmol), to yield a white solid (27 mg, 57%). ESI-LCMS (+) *m/z* 791.2 $[M+H]^+$; ESI-HRMS (+) calcd for $[C_{37}H_{50}N_8O_6{}^{170}Yb]^+$ 872.3201, found 872.3242.

[YL^7]

An analogous procedure to that described for the synthesis of [DyL^7] was followed using 1,4,7-tris(acetic acid)-10-(2-(dipicolylaminomethyl)-3-*tert*-butyl-pyridin-6-yl) methyl-1,4,7,10-tetraazacyclododecane (54 mg, 0.06 mmol) and $YCl_3 \cdot 6H_2O$ (27 mg, 0.09 mmol), to yield a white solid (27 mg, 57%). ESI-LCMS (+) *m/z* 791.2 $[M+H]^+$; ESI-HRMS (+) calcd for $[C_{37}H_{50}N_8O_6{}^{89}Y]^+$ 791.2912, found 791.2921. ^{1}H NMR (700 MHz, D_2O) δ 8.60-6.81 (br, m, 6H, H^A, H^C, H^D), 7.94 (d, ^3J = 8, 1H, H^4), 7.68 (m, 2H, H^B), 7.30

(d, ^3J = 8, 1H, H^5), 7.53 (d, ^3J = 8, 2H, H^D), 4.85 – 3.72 (br, m, 11H, NCH_2py, $NC\underline{H}_2CO_2H$) 3.62 – 2.07 (br, m, 19H, cyclen CH_2, $NC\underline{H}_2CO_2H$), 1.25 (s, 9H, $C(CH_3)_3$); ESI-LCMS (+) *m/z* 873.0 $[M+H]^+$; ESI-HRMS (+) calcd for $[C_{54}H_{77}N_6O_4]^+$ 873.6006, found 873.5986.

$[Zn_2L^7]Cl$

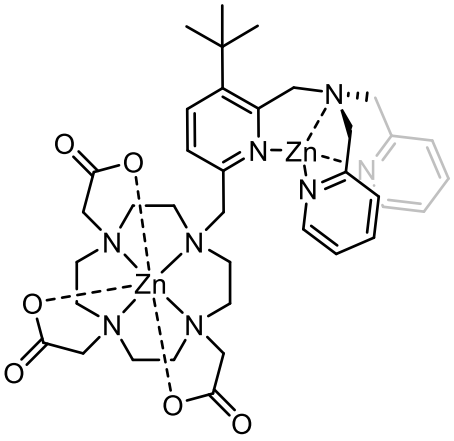

$ZnCl_2$ (3 eq.) was added to a solution of the yttrium(III) complex of 1,4,7-tris(acetic acid)-10-(2-(dipicolylaminomethyl)-3-*tert*-butyl-pyridin-6-yl)-methyl-1,4,7,10-tetraazacyclododecane (1 eq.) in D_2O (0.5 mL). The resulting solution was centrifuged and the white precipitate was isolated and washed with water (2 mL), methanol (2 mL) and dichloromethane (5 mL). ESI-LCMS (+) *m/z* 833.3 $[M]^+$.

Crystals of the di-Zinc complex were grown by slow diffusion of diethyl ether into a solution of methanol containing 1 eq. of hexafluorophosphate and examined by X-ray crystallography: $C_{37}H_{49}N_8O_6Zn_2$ x Cl x 6 CH_3OH x H_2O, M_r = 1078.30 g/mol, monoclinic, space group $P2_1/C$ (no. 14), a = 20.8675(15) Å, b = 15.3507(11) Å, c = 16.1152(12) Å, β = 94.545(2), V = 5146.0(6) $Å^3$, Z = 4, T = 120 K, μ(MoKα) = 1.051 mm^{-1}, D_{calc} = 1.392 g/cm^3, 77628 reflections measured (4.064° ≤ 2Θ ≤ 50.052°), 9090 unique (R_{int} = 0.0593, R_{sigma} = 0.0383) which were used in all calculations. The final R_1 was 0.0677 (I > 2σ(I)) and wR_2 was 0.1722 (all data).

6.10 References

1 O. V. Dolomanov, L. J. Bourhis, R. J. Gildea, J. A. K. Howard and H. Puschmann, *J. Appl. Crystallogr.*, 2009, **42**, 339–341.

2 G. M. Sheldrick, *Acta Crystallogr. Sect. A Found. Crystallogr.*, 2015, **71**, 3–8.

3 G. M. Sheldrick, *Acta Crystallogr. Sect. C Struct. Chem.*, 2015, **71**, 3–8.

4 Lee, Yang and Parr, *Phys. Rev. B. Condens. Matter*, 1988, **37**, 785–789.

5 A. D. Becke, *J. Chem. Phys.*, 1993, **98**, 5648–5652.

6 J. Binkley and J. Pople, *J. Am. Chem. Soc.*, 1980, **102**, 939–47.

7 W. J. Pietro, M. M. Francl, W. J. Hehre, D. J. Defrees, J. A. Pople and J. S. Binkley, *J. Am. Chem. Soc.*, 1982, **104**, 5039–5048.

8 M. S. Gordon, J. S. Binkley, J. A. Pople, W. J. Pietro and W. J. Hehre, *J. Am. Chem. Soc.*, 1982, **104**, 2797–2803.

9 K. D. Dobbs and W. J. Hehre, *J. Comput. Chem.*, 1986, **7**, 359–378.

10 K. Dobbs and W. Hehre, *J. Comp. Chem.*, 1987, **8**, 861–879.

11 D. J. Frisch, M. J.; Trucks, G.W.; Schlegel, H. B.; Scuseria, G. E.; Robb, M. A.; Cheeseman, J. R.; Scalmani, G.; Barone, V.;Mennucci, B.; Petersson, G. A.; Nakatsuji, H.; Caricato, M.; Li, X.; Hratchian, H. P.; Izmaylov, A. F.; Bloino, J.; Zheng, G.; Sonnenber, *Gaussian, Inc. Wallingford CT*, 2009.

12 E. R. Neil, M. A. Fox, R. Pal, L.-O. O. Pålsson, B. A. O'Sullivan and D. Parker, *Dalton Trans.*, 2015, **44**, 14937–14951.

13 J. Tomasi, B. Mennucci and E. Cancès, *J. Mol. Struct. THEOCHEM*, 1999, **464**, 211–226.

14 Y. Zhao and D. G. Truhlar, *Theor. Chem. Acc.*, 2008, **120**, 215–241.

15 D. Andrae, U. Haeussermann, M. Dolg, H. Stoll and H. Preuss, *Theor. Chim. Acta*, 1990, **77**, 123–141.

16 K. Mason, N. J. Rogers, E. A. Suturina, I. Kuprov, J. A. Aguilar, A. S. Batsanov, D. S. Yufit and D. Parker, *Inorg. Chem.*, 2017, **56**, 4028–4038.

17 R. Dennington, T. Keith and J. Millam, *Semichem Inc. , Shawnee Mission. KS*, 2009.

Appendix

Comparison of tri- and dibenzylphosphinate complexes

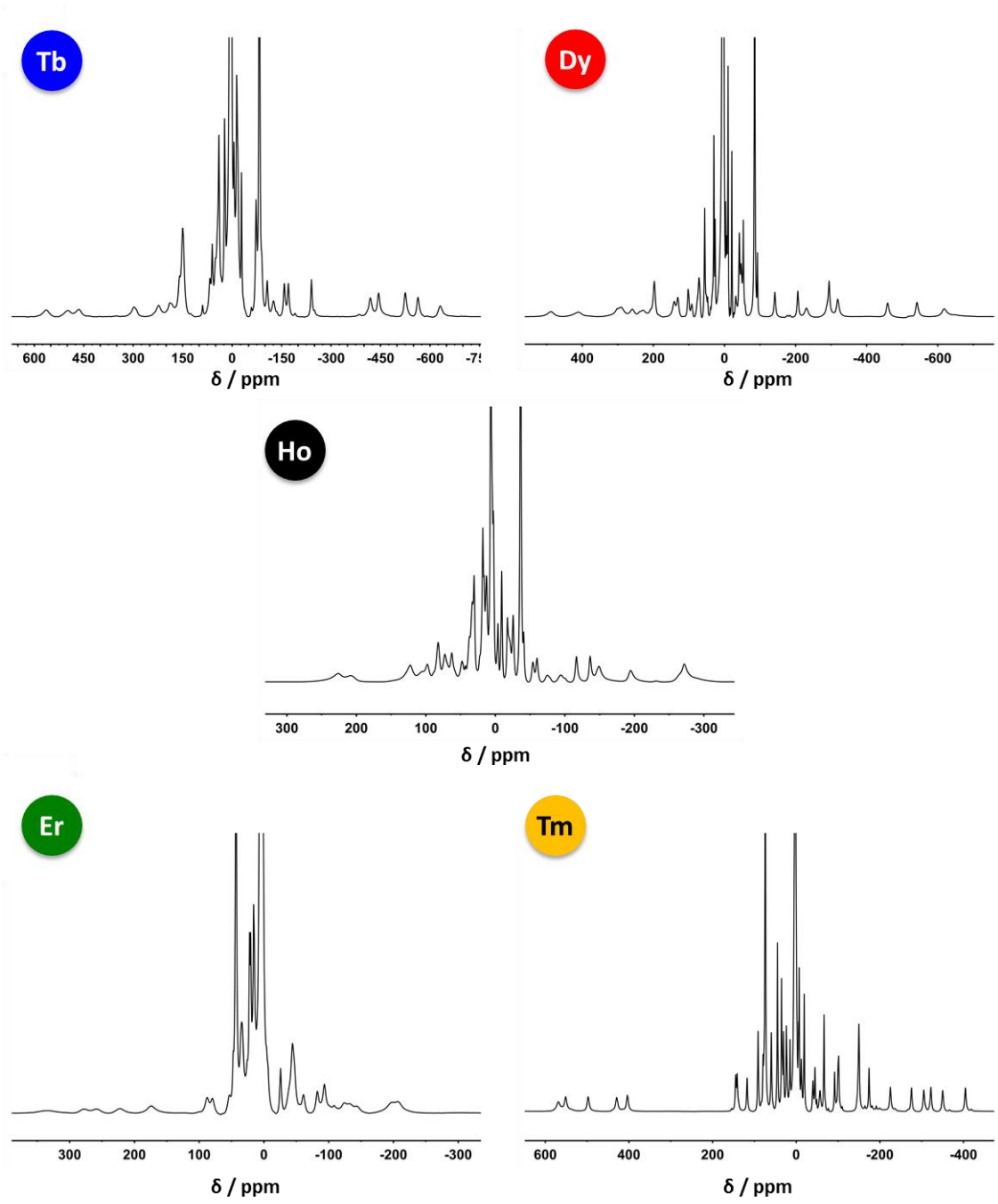

Figure S1 ^{1}H NMR spectra of the phosphinate resonances of **[LnL^{4}]** (CD_3OD, 1 T, 295 K).

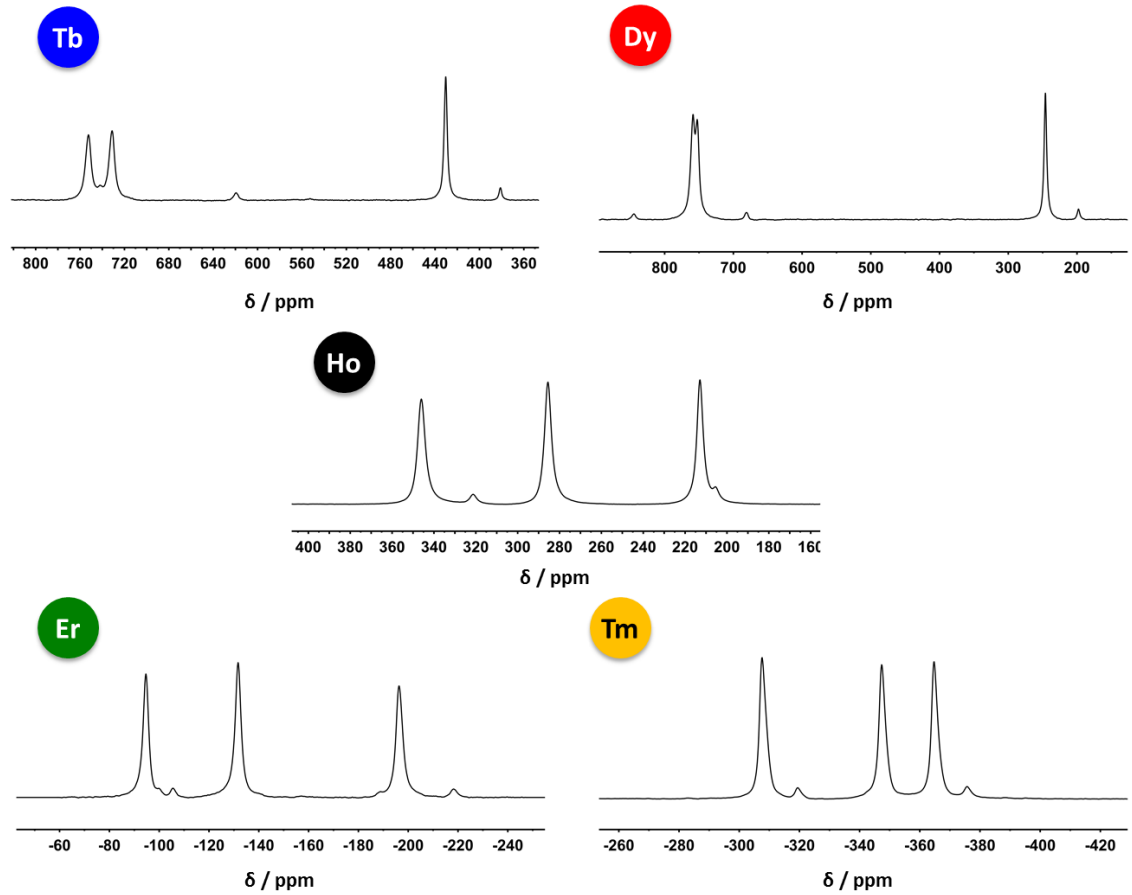

Figure S2 ^{31}P NMR spectra of the phosphinate resonances of **[LnL^4]** (CD_3OD, 4.7 T, 295 K).

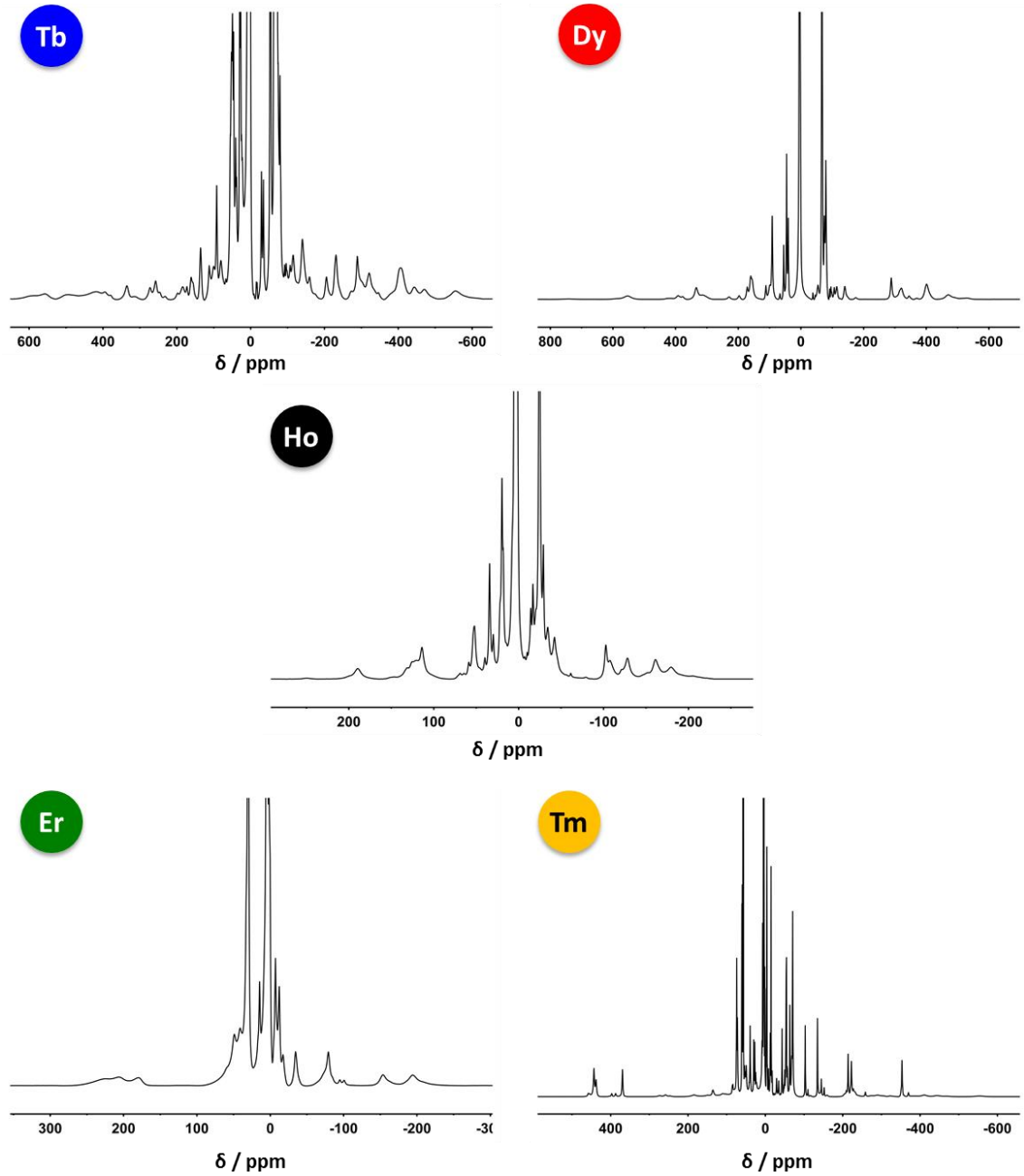

Figure S3 ^{1}H NMR spectra of the phosphinate resonances of **[LnL^{5}]Cl** (CD_3OD, 1 T, 300 K).

Table S1 Assigned proton chemical shifts of **[LnL^4]** excluding benzyl resonances (CD_3OD, 1 T, 300 K).

Proton Label	[YL^4]	[YbL^4]	[TbL^4]	[DyL^4]	[ErL^4]	[TmL^4]
py3	7.45	9.6			-25.9	
py4	8.05					
py6	9.04	144.7	-631.5	-619.0	331.4	570.8
tbu	1.39	20.2	-82.6	-85.0	44.2	76.0
c1ax	3.69	-40.8	189.4		-108.3	-146.4
c1eq	2.5			-46.9		61.6
c2ax	3.81	52.9	-555.8	-459.1	220.9	405.7
c2eq	2.59		-106.3	-46.9		93.2
c3ax	3.56	-18.3	184.0	290.5	-54.8	-223.3
c3eq	2.43		-158.1	-41.6		93.2
c4ax	3.85	122.4	-563.6	-619.0	276.8	553.2
c4eq	2.5	49.8	-240.5	-206.4	87.6	143.1
c5ax	3.6	38.7		-230.6		-55.0
c5eq	2.33	56.6	-170.6	-294.4	79.2	146.7
c6ax	4.27	102.8	-444.1	-541.7	257.9	499.5
c6eq	2.45	36.3		-141.8		119.5
c7ax	3.56	-73.0	465.5	489.3	-196.7	-273.7
c7eq	2.36	-5.7		91.86		35.1
c8ax	3.21	47.6	-419.2	-318.9	172.6	431.1
c8eq	2.51			50.8		61.6
apax	4.72	-57.7	564.3	412.5	-208.0	-402.8
apeq	3.72			131.2	-93.5	-99.6
a1ax	3.67	-71.4	222.6	290.5	-133.1	-320.2
a1eq	2.52			197.1	-61.9	-147.8
a2ax	4.04	-39.3	498.6	259.5	-144.1	-348.5
a2eq	2.54	16.3		-52.5		-90.0
a3ax	2.95	-50.8	298.7	228.4	-124.0	-303.2
a3eq	2.44			197.1	-82.5	-148.5

Table S2 Assigned proton chemical shifts of **[LnL^5]Cl** excluding benzyl resonances (CD_3OD, 1 T, 300 K).

Proton Label	[YL^5]Cl	[YbL^5]Cl	[TbL^5]Cl	[DyL^5]Cl	[ErL^5]Cl	[TmL^5]Cl
py3	7.60	13.2		-76.6		-54.6
py4	8.22	14.8		-81.2	14.5	1.6
py6	8.94	63.5	-565.5	-470.5	225.6	438.1
tbu	1.39	9.3	-72.1	-66.8	30.0	57.4
c1ax	3.84	44.1	-414.5	-320.9	179.7	369.6
c1eq	2.58		-142.4	-54.2	49.2	74.2
c2ax	4.25	32.5	-406.8	-401.7		-67.9
c2eq	2.64	25.8	-234.0	-288.2	49.2	74.2
c3ax	3.64	57.1	-447.3	-401.7	204.2	443.4
c3eq	2.53	15.5	-117.7	-114.4	41.2	72.3
c4ax	3.34	-50.7	553.8	553.5	-154.2	-214.0
c4eq	2.59	-6.4	78.0	99.7	7.5	39.5
apax	5.15	-27.2	255.0	312.5	-194.9	-353.3
apeq	3.87	13.74	413.9	-140.2	-34.9	-103.0
a1ax	3.06	-34.1		333.6	-73.7	-222.4
a1eq	2.56	-34.5		334.2	-79.5	-134.8

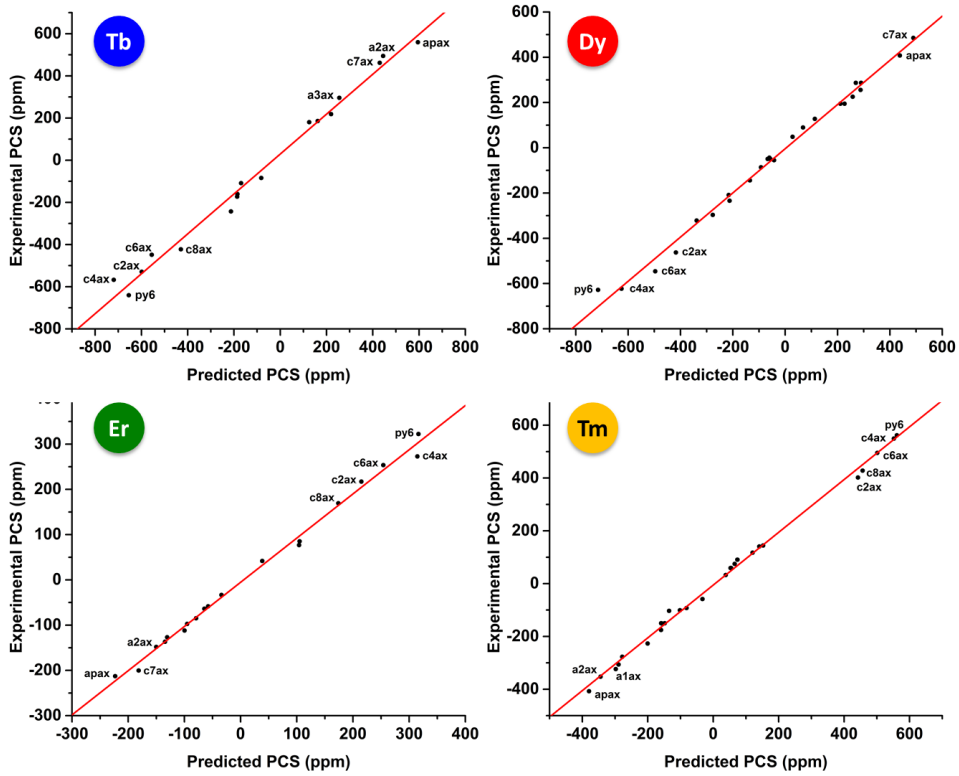

Figure S4 Comparison of the observed and 'best- fit' PCS values for **[LnL^4]**. Tm: R^2 = 0.996; Er: R^2 = 0.994; Dy: R^2 = 0.992; Tb: R^2 = 0.999. Assignments of selected resonances have been highlighted.

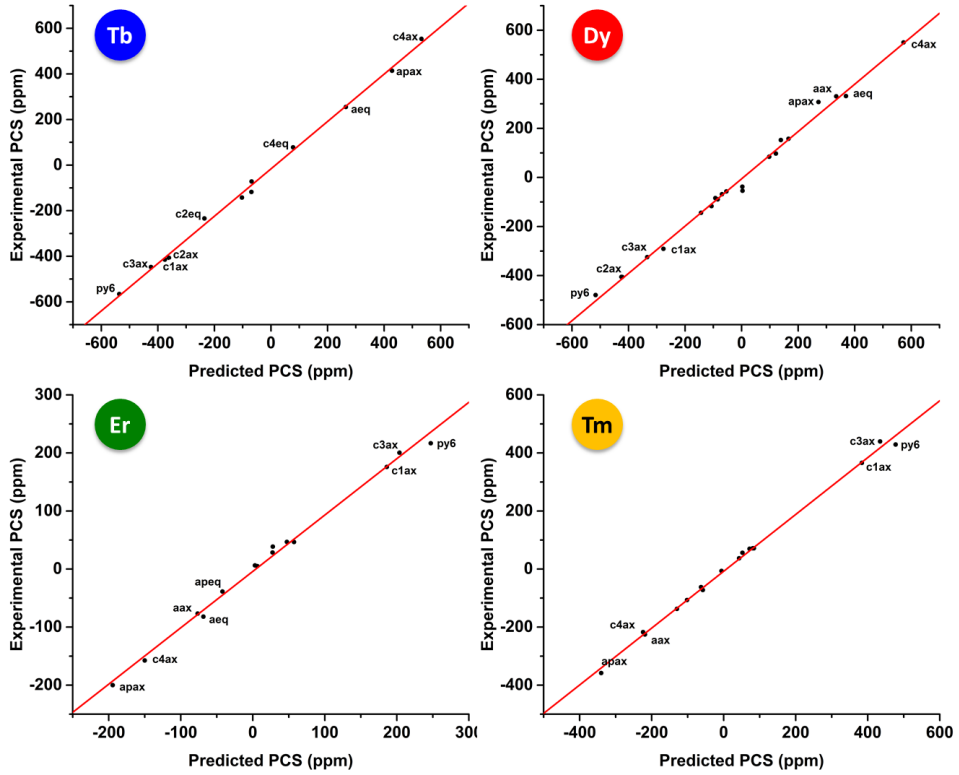

Figure S5 Comparison of the observed and 'best- fit' PCS values for **[LnL^5]Cl**. Tm: R^2 = 0.997; Er: R^2 = 0.995; Dy: R^2 = 0.994; Tb: R^2 = 0.998. Assignments of selected resonances have been highlighted.

Publications arising from PhD research

1. *Simultaneous Triple Imaging with Two PARASHIFT Probes: Encoding Anatomical, pH and Temperature Information using Magnetic Resonance Shift Imaging*, K.-L. N. A. Finney, A. C. Harnden, N. J. Rogers, P. K. Senanayake, A. M. Blamire, D. O'Hogain and D. Parker, *Chem. A Eur. J.*, 2017, **23**, 7976–7989.

2. *Exquisite sensitivity of the ligand field to solvation and donor polarisability in coordinatively saturated lanthanide complexes*, K. Mason, A. C. Harnden, C. W. Patrick, A. W. J. Poh, A. S. Batsanov, E. A. Suturina, M. Vonci, E. J. L. McInnes, N. F. Chilton and D. Parker, *Chem. Commun.*, 2018, **54**, 8486–8489.

3. *Employing Paramagnetic Shift for Responsive MRI Probes*, A.C. Harnden, N.J. Rogers and D. Parker, *Coord. Chem. Rev.*, 2019, **383**, 30-42.